Mechanical Properties and Failure Behavior of Resistance Spot Welded Third-Generation Advanced High Strength Steels

by

Mohammad Shojaee

A thesis
presented to the University of Waterloo
in fulfillment of the
thesis requirement for the degree of
Doctor of Philosophy
in
Mechanical and Mechatronics Engineering

Waterloo, Ontario, Canada, 2024

© Mohammad Shojaee 2024

Examining Committee Membership

The following served on the Examining Committee for this thesis. The decision of the Examining Committee is by majority vote.

External Examiner:	**Professor Ali Nasiri** Mechanical Engineering, Dalhousie University, Halifax, Nova Scotia, Canada
Supervisor(s):	**Professor Elliot Biro** Mechanical Engineering, University of Waterloo, Waterloo, Ontario, Canada
	Professor Cliff Butcher Mechanical Engineering, University of Waterloo, Waterloo, Ontario, Canada
Internal Member(s):	**Professor Hamid Jahed** Mechanical Engineering, University of Waterloo, Waterloo, Ontario, Canada
	Professor Adrian Gerlich Mechanical Engineering, University of Waterloo, Waterloo, Ontario, Canada
Internal-External Member:	**Professor Scott Walbridge** Civil and Environmental Engineering, University of Waterloo, Waterloo, Ontario, Canada

Author's Declaration

This thesis consists of material all of which I authored or co-authored: see Statement of Contributions included in the thesis. This is a true copy of the thesis, including any required final revisions, as accepted by my examiners.

I understand that my thesis may be made electronically available to the public.

Statement of Contributions

This thesis includes seven chapters, including the introduction (Chapter One) and literature review (Chapter Two), which were written based on available published literature. Chapters three through six include a series of published or under-review manuscripts the candidate authored. The manuscripts have been modified to best fit the style of a thesis. The candidate is the primary author of all the manuscripts mentioned above. The candidate performed the majority of the lab work, including preparation of the coupons, process optimization, experimental design, welding, metallographic preparation, mechanical testing, and microstructural characterization except where noted. The candidate wrote the original draft of all published and under review manuscripts and revised them according to input from all co-authors and journal reviewers. The following co-authors have made specific contributions to the present work, as described below:

Professor Elliot Biro, Professor Cliff Butcher, and Professor Michael Worswick from the University of Waterloo supervised the research progress, advised on research direction, offered technical discussions, assisted with data analysis, and reviewed and revised the manuscripts.

Dr. Hassan Ghassemi-Armaki from General Motors R&D, Michigan, USA, and Dr. TingTing Zhang, from Metallics & Joining of General Motors, Michigan, USA, acted as industrial supervisors, provided the materials, financially supported the project, reviewed, and commented on the manuscripts. Eric McCarty from Auto/Steel Partnership acted as industrial project manager.

Chapter 3

Shojaee M, Midawi ARH, Barber B, Ghassemi-Armaki H, Worswick M, Biro E. Mechanical properties and failure behavior of resistance spot welded third-generation advanced high strength steels. J Manuf Process 2021;65:364–72. https://doi.org/10.1016/j.jmapro.2021.03.047.

The candidate's contribution was as described above. Dr. Midawi provided technical discussions, reviewed the manuscript, conducted base material tensile testing, and assisted with welding and weld lobe development. Barber B. assisted with welding and weld lobe development. Dr. Ghassemi-Armaki, Prof. Worswick, and Prof. Biro's roles were described above.

Chapter 4

Shojaee M, Tolton C, Midawi ARH, Butcher C, Ghassemi-Armaki H, Worswick M, Biro E. Influence of loading orientation on mechanical properties of spot welds. Int J Mech Sci 2022;224:107327. https://doi.org/10.1016/j.ijmecsci.2022.107327.

The candidate's contribution was as described above. Tolton C. proposed the triangulation methodology, wrote the initial MATLAB code for calculating nugget orientation, and assisted with KS-II mechanical testing and DIC setup. Dr. Midawi ARH. was involved in technical discussions and assisted with KS-II coupon preparation, welding, and mechanical testing. The roles of Prof. Butcher, Dr. Ghassemi-Armaki, Prof. Worswick, and Prof. Biro were described above.

Chapter 5

M. Shojaee, Tolton C, Midawi ARH, Zhang T, Ghassemi-Armaki H, Worswick M, Butcher C, Biro E, An experimental methodology to characterize load-based fracture models of third generation advanced high strength steel resistance spot welds, Int. J. Adv. Manuf. Technol. (2024) 1–23. https://doi.org/10.1007/s00170-024-13438-6.

The candidate's contribution was as described above. Tolton assisted with KS-II mechanical testing and DIC setup. Dr. Midawi was involved in technical discussions and assisted with KS-II coupon preparation, welding, and mechanical testing. Dr. Zhang, Dr. Ghassemi-Armaki, Prof. Worswick, Prof. Butcher, and Prof. Biro's roles were described above.

Chapter 6

Shojaee M, Betiku O.T, Tolton C, Midawi ARH, Ramachandran D, Zhang T, Ghasssemi-Armaki H, Worswick M, Butcher C, Biro E. Investigating the mechanical properties and failure behavior of groups of resistance spot welds under tensile-bending loading conditions (under review).

The candidate's contribution was as described above. Betiku assisted with EBSD post-processing and hardness testing and was involved in technical discussions. Tolton assisted with Caiman mechanical testing and thermal, optical, and DIC camera setup. Dr. Midawi assisted with coupon

preparation, welding, and Caiman mechanical testing and operated the instrumented indentation equipment. Dr. Ramachandran assisted in EBSD post-processing and was involved in technical discussions. Dr. Zhang, Dr. Ghassemi-Armaki, Prof. Worswick, Prof. Butcher, and Prof. Biro's roles were described above.

Abstract

Acceptable crash performance and fuel efficiency are vital requirements for any modern automobile. To meet these requirements, the automotive industry is designing lighter vehicles by further adopting third-generation advanced high strength steels (3G-AHSS) within their vehicle assemblies. 3G-AHSS possess multiphase microstructures that provide a favorable combination of strength-ductility relative to existing commercial AHSS. A safe and reliable migration to 3G-AHSS within automotive body-in-white (BIW) structure demands, among other requirements, the ability to predict the onset of failure from components fabricated using common joining techniques such as resistance spot welding (RSW). A fast and reliable approach for RSW failure prediction within the automotive industry is utilizing force-based RSW failure criteria that are calibrated using critical loads/moments at the onset of RSW failure from various mechanical tests. Aside from conventional tensile shear (TS) and cross tension (CT) mechanical tests, characterizing the 3G-AHSS RSW failure strength components at various complex loading conditions can improve the calibration accuracy of experimental RSW failure loci. Some of such complex loading conditions include various ratios of shear-tension loading, characterized by KS-II tests, and tension-bending loading mode, characterized by coach peel (CP) tests. Accurate quantification of RSW mechanical performance indices, such as load-bearing capacity and energy absorption capability from single spot weld characterization technique is accompanied by unique challenges due to rotation of the joint and plastic work due to coupon deformation at regions away from the joint during mechanical testing. The influence of such unintended phenomena on extracted mechanical performance indices is commonly acknowledged but not accounted for.

In this research program, the RSW process parameters were optimized for two grades of 3G-AHSS, referred to as 3G-980 and 3G-1180, via the development of a weldability lobe, and performing traditional TS and CT mechanical tests for various RSW nugget diameters while following the welding schedule recommended by AWS D8.9 standard. Thereafter, the mechanical performance of optimized and sub-optimal 3G-AHSS spot welds were characterized under various combinations of shear/tension loading ratios as well as different combinations of tension-bending loading modes. The rotation and slippage of combined loading specimens within the testing fixtures posed a challenge leading to overestimation of spot weld performance indices, such as failure load components and absorbed energy during failure. These challenges were overcome via

quantification of rotation during mechanical tests and proposing novel post-processing methodologies that approximate local nugget displacement fields by coupling tests with stereoscopic digital image correlation (DIC) techniques. Upon attainment of critical load components and moments at various shear-tension and tension-bending loading modes, the accuracy of various force-based RSW failure criteria was evaluated independently. It was shown experimentally that while the commonly used force-based RSW failure criteria, proposed by Seeger, is fairly accurate in shear-tension loading mode, it loses accuracy by a relatively large margin in determining critical bending moments the spot welds withstand at the onset of failure. Alternative mathematical functional forms of RSW failure loci were proposed that can be readily implemented in finite element analysis for the potential improvement of 3G-AHSS RSW failure predictions. Calculations related to quantifying the energy absorption capability of the joints showed that brittle propagation of cracks into the columnar structure of fusion zone (FZ), leading to partial interfacial- partial pullout failure, significantly limits the post-failure energy absorption capability of the investigated joints in both shear-tension and tensile-bending loading conditions.

The understanding of single spot weld characterization techniques were expanded to weld group (component) tests that evaluate the mechanical performance and failure characteristics as groups of spot welds separate under tensile-bending loading conditions. It was shown that the energy absorption capability of groups of spot welds is a function of the extent to which the base materials involved in the tests dissipate energy by plastically deforming throughout the tests, as well as the failure mode of the spot welds. The components made of the more ductile 3G-980 material exhibited superior energy absorption capability due to a higher degree of parent metal deformation and ductile pullout failure mode compared with the less parent metal plastic work and partial pullout failure of components from 3G-1180 material.

This research program is comprised of various sections including the 3G-AHSS RSW process optimization, detailed microstructural characterizations of optimized joints, mechanical performance and failure characterization of the joints under combined shear-tensile loading using KS-II tests, tensile-bending loading using various geometries of CP test, weld-group tests, and novel post-processing techniques used for improving the accuracy of force-based RSW failure criteria, which were the key takeaways of this research.

Acknowledgments

I want to thank my Supervisors, Professor Elliot Biro and Professor Cliff Butcher, for their invaluable guidance, constant support, and expertise throughout my doctoral journey. Their insightful feedback and criticisms have been integral in shaping my research, and I sincerely appreciate the time they have dedicated to mentoring me. Ironically, while significant, the feedback from journal reviewers seemed somewhat trivial compared to the thorough internal critiques. The guidance of my supervisors strengthened the quality of my research and equipped me with a deeper understanding of scholarly discourse.

I would also like to extend my appreciation to Professor Michael Worswick. Although not officially my supervisor, Professor Worswick played a pivotal role throughout my research endeavors. I am immensely thankful for his keen insights and willingness to engage in rigorous discussions about my work. His comments on my work have been instrumental in broadening my perspectives, and I am fortunate to have benefited from his mentorship alongside my supervisors.

I want to thank the Auto/Steel Partnership (ASP) team members, especially my project's industrial supervisors, Dr. Hassan Ghassemi-Armaki, Dr. Tingting Zhang, and Eric McCarty. The thoughtful comments and challenging discussions throughout numerous update meetings with the ASP members fostered a collaborative environment to exchange ideas and push the boundaries of innovation. I extend my sincerest appreciation for their support and guidance throughout my program.

I am grateful to our postdoctoral researcher, Dr. Baset Midawi, and my friend Cameron Tolton, with whom I have extensively collaborated for the last five years. When I first embarked on my studies as a master’s student at the University of Waterloo, my knowledge in the field of material science was limited. Under Dr. Baset’s guidance and cooperation with Cameron, I underwent a transformative experience that significantly boosted my learning pace. I am profoundly thankful for Dr. Baset and Cameron’s assistance throughout the years and look forward to our lifelong friendship moving forward.

I am grateful for all the friends I made during my PhD endeavor at the Centre for Advanced Materials Joining (CAMJ), especially Dileep, Kunle, and Ji, with whom I shared an office. Your friendship has brought laughter, joy, and camaraderie amidst all the academic challenges. I hope our friendships grow stronger with each passing year. I want to thank all my friends: Bruna, Chris, Josh, Brendan, Kate, Advaith, Ali, Shadab, Shima, Mohammadreza, Adib, Meet, and many more.

Lastly, I am profoundly grateful to my parents and younger sister for their unwavering support, love, and understanding. Their encouragement and sacrifices have been the cornerstone of my academic journey.

Dedication

To my beloved mother, father, and little sister. This achievement is as much yours as it is mine.

Table of Contents

Examining Committee Membership ii
Author's Declaration iii
Statement of Contributions iv
Abstract vii
Acknowledgments ix
Dedication xi
List of Tables xxvi
List of Abbreviations xxviii
1 Chapter 1: Introduction 1
1.1 Background 1
1.2 Objectives 2
1.3 Thesis outline 4
2 Chapter 2: Literature Review 5
2.1 Overview 5
2.2 Three Generations of Advanced High Strength Steels 5
2.2.1 Dual-Phase (DP) AHSS 6
2.2.2 Quenched & Partitioned (Q&P) AHSS 7
2.3 Resistance Spot Welding (RSW) Process 10
2.3.1 Evolution of Resistance During RSW Process 11
2.3.2 RSW Process Parameters 13
2.4 RSW Joint Quality 16
2.4.1 Physical Attributes of RSW Joints 17
2.4.2 Metallurgical Characteristics of RSW Joints 18
2.4.3 Mechanical Properties of RSW Joints 23
2.4.4 Failure Behavior of RSW Joints 35
2.5 Failure Prediction in RSW Joints 39
2.5.1 Analytical/Geometrical Models for RSW Failure Prediction 39
2.5.2 Finite Element Models for RSW Failure Prediction 40
2.5.3 Strength-based Criteria for RSW Failure Prediction 43
2.6 General Remarks 47
3 Chapter 3: Spot Weld Process Development and Baseline Characterizations 48
3.1 Overview 48

3.2 Background 48
3.3 Materials and Methods 50
3.3.1 As-received Materials 50
3.3.2 Resistance Spot Welding 52
3.3.3 Tensile Shear and Cross Tensile Mechanical Tests 53
3.3.4 Microstructural Characterization 54
3.4 Results and Discussions 55
3.4.1 Spot Weldability Lobes 55
3.4.2 Spot Weld Optimization by TS and CT tests 56
3.4.3 Optimized (FDWS) and Sub-optimal (MWS) Weld Conditions 60
3.4.4 Microstructural Evolution of the Welds 61
3.4.5 Summary 65
4 Chapter 4: Combined Shear-tensile Loading of Spot Welds via KS-II tests 67
4.1 Overview 67
4.2 Background 68
4.3 Materials and Methods 70
4.3.1 As-received Materials 70
4.3.2 Resistance Spot Welding 70
4.3.3 KS-II Testing 71
4.3.4 Digital Image Correlation 74
4.3.5 Fracture Analysis by Interrupted Tests 81
4.4 Results and Discussions 82
4.4.1 Spot Weld Loading Histories 82
4.4.2 Failure Modes 84
4.4.3 Failure Path Characterization by Interrupted Tests 86
4.4.4 Energy Absorption Capability 91
4.4.5 Comparison of KS-II with TS and CT tests 95
4.5 Summary 97
5 Experimental Characterization of Load-based Fracture Models for 3G-AHSS Resistance Spot Welds in Shear-tensile and Tensile-bending Loading Conditions 100
5.1 Overview 100
5.2 Background 101
5.3 Materials and Methods 102

5.3.1 As-received Materials 102
5.3.2 Resistance Spot Welding 102
5.3.3 Digital image correlation 103
5.3.4 CP tests to characterize combined bending and tensile loading 103
5.3.5 KS-II tests to characterize combined shear and tensile loading 110
5.4 Results and Discussions 111
5.4.1 CP Mechanical Test Results 111
5.4.2 KS-II Mechanical Test Results 117
5.4.3 Calibration of RSW Failure Loci 120
5.5 Summary 130
6 Characterization of Weld Group Failure under Predominantly Tensile-bending Loading 133
6.1 Overview 133
6.2 Background 134
6.3 Materials and Methods 135
6.3.1 As-received Materials 135
6.3.2 Resistance Spot Welding 135
6.3.3 Caiman Mode I Mechanical Test 135
6.3.4 Double-half CP (DHCP) Mechanical Test 137
6.3.5 Metallurgical and Mechanical Characterizations 139
6.4 Results 140
6.4.1 DHCP Test Results 140
6.4.2 Caiman Test Results 144
6.5 Discussions 153
6.5.1 Correlation Between Failure Behavior and Local Mechanical/Metallurgical Characteristics of the Joints 154
6.6 Summary 159
7 Conclusions and Future Recommendations 162
7.1 Conclusions 162
7.2 Areas of Future Research and Recommendations 163
References 166
Appendix A: In-situ Tracking of Projected Nugget Orientation Throughout CP Tests 190

List of Figures

Figure 2.1. Comparison of ultimate tensile strength vs elongation graph for mild steels, high strength steels (HSS), and three different generations of AHSS [13]..... 5
Figure 2.2. (a) Schematic diagram of the processing of a DP AHSS [10], and (b) scanning electron micrograph showing the final microstructure of DP980; F, ferrite; M, martensite [5]. 7
Figure 2.3. (a) Schematic diagram of the processing of a Q&P AHSS (A_{c1} and A_{c3} are austenitization start and finish temperatures; M_s and M_f are martensite start and finish temperatures; C_i, C_γ, C_m represent the carbon content of the initial alloy, austenite, and martensite respectively [14]), and (b) scanning electron micrograph showing the final attained microstructure of Q&P980 (F, ferrite; M, martensite; TM, tempered martensite; RA, retained austenite [5]). 8
Figure 2.4. Contributions of “austenite +martensite” and ‘‘ferrite +martensite” microstructural combinations to the mechanical properties of AHSS [14], (b) schematic illustration of TRIP effect during deformation responsible for superior properties of “austenite +martensite” microstructure [25]. 9
Figure 2.5. (a) Assessing the effect of austenite stability against transformation to martensite with strain for four hypothetical materials (material A possesses the most stable austenite as the transformation to martensite occurred at higher strain values, whereas material D has the least stable austenite that transformed to martensite at lower strains). (b) Mechanical property combinations corresponding to ferrite and austenite with different stabilities are outlined in (a) [10]. 10
Figure 2.6. Schematic representation of different stages of RSW process. 11
Figure 2.7. (a) Resistances encountered during RSW and their corresponding temperature distribution at different regions (adapted from [31]), (b) Correlation between dynamic resistance curve and different stages related to the formation of an RSW nugget [33]. 13
Figure 2.8. (a) Resistances encountered during RSW and their corresponding temperature distribution at different regions, (b) current range curve, and (c) weldability lobe for the RSW process (adapted from [31] and [229])..... 14
Figure 2.9. Some of the most important RSW process parameters. 16
Figure 2.10. Factors used to evaluate the quality of resistance spot welds. Images from [31,47–49]. 17

Figure 2.11. Cross-sectional view of the typical macrostructure of resistance spot welds showing various physical attributes..... 18
Figure 2.12. (a) Sub-division of different RSW microstructures with respective peak temperatures shown on Fe-C equilibrium diagram (adapted from [31,59,230]), (b) SEM micrographs of (c) FZ, (d) CGHAZ, (e) FGHAZ, (f) ICHAZ, (g) SCHAZ, of Q&P 3G-AHSS RSW [64]. 20
Figure 2.13. (a) Vickers micro-hardness indentation profile across a DP980 spot weld cross-section, (b–c) SEM micrographs for BM and the sub-critical region (HAZ) respectively, (d) nano hardness characteristics of the martensite and ferrite in BM and SCHAZ [69]. 22
Figure 2.14. (a) formation of a liquated crack at the FZ boundary of 3G-AHSS Q&P resistance spot welds. A characteristic of liquation cracks is Mn and Si segregation, as demonstrated in elemental maps in (b) and (c). (d) and (e) local softened region referred to as the “halo ring” is characterized via hardness drop at the FZ boundary of 3G-AHSS spot welds..... 23
Figure 2.15. A typical load-displacement curve, output of an RSW mechanical test. 25
Figure 2.16. Standard (a) Tensile shear (TS), and (b) cross-tension (CT) coupon geometries and dimensions utilized to evaluate shear and tensile strengths of spot welds, along with the corresponding stress state induced around the nugget periphery in the beginning of the tests (based on [231] and [106]). 26
Figure 2.17. (a) Rotation of coupons during TS test using side digital image correlation (DIC) technique, (b) schematic illustration for bending of material surrounding spot weld during CS test [49,87]. (c) and (d) show rotation and deformation of the coupons during a modified CT test that was performed in shear and tensile-dominated loading orientations, respectively. 27
Figure 2.18. (a) Fixture for testing spot welds under combined loading, (b) U-tension specimen to be installed in the fixture, and (c) KS-II coupon [31,92,94]..... 29
Figure 2.19. (a) Geometry of CP specimen [113]; (b) schematic describing stress distribution at the interface and circumference of the nugget during tensile-bending loading of CP tests [52]; (c) the bending moment arm in the CP test is defined as the distance between the loading axis and the spot weld [109]; (d)-(f) show examples of severe deformation of the vertical and horizontal arms after CP tests [110,111]..... 32
Figure 2.20. Idealized deformation process of the CP samples according to Xu et al. [112]..... 33
Figure 2.21. Schematic drawing of (a) H-specimen and (b) T-section specimen [120]..... 34

Figure 2.22. (a) Caiman mode I, (b) Caiman mode III coupon geometries, and (c) load-displacement characteristics of Caiman mode I test [121,123]. 35
Figure 2.23. Schematic representation of different failure modes in spot welds and their corresponding fracture surfaces (based on [11]). 36
Figure 2.24. Failure load versus nugget diameter for both interfacial and pullout failure modes [134]. 38
Figure 2.25. (a) Discretized weld geometry in finite element analysis. The weld is divided into several sub-regions based on local microhardness values. (b) Miniature tensile specimens extracted directly from the spot weld to characterize the constitutive flow curve of various regions [145,146]. (c) Fracture loci of the BM attained from mechanical tests with various stress triaxialities. The fracture loci of other regions were approximated by linearly translating the BM fracture loci [78]. 42
Figure 2.26. Comparison between the stress-strain flow response from the hardness scaling and experimental approach for (a) 3G-980 FZ, (b) 3G-1180 FZ, and (c) PHS-1500 FZ. Figures show that the hardness scaling approach accurately predicts the strain hardening response in the case of PHS spot welds comprising martensite with various strengths. However, the hardness scaling approach did not yield accurate hardening predictions for the FZ of either 3G-AHSS spot welds [152]. 42
Figure 2.27. A failure locus for resistance spot welds under combined shear/tensile loading conditions [158] 43
Figure 2.28. Comparison between prediction accuracy of three different RSW failure criteria proposed by Lin [159], Lee [160], and Song and Huh [162] for (a) SPCUD spot welds, (b) SPRC340R spot welds, and (c) DP590 spot welds under combined shear-tensile loading [162]. (d) and (e) show interpolation of failure contour for stitch-type and O-type laser welds made of CR340 material subjected to combined shear-tensile loading. It is observed that a transition in failure mode alters the trends related to the load-bearing capacity of the laser welds [163]. 46
Figure 3.1. (a) and (b) scanning electron micrographs; (c) and (d) phase maps showing the body-centered cubic (BCC) and face-centered cubic structures in different colors; (e)- (h) Mn and Si elemental distribution maps of the investigated 3G-980 and 3G-1180 base materials..... 51
Figure 3.2. Representative engineering stress-strain curves for as-received 3G-980 and 3G-1180 materials in the rolling direction. 52

Figure 3.3. Schematic representation of double pulse RSW schedule opted in this research program. Welding current was varied from below undersized welds up to expulsion region. The highlighted welding currents correspond to FDWS and MWS conditions..... 53
Figure 3.4. Schematic representation of (a) tensile shear and (b) cross tensile test specimens.... 54
Figure 3.5. (a) Current range curve of the investigated steels for 334 ms welding time, and (b) weldability lobes for 3 total welding times: 250, 334, and 417 ms (MWS, Minimum Weld Size; FDWS, Face Diameter Weld Size of 7 mm)..... 56
Figure 3.6. Representative load-displacement curves for (a) 3G-980 and (b) 3G-1180 resistance spot welds during lap-shear tests of different welding currents. 57
Figure 3.7. Load-displacement characteristics of (a) 3G-980 and (b) 3G-1180 resistance spot welds during cross tension tests. 58
Figure 3.8. Effect of welding current on load-bearing capacity during (a) tensile shear, and (b) cross tension mechanical tests of 3G-980 and 3G-1180 spot welds..... 59
Figure 3.9. (a) Nugget sizes and dynamic resistance profiles, (b) generated power, and (c) accumulated energy during the RSW process of the investigated steels. 61
Figure 3.10. Optical images of RSW cross sections for (a) and (b) electrode face diameter weld size (FDWS), (c) and (d) minimum allowable weld size (MWS) illustrating the FZ diameters.. 61
Figure 3.11. (a) Sub-division of different RSW regions with their respective peak temperatures shown on Fe-C equilibrium phase diagram; (b) and (c) show optical micrographs of all the corresponding regions along with their average microhardness values for 3G-980 and 3G-1180 spot-welded joints. (d)-(m) high magnification scanning electron microscope (SEM) images of spot welds indicating the RSW sub-regions for 3G-980, and 3G-1180. 63
Figure 3.12 Microhardness maps for (a) 3G-980 and (b) 3G-1180 resistance spot welds superimposed on the optical micrographs of the corresponding FDWS RSW cross sections. (c) Average hardness values of RSW sub-regions (error bars are 95% confidence intervals). 65
Figure 4.1. Schematic representation of a welded KS-II specimen suitable for applying a combined loading mode to the spot weld; (b) the load F applied to the spot weld at the angle θ can be resolved into tensile and shear components. 72
Figure 4.2. Schematic representation of (a) KS-II coupon geometry and dimensions, (b) welded KS-II specimen, (c) and (d) KS-II specimen mounted on the KS-II holder ready for testing (orientation shown corresponds to a KS-II test at 0º); (e) and (f) computer-aided design (CAD)

drawing and manufactured KS-II fixture assembly mounted on the tensile frame (orientation shown corresponds to a KS-II test at 90º). 73
Figure. 4.3 Schematic representation of different KS-II loading orientations showing the shear and tensile components of force acting on the spot welds. (Loading in 10° orientation not shown for clarity) 74
Figure 4.4. Comparison of first and last DIC frames of KS-II tests performed at 0° and 90° loading orientations for 3G-980 samples. Slippage and rotation of coupons within the fixture were difficult to prevent, especially at lower loading angles. The contour levels represent the vertical displacement within the region of interest. 77
Figure 4.5. (a) Triangulation method implemented to locate weld center (red cross) before performing a KS-II test at 45° for 3G-980, (b) displacement and rotation of extracted pixels between first and last frame of the same test, and (c) detailed view of the nugget center point and measuring its projected locations in local s-t coordinate system during a test. 78
Figure 4.6. Summary of procedure to calculate total energy absorption capability ($Etotal$) of a spot weld after performing a KS-II test. The data shown corresponds to a 3G-980 spot weld tested at 30° loading orientation. 80
Figure 4.7. (a) and (c) Negligible value of strain components in triangular element C0C1C2 throughout a KS-II test at 0° and 45° loading orientations, respectively. (b) and (d) show the evolution of Z displacement related to points C0-C5 throughout the same KS-II test at 0° and 45° loading orientations. The Z displacement is an order of magnitude smaller than the in-plane displacement. 81
Figure 4.8. (a) Comparison between load-crosshead and load-projected nugget displacement characteristics of a spot-welded 3G-980 KS-II test at 45° loading orientation. (b)-(f) Correspond to the vertices' current locations at points highlighted on the load-crosshead displacement curve in (a). 83
Figure 4.9. (a) Effect of loading orientation on load-projected nugget displacement characteristics of 3G-980 and 3G-1180 resistance spot welds for three selected KS-II tests; (b) loading path acting on the spot welds at various loading orientations. 84
Figure 4.10. Effect of loading orientation on the final fracture surface of 3G-980 and 3G-1180 resistance spot welds after KS-II tests at different loading orientations. 85

Figure 4.11. (a) Schematic illustration of a partial pullout failure surface along with the average measurements of the nugget diameter (D_{Nugget}) and pullout diameter ($D_{Pullout}$), (b) changes of plug ratio during different loading orientations of KS-II tests..... 86
Figure 4.12. (a) and (d) overall macrographs of interrupted KS-II tests for 3G-980 and 3G-1180 tested at 0° loading orientation; (g) and (j) overall macrographs of interrupted KS-II tests for 3G-980 and 3G-1180 tested at 10° loading orientation. Other images show the magnified micrographs of the highlighted regions within the macrographs..... 88
Figure 4.13. (a) and (d) overall macrographs of interrupted KS-II tests for 3G-980 and 3G-1180 tested at 60° loading orientation; (g) and (j) overall macrographs of interrupted KS-II tests for 3G-980 and 3G-1180 tested at 90° loading orientation. Other images show the magnified micrographs of the highlighted regions within the macrographs..... 90
Figure 4.14. The effect of loading orientation on total energy absorption capability ($Etotal$) of (a) 3G-980, and (b) 3G-1180 resistance spot welds during KS-II tests. 93
Figure 4.15. The effect of loading orientation on energy absorption capability due to shear displacement of projected nugget ($E\delta s$) for (a) 3G-980, and (b) 3G-1180 resistance spot welds during KS-II tests. 94
Figure 4.16. The effect of loading orientation on energy absorption capability due to tensile displacement of projected nugget ($E\delta t$) for (a) 3G-980, and (b) 3G-1180 resistance spot welds during KS-II tests. 94
Figure 4.17. Comparison between load-displacement responses of cross-tension and KS-II tests at 90° loading orientation for (a) 3G-980 and (b) 3G-1180 resistance spot welds. 96
Figure 4.18. Comparison between load-displacement responses of cross-tension and KS-II tests at 90° loading orientation for (a) 3G-980 and (b) 3G-1180 resistance spot welds. 97
Figure 5.1. Schematic representation of (a) CP coupon geometry and dimensions, (b) welded CP specimen showing the speckled region of interest; (c) “h” is the vertical distance from the grip to the centerline of two sheets; “d” is the horizontal distance from mid-thickness of the sheet at the grip to projected FZ boundary; “s” is the over-hang distance after the spot weld on the horizontal flange; (d) three different CP geometries with various horizontal flange lengths (L_{Flange}) were considered. Dimensions L_{Flange}, h, d, and s are outlined in Table 3 for all three experimented CP geometries. 104

Figure 5.2. Comparison between (a) first, (b) peak load, and (c) final frame of a short arm (geometry 1) 3G-980 FDWS CP test. Figures highlight the deformation of the coupons and the continuous reduction of the effective bending moment arm acting on the projected FZ center throughout the test. The color contour U shows horizontal displacement within the region of interest. 106
Figure 5.3. Schematic drawing showing the configuration of the CP specimen (a) at the beginning of the test, and (b) n^{th} frame after starting the test. (c) Forces and moments acting at the center of the spot weld. 107
Figure 5.4. Representative evolution of effective bending moment arm (d_e), opening angle (α), bending moment (M_{RSW}), and tensile force ($F_{T,\,RSW}$) applied to the projected RSW FZ throughout (a) and (b) 3G-980 FDWS, and (c) and (d), 3G-980 MWS geometry 1 (short arm) CP tests. ... 109
Figure 5.5. Comparison between (a) first and (b) final frame of a KS-II test at 10° loading orientation. The color contour V represents vertical displacement within the region of interest. (c) load- displacement and nugget orientation plot of the same test shows the instantaneous orientation of the nugget throughout the test. 111
Figure 5.6. Representative plots showing the evolution of $F_{Load\ cell}$, $F_{T,\,RSW}$, and M_{RSW} during testing of three different CP geometries of (a) 3G-980 FDWS, (b) 3G-1180 FDWS, (c) 3G-980 MWS, and (d) 3G-1180 MWS welding schemes. 113
Figure 5.7. Influence of CP coupon geometry on average critical $F_{T,\,RSW}$, and M_{RSW} applied to the projected center of the RSW FZ for (a) 3G-980 FDWS, (b) 3G-1180 FDWS, (c) 3G-980 MWS, and (d) 3G-1180 MWS welding conditions. 114
Figure 5.8. Influence of CP coupon geometry on average $E_{T,\,RSW}$, $E_{M,\,RSW}$, $E_{Total,\,RSW}$ of the projected center of the RSW FZ, and E_{Global} for (a) 3G-980 FDWS, (b) 3G-1180 FDWS, (c) 3G-980 MWS, and (d) 3G-1180 MWS welding conditions. 115
Figure 5.9. Changes in effective bending moment arm from the beginning of the tests up to the peak load frame of (a) 3G-980, and (b) 3G-1180 CP tests with various geometries and welding schemes. 117
Figure 5.10. Representative failure behavior of CP geometry 1 (short arm) tests for (a) 3G-980 FDWS and (b) 3G-1180 FDWS conditions. 117

Figure 5.11. Representative KS-II load-crosshead displacement plots for different loading orientations of (a) 3G-980 FDWS, (b) 3G-1180 FDWS, (c) 3G-980 MWS, and (d) 3G-1180 MWS conditions. 118
Figure 5.12. Influence of KS-II loading orientation on peak load of (a) FDWS and (b) MWS welding schemes. 119
Figure 5.13. (a) Summary of procedure for calculating in-plane rotation using DIC data (rotation of the coupons is exaggerated for better visualization of changes in θ). In-plane rotation values at peak load frame for (b) FDWS and (c) MWS conditions. 119
Figure 5.14. Comparison between different RSW failure criteria along with the experimental KS-II data points, decomposed according to their final orientations, for (a) 3G-980 and (b) 3G-1180 spot welds (all shown calibrated models correspond to the final orientation data points upon using the DIC triangular analysis); (c) average error of predictions corresponding to different models calibrated in (a) and (b). 121
Figure 5.15. Three-dimensional RSW failure surfaces calibrated using Equation 5.5 and Equation 5.6 according to the final orientation of the KS-II coupons following the DIC triangular analysis and short arm CP tests for (a) 3G-980 FDWS, (b) 3G-1180 FDWS, (c) 3G-980 MWS, and (d) 3G-1180 MWS welding schemes 122
Figure 5.16. Comparison between failure predictions of proposed and Seeger's RSW failure loci in tensile-bending dominated conditions for (a) 3G-980 FDWS, (b) 3G-1180 FDWS, (c) 3G-980 MWS, and (d) 3G-1180 MWS conditions. The developed shear strength component is not shown. 125
Figure 5.17. Seeger's failure loci in shear-tensile loading conditions while considering (a) and (b) the nominal orientation of the 3G-980 and 3G-1180 KS-II coupons; (c) and (d) final orientation of the 3G-980 and 3G-1180 KS-II coupons measured using DIC analysis. The hollow scattered symbols represent the individual data points attained from each test repetition, while the solid symbols show the average values at each loading orientation. The color scale represents the % error of calibrated model predictions compared to the experimental average at each loading orientation. 127
Figure 5.18. Representative failure behavior of (a) 3G-980 and (b) 3G-1180 FDWS conditions within the tensile-dominated KS-II loading orientations. The shown micrographs correspond to KS-II tests performed at θ=60° loading orientation. 128

Figure 5.19. Proposed failure loci in shear-tensile loading conditions while considering the final orientation of the 3G-980 and 3G-1180 KS-II coupons measured using DIC analysis. (a) and (b) show an exponential function with six calibrated coefficients; (c) and (d) show two different functional forms of failure loci before and after the failure transition points. Seeger's model was used within the IF region whereas a modified version of the power law equation was used within the PO or P-PO regions. The color scale represents the % error of calibrated model predictions compared to the experimental average at each loading orientation (IF, interfacial failure; PO, pullout failure; P-PO, partial pullout failure)..... 129
Figure 6.1. (a) Hat channel cross-section and (b) resistance spot-welded Caiman mode I component geometry and dimensions (all dimensions are in mm); (c) Caiman component installed on the MTS tensile frame using a fixture consisting of clevises, pins, inner and outer bosses (inner bosses not visible). (d) and (e) show the location of cameras to record optical and thermal images throughout the tests..... 137
Figure 6.2. (a) DHCP coupon geometry and dimensions, including the location of spot welds; (b) DHCP specimen before sectioning the two spot welds; (c) DHCP specimen after sectioning the spot welds through their centerlines; (d) DHCP specimen installed on a tensile frame; (e) all DHCP tests were accompanied with DIC technique for in-situ strain measurement. The schematic shows the placement of the DIC cameras. 138
Figure 6.3. (a) Representative load-displacement characteristics of the 3G-980 DHCP test with a magnified inset highlighting the strength loss after the first PO failure. Full section double coach peel test's load-displacement response is also included for comparison. (b-e) show the distribution of major principal strain (e_1) for the cross-section of the first half weld to fail at different crosshead displacements. (f) to (i) show the distribution of e_1 at different crosshead intervals for the second half weld failure. DIC strain maps highlight a higher susceptibility of failure through yielded BM of the 3G-980 spot welds during combined tensile-bending loading. 142
Figure 6.4. (a) Representative load-displacement characteristics of the 3G-1180 DHCP test with a magnified inset highlighting the strength loss after the first IF. Full section double coach peel test's load-displacement response is also included for comparison. (b-e) show the distribution of major principal strain (e_1) for the first half weld cross-section to fail at different crosshead displacements. (f) to (i) show the distribution of e_1 at different crosshead intervals for second half weld failure.

DIC strain maps highlight a higher failure susceptibility through the FZ of the 3G-1180 spot welds during combined tensile-bending loading..... 143
Figure 6.5. Differences in opening angle of the parent metals for (a) 3G-980 and (b) 3G-1180 DHCP tests. (c) and (d) illustrate a representative cross-sectional view of the failed joints after the DHCP tests..... 144
Figure 6.6. (a) and (b) experimental quasi-static load- crosshead displacement characteristics, and (c) summary of peak load and absorbed energy of the Caiman mode I component tests. (d)- (h) and (j)- (n) left side view of the components at different crosshead-displacement intervals highlighted in (a) and (b). (i) and (o) top view of the components after 250 mm crosshead displacement comparing the sidewall and channel plastic deformation between the investigated 3G-AHSS Caiman components. 145
Figure 6.7. (a) Load- displacement of a 3G-980 quasi-static Caiman mode I test; (b) and (c) show a magnified view of (a) at different displacement intervals. (d)-(i) top and bottom view thermal images of the same test highlighting heat generation associated with weld failure and flange/channel deformation and tearing. (j)-(l) are temperature line scans from top view thermal images shown in (d)-(f)..... 146
Figure 6.8. (a) Load- displacement of a 3G-1180 quasi-static Caiman mode I test. (b) and (c) show a magnified view of (a) at different displacement intervals. (d)-(i) top and bottom view thermal images of the same test highlighting heat generation associated with weld failure and flange/channel deformation and tearing. (j)-(l) are temperature line scans from top view thermal images shown in (d)-(f)..... 147
Figure 6.9. (a) the “crack” opening length is defined as the instantaneous distance from the central axis of the stationary clevis until the last failed spot weld. (b) Comparison between the Caiman component “opening length” at different crosshead displacements. Individual weld failure was determined using a combination of thermal videos and optical images. The data shown corresponds to three Caiman test repetitions of each investigated 3G-AHSS. 148
Figure 6.10. Failure behavior of spot welds after quasi-static Caiman mode I mechanical tests for (a) 3G-980 and (b) 3G-1180 spot welds. (c-j) show a detailed view of the spot welds in (a) and (b). (k) and (l) are cross-sectional views of spot welds shown in (f) and (j), respectively..... 149

Figure 6.11. (a) and (d) cross-sectional view of spot welds shown in Figure 6.14 (f) and (j), respectively. (b-c) and (e) show inverse pole figure EBSD scans of the failure initiation regions and crack propagation paths after the Caiman mode I test. 150
Figure 6.12. (a) and (f) Three-dimensional depth maps of the failed 3G-980 and 3G-1180 spot welds shown previously in Figure 14 (f) and (j), respectively, upon performing Caiman mode I quasi-static tests. (b)-(e) and (g)-(j) show scanning electron microscope fractography images of failed interfaces at different magnifications. 151
Figure 6.13. Representative load-displacement curves were obtained through instrumented indentation tests for various sub-regions of (a) 3G-980 and (b) 3G-1180 resistance spot welds. (c) Summary of yield strengths calculated using Equation 6.1 for different RSW sub-zones. 153
Figure 6.14. Inverse pole figure (IPF) maps at the edge of the FZ for (a) 3G-980 and (d) 3G-1180 spot welds; reconstructed maps showing PAGB represented with the black lines in the FZ edge of (b) 3G-980 and (e) 3G-1180 joints; Kernel average misorientation (KAM) maps at the edge of the FZ for (c) 3G-980 and (f) 3G-1180 joints..... 157

List of Tables

Table 2.1. Summary of failure behavior and characteristics reported for RSW of 3G-AHSS under conventional TS and CT mechanical tests. 28
Table 2.2. Summary of significant contributions regarding combined loading of resistance spot welds. 30
Table 2.3. Summary of empirical formulae proposed in the literature to calculate the minimum allowable nugget size (MWS) ensuring pullout failure mode of resistance spot welds. 40
Table 3.1. Chemical composition of the investigated 3G-AHSS. Reported values are in wt.%. . 50
Table 3.2. Average tensile properties of the investigated steels in the rolling direction. 52
Table 4.1. Resistance spot welding process parameters. 71
Table 4.2. Summary of DIC parameters for KS-II tests. 75
Table 5.1. Resistance spot welding process parameters used in this study. 103
Table 5.2. Summary of average horizontal flange length (L_{Flange}), initial bending moment arm on the horizontal arm “d”, initial bending moment arm on the vertical arm “h”, and free over-hang distance (s) for 3 different CP coupon geometries and 4 different welding schemes investigated in this study. Errors are 95% confidence interval values. 105
Table 5.3. Summary of calibrated force-based RSW failure model parameters for Seeger’s three-dimensional criteria including failure strengths and exponents. 123
Table 5.4. Summary of calibrated parameters for the proposed force-based RSW failure model in tensile-bending conditions. 126
Table 5.5. Summary of calibrated parameters for an ideal exponential RSW failure model with six coefficients (based on final orientation KS-II data points). 130
Table 5.6. Summary of calibrated parameters for two RSW failure models valid before and after failure transitions (based on final orientation KS-II data points). 130
Table 6.1. Summary of resistance spot welding process parameters used in this study. 135
Table 6.2. Summary of DIC post-processing parameters. 139
Table 6.3. Summary of calculated indices from FZ edge EBSD maps of investigated spot welds. 158
Table 6.4. Summary of contributions from various strengthening mechanisms on yield strength of martensite formed in resistance spot welds of 3G-980 and 3G-1180. % difference refers to the

comparison between the sum of theoretical yield strength values and yield strength measurements from instrumented indentations shown in Figure 17. 159

List of Abbreviations

3G-AHSS	Third Generation Advanced High Strength Steel
AHSS	Advanced High Strength Steel
AWS	American Welding Society
BIW	Body-In-White
BM	Base Metal
CGHAZ	Coarse Grain Heat Affected Zone
CP	Coach Peel Test
CT	Cross-Tensile Test
CTS	Cross Tensile Strength
DIC	Digital Image Correlation
DP	Dual Phase
EBSD	Electron Backscatter Diffraction
FDWS	Face Diameter Weld Size
FZ	Fusion Zone
HAZ	Heat Affected Zone
IF	Interfacial Failure
IPF	Inverse Pole Figure
KS-II	Modified Kopfzup-Scherzug Test
MFDC	Medium Frequency Direct Current
MWS	Minimum Weld Size
PAG	Prior Austenite Grain
PAGS	Prior Austenite Grain Size
PHS	Press-Hardened Steel
PO	Pullout Failure
PPO	Partial Pullout Failure
PWHT	Post Weld Heat Treatment
Q&P	Quenching and Partitioning
RA	Retained Austenite
RSW	Resistance Spot Welding
SCHAZ	Sub-critical Heat Affected Zone
SEM	Scanning Electron Microscope
TRIP	Transformation Induced Plasticity
TS	Tensile Shear Test
TSS	Tensile Shear Strength
UCHAZ	Upper Critical Heat Affected Zone
UTS	Ultimate Tensile Strength
YS	Yield Strength

1 Chapter 1: Introduction

1.1 Background

In 2019, about 15% of net anthropogenic greenhouse emissions were associated with the transport sector [1]. Transportation sector emissions are expected to increase rapidly over the next few decades due to the increased popularity of personal travel and goods movement while primarily relying on fossil fuels for transportation energy [2][3]. In the face of growing concerns regarding climate change, long-term policies have been mandated to minimize the potential impact of greenhouse emissions from the transportation sector on global climate change. For example, all passenger vehicles manufactured within the United States of America must meet fuel consumption standards enforced by the Corporate Average Fuel Economy (CAFE) program. The latest amendment to the CAFE program, the Safer Affordable Fuel-Efficient (SAFE) Vehicles Rule, requires 1.5 percent yearly reductions in CO_2 emissions for vehicle model years 2021 to 2025 [4,5].

Light-weighting vehicle components is one approach the automotive industry has been investigating to lower emissions [6]. In fact, the need for vehicle weight reduction has further intensified with the popularity of battery electric vehicles (BEVs) with powertrains that are, on average, 125% heavier than the internal combustion engine (ICE) vehicles [7,8] However, structural weight reduction should not compromise vehicle safety. To this end, different generations of steels, referred to as "advanced high strength steels (AHSS)," have been developed to allow a reduction in the thickness of the sheets utilized in auto assemblies while maintaining or improving crashworthiness [9]. Auto manufacturers now widely use AHSS within their designs [7], with a four-fold increase in AHSS adoption from 2006 to 2016 [10]. The third generation of AHSS (3G-AHSS), the latest generation of AHSS, provides the potential for additional weight reduction because of their favorable combination of high strength and high ductility. The favorable properties of 3G-AHSS are attributed to their complex microstructures attained from multi-step thermomechanical processing and high alloying contents [11,12]. Currently, the 3G-AHSS are primarily at the research and development stage and are regarded as future opportunities for automotive and structural applications to reduce their weight further [13]. Enabling the transition from conventional AHSS to 3G-AHSS requires considering the subsequent manufacturing steps, such as the joining processes used to assemble vehicle body-in-white (BIW).

Resistance spot welding (RSW) is the most commonly adopted joining technique within the automotive industry due to its rapid process speed, suitability for automation, and absence of a requirement for filler metals [14]. Although the intrinsic properties of 3G-AHSS are promising, the RSW joints in a typical modern vehicle play a critical role in maintaining the integrity of the vehicle structure, crashworthiness, durability, vibration, and harshness [15]. Spot-welded joints in body structures can be critical failure initiation regions and impact the integrity of the whole structure in the case of a vehicle crash event [14]. Resistance spot welds exhibit different failure characteristics (failure modes) depending on the loading mode, material properties, and welding parameters, which influence the structure's strength and energy absorption capability. Considering the large number of resistance spot welds within an automotive BIW, an accurate representation of a joint's mechanical response and failure characteristics is crucial to predicting the global response of a car during complex loading events.

Considering that the available literature on mechanical performance and failure characteristics of resistance spot welds primarily focuses on the mechanical performance of resistance spot welds from conventional AHSS upon tensile shear (TS) and cross-tensile (CT) mechanical tests, a more comprehensive understanding of 3G-AHSS spot welded joints under complex loading conditions is required. Combined shear/tensile loading of the joints and tensile-bending loading conditions are among such complex loading modes. A detailed understanding of the 3G-AHSS RSW joint mechanical performance analysis and failure mechanism under these loading conditions remains unexplored within the existing literature. Moreover, numerous spot welds are regularly used with assembled components such as the A, B, and C pillars of BIW. It is also essential to expand the knowledge from single spot weld characterization techniques to component scales and track the failure behavior as groups of spot welds fail under specific loading modes.

1.2 Objectives

A comprehensive study on the alteration of commonly used RSW performance indices, such as strength and energy absorption capability and the failure characteristics of RSW joints when subjected to different loading conditions, is vital for a safe and reliable transition from previous generations of AHSS to 3G-AHSS within the automotive assemblies. The literature does not fully address the relationship between RSW process parameters, mechanical properties, and failure characteristics of spot-welded connections for single-spot weld or multi-weld component

characterization methods of 3G-AHSS RSW joints. The proposed research aims to understand the performance of spot welds in 3G-AHSS under varying loading scenarios, such as shear/tensile and tensile/bending loading conditions, focusing on the applicability of findings to the automotive industry. Acquiring the critical failure strength of 3G-AHSS spot welds under shear-tensile and tensile-bending loading modes enables more accurate calibration of force-based failure criteria commonly implemented for spot weld failure prediction within the automotive industry. Therefore, another objective of this study program is to evaluate pre-existing force-based failure criteria on spot welded joints made from 3G-AHSS. The knowledge from single spot weld characterization techniques is also expanded to component scale by investigating mechanical properties and failure characteristics as groups of joints sequentially fail in a weld-group assembly. The specific objectives of the proposed research are outlined below:

1. Develop a unified set of welding parameters for the investigated steels concerning the recommendations of AWS standards by attaining enhanced mechanical properties under standard mechanical tests.
2. Evaluate weld strength, energy absorption capability, and failure mechanisms of the optimized spot welds under combined shear-tensile and tensile-bending loading conditions.
3. Develop failure loci for spot welds with optimal and sub-optimal nugget sizes in shear-tensile and tensile-bending loading conditions providing insight into upper and lower bounds of joint mechanical performance, respectively.
4. Characterize the failure progression as a group of spot-welded connections sequentially fail under tensile-bending loading conditions.
5. Pinpoint critical failure initiation sub-regions under tensile-bending loading of 3G-AHSS spot welds and identify the reasons related to differences in failure characteristics of spot welds from the two investigated grades of 3G-AHSS.

Results from this work will inform the original equipment manufacturers (OEMs) about the potential benefits of two grades of 3G-AHSS in BIW structures, further support the implementation of the RSW process for automotive structures comprised of 3G-AHSS and provide accurate empirical failure loci under complex loading modes that can potentially improve the accuracy of spot weld failure predictions in finite element models.

1.3 Thesis outline

This thesis consists of seven chapters. The first chapter introduces the research topic and sheds light on the background and objectives of this research. A comprehensive review of relevant information from the literature is provided in Chapter Two. The literature review introduces three generations of AHSS, RSW process principles and parameters, typical spot weld microstructure and phase transformations, the mechanical performance of spot welds under various geometries and loading modes, and the corresponding RSW failure characteristics and mechanisms. Additionally, the literature review covers the mechanical performance quantification of multi-spot welds using component tests. The scope and objectives of the current work were established based on identified gaps from the available literature, summarized at the end of chapter two.

Chapters three through six outline results and discussions from original research publications. Chapter three introduces the investigated materials and examines their weldability via developing a welding current domain (welding lobe). Suitable welding parameters for the rest of this research program, along with the microstructural development during double pulse welding, hardness distribution, and mechanical response of the welds using traditional TS and CT tests, were discussed in chapter three. In chapter four, the combined shear and tensile loading of selected welding conditions were studied using KS-II mechanical tests. Novel methodologies were developed in this chapter that assist in a more accurate interpretation of the joint mechanical response regarding strength and energy absorption capability. Chapter five investigates the mechanical performance of the joints under various combinations of tensile-bending loading conditions using coach peel (CP) tests. The validity of some of the most common RSW failure prediction criteria was also assessed based on results from chapters four and five. Chapter Six builds on the knowledge attained from previous chapters by evaluating the mechanical performance and failure behavior of multiple spot welds loaded under tensile-bending loading conditions of Caiman component tests. This chapter also analyzes the discrepancy in terms of failure behavior of the joints made of two grades of 3G-AHSS from a metallurgical standpoint. Lastly, chapter seven summarizes the primary findings of the current research program and proposes suggestions for future work.

2 Chapter 2: Literature Review

2.1 Overview

The geometrical and microstructural characteristics of the spot weld play a critical role in determining the overall mechanical performance of the joint. Spot welds exhibit different failure behaviors under different loading modes and stress states. Predicting the mechanical performance of resistance spot welds can be challenging due to severe inhomogeneities of the formed microstructures, complex stress state around the nugget, and the joint hidden from the exterior. This chapter critically reviews the RSW process fundamentals, mechanical properties, and failure prediction modeling of resistance spot welded advanced high strength steels for automotive applications. This review summarizes the most critical challenges and achievements regarding spot weld mechanical property quantification and microstructural characterizations while highlighting existing deficiencies within the literature.

2.2 Three Generations of Advanced High Strength Steels

The constant demand for lighter and safer vehicles has led to the continued development of different generations of AHSS to meet functional requirements regarding strength and formability. AHSS are divided into three generations based on their processing and final mechanical properties. Figure 2.1 schematically illustrates the location of each of the three generations of AHSS in a strength-elongation chart [13].

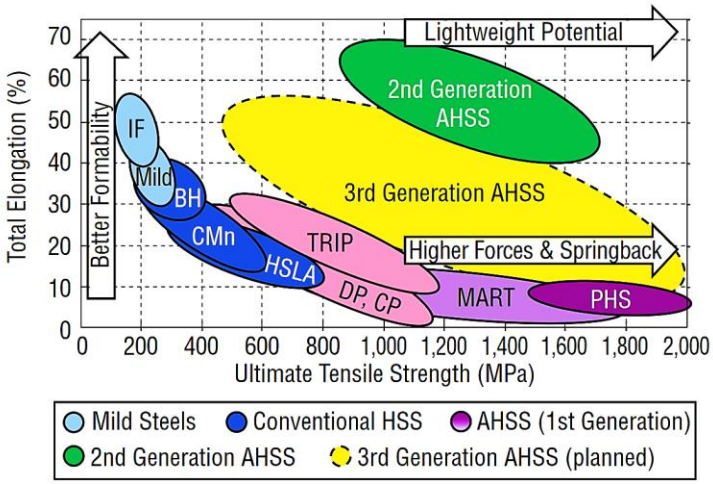


Figure 2.1. Comparison of ultimate tensile strength vs elongation graph for mild steels, high strength steels (HSS), and three different generations of AHSS [16].

The first generation of AHSS (1G-AHSS) includes, amongst others, dual-phase (DP), transformation-induced plasticity (TRIP), and martensitic (MART) steels. These steels contain relatively low amounts of alloying elements and usually possess either ferrite-based microstructures (such as DP and TRIP steels) or a fully martensitic microstructure (such as martensitic steels or press-hardened steels) [17]. The main drawback of 1G-AHSS is their noticeable ductility deterioration in applications requiring ultra-high-strength values. The second generation of AHSS (2G-AHSS), such as austenitic stainless steels and twinning-induced plasticity (TWIP) steels, demonstrate a superior combination of strength and ductility compared to 1G-AHSS. Such superior properties are achieved at the cost of an elevated amount of expensive alloying elements such as chromium and nickel [18,19] that led to adverse phenomena during welding, such as undesirable phase transformations, cracking, and high residual stresses. Consequently, 2G-AHSS did not receive widespread adoption by the automotive industry.

Against this background, the 3G-AHSS emerged as a compromise between the first and second generations to obtain favorable strength and ductility combinations at lower alloying levels and costs. Increased adoption of 3G-AHSS in automotive body-in-white (BIW) assemblies can allow further weight reduction by reducing the gage thickness and providing favorable crashworthiness for automotive applications. The required properties are achieved in these steels using multi-step thermomechanical processing that typically results in a multi-phase microstructure. To further clarify the differences between characteristics of different generations of AHSS, a comparison between the heat treatments and attained microstructure of dual-phase (DP) AHSS, as a member of 1G-AHSS, and quenched and partitioned (Q&P) AHSS, as a member of 3G-AHSS, is provided in the following two sections.

2.2.1 Dual-Phase (DP) AHSS

Due to the relatively lean composition and straightforward processing route of DP steels, they are considered the flagship of AHSS and have been well integrated into the automotive industry [17,20]. As shown in Figure 2.2 (a), DP alloys are initially intercritically heated to achieve a combination of austenitic and martensitic microstructure. This is followed by a controlled cooling from the austenite + ferrite region (intercritical annealing for cold-rolled products) to generate a portion of ferrite before transforming the remaining austenite to martensite upon rapid cooling [21]. The attained microstructure of DP steels consists of a ductile ferritic matrix embedded within hard martensitic islands [22], as shown in Figure 2.2 (b). The excellent ductility of DP steels is

primarily attributed to the concentration of strain within the lower-strength ferrite phase surrounding martensitic islands, which creates the unique high initial work-hardening rate and continuous yielding exhibited by DP AHSS [23].

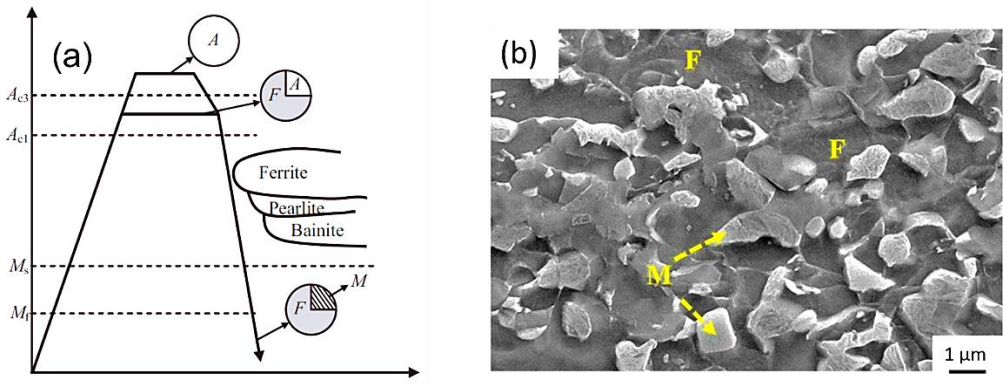


Figure 2.2. (a) Schematic diagram of the processing of a DP AHSS [13]*, and (b) scanning electron micrograph showing the final microstructure of DP980; F, ferrite; M, martensite* [6].

2.2.2 Quenched & Partitioned (Q&P) AHSS

The quenching and partitioning (Q&P) heat treatment was proposed in 2003 by Speer *et al.* [24]. Q&P steels undergo a four-step thermal treatment (Figure 2.3 (a)) to create a mixture of carbon-depleted martensite and carbon-enriched austenite. The steel is initially heated above the A_{c3} temperature, followed by rapid cooling to the quenching temperature (QT). After that, the steel is held isothermally at the partitioning temperature (PT) during the partitioning step. During the partitioning step, the diffusion of carbon from martensite to austenite stabilizes the remaining austenite. Lastly, the stabilized and carbon-enriched austenite is retained at ambient temperature after the steel is fully quenched.

Figure 2.3 (b) shows the micrograph of a resultant Q&P980 microstructure with phases including ferrite, martensite (both in tempered and untempered conditions), and retained austenite (RA). The favorable combination of increased work-hardening rate (strength) and ductility of Q&P 3G-AHSS is primarily attributed to the simultaneous existence of martensite and RA in the microstructure of these advanced steels.

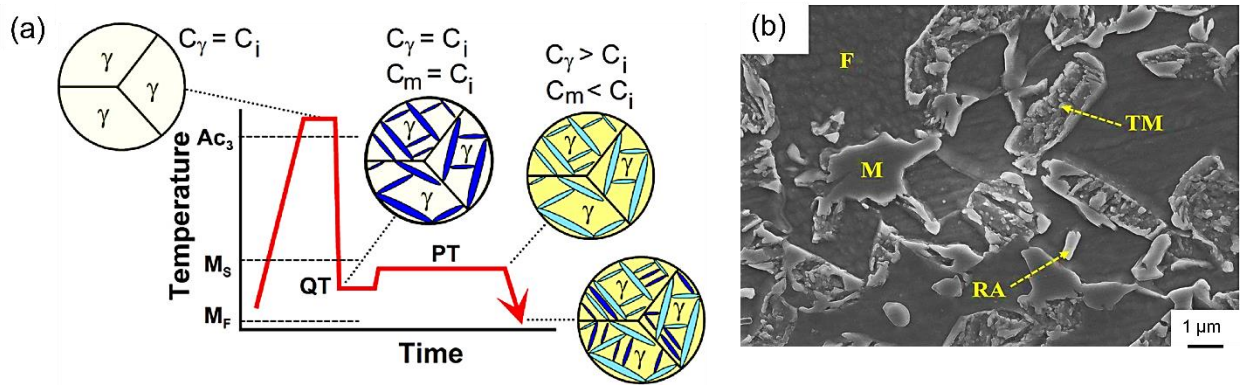


Figure 2.3. (a) Schematic diagram of the processing of a Q&P AHSS (A_{c1} and A_{c3} are austenitization start and finish temperatures; M_s and M_f are martensite start and finish temperatures; C_i, C_γ, C_m represent the carbon content of the initial alloy, austenite, and martensite respectively [17]*), and (b) scanning electron micrograph showing the final attained microstructure of Q&P980 (F, ferrite; M, martensite; TM, tempered martensite; RA, retained austenite* [6]*).*

The contribution of "austenite + martensite" and "ferrite + martensite" microstructural combinations on the strength and ductility of AHSS are compared in Figure 2.4 (a). Austenitic-martensitic microstructures have a more substantial contribution to improving ductility than increasing the volume fraction of ferrite. The mechanical properties of "austenite + martensite" microstructures fall within the desired strength-ductility domain for 3G-AHSS [25,26]. Therefore, 3G-AHSS thermomechanical processes are commonly applied as a new way of producing martensite-containing steels with enhanced levels of RA that can induce austenite-to-martensite transformation [27].

Increased ductility of the austenitic-martensitic microstructure of 3G-AHSS is attributed to a phenomenon referred to as "transformation-induced plasticity (TRIP)." During the TRIP phenomenon, RA accommodates part of the applied strain to the steel and transforms to martensite, increasing the work hardening rate and delaying the onset of strain localization and fracture, as shown schematically in Figure 2.4 (b) [28]. The strain level at which the TRIP mechanism is triggered is primarily controlled by manipulating the stability of RA. However, the volume fraction of available RA is reported to also affect the onset of TRIP phenomenon occurrence [13]. Deformation of a 3G-AHSS with highly stable RA will delay the austenite-to-martensite transformation to relatively high strain values such as the ones experienced in crash events, which is desired for continuous strain-hardening and improved safety [29].

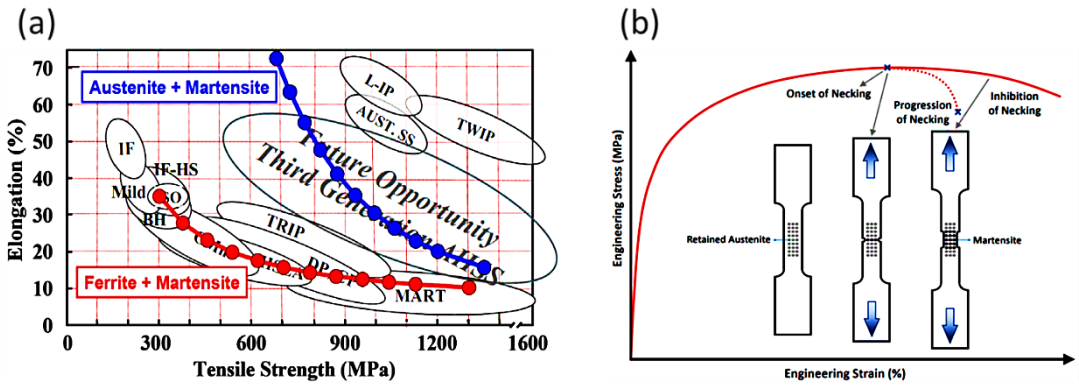


Figure 2.4. Contributions of "austenite +martensite" and "ferrite +martensite" microstructural combinations to the mechanical properties of AHSS [17], *(b) schematic illustration of TRIP effect during deformation responsible for superior properties of "austenite +martensite" microstructure* [28].

Figure 2.5 (a) illustrates four hypothetical austenite stability curves calculated according to Olson and Cohen's austenite stability function [30]. As the stability of austenite increases (from material D to A), the strain level at which the TRIP phenomenon occurs increases, which is desirable for high-strain failure applications. The mechanical property combinations attained from different austenite stabilities are summarized in Figure 2.5 (b), where each data point corresponds to a different initial volume fraction of austenite, with the remainder of the microstructure being ferrite. It is observed that the material with the least stable austenite (Material D) exhibited mechanical property combinations like that of 1G-AHSS, and the inclusion of the austenite did not lead to a noticeable improvement in strength and ductility combinations. However, with the improvement of the austenite stability, new combinations of strength and ductility were achieved that can fulfill mechanical property requirements for 3G-AHSS. According to the composite material modeling performed by Matlock *et al.* [17] based on Olson and Cohen's austenite stability function [30], factors such as carbon content, chemical composition, grain size, and morphology influence the stability of RA within the 3G-AHSS microstructure. During the processing of 3G-AHSS, considerations should be made about these factors to optimize the microstructure and achieve the targeted mechanical properties [31]. It is noted that subsequent joining processes can profoundly alter the precisely engineered microstructure of 3G-AHSS and, therefore, influence the mechanical response of the BIW.

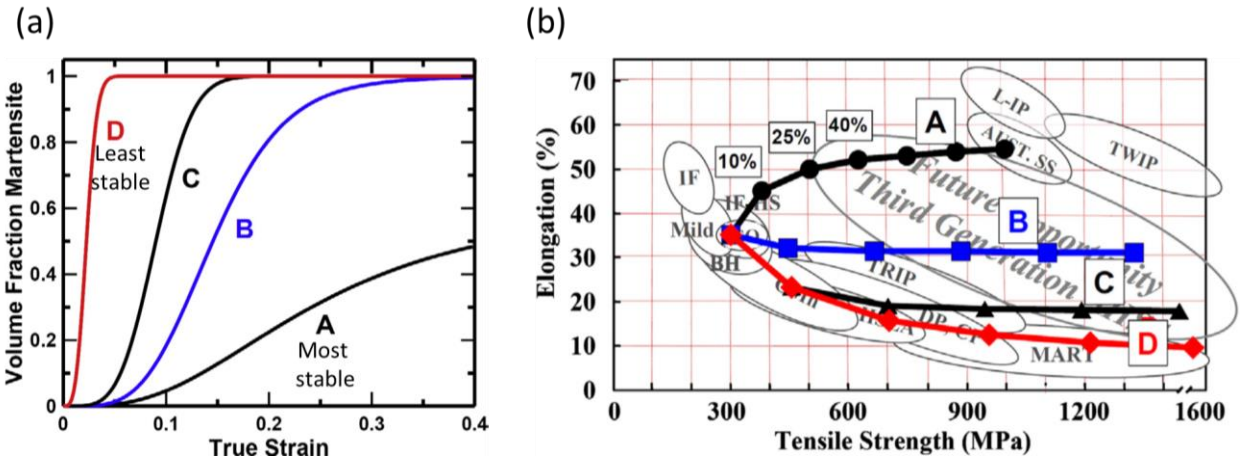


Figure 2.5. (a) Assessing the effect of austenite stability against transformation to martensite with strain for four hypothetical materials (material A possesses the most stable austenite as the transformation to martensite occurred at higher strain values, whereas material D has the least stable austenite that transformed to martensite at lower strains). (b) Mechanical property combinations corresponding to ferrite and austenite with different stabilities are outlined in (a) [13].

2.3 Resistance Spot Welding (RSW) Process

RSW is the dominant joining method in the automotive industry, with a BIW containing approximately 5000 spot welds [30,31], the quality of which directly impacts vehicle safety in a crash event [14,32]. RSW involves joining two or more sheets through resistive heat generation at discrete contact points. An RSW setup usually includes a pair of water-cooled copper-alloyed electrodes installed on a servo-controlled or hydraulic/pneumatic jaw [33]. Figure 2.6 schematically illustrates the different stages of joining two sheets using the RSW process. Initially, the sheets are placed between the two electrodes; then, the sheets are squeezed together by applying a predetermined amount of force from the electrodes. Establishing an electrical current flow through the sheets causes localized heating at the sheet-sheet interface. After the temperature in this region exceeds the melting temperature of the joining material, an enclosed molten pool will form and grow continuously. Lastly, the current flow is terminated while the water-cooled electrodes stay in contact with the sheets to allow for heat transfer in the axial direction through conduction until the solidification of the molten nugget. This process forms an elliptical-shaped joint between the sheets known as the weld nugget [34]. The most implemented criterion in determining whether an RSW joint meets minimum property requirements is nugget diameter. According to the American Welding Society (AWS) standard for spot welds in automotive applications [35], only nugget diameter values exceeding $4\sqrt{t}$, where t is the sheet thickness, are

acceptable. The minimum nugget diameter requirement can vary based on the selected weld standard, material strength, and thickness.

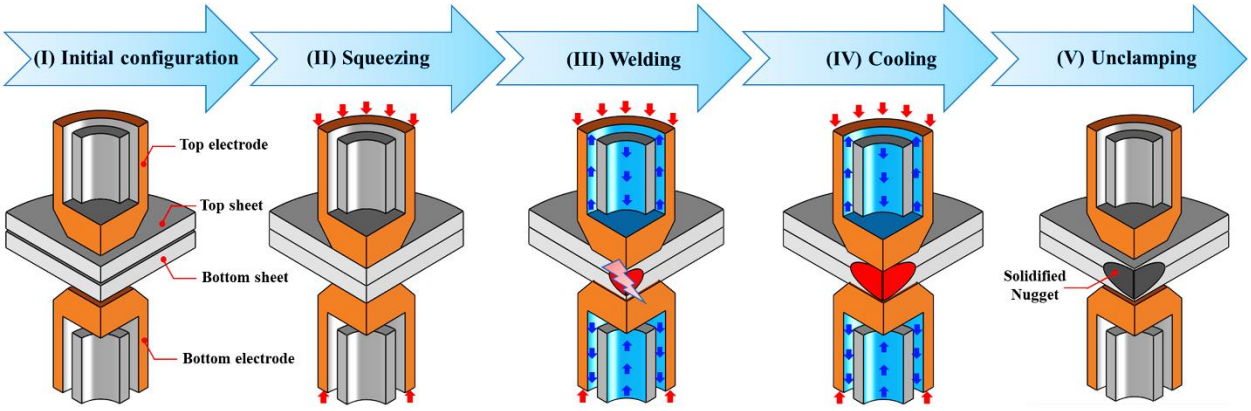


Figure 2.6. Schematic representation of different stages of RSW process.

2.3.1 Evolution of Resistance During RSW Process

The RSW process is based on the principle of resistance to current flow that generates intense localized heating. During the welding portion of the RSW cycle, the heat generated may be described using the models for resistive heating, as seen in Equation 2.1:

$$Q = \int_0^t R(t) \cdot I^2(t) dt = \int \frac{V(t)^2}{R(t)} dt = \int V(t) \cdot I(t) dt \qquad (2.1)$$

where Q is the generated heat, I is the applied welding current, R is the total resistance of the joint, and t is the welding time during which current flows through the sheets. R, V and I are all functions of time and dynamically change throughout a complete RSW cycle. Equation 2.1 states that parameters including the magnitude of welding current, welding time, and electrical resistance can immensely influence the amount of heat generated during the RSW process and, consequently, affect the nugget diameter and properties of RSW joints [34].

The resistance during a complete cycle of the RSW process is composed of numerous resistances at different interfaces, as schematically shown in Figure 2.7 (a). These resistances include electrode bulk resistance (R_1 and R_7), sheet-bulk resistance (R_3 and R_5), contact resistance at electrode/sheet interfaces (R_2 and R_6), and sheet faying interface resistance (R_4). As a result of the low bulk resistance of the electrodes and their active cooling, most of the heat is generated at the faying interface between the two sheets. Resistance is highest at the sheet-sheet interface because of roughness, asperities, oxides, and contaminations. The value of R throughout a spot weld cycle dynamically changes since electrical resistance is a function of temperature.

Monitoring the evolution of resistance throughout a weld cycle provides important information about the welding process such as the occurrence of expulsion and the total energy input into the weld pool. It is common practice to plot changes in *R* with respect to the welding duration and interpret nugget growth throughout a spot-welding cycle. Different stages of a dynamic resistance curve, related to a typical single pulse welding schedule, are illustrated in Figure 2.7 (b). An area of electrical contact is created at the sheet/sheet interface after bringing the workpieces together and applying the electrode force. Due to the existence of insulators (incomplete contact, oxide films, and contaminations), the initial contact resistance will be very high, which will heat the sheet/sheet interface rapidly. Upon breakage of the contaminants, a sharp drop in resistance will be recorded (end of stage 1 in Figure 2.7 (b)).

Further heating concentrated at the workpiece interface softens the asperities, increasing the contact area and further reducing the resistance (end of stage 2). It is noted that while asperity collapse reduces the resistance, continued heating at the interface will increase local temperatures, which can have the opposite effect on the resistance (increasing the *R*-value). The competition between these two phenomena (reduction of *R* due to asperity collapse and rise of *R* due to higher temperatures) will dictate the minimum resistance of the dynamic resistance curve (α). Ultimately, the resistance increases with temperature increase will overcome the increase in contact area, and the total resistance will begin to rise (beginning of stage 3). Local melting begins during stage 3 as the resistivity continuously increases due to higher temperatures. Resistance will increase at the beginning of stage 4 since the bulk of the workpieces heats up. However, further expansion of the molten pool increases the cross-sectional area for current flow, reducing the resistance. Electrode collapse can also shorten the current flow path, further intensifying the resistance drop after the β peak. From this point onwards, the growth of the nugget and severe electrode collapse further reduce the resistance. Expulsion can occur if the nugget grows excessively, where it is no longer contained under the compressive pressure from the electrodes. It is noted that different variables, such as electrode size and shape, material thickness, welding schedules, and durations, can significantly alter the general shape of the dynamic resistance curve.

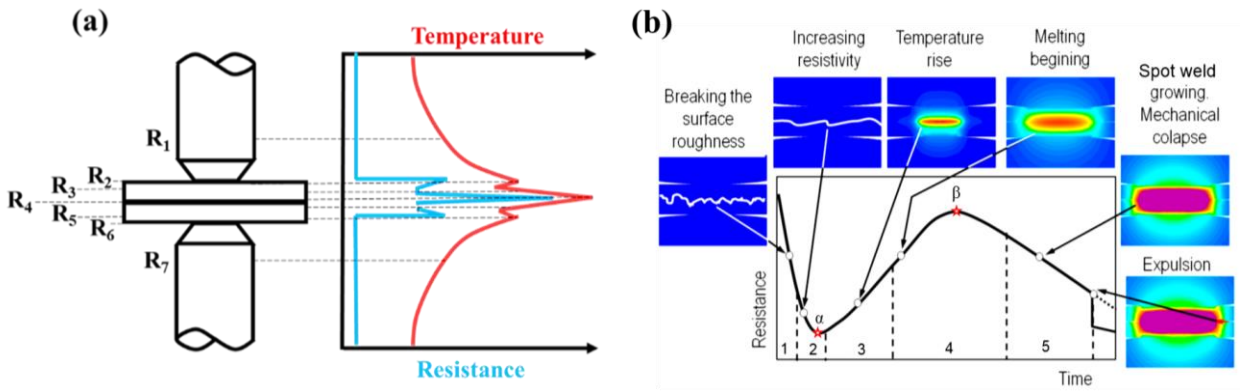


Figure 2.7. (a) Resistances encountered during RSW and their corresponding temperature distribution at different regions (adapted from [34]*), (b) Correlation between dynamic resistance curve and different stages related to the formation of an RSW nugget* [36].

2.3.2 RSW Process Parameters

A conventional weld cycle initiates with the squeeze time, the required time for the force to reach the nominal adjusted value. Squeeze times can vary based on the type of force application mechanism (hydraulic vs pneumatic or servo). Welding time is when current flows between the two electrodes, and hold time refers to the time allowed for the solidification of the nugget. In contrast, the current flow is terminated, and electrode force is maintained. It is noted that welding schedules can be more complex and include other parameters such as pre-pulse, post-pulse, and force amplifications, as schematically shown in Figure 2.8 (a).

The most critical RSW process parameters influencing the nugget diameter are welding time (duration), welding current, and electrode force. A direct result of low welding time and welding current will be insufficient nugget growth and poor joint quality. In contrast, a high welding current and welding time will lead to the growth of the nugget past the interface compressed by the electrodes and the ejection of molten metal in the form of expulsion, which is known to cause degradation of joint strength and compromise mechanical performance [34,37]. As a result, the magnitude and duration of the applied current should be optimized and selected to lead to the maximum nugget size while avoiding expulsion. It is common to develop weldability lobes for a specific joining stack up to aid in choosing the welding current and time to produce an optimized nugget diameter. To evaluate the weldability, as measured by the welding lobe or process window, the minimum and maximum currents resulting in welds at a particular welding time are determined. It is desirable to have a wide welding lobe so that subtle changes in welding conditions, such as inconsistent part fit-up during manufacturing, do not drastically affect the

quality of RSW joints [38]. An example of a current range curve is shown in Figure 2.8 (b). Current range curves are developed at different welding times to locate the minimum and maximum currents of one welding time within the weldability lobes (Figure 2.8 (c)). In common use, the minimum allowable weld size (MWS) is defined as a nugget diameter equal to $4\sqrt{t}$ where t is the thickness of the joining sheet, the MWS criterion has been adopted in most standards applicable to the automotive industry, including the AWS D8.9 [39] and International Standardization Organization (ISO) 18278 [40]. On the other hand, the occurrence of expulsion (forceful ejection of molten metal from the sheet/sheet interface) is commonly regarded as the maximum allowable welding current in the weldability lobe diagrams. It has been reported that the spot weldability lobe of modern grades of AHSS (such as 3G-AHSS) can be narrower than the weldability range of conventional high strength steels (HSS) due to a higher rate of heat generation during RSW of AHSS with relatively higher alloying content compared to HSS [34].

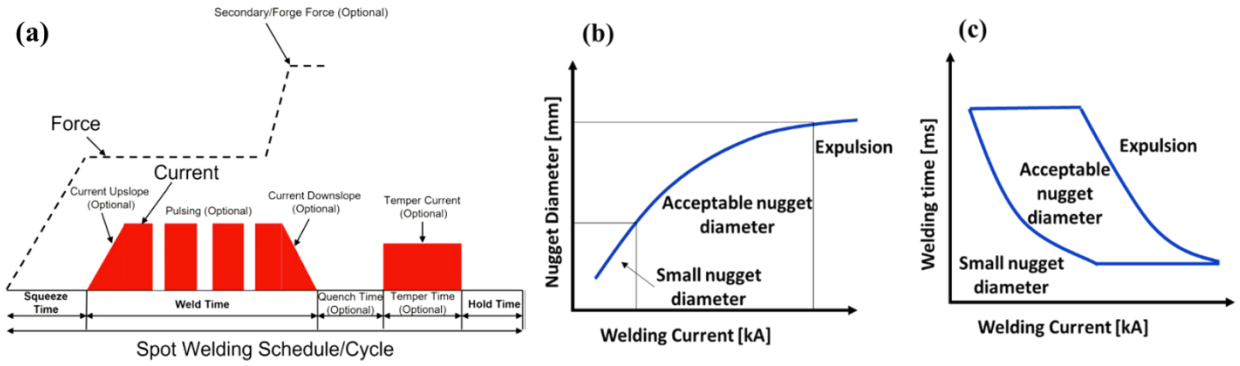


Figure 2.8. (a) Resistances encountered during RSW and their corresponding temperature distribution at different regions, (b) current range curve, and (c) weldability lobe for the RSW process (adapted from [31] *and* [229]*).*

Another RSW process parameter that affects the boundaries of weldability lobes is electrode force [41]. Most lobe diagrams are constructed with a fixed value of electrode force since the minimum and maximum welding currents are a strong function of electrode force. Applying higher electrode force reduces contact resistances at the sheet-to-sheet interface since all metals have some surface roughness that will limit the contact area when the two sheets are brought together [42]. Insufficient electrode force leads to the flow of electrons through the narrow regions where the surface asperities touch at the sheet-sheet interface. However, when a suitable electrode force is applied, surface asperities collapse, and the contact resistance decreases. Using high

electrode force also delays expulsion occurrence because more confinement is imposed onto the weldment [14].

Other than the main RSW process parameters discussed above, some material-related parameters such as strength, thickness, coating type, and surface oxides or contaminations can significantly influence resistance during the welding process and heat generation. For example, Saha *et al.* [43] investigated the effect of different Al-Si and Zn coating compositions on heat generation and nugget formation during RSW of hot press-forming steels. Their study showed that coatings can be responsible for inhomogeneous current flow and impede the nugget growth rate during the RSW process. Studies by Han *et al.* [44] and Ghatei Kalashami *et al.* [45] showed that the formation of internal oxides during a controlled atmosphere galvanizing process reduced the resistance and heat input, which delayed nugget growth in the RSW process, compared to the as-received condition of cold-rolled CMn1.8Si steel. Resistance to electrode indentation is another parameter affected by the strength of the to-be-welded material. Investigations by Uijl *et al.* [46] revealed that lower weldability could be due to high strength and resistance to electrode indentation.

In contrast, softer materials tend to deform more easily under electrode force, making full contact area with the electrodes. Different material and coating thicknesses also alter the heat dissipation rate during the RSW process, which, in turn, should be compensated for by properly adjusting the welding current value and heat input, as pointed out by Ighodaro *et al.* [47]. Electrode shape, which determines the contact area in RSW, is another parameter that affects the current density, rate of heat generation, and heat extraction during the RSW cycle [48]. Li *et al.* studied the effect of varying truncated electrode cone angles on nugget formation. They showed that the lower cone angles lead to a more uniform temperature field in the molten pool due to more severe electromagnetic stirring and also more efficient cooling [49]. Figure 2.9 summarizes the most important RSW process parameters that were introduced in this section.

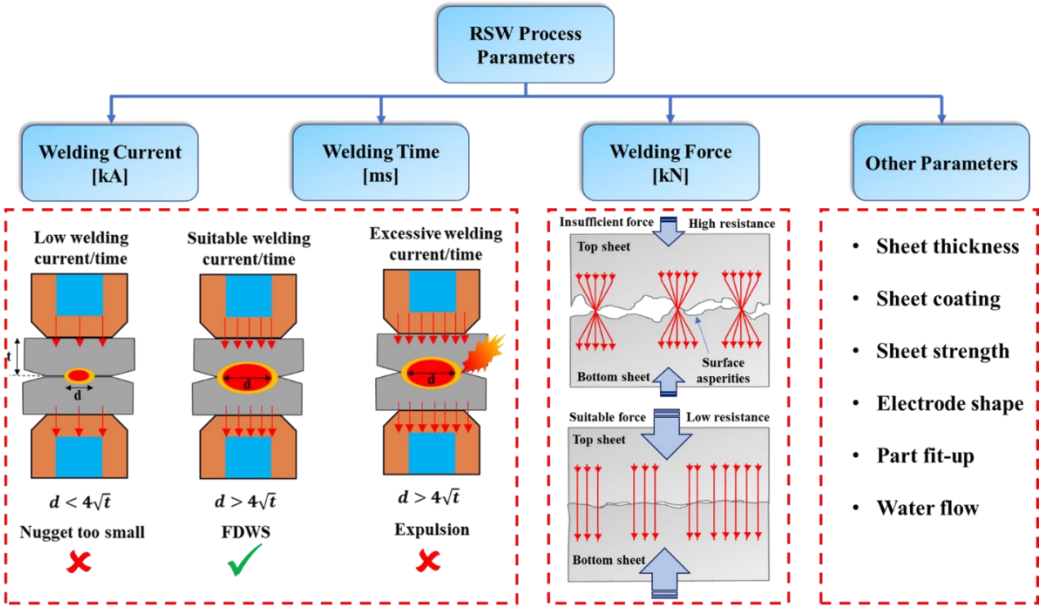


Figure 2.9. Some of the most important RSW process parameters.

2.4 RSW Joint Quality

The quality of a weld is expressed by a combination of quantitative and qualitative features when inspected in either a destructive or non-destructive manner. Generally, four indices are considered when assessing the quality of RSW joints as outlined in Figure 2.10: (i) physical attributes, (ii) metallurgical characteristics, (iii) mechanical performance, and (iv) failure mode. More than one quality index is expected to be considered to judge the quality of a weld. The following subsections will expand on these four major RSW quality indices.

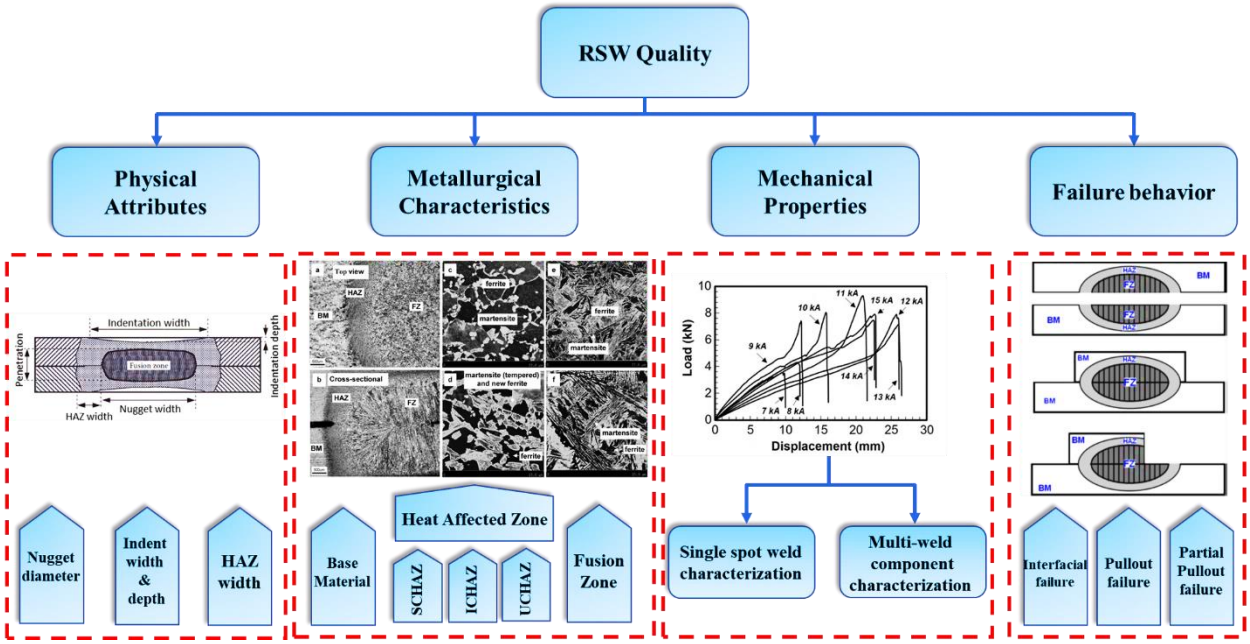


Figure 2.10. Factors used to evaluate the quality of resistance spot welds. Images from [34,50–52].

2.4.1 Physical Attributes of RSW Joints

Physical (or geometrical) attributes refer to features of a weldment that are directly visible after a weld is made or indirectly revealed after cross-sectioning or peeling the weld apart. Some of the commonly inspected physical attributes of RSW weldments include the appearance of the weld, electrode indentation depth, nugget width, heat affected zone (HAZ) width, penetration of molten metal, the existence of voids, and shape of the notch at the sheet-sheet interface (see Figure 2.11). Among these features, the diameter of the nugget defines the bonding area between the two sheets and is the most important physical feature since it significantly influences the mechanical properties of the joint. For example, a study on RSW of DP AHSS by Kishore *et al.* [53] has shown that increasing the heat input via the welding time and current spurs nugget growth, which, in turn, enhances the shear and tensile strength of the weldments. A low nugget size to sheet thickness ratio is usually attributed to elevated stress concentration at the sheet-sheet interface. In contrast, a high nugget-to-sheet thickness ratio is regarded as favorable for the mechanical properties of the joint by reducing the stress concentration at weld edges [54]. Regarding other visual features, it has been reported that the existence of sharp notches compared to squared ones, extreme electrode indentations due to high electrode force or expulsion phenomenon, and the existence of shrinkage voids/porosities, which reduce effective nugget size, can have detrimental effects on joint

performance by providing more stress concentration regions during mechanical tests and result in premature failures [52,55,56].

It is noted that different mechanisms can be responsible for the formation of voids/porosities. Vijayan *et al.* [57] reported that these defects lead to differences between axial and radial solidification rates (axially dendritic solidification growth in the sheet through-thickness direction vs interdendritic feeding along the nugget diameter). This mechanism is believed to be more dominant in relatively thicker RSW stack-ups or multi-sheet welding. Another source of void formation is related to the gases and moisture trapped within the coating layer of joining materials brought into the nugget during welding [58]. This type of pore, which possesses a characteristic smooth and circular shape, is not typically observed during the welding of uncoated materials.

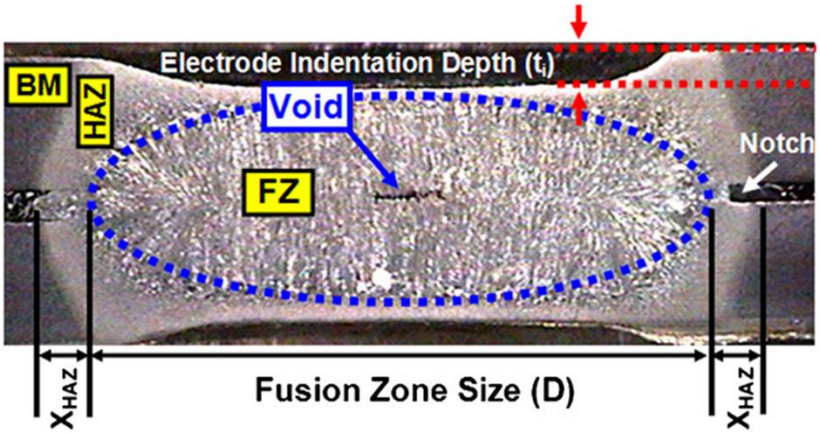


Figure 2.11. Cross-sectional view of the typical macrostructure of resistance spot welds showing various physical attributes.

2.4.2 Metallurgical Characteristics of RSW Joints

Thermal cycling from the RSW process alters the microstructure of the surrounding material through different phase transformations, which create three distinct regions: Fusion zone (FZ), heat-affected zone (HAZ), and base material (BM). FZ is the region where the local temperature exceeds the melting temperature (T_m) of the steel during the heating stage of the process and resolidifies upon cooling. The HAZ is the region surrounding the FZ, which does not melt but experiences solid-state microstructural changes due to its proximity to the FZ. The increase in temperature and amount of time BM stays at elevated temperatures is not high enough to promote microstructural changes.

Two parameters govern the microstructural evolution within the FZ of RSW joints: (i) chemical composition and (ii) cooling rate [14]. The chemical composition of the FZ is only

affected by the chemical composition of the BMs being spot welded. As for cooling rates, numerical investigations by Gould *et al.* [59] showed that depending on the sheet thickness and electrode face diameter, cooling rates higher than the critical value required for the formation of martensite are typical in RSW of different grades of AHSS. The water-cooled electrodes and their quenching effect, especially in low-nugget diameter-to-sheet thickness ratios, are the main reason for high cooling rates within the FZ of the RSW process [59,60], making the formation of martensite in FZ of AHSS RSW unsurprising. For fusion joining processes, it is common to explain the solidified microstructure morphology and size by the effect of the temperature gradient at the solidifying interface and the solid growth rate [61]. Fast cooling and rapid solidification within a few cycles in RSW noticeably increase the degree of constitutional supercooling and usually cause dendritic growth morphologies within the FZ [62].

The HAZ is another important welding region located adjacent to the FZ. The HAZ has several sub-areas owing to its range of possible microstructural evolutions and metallurgical reactions as it experiences a spectrum of peak temperatures and cooling rates. The peak temperature experienced in the HAZ close to the FZ boundary is just below T_m and gradually decreases towards the BM [63]. The HAZ due to spot welding is commonly split into four sub-regions: coarse-grained HAZ (CGHAZ), fine-grained HAZ (FGHAZ), intercritical HAZ (ICHAZ), and the subcritical HAZ (SCHAZ) [34]. Within CGHAZ, the temperature is well above the A_{c3} temperature, and the microstructure is fully austenitic; thus, higher peak temperatures in this region promote rapid grain growth. Large martensite packets and prior austenitic grain boundaries (PAGB) are characteristics of the CGHAZ. The FGHAZ thermal cycle nucleates (recrystallizes) austenite grains, but the temperature is insufficient for significant grain coarsening, resulting in grain refinement. Therefore, refined martensitic grains with relatively finer PAGBs compared with the CGHAZ are the key characteristics of FGHAZ. The ICHAZ peak temperatures are between the A_{c1} and A_{c3} temperatures, causing partial transformation to austenite, resulting in a final martensite + ferrite microstructure upon cooling. The type and fraction of micro-constituents in the ICHAZ are strongly dependent on the initial microstructure of the BM and can be complex [64]. For example, Q&P with ferrite, martensite, and RA can partially transform into austenite during the welding cycle. The austenite can be converted into complex martensite/austenite constituents with the untransformed microstructure from the BM remaining during the cooling cycle. The temperature in SCHAZ is below A_{c1}, which enables long-range

diffusion of interstitial solute atoms and carbide precipitations. The changes mentioned above can result in tempering the metastable martensite and bainite phases, if available, as shown by Eller *et al.* [65]. Similarly, carbides within the BM of AHSS can act as carbon sources upon heating and undergo phase transformations in any of the regions mentioned earlier based on the thermal history and chemical composition of the AHSS. For example, Saha *et al.* reported the transformation of pre-existing Fe_3C in DP780 to more complex carbides, leading to the secondary hardening of the SCHAZ [66].

Figure 2.12 (a) shows the correlation between peak temperatures experienced during welding and the approximate location of each of the FZ and HAZ sub-regions on a Fe-C phase diagram for a Q&P 3G-AHSS with 0.1 wt.%C. It should be noted that equilibrium phase diagrams cannot be used to analyze the non-equilibrium transformations occurring during RSW quantitatively. Continuous-cooling transformation (CCT) diagrams are helpful since they can predict transformations not shown in phase diagrams, such as metastable martensite and bainite formation during the RSW of steels. However, CCT diagrams are material-dependent, and a lack of information exists regarding phase transformations at high cooling rates, as experienced in the RSW process for 3G-AHSS. Therefore, equilibrium phase diagrams are utilized as a guideline for determining possible transformations during the RSW process.

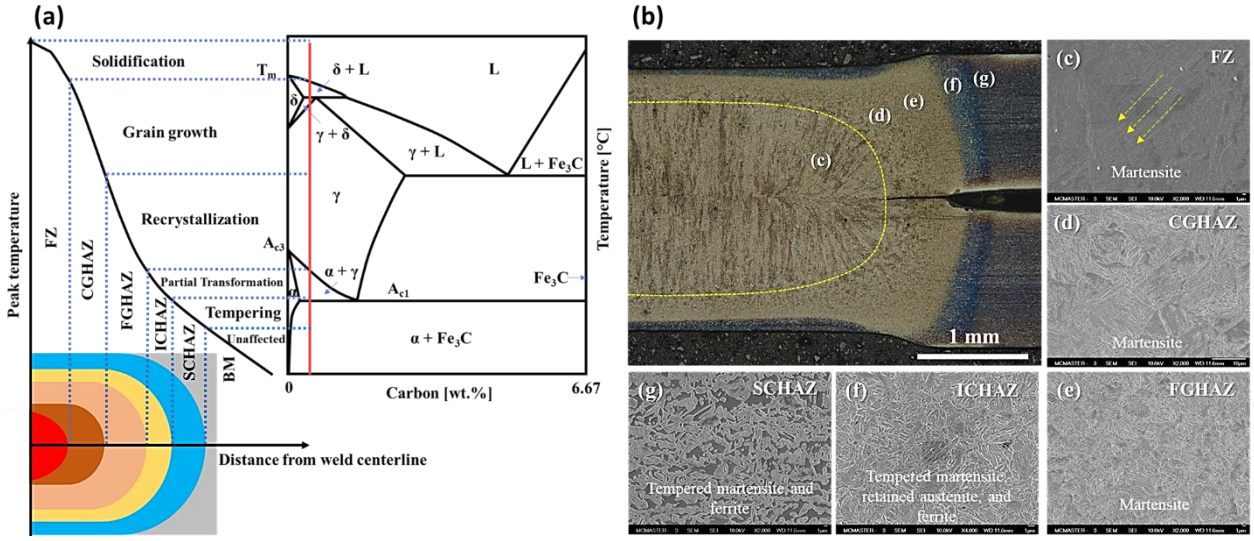


Figure 2.12. (a) Sub-division of different RSW microstructures with respective peak temperatures shown on Fe-C equilibrium diagram (adapted from [31,59,230]*), (b) SEM micrographs of (c) FZ, (d) CGHAZ, (e) FGHAZ, (f) ICHAZ, (g) SCHAZ, of Q&P 3G-AHSS RSW* [64].

An example of the microstructural evolution in different regions of a Q&P 3G-AHSS after a single pulse RSW schedule is shown in Figure 2.12 (b). The FZ exhibited a fully coarse columnar lath martensitic microstructure with the epitaxial growth direction favored along the most effective cooling direction. The CGHAZ and FGHAZ have a fully martensitic microstructure like that of FZ, but the grains in CGHAZ are coarser due to higher peak temperatures. Figure 2.12 (f) shows the microstructure of the ICHAZ, which exhibits a microstructure containing ferrite and martensite due to partial austenitization. The existence of austenite in the ICHAZ of Q&P steels has been attributed to the high content of austenite stabilizing elements such as Carbon, Manganese, and Silicon in 3G-AHSS [67]. The SCHAZ experiences the tempering of the available martensite in the BM. The tempered martensite is observed as broken laths of martensite in the micrograph (Figure 2.12 (g)). The broken martensite lath morphology within SCHAZ is attributed to the high density of precipitation in SCHAZ and also the decomposition of martensite by carbon diffusion from supersaturated martensite and the formation of various types of carbides such as cementite [52,68].

A direct consequence of the microstructural evolution in an RSW weldment is the alteration of the local hardness according to the micro-constituents formed in different regions. Microhardness tests correlate the microstructure of RSW sub-regions with mechanical properties. Figure 2.13 (a) shows a typical microhardness profile across the diagonal cross-section of a spot-welded DP980 AHSS. As shown, the microhardness characteristics of different regions are heavily affected by the thermal cycle from the RSW process. Typically, an increase in the hardness of FZ is expected compared to the BM since this region's extremely high cooling rate promotes martensitic transformations. Tamizi *et al.* [69] have shown that the FZ of MS1400 steel is fully martensitic regardless of the implemented RSW welding schedule. Similarly, a fully martensitic microstructure has been reported for 3G-AHSS RSW as well in the work of Wang *et al.* and Liu *et al.* [70,71], where the FZ harnesses were 1.5 to 1.7 times higher than that of BM.

The most critical zone in terms of local hardness is the SCHAZ since it experiences temperatures in the range of 350°C to $A_{c1,}$ suitable for martensite tempering. According to Hernandez *et al.* [72], decomposed martensite is the major contributor to the observed softening in micro-scale hardness measurement. In contrast, the hardness reduction of ferrite in this region is less discernible (Figure 2.13 (d)). Severe tempering of martensite can cause the SCHAZ to be

softer than the surrounding BM and FZ, making it a possible weak region in terms of mechanical properties. While SCHAZ softening in DP and Martensitic AHSS such as DP600, DP980, and MS1200 is well documented in the literature [69,73], conflicting data regarding the hardness of the SCHAZ region exists for 3G-AHSS. For instance, while Wang *et al.* [70] reported an approximately 34 HV drop in the hardness of the sub-critical HAZ compared to the BM of 3G-980 RSW joints, Lei and Pan [74] and Speer *et al.* [75] did not observe a softened HAZ during RSW of this particular steel. The degree of softening in the SCHAZ is reported to be a function of steel chemistry, heat input, and martensite content. Biro *et al.* studied the softening kinetics of SCHAZ in DP steels and found that the heat input required for HAZ softening decreased as the carbon content of the martensitic phase increased. Furthermore, they reported that while the decomposition of martensite to cementite and ferrite promoted martensite softening, carbide-forming alloying elements such as Cr and Mo increased resistance to the softening phenomenon [76]. Transformation of austenite to martensite during cooling in the CGHAZ and FGHAZ, and the formation of martensite from partially transformed austenite in the ICHAZ also increases the hardness in different regions of the HAZ. The BM does not show any discernable changes in hardness due to the low-temperature regime it experiences during the RSW process.

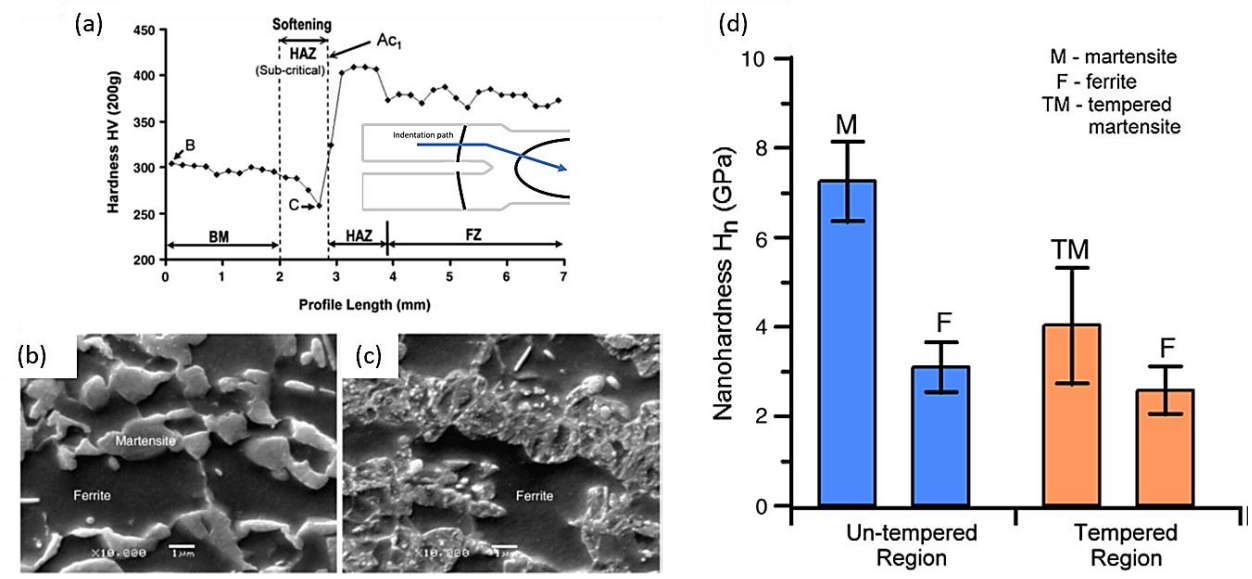


Figure 2.13. (a) Vickers micro-hardness indentation profile across a DP980 spot weld cross-section, (b–c) SEM micrographs for BM and the sub-critical region (HAZ) respectively, (d) nano hardness characteristics of the martensite and ferrite in BM and SCHAZ [72].

RSW thermal cycle can be the source of many imperfections in the formed microstructures and heterogeneities in local properties. In addition to the formation of a nugget and softened/ hardened heat-affected zones (HAZ) [66], liquation cracks due to tensile stresses imposed on the partially melted zone (PMZ) upon solidification have been reported for RSW of Q&P 3G-AHSS [71], TWIP [77], and TRIP steels [78]. Other studies have reported a carbon-depleted region referred to as the "halo ring" at the boundary of the FZ of 3G-AHSS [79] and press-hardened steels (PHS) resistance spot welds [80,81]. Both liquation cracks and the softened halo ring are associated with micro/macro alloying element segregations, which could compromise the quality of the joints (see Figure 2.14). Therefore, it is essential to understand whether the implemented RSW thermal cycle leads to any of the issues above.

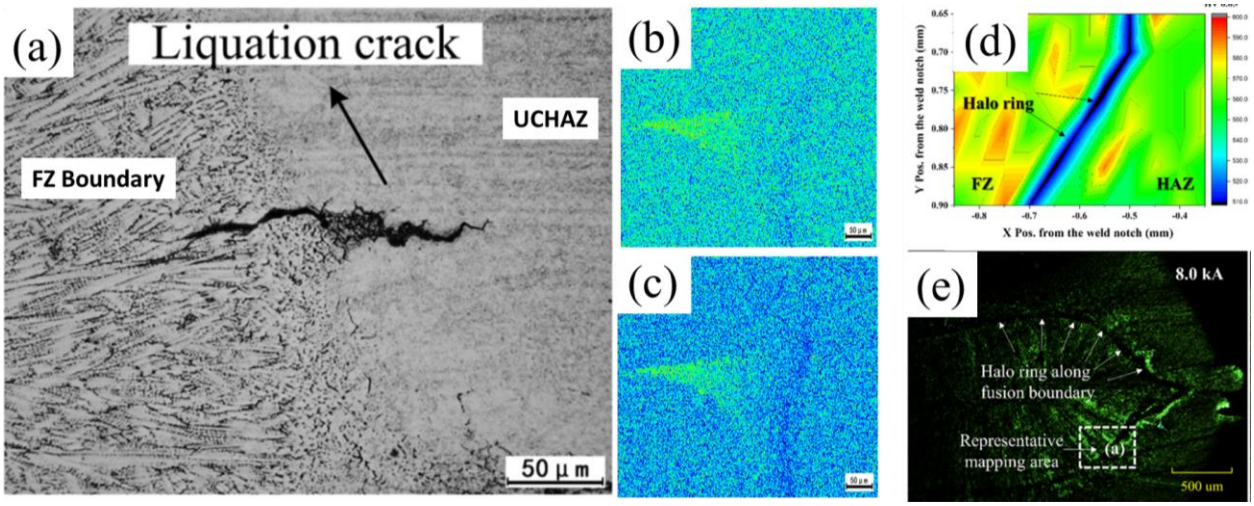


Figure 2.14. (a) formation of a liquated crack at the FZ boundary of 3G-AHSS Q&P resistance spot welds. A characteristic of liquation cracks is Mn and Si segregation, as demonstrated in elemental maps in (b) and (c). (d) and (e) local softened region referred to as the "halo ring" is characterized via hardness drop at the FZ boundary of 3G-AHSS spot welds.

Eftekharimilani *et al.* [82] reported that implementing a double pulse welding schedule can partially remelt the primary nugget and anneal the FZ boundary. It was shown that the annealing treatment could effectively enhance the local properties of the spot weld by redistributing alloying elements such as P towards the FZ interior, which ultimately promoted the formation of more equiaxed martensitic grains with smaller average block widths.

2.4.3 Mechanical Properties of RSW Joints

From a general perspective, RSW mechanical property evaluation can be categorized into two groups: (i) single-spot weld mechanical tests and (ii) multi-weld (component) tests. In the case

of a vehicle crash event, complex and dynamic loading is applied to a group of spot welds [83]. However, the mechanical properties of spot welds are frequently evaluated under quasi-static loading of a single spot weld for fundamental studies. This way, the dynamic testing apparatus's complexities, and high component-scale testing costs are eliminated [84]. Single and multi-weld mechanical characterization methodologies are discussed in the following two sections.

2.4.3.1 Single Spot Weld Mechanical Characterization

The mechanical performance of single spot welds is typically assessed under shear loading due to the relative displacement/rotation of sheets and tensile loading due to separating loads normal to the sheets [14]. For this purpose, two standard mechanical tests, tensile-shear (TS) and cross-tension (CT), are commonly performed [6,85]. The main advantages of these standardized characterization geometries include easy, inexpensive specimen fabrication and straightforward interpretation of the results [14]. More advanced characterization techniques of spot welds can be utilized to investigate the mechanical properties of spot welds in loading conditions other than predominant shear or tension. These advanced testing methodologies include, among others, CP (CP) and the modified version of the Kopfzup-Scherzug mechanical test (also known as the KS-II test) [86].

The output of the aforementioned RSW mechanical tests is usually measured in the form of applied load vs displacement, as shown in Figure 2.15. In the loading stage of the test, the specimen work hardens, and the applied load continuously increases until the peak load is reached. At the peak load point, failure initiates, and upon propagation of the formed cracks at the notch region in the sheet-sheet interface, strength loss appears within the unloading regime of the curve until complete failure. A few parameters are extracted from such curves: (i) peak load, which is representative of spot weld strength; (ii) displacement up to the peak load value representative of weldment ductility; and (iii) absorbed energy up to peak load, representative of weld toughness (highlighted in blue in Figure 2.15) [14]. Damage accumulation or energy dissipation after peak load, defined as the area under the curve during the unloading regime of the curves (highlighted in red in Figure 2.15), is often neglected according to the instructions of AWS standard [35,87]. However, recent work by O'Keeffe and Tolton has shown that if correlating mechanical test data with the actual crash scenario is intended, accounting for the curves' unloading regime is critical to accurately predicting the deformation of automotive structures [88,89]. The value of peak load, energy absorption, and the shape of the load-displacement curves are a function of numerous

parameters, most notably the stress state of the nugget, testing geometry, and type of failure. Generally, better strength and energy absorption values are achieved as larger nugget diameters are tested, as shown in the work of Liu *et al.* on TS and CT of Q&P 3G-AHSS spot welds [71]. The following sections introduce and discuss the TS, CT, CP, and KS-II mechanical tests in more detail.

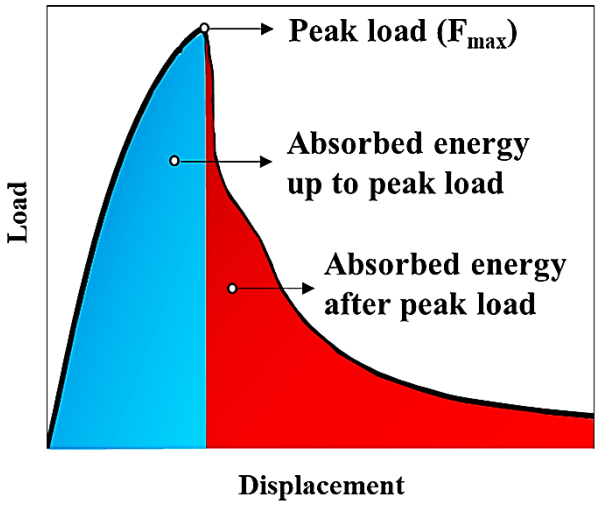


Figure 2.15. A typical load-displacement curve, output of an RSW mechanical test.

2.4.3.1.1 Tensile Shear (TS) and Cross Tensile (CT) Tests

During the TS test, one leg of the upper sheet and one of the lower sheet are subjected to tensile stresses such that the nugget is primarily under shear stresses at the sheet-sheet interface (Figure 2.16 (a)). As for the CT test, tensile loads are applied to the weld in a direction perpendicular to the sheet surface, as shown in Figure 2.16 (b). The ideal initial stress state of the nugget for both tests, shown in Figure 2.16, is subject to changes as the tests continue. For instance, loading conditions can change during the CT test as the specimen may slip within the gripping fixtures, and the BM surrounding the spot weld can bend before the welded joint is fully loaded. A similar issue can arise for TS mechanical tests as well. When the specimen is under shear loading, it tends to rotate to align the gripped ends with the welded joint. Coupon rotation can be exacerbated by any moment induced by off-plane loading [88]. In both cases, coupon slippage and BM plastic deformation during the CT test and rotation of the coupons during TS tests, the applied loading condition will change from initial pure tension or pure shear to a combination of shear and tensile loading condition (mixed state).

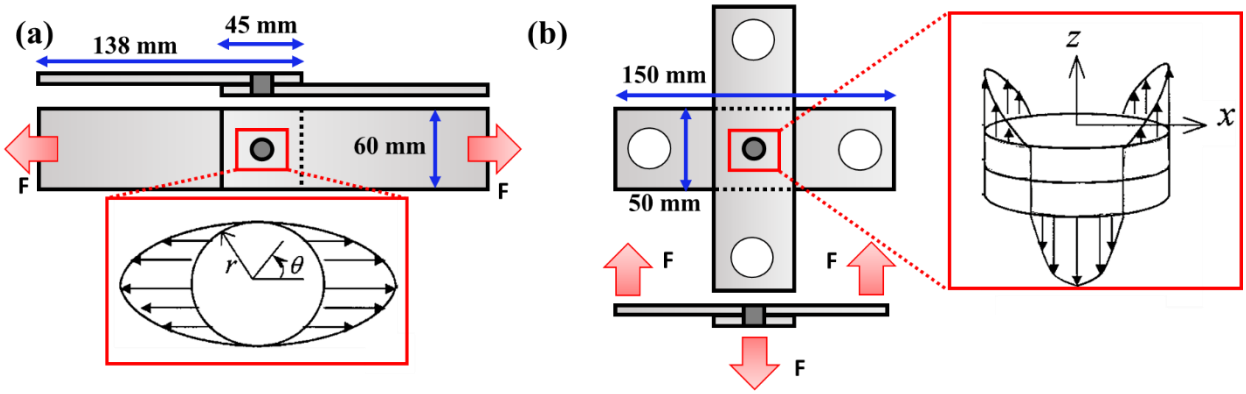


Figure 2.16. Standard (a) Tensile shear (TS), and (b) cross-tension (CT) coupon geometries and dimensions utilized to evaluate shear and tensile strengths of spot welds, along with the corresponding stress state induced around the nugget periphery in the beginning of the tests (based on [231] *and* [106]*).*

Figure 2.17 shows examples of the rotation and bending of coupons as the TS and CT tests continue. A few studies have tried to quantify and account for the effect of rotation of RSW joints during the TS test on mechanical properties. Still, they all cross-sectioned the nugget in half to expose the hidden nugget, which affected the mechanical performance of the joint [89,90]. As for the CT test, although BM deformation is widely acknowledged, the fixturing required for this test makes in-situ analysis of joint rotation or slippage a challenging task [91].

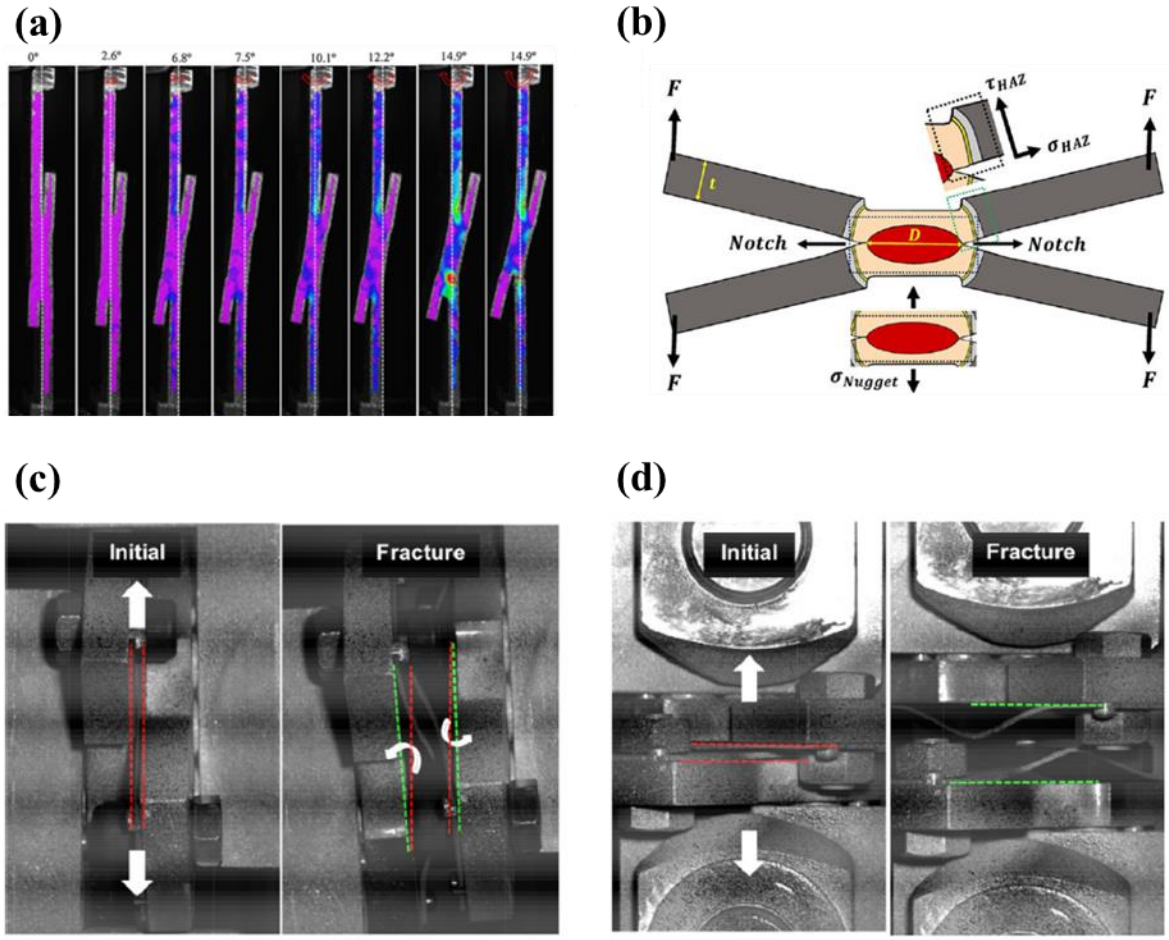


Figure 2.17. (a) Rotation of coupons during TS test using side digital image correlation (DIC) technique, (b) schematic illustration for bending of material surrounding spot weld during CS test [49,87]. *(c) and (d) show rotation and deformation of the coupons during a modified CT test that was performed in shear and tensile-dominated loading orientations, respectively.*

Table 2.1 summarizes the findings from previous investigations on 3G-AHSS resistance spot weldability and failure characterization under conventional TS and CT mechanical tests. Although the available literature explains the mechanical properties and failure characteristics of 3G-AHSS under TS and CT mechanical tests to some extent, no coherent conclusion has been reached regarding the dominant failure behavior of these novel steels. For example, while Liu *et al.* reported liquation cracking and P segregation at the partially melted zone as the mechanism responsible for their observed failure behavior during TS and CT tests, Ramachandran *et al.* [79] considered the formation of a carbon-depleted and locally softened zone at the boundary of the nugget, as the crack initiation region during CT tests of 3G-AHSS spot welds. Moreover, more

work is required for more complex loading conditions, such as combined/mixed loading mode and weld-group tests, especially for RSW of different grades of 3G-AHSS.

Table 2.1. Summary of failure behavior and characteristics reported for RSW of 3G-AHSS under conventional TS and CT mechanical tests.

Type of 3G-AHSS	Type of Mechanical Test	Type of Failure	Failure Explanation	Main Contribution on 3G-AHSS Weldability	Year [Ref]
Q&P (UTS 980 MPa)	Standard TS and CT	• Did not discuss	• Did not discuss	• Developed weldability lobes • Reported ductility ratios	2012 [74]
Q&P (UTS 970 MPa)	Standard TS and CT	• IF for low heat input regime • The PO for the medium heat input regime was initiated at either the softened HAZ or FZ lateral border.	• IF through the FZ due to a small nugget • The transition between PO failure initiation regions is related to the amount of bending moment induced by rotation	• Expulsion causes HAZ failure and strength loss in TS • Reported SCHAZ softening	2016 [92]
Q&P (UTS 980 MPa)	Standard TS and CT	• IF for single pulse welds • PO and P-PO for double pulse welds	• Q&P is susceptible to liquation cracking at a partially melted zone (PMZ) • P-PO failures have three stages: crack initiation, propagation, and instantaneous failure	• Identified PMZ as a crack-sensitive area • P segregation at PMZ • Pulsing can homogenize the P segregation	2019 [71]
Q&P (UTS 980 MPa)	Standard TS and CT	• PO and P-PO	• Did not observe liquation cracking • Failures followed softened FZ boundary known as the "halo ring."	• Reported SCHAZ secondary hardening	2021 [93]
Q&P (UTS 1180 MPa)	Standard TS and CT	• PO and P-PO	• The toughness of the nugget influences tensile shear strength	• Improved mechanical properties by post-weld heat treatment	2021 [94]
Q&P (UTS 980 MPa)	Standard CT	• PO	• PO failure propagated through the softened halo ring around the FZ boundary	• The halo ring can be eliminated by pulsing • C, Mn, and Si segregation form the halo	2022 [67]

2.4.3.1.2 KS-II Tests

Lee *et al.* [95] designed a dedicated fixture specifically for evaluating the mechanical response of a weldment under combined shear and tensile loading conditions, as shown in Figure 2.18 (a). The specimen required for this fixture was referred to as a U-tension specimen, as shown in Figure 2.18 (b). They performed their tests on spot welds of mild steel in four loading orientations: 30°, 50°, 70°, and 90°, and reported a 20% reduction in weld strength as the loading angle increased to 90°. However, the nugget diameter was inconsistent throughout the tests in different orientations [34]. Their design of experiment (DOE) analysis also indicated that the U-tension coupon width and length had minimal influence on the results of their tests [96].

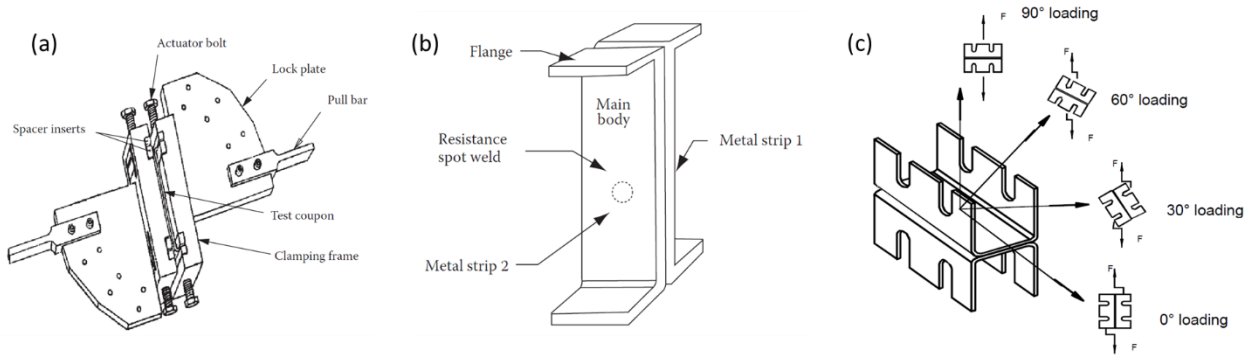


Figure 2.18. (a) Fixture for testing spot welds under combined loading, (b) U-tension specimen to be installed in the fixture, and (c) KS-II coupon [34,95,97].

More recently, a modified U-tension coupon, referred to as the KS-II coupon, developed by Özdem Hahn *et al.* (Figure 2.18 (c)) [97], was introduced, which provided more rigidity to combined loading tests due to better gripping utilized using clearance holes [97]. So far, the KS-II test has primarily been used to evaluate the accuracy of predictions from spot weld models [32,98–100]. For instance, Khan *et al.* performed KS-II tests on numerous homogeneous and heterogeneous stack-ups of different grades AHSS (including USIBOR® 1500 and TRIP steels). They developed a 3D stress-based failure criterion for all the stack-ups. Their model reasonably agreed with the experimental strength values but failed to account for the damage accumulation after the peak load point. Ghassemi-Armaki *et al.* performed the KS-II test in three different combinations of shear and tensile loads (30°, 60°, 90°) to calibrate a finite-element model in LS-DYNA. They successfully implemented their model in full vehicle LS-DYNA simulation, which allowed them to optimize the vehicle weld layout. Table 2.2 outlines some of the most important outcomes from the studies that characterized the combined shear-tensile loading of spot welds.

Table 2.2. Summary of significant contributions regarding combined loading of resistance spot welds.

Investigated Material	Fixture Type	Coupon Type	Main Contribution Regarding Combined Loading of RSW	Comments	Year [Ref]
Mild steel (UTS 282 MPa)	Custom 2-unit Lock Plates	Flanged Metal Strips	• Performed combined loading of RSW for the first time • Proposed an empirical equation to predict RSW strength under combined loading	• Did not report load-displacement characteristics • Failure criterion did not predict failure strength accurately	1998 [101]
Mild steel (UTS 302 MPa)	Custom 4 Rectangular Tubes with Inclined Angles	Square Cup with Arc Welded Plates	• Improved specimen stiffness by welding reinforcement plates and better grip using clearance holes • Conducted a lower bound load limit analysis on RSW failure	• Multiple fixtures required • Did not perform pure shear tests	2001 [102] 2004 [103]
XES Mild steel (UTS 300 MPa)	Arcan Apparatus	Spot Welded Plates and Heels	• Utilized Arcan device for simplicity of RSW combined loading • Proved strain rate dependency of failure loads at different orientations	• Highlighted the importance of absorbed energy after peak load but did not report any energy calculations • Did not perform pure shear tests	2004 [104] 2010 [105]
Mild steel (UTS 410 MPa)	Arcan Apparatus	KS-II	• Suggested RSW combined loading methodologies to be used as a tool for model validation • Used KS-II test to validate the developed model	• Calibrated their model using TS and CP mechanical tests • Post-failure predictions were not accurate	2010 [100]
DP AHSS (UTS 590 MPa)	Custom 6 Sets of Fixtures With Pin-joint	Cross-type Specimen with Guide Plates	• Recognized alteration of the ratio between shear and tensile components of force due to the rotation of coupons as combined loading of spot welds continued	• Used guide plates to keep the ratio of shear and tensile components of force constant • Minimized BM deformation using six extra spot welds around the main weld	2011 [106]
DP AHSS (UTS 590 MPa)	Arcan Apparatus	KS-II	• Combined loading tests can be used to calibrate a force-based failure criterion	• Did not account for the rotation • Did not report load-displacement characteristics	2019 [86]
DP AHSS (UTS 600 MPa)	Custom 2 Clevis Joints	Modified Cross Tension	• Coupled combined loading experiments of RSW with digital imaging techniques	• Reported severe BM deformation • Reported rotation, but fixturing did not allow quantification	2020 [107]

Based on Table 2.2, although a few studies have reported the rotation and deformation of coupons during combined loading tests [108], the main focus was on minimizing the rotation. A methodology for quantification of this unwanted phenomenon is still lacking in the available literature. Evaluation of AHSS spot weld mechanical properties under combined loading induced by KS-II mechanical tests has also received limited attention in the literature. Although previous investigations using Arcan-type testing fixtures were capable of imposing various combinations of loads on the spot welds [109–111], the significant effect of clamping condition, amount of slippage or nugget rotation, and loading histories acting on the spot weld have been generally ignored. Minimizing the rotation of the nugget by proposing modifications to the testing fixture while quantifying the amount of nugget rotation during testing is still required for the most accurate

experimental characterization of spot weld mechanical performance under combined shear-tensile loading.

2.4.3.1.3 CP (CP) Tests

Spot welds in automotive structures can experience tensile loading induced by bending moments due to the separating forces applied between the joined sheets. Failure of spot welds under bending moments caused by eccentric loading is typically characterized using the CP geometry. The CP geometry comprises two L-shaped coupons with the spot weld located on the horizontal flange region, as shown schematically in Figure 2.19 (a). The schematic in Figure 2.19 (b) describes the stress distribution at the interface and circumference of a spot weld during the CP test. During this test, the weld is subjected to tensile stresses perpendicular to the plane from the applied vertical load and bending that applies a tensile stress parallel to the weld. According to Pouranvari and Marashi, the tensile stresses at the sheet/sheet interface drive failure through the nugget. In contrast, bending stresses are the driving force for failure through the sheet thickness [55]. The severity of the bending moment is directly proportional to the moment arm length in the CP geometry. As shown in Figure 2.19 (c), the length of the bending arm is defined as the distance between the loading axis and the location of the spot weld on the lower flange. The rather poor boundary conditions during the CP test can lead to large amounts of coupon plastic deformation as shown in multiple studies that conducted CP tests on spot welds of AHSS [112–114]. The coupon deformation can reduce the initial bending moment arm by the end of the test. Recently, Xu *et al.* idealized the CP geometry according to the schematic shown in Figure 2.20 and proposed calculating the bending moment applied to the spot weld according to Equation 2.2 [115]:

$$M_{CP} = F_{CP} \times \Delta L_{PF}; \Delta L_{PF} = \sqrt{L^2 - \left(\frac{\Delta L_{CP}}{2}\right)^2} \quad (2.2)$$

where M_{CP} is the bending moment applied to the spot weld, F_{CP} is the peak load from the acquired crosshead load-displacement response, ΔL_{PF} is the moment arm related to F_{CP}, and ΔL_{CP} is the crosshead displacement up to the point of peak load. The methodology of Xu *et al.* to track bending moment induced to spot welds during CP tests does not provide a viable approach to track the evolution of the moment arm throughout the test. The proposed methodology assumes the spot weld maintains its alignment along the horizontal flange throughout the test. Unlike the standard TS and CT tests, which have been extensively studied on 3G-AHSS spot welds, limited literature exists on CP testing of 3G-AHSS spot welded joints.

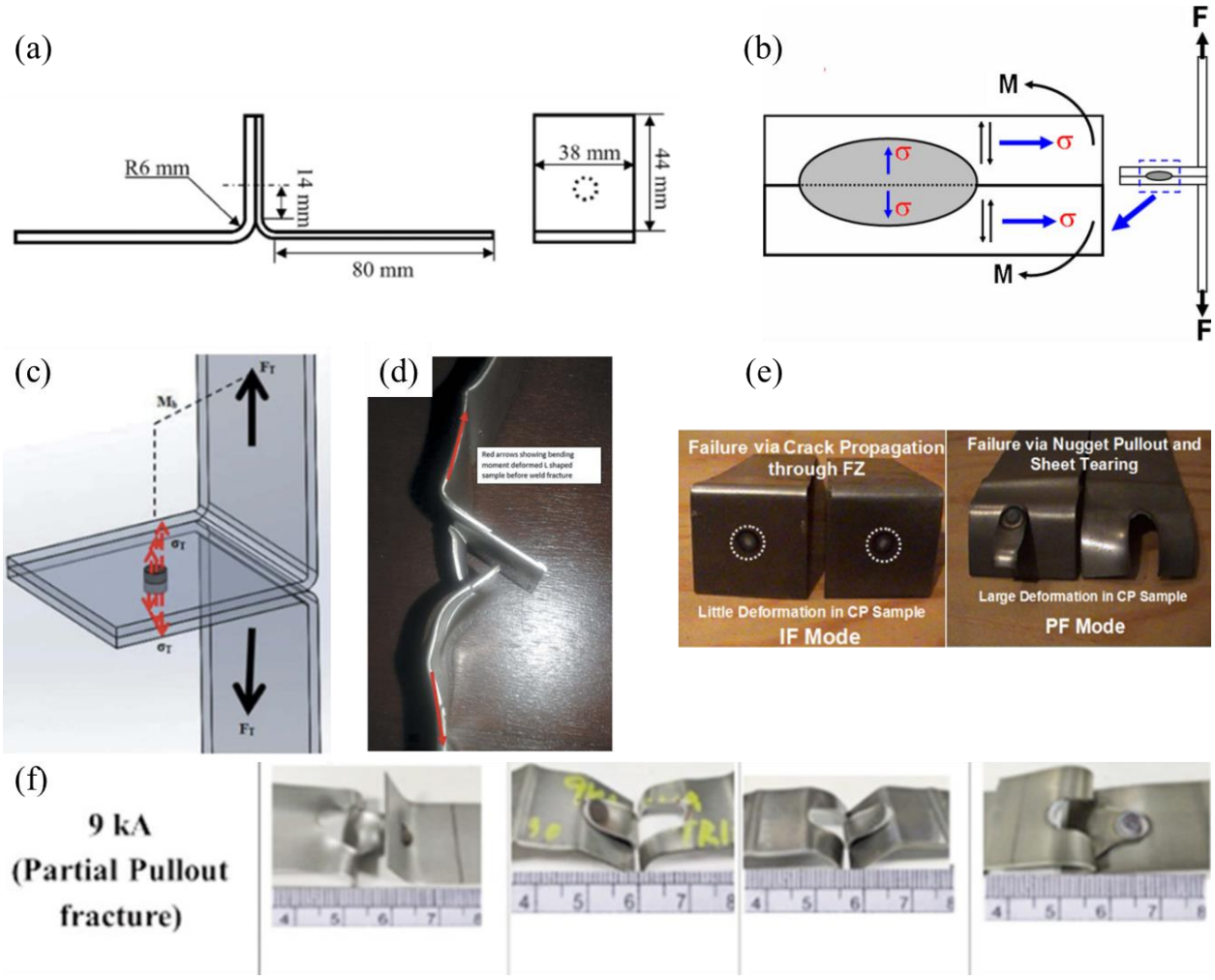


Figure 2.19. (a) Geometry of CP specimen [116]*; (b) schematic describing stress distribution at the interface and circumference of the nugget during tensile-bending loading of CP tests* [55]*; (c) the bending moment arm in the CP test is defined as the distance between the loading axis and the spot weld* [112]*; (d)-(f) show examples of severe deformation of the vertical and horizontal arms after CP tests* [113,114].

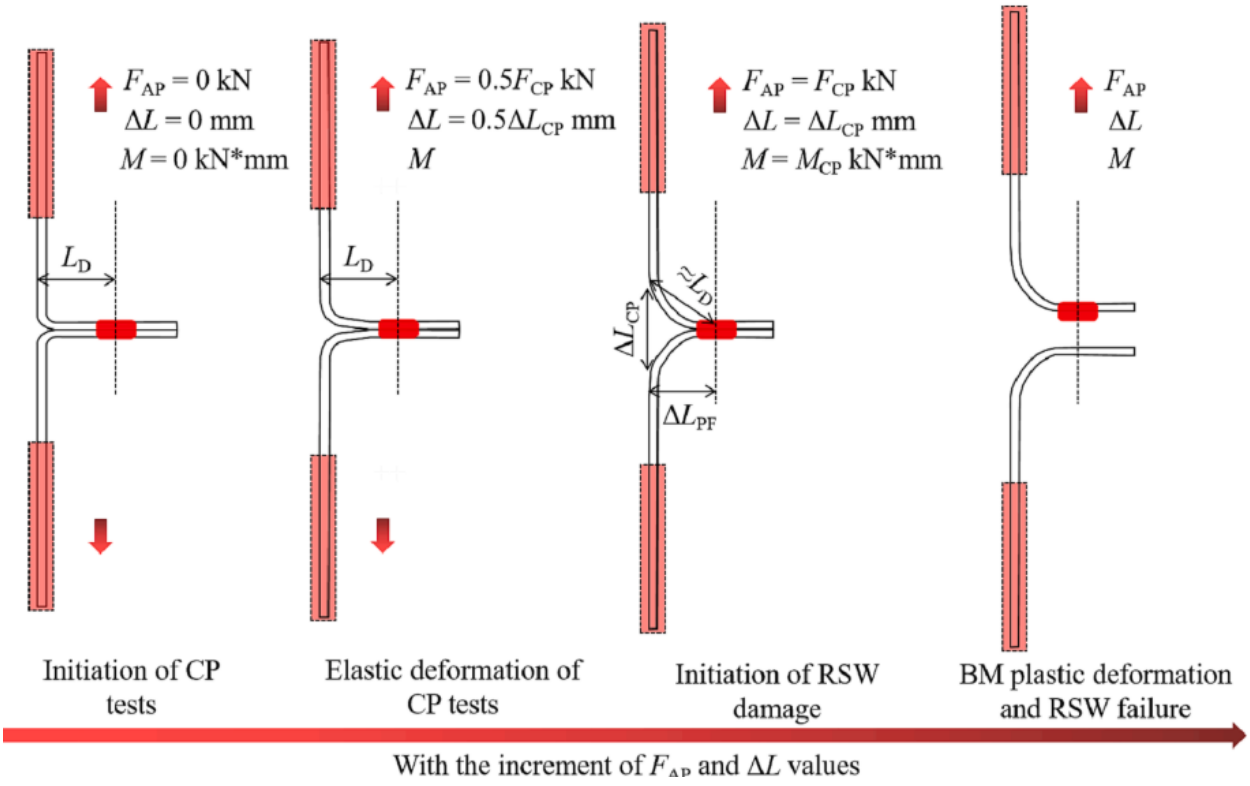


Figure 2.20. Idealized deformation process of the CP samples according to Xu et al. [115].

2.4.3.2 Multi-Spot Weld Mechanical Characterization

Although the single spot weld characterization techniques discussed above provide fundamental insights about the mechanical performance of single spot welds, expanding this knowledge about mechanical properties and failure behavior of spot welds to weld-groups is necessary because numerous spot welds are regularly used to assemble different BIW components. Multi-spot weld mechanical tests (or weld group tests) examine the behavior of spot welds at the component level and incorporate multiple spot welds in one testing structure [117]. These tests serve two primary purposes: (i) characterization of how failure progresses between welds when the structure is loaded and (ii) evaluation of weld failure models calibrated using single spot weld tests.

Different multi-weld component geometries have been proposed in the literature for evaluating weld-groups' mechanical properties. The H-specimen developed by Singh *et al.* [118] is a scaled-up version of U-shaped KS-II coupons that can accommodate multiple spot welds. The H-specimen geometry has been used for quasi-static and fatigue loading of multiple spot welds under peeling and shear loading scenarios. Zhang [119] analytically approximated the stress

intensity factor of different spot weld testing geometries, including the H-specimen. Another commonly adopted multi-weld component geometry is the T-section (T-joint) specimen [120,121]. The T-section specimen contains many spot welds that simultaneously undergo different complex loading modes. Therefore, it is predominantly used as a tool for weld model validation. For instance, Qian *et al.* [122] calibrated a failure criterion for Al-steel dissimilar spot welds by performing TS and CP single spot weld tests. They assessed the accuracy of the developed model based on single spot weld characterization techniques by performing T-joint structure tests. A schematic drawing of both the H-specimen and the T-section specimen has been shown in Figure 2.21.

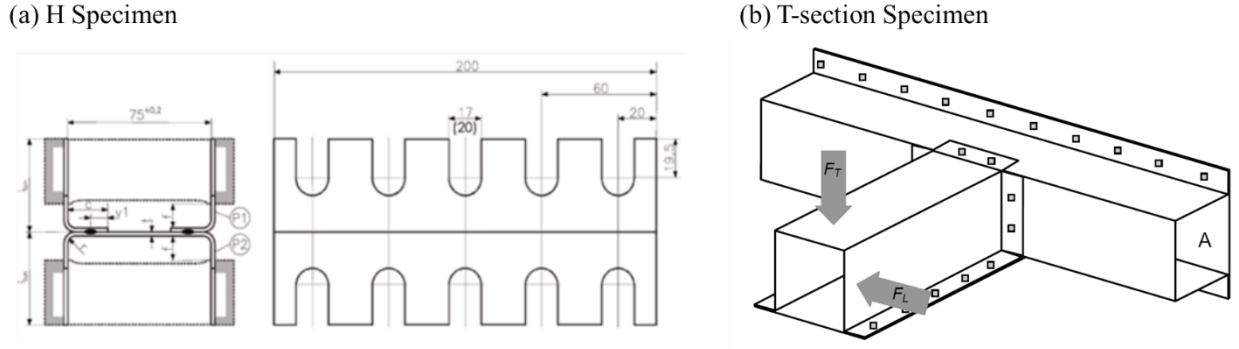


Figure 2.21. Schematic drawing of (a) H-specimen and (b) T-section specimen [123].

More recently, Caiman multi-weld component tests were developed to characterize how spot welds progressively fail as two partially joined hat-channel rails are separated [124,125]. Two versions of the Caiman test have been implemented so far: separation due to tensile loading (Caiman mode I), and separation due to shear loading (Caiman mode III) [124,126].

Caiman mode I utilizes two hat-channel rails that have spot welds along the length of the flange region, as shown in Figure 2.22 (a), and produces a characteristic load-displacement response distinguished by smooth loading up to peak load, followed by stepped unloading as the welds fail sequentially. So far, the Caiman mode I test has been performed at quasi-static and dynamic strain rates on hot-stamped USIBOR® 1500 with different tailored flange microstructures. Results indicated that increasing the parent metal ductility improves the energy absorption capability in both experimented strain rates. It has been reported that BM strength largely affects weld toughness in these tests since softer materials allow increased plastic deformation. Failure analysis of Caiman mode I spot welds have been predominantly limited to surface measurements

due to the nugget being hidden at the sheet/sheet interface. For example, Tolton *et al.* [125] investigated individual weld failures during the Caiman test by correlating thermal spikes on the flange surface due to strain energy release of weld failure. More work is required on the characterization of mechanical properties, failure behavior, and local properties of failure initiation sites in multi-weld structures assembled using 3G-AHSS spot-welds. Specifically, how fracture propagates in consecutive welds during tensile-bending loading conditions is unclear. Failure of spot welds initiates in an enclosed region at the sheet/sheet interface. In-situ observation of strain localization during different stages of spot weld failure demands sectioning of the weld similar to the studies by Mohamadizadeh *et al.* [127] and Ghatei-Kalashami *et al.* [90].

Tolton [126] performed Caiman mode III tests on PHS spot welds. Extensive efforts were made to reinforce and increase the structure's stiffness so that BM buckling is minimized, which led to including C channels inside side walls, as shown in Figure 2.22 (b). Although the thermography of the coupons provided some insight regarding the onset of failure, no information regarding the failure mechanism has been reported for either of the Caiman tests. Moreover, the researchers reported expulsion due to inconsistent part fit-up, which varied the mechanical performance of the weldments.

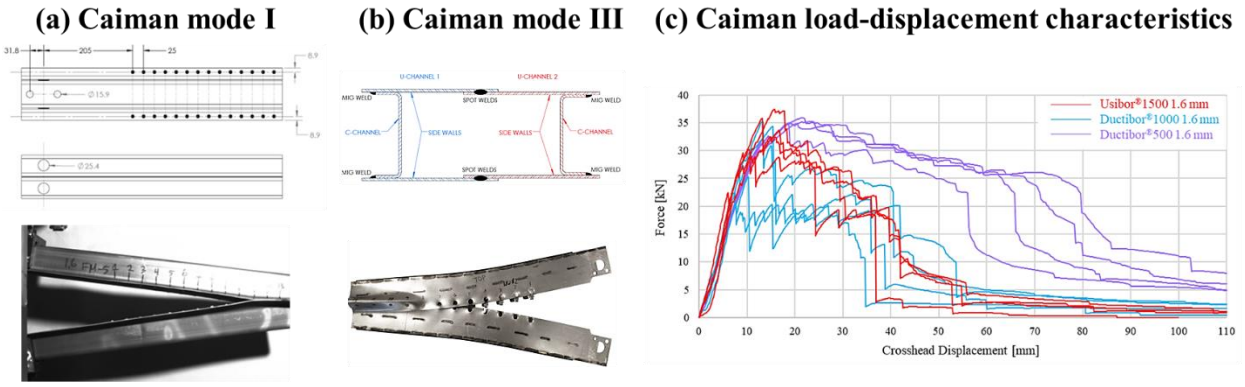


Figure 2.22. (a) Caiman mode I, (b) Caiman mode III coupon geometries, and (c) load-displacement characteristics of Caiman mode I test [124,126].

2.4.4 Failure Behavior of RSW Joints

The way a spot weld fails, the shape of the nugget, and the crack propagation path after a mechanical test provide valuable information for understanding the failure mechanism of spot welds under different loading conditions. Spot weld failure mode is a qualitative measure commonly attributed to the load-bearing capacity and energy absorption [33,128]. Figure 2.23

schematically illustrates the most common failure modes that can occur during mechanical testing of spot welds.

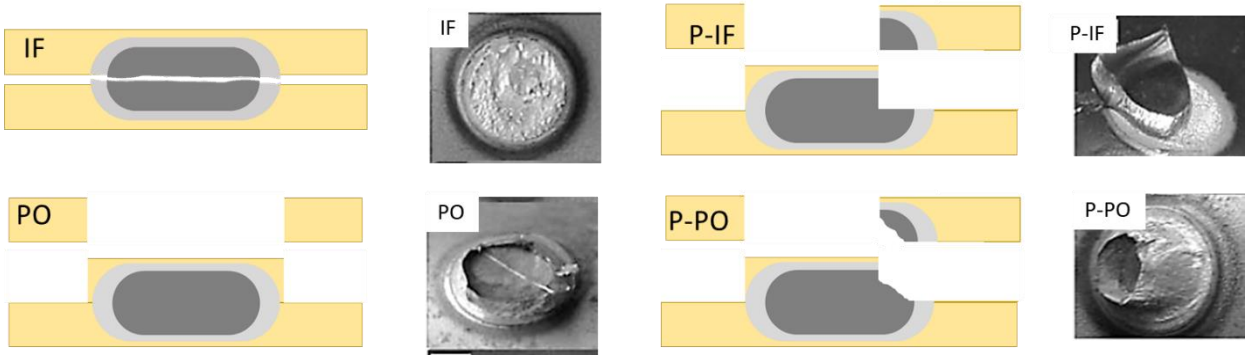


Figure 2.23. Schematic representation of different failure modes in spot welds and their corresponding fracture surfaces (based on [14]*).*

Interfacial failure (IF) is recognized by the propagation of the failure through the FZ. In contrast, complete pullout (PO) failure is related to sheet through-thickness crack propagation and, thereafter, growth of the emerging cracks on the surface of the sheets around the circumference of the nugget, causing the withdrawal of the nugget from one sheet. It is possible to have a combination of both IF and PO failure modes. For example, during partial-interfacial (P-IF) or partial-pullout (P-PO) failure modes, the failure is initiated by the propagation of the cracks into the FZ followed by redirection towards the faying interface. Traditionally, IF is regarded as an undesirable failure mode of spot welds since it occurs instantaneously without much plastic deformation of the surrounding material, resulting in inferior energy absorption capability [129]. Therefore, PO failure mode or P-PO failure modes with higher plug ratios are typically favored over IF and P-IF failures with lower plug ratios. Recent investigations by Radakovic and Tumurulu [128] showed that for RSW of AHSS, load-bearing capacity should be considered a more critical quality criterion compared to failure mode.

Moreover, the latest revision of the AWS D8.1 standard allows the IF failure of AHSS spot welds, unlike the IF of conventional HSS spot-welded joints because full PO is less common due to the increased hardness of the FZ. Chao [130] has shown that the IF of spot welds is analogous to the unstable fracture of a crack containing solid since a typical spot weld contains a natural intrinsic three-dimensional slit (notch) at the sheet-sheet interface. Chao's studies concluded that the fracture toughness of the FZ, the diameter of the FZ, and sheet thickness influence the strength

of the weldment during IF. Moreover, investigations by Pouranvari *et al.* [131] have shown that shear stresses at the sheet/sheet interface, porosity and shrinkage voids within the FZ, and the expulsion phenomenon promote IF failure.

As for PO failure, numerical simulations by Radakovic and Tumuluru [132] during CT testing of spot welds showed that maximum tensile stresses occur in front of the notch within the UCHAZ. However, as demonstrated by Tamizi *et al.* [52], excessive heat input and softening in SCHAZ can still lead to localized straining and pullout (PO) failure initiation away from the notch. These findings indicate that competing failure mechanisms can be responsible for PO failure: first, ductile yielding (necking) of the weakest sub-region of the joint; second, crack initiation and propagation due to stress concentration at the notch tip. The dominant PO mechanism will ultimately depend on factors such as local microstructures, notch shape, weld defects, and orientation of the nugget (stress state) [133]. In the case of TS tests, interfacial failure (IF) is generally believed to be a rapid brittle failure [14]. However, recent studies have shown that IF can also possess ductile characteristics [134]. For instance, interrupted TS testing micrographs of spot-welded 3G-AHSS have shown partially propagated cracks into the FZ [135]. Moreover, *in-situ* observations by Mohamadizadeh *et al.* [127] on TS testing of martensitic steels revealed corona debonding followed by shear banded fracture along the faying surface of the welds which is indicative of a ductile failure mechanism. Studies by Pouranvari [129] and Nadimi *et al.* [136] showed that the FZ hardness controls the peak load of TS tests when fractography of IF exhibits ductile features such as elongated dimples. On the other hand, the strength of IF during TS tests upon observing the cleavage crack growth mechanism is dictated by the fracture toughness of the FZ.

As discussed, the driving force for IF and PO failure modes are shear stresses parallel to the joint and tensile stresses in the sheet through-thickness direction, respectively. Weld nugget size is the most critical parameter influencing stress distribution during a spot weld mechanical test. In nuggets smaller than MWS, shear overload occurs sooner than the tensile stresses and can lead to necking in BM or cracking through the UCHAZ [137]. Therefore, failure tends to proceed in an IF manner without much plastic deformation of the joint. Pouranvari *et al.* [137] proposed the following equation to predict the IF load (P_{IF}):

$$P_{IF} = \left(\frac{\pi d^2}{4}\right)\tau_{WN} \qquad (2.3)$$

where d is the nugget diameter, and τ_{WN} is the weld nugget shear strength. As for the tensile mechanism of PO failure mode, Pouranvari *et al.* [137] explained that failure occurs when tensile stresses at the edge of the nugget reach the UTS values of the failure sub-region. The following equation has been suggested for predicting PO failure load:

$$P_{PO} = \pi dt(\sigma_{UTS})_{FL} \quad (2.4)$$

where $(\sigma_{UTS})_{FL}$ is the ultimate tensile strength of the failure location. The intersection point for the plots of Eq.2 and Eq.3 is referred to as the critical nugget diameter (d_{cr}) above which a transition of IF to PO failure mode occurs (see Figure 2.24). Quantification of d_{cr} which is a function of weld nugget strength and the strength of failure subregion, is a difficult task owing to the small size of RSW subregions (typically on the scale of mm). Hence, hardness profiles are commonly used to estimate the UTS of critical subregions and predict failure regions. A rather straightforward index that can be used to predict the failure location of spot welds is the relative hardness ratio between the FZ and BM [129,133,138]. Experimental and finite element analysis by Ghatei-Kalashami *et al.* [90] and Zhang *et al.* [139,140] showed that a higher FZ/BM hardness mismatch (higher difference in the local mechanical properties of the FZ and BM) leads to failure initiation within the HAZ, whereas a lower FZ/BM hardness ratio can result in failure initiation closer to the FZ.

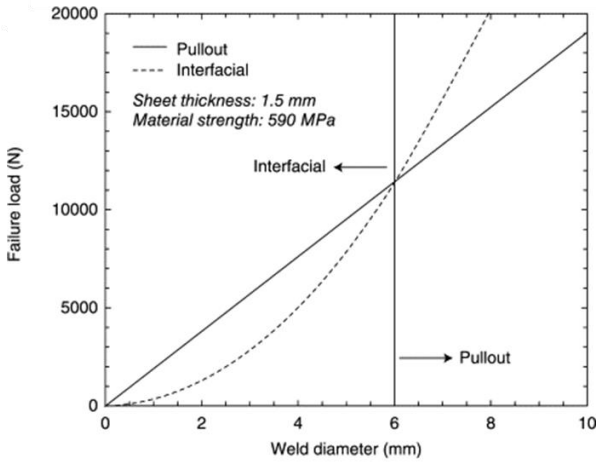


Figure 2.24. Failure load versus nugget diameter for both interfacial and pullout failure modes [134].

2.5 Failure Prediction in RSW Joints

Prediction of spot weld failure is difficult since it is a multi-faceted phenomenon contingent upon various factors, including testing geometry, loading condition, strain rate sensitivity, and mechanical property heterogeneity of different weld regions [141]. Various approaches are implemented to predict the failure of spot welds. The available literature regarding spot weld failure prediction can be categorized into analytical/geometrical models, finite element models, and strength-based failure criteria. All three of these approaches are designed to accomplish the same general task: to predict the failure of spot welds, but they provide results with various levels of accuracy. The following sections discuss each of the three main approaches for RSW failure prediction in detail.

2.5.1 Analytical/Geometrical Models for RSW Failure Prediction

First are analytical/geometrical models, such as the $4\sqrt{t}$ proposed by the AWS standard or the models suggested by Chao [109] and Pouranvari and Marashi [133], which can be used for the prediction of the critical nugget diameter required to ensure PO failure of resistance spot welds. More advanced models that addressed the shortcomings of the traditional $4\sqrt{t}$ criterion have also been suggested. For example, Chen *et al.* [142] recently developed a new analytical model that considers the effect of sheet coating and failure location on predicting critical nugget diameter for press-hardened AHSS spot welds. A summary of such models has been provided in *Table 2.3*. Such failure criteria are usually calibrated for an isolated loading condition and implementing them requires knowledge regarding local mechanical properties of the failure initiation region such as shear yield strength, ductility, or fracture toughness. Detailed crystallographic observations combined with miniature tests like micro-cantilever, micro-tensile, and nanoindentation can assist with acquiring local constitutive properties of different RSW regions, as seen in the works of Chabok *et al.* [143,144].

Table 2.3. Summary of empirical formulae proposed in the literature to calculate the minimum allowable nugget size (MWS) ensuring pullout failure mode of resistance spot welds.

Proposed Equation	Remarks	Author [Ref]
$d_{cr} = C\sqrt{t}$	• C is a constant varying from 3 to 6 • t is the sheet thickness • The AWS standard recommends C=4	AWS D8.9 standard [35]
$d_{cr} = 3.41t^{4/3}$	• The proposed equation is weakly linked with the grade of AHSS	Chao *et al.* [145]
$d_{cr} = 8t(\frac{H_{FL}}{H_{WN}})$	• H_{FL} and H_{WN} are the microhardness values of the fracture location and weld nugget	Pouranvari and Marashi [133]
$d_{cr} = 3.2\frac{t}{f_P}$	• f_P is the porosity factor	Sun *et al.* [146]
$d_{cr} = 4\left(\frac{\tau_{HAZ}}{\tau_{WN}}\right)(1-\varepsilon)t$	• Valid for Al-steel dissimilar RSW joints • $\frac{\tau_{HAZ}}{\tau_{WN}}$ is the shear strength ratio between HAZ and WN • ε is the Al thickness reduction rate	Shi *et al.* [147]
$d_{cr} = \frac{0.694\sigma_{BM}D_{CHAZ}}{kK_C\sqrt{\frac{1}{4t}+\frac{12t}{\pi^2 D_{CHAZ}^2}}}\frac{H_{CHAZ}}{H_{BM}}$	• This model considers the coating and CHAZ location • K_C is FZ fracture toughness, k is a constant dependent on the type of coating, CHAZ is critical failing HAZ, D_{CHAZ} is the diameter of CHAZ	Chen *et al.* [142]

2.5.2 Finite Element Models for RSW Failure Prediction

The second group of studies related to the prediction of RSW failure are the ones that develop a detailed finite element model of the spot-welded joint and assign constitutive properties to different RSW subregions in an attempt to capture information regarding the onset of failure, failure path, and damage evolution [81,148]. An example of the discretized RSW cross-section according to their respective hardness values has been shown in Figure 2.25 (a). Such models are referred to as "mesoscale" models since they use sub-millimeter solid elements to capture the mesoscale micromechanics. The accuracy of the FEM approach is dependent on capturing the mechanical properties of local regions formed during a spot welding cycle, as introduced before. Calibrating a comprehensive weld model that accurately predicts a spot-welded joint's mechanical performance and failure behavior is challenging due to inhomogeneities in local microstructures

and mechanical properties caused by thermal gradients during the RSW process [55]. The property variations in the RSW subregions require local characterization due to the relatively small size of each zone, typically smaller than 1 mm in length in the heat-affected zones [144]. To account for the inhomogeneity of different RSW regions, Ma *et al.* [148,149] recently fabricated sub-sized specimens to determine the hardening and fracture behavior of different RSW regions in AHSS spot welds, as shown in Figure 2.25 (b). Their developed finite element models consider the contribution of the mechanical properties of each RSW sub-zone at the mesoscale upon TS and CT tests. In this approach, individual elements of the RSW sub-zones are assigned constitutive properties and fracture strains. Upon calibration of such finite element model, they correlated the observed experimental failure behavior of the spot welds with the damage accumulation index from the fracture model. They concluded that while the transition of crack onset location is related to the growth rate of the damage accumulation index, the crack propagation path follows regions with high damage accumulation index.

The hardness scaling approach has been used to predict the mechanical properties of RSW sub-regions. In this approach, the constitutive and fracture behavior of the BM is scaled depending on the relative hardness ratio between the BM and HAZ or FZ (see Figure 2.25 (c)). This technique is reported to give acceptable accuracy in failure prediction of ultra-high-strength press-hardened steel (PHS) resistance spot welds [140,150,151]. Recently, Midawi *et al.* [152] raised concerns regarding the validity of characterizing 3G-AHSS RSW FZs or HAZs using the hardness scaling approach. Compared to PHS steels where the weld zones are comprised of fully martensitic structures of various strengths, the microstructure in the 3G-AHSS RSW sub-regions can be complex and vary significantly from that of the BM [153]. The assumption that the constitutive behavior of a particular material scales linearly with the corresponding hardness ratios after welding heat treatment is not valid in all cases. This is especially questionable for welding of 3G-AHSS, where the strain hardening of the RSW sub-zones can significantly differ from that of the BM (see Figure 2.26). The extraction of miniature coupons directly from the FZ or HAZ [143,147] and the reproduction of representative microstructures using thermomechanical simulators [98,149] have been used in the literature for local RSW mechanical property evaluation. Ghassemi-Armaki *et al.* [154] performed extensive failure characterization under different stress triaxialities to calibrate the BM failure locus, which was linearly interpolated to predict HAZ fracture loci. Detailed mesoscopic finite-element models of spot welds have also been considered [81].

Mesoscale models are informative in terms of providing insight into the fracture initiation sites, damage accumulation trends, and crack propagation mechanisms but require extensive BM, HAZ, and FZ fracture characterization. At present, the application of mesoscale models in full BIW assemblies, which contain an average of 6000 spot welds [69], is computationally prohibitive due to the fine mesh size required, and as such modeling of RSW sub-regions such as various HAZ has not yet been applied to full vehicle simulation in the current literature.

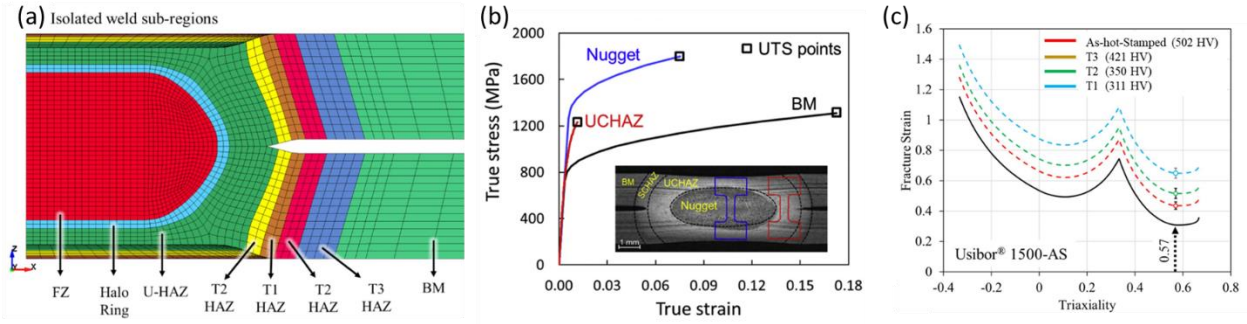


Figure 2.25. (a) Discretized weld geometry in finite element analysis. The weld is divided into several sub-regions based on local microhardness values. (b) Miniature tensile specimens extracted directly from the spot weld to characterize the constitutive flow curve of various regions [145,146]. *(c) Fracture loci of the BM attained from mechanical tests with various stress triaxialities. The fracture loci of other regions were approximated by linearly translating the BM fracture loci* [78].

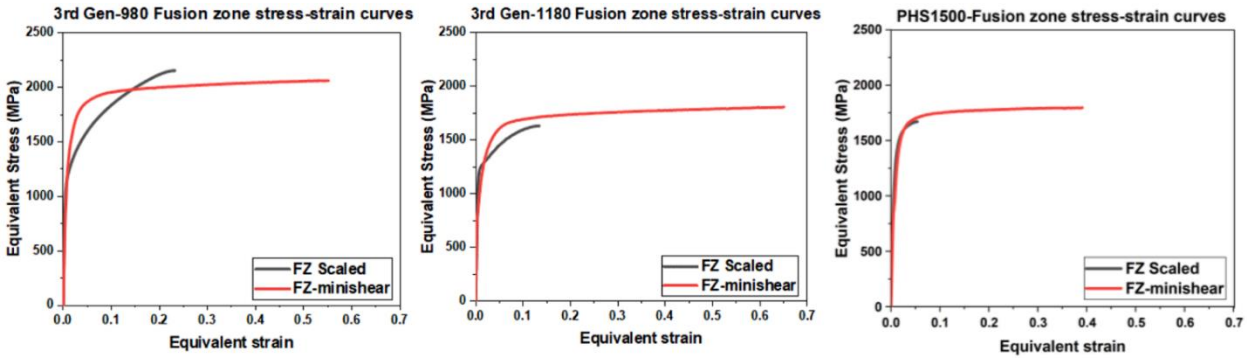


Figure 2.26. Comparison between the stress-strain flow response from the hardness scaling and experimental approach for (a) 3G-980 FZ, (b) 3G-1180 FZ, and (c) PHS-1500 FZ. Figures show that the hardness scaling approach accurately predicts the strain hardening response in the case of PHS spot welds comprising martensite with various strengths. However, the hardness scaling approach did not yield accurate hardening predictions for the FZ of either 3G-AHSS spot welds [155].

2.5.3 Strength-based Criteria for RSW Failure Prediction

The third approach to model spot weld failure is to perform various mechanical tests to develop an experimental failure locus based on the critical loads that can be readily interpolated in finite-element models [156–158]. A functional form to describe the failure locus is then assumed and calibrated using the experimental data [86]. An example failure locus related to combined shear-tensile loading of spot welds is shown in Figure 2.27. Typically, failure strengths from mechanical tests that impose various ratios of load components on the joint are used to improve the accuracy of such experimental failure loci in loading conditions other than pure shear/ pure tensile extremes.

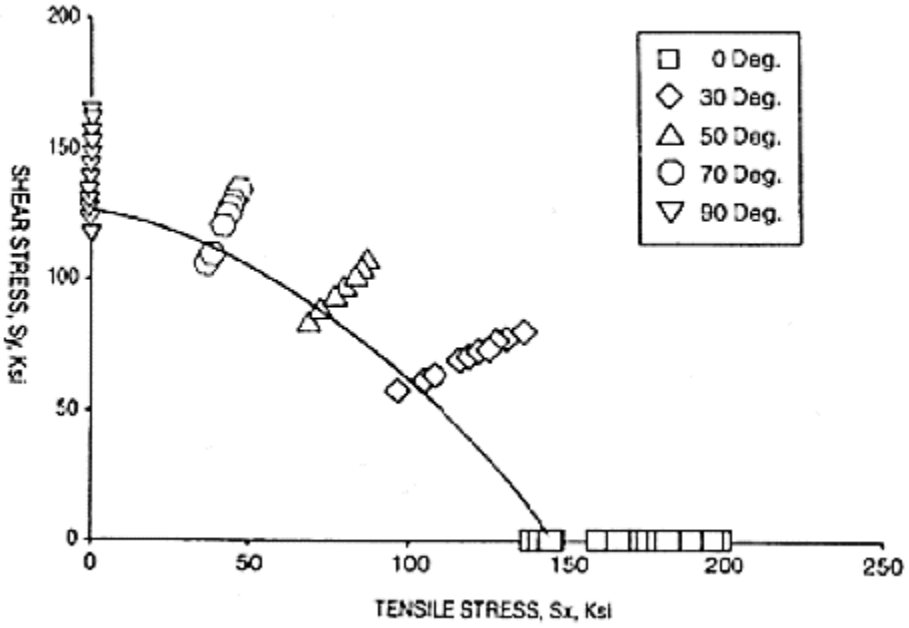


Figure 2.27. A failure locus for resistance spot welds under combined shear/tensile loading conditions [158]

Although the force-based failure loci approach does not comprehensively account for RSW metallurgical inhomogeneities and provides limited insight into the underlying mechanics of weld failure compared to mesoscale modeling, it is well-suited for industrial application and implementation into finite-element software used for vehicle crash simulation such as LS-DYNA [159]. In this approach, the failure response of spot welds is most commonly characterized under bending-dominated, shear-dominated, and tensile-dominated loads using CP [156], TS, and CT tests [55], respectively.

Different models have been proposed to describe the failure locus of resistance spot welds in various loading conditions. Chao proposed a failure criterion based on TS and CT test failure loads as shown in Equation 2.5 [160].

$$1.623\left(\frac{f_s}{td}\right)^2 + 3\left(\frac{f_n}{td}\right)^2 = \sigma_f^2 \qquad (2.5)$$

where f_s and f_n are shear and tensile components of the applied load. Lim *et al.* [161] evaluated Chao's proposed criterion and showed rather low prediction accuracy, especially in the shear-dominated loading domain of spot welds made of mild steel. Lin *et al.* [162] proposed an approximate limit load solution for spot welds under combined shear-tensile loading conditions:

$$[1 - 2\alpha + 2\alpha^2]\left(\frac{f_n}{\pi Dt\tau_0}\right)^2 + \left[\frac{1}{3} + \left(\frac{4t}{\pi D}\right)^2\right]\left(\frac{kf_s}{\pi Dt\tau_{WN}}\right)^2 = 1 \qquad (2.6)$$

This solution was obtained based on a simplified stress field assumption around the spot weld under combined axial and shear loading conditions and considers the effects of sheet thickness (t), nugget diameter (D), and combinations of shear and tensile loads (f_s and f_n, respectively). τ_{WN} is the shear stress of the weld nugget, α is a load parameter, and k is a fitting coefficient. Evaluations of this failure criteria by Lee *et al.* [163] and Combescure [111] using U-shaped and square-cup specimens revealed low prediction accuracy, especially in shear-dominated loading orientations, for combined loading of spot welds made of mild steel. Moreover, the shear strength of the spot weld is a function of nugget diameter and is not readily available, which limits the widespread adoption of this model within the automotive industry.

Lee *et al.* [163] proposed a stress-based elliptic RSW fracture criterion:

$$f^L = \left(\frac{\sigma_n}{\sigma_N}\right)^2 + \left(\frac{\tau_s}{\sigma_S}\right)^2 = 1 \qquad (2.7)$$

where σ_n and τ_s are nominal tensile and shear stresses applied to the spot weld, and σ_N and τ_S are nominal tensile and shear fracture stresses of the joint. The nominal stresses included in Equation 7 are calculated by normalizing the load components from the crosshead by nugget diameter and sheet thickness and are not true stresses acting on the spot weld throughout the test. As reported by Lee *et al.*, a key assumption in the proposed fracture criterion is the negligence of weld nugget rotation throughout the tests [163]. Later on, Seeger *et al.* [120] expanded Lee's general quadratic

formula by adding a third term that accounts for bending-dominated loading cases. The phenomenological failure function of Seeger to describe the RSW failure is defined as:

$$f^S = \left[\frac{f_n}{S_N(\dot{\varepsilon}_{eff})}\right]^a + \left[\frac{f_s}{S_S(\dot{\varepsilon}_{eff})}\right]^b + \left[\frac{m_b}{S_{B(\dot{\varepsilon}_{eff})}}\right]^c \geq 1 \qquad (2.8)$$

in which F_n, F_S, and m_b denote the loads associated with tensile (axial), shear, and bending loading. S_N, S_S, and S_B are the corresponding failure strengths, which need to be calibrated from KS-II 90°, KS-II 0°, and CP experiments, respectively, and are expressed as a function of the operative strain rate, $\dot{\varepsilon}_{eff}$. Typically, the empirical failure loads and the exponents are optimized for the best fit of data from experiments using the least square regression method. In this regard, performing KS-II tests at intermediate proportions of tensile and shear loading assists with more accurate calibration of the exponents *a* and *b*. Seeger's failure model has become widely adopted in finite element solvers such as ABAQUS and LS-DYNA and is by far the most commonly implemented RSW strength-based failure criterion within the literature. Khan *et al.* [164], Ghassemi-Armaki *et al.* [156], Patil and Lankarani [99], and Yang *et al.* [100] have calibrated Seeger's force-based failure criteria for different stack-ups of spot-welded AHSS and used the KS-II testing geometry as a tool to optimize the accuracy of failure prediction in shear/tensile loading conditions. It is noted that no study has yet assessed the validity of Seeger's RSW failure criteria in tensile-bending loading conditions.

More recently, Song and Huh [165] proposed a β-norm elliptical fracture model for spot welds under combined shear-tensile loading:

$$f^{SH} = \left[\frac{F_n}{S_N}\right]^2 + \varphi\left(\frac{F_n}{S_N}\right)\left(\frac{F_S}{S_S}\right) + \left[\frac{F_S}{S_S}\right]^2 \leq 1 \qquad (2.9)$$

where φ is a shape parameter. This failure contour takes the form of f^L if $\varphi=0$ and becomes a straight line when $\varphi=2$. This failure criterion was derived based on an idealized linearly distributed stress through the sheet thickness while ignoring the influence of the notch as an intrinsic stress raiser.

Figure 2.28 compares the failure loci suggested by Lin (Equation 2.6), Lee (Equation 2.7), and Song and Huh (Equation 2.9) for combined shear-tensile loading of spot welds made from SPCUD cold rolled steel, SPRC steel, and DP steel. Song and Huh reported that the maximum difference in failure contours predicted from their failure model was less than 4.1% between the

optimized and sub-optimal β values. Figure 2.28 shows a good agreement between experimental strength data points and the predictions from Equation 2.9 was achieved. However, it is essential to highlight that in the work of Song and Huh, no alteration in the failure mode of the spot welds was reported. All fractured spot welds, evidenced via fractography micrographs, that were loaded between 0° and 90° loading orientation exhibited pullout failure mode. The deficiency of Song and Huh's model in predicting the failure upon different failure modes is evidenced in a separate work by Ha and Huh, where the mechanical performance of laser welds is analyzed under combined shear-tensile loading conditions with a transition in the dominant failure mechanism (Figure 2.28 (d) and (e)) [166]. The accuracy of pre-existing strength-based failure criteria is currently unclear for spot welds made of 3G-AHSS. This issue is further exacerbated as 3G-AHSS spot weld failure modes vary under different loading conditions.

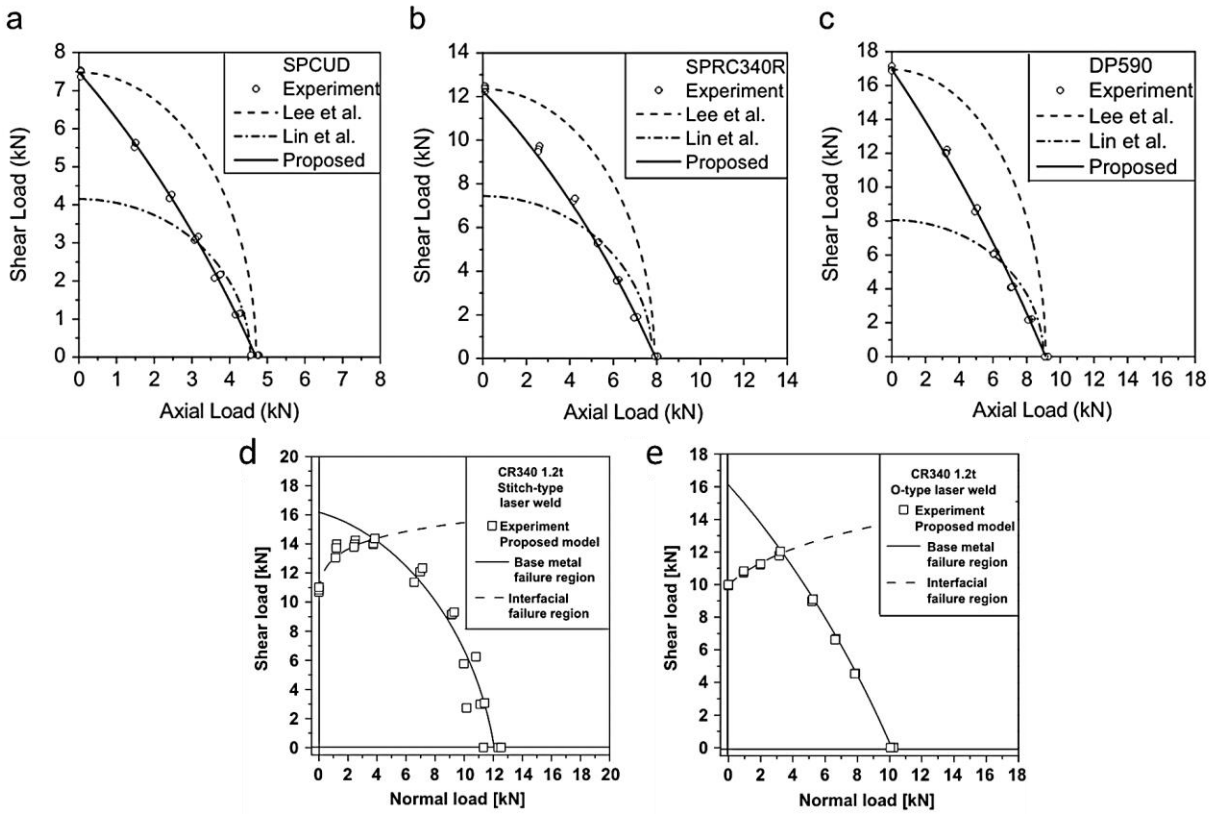


Figure 2.28. Comparison between prediction accuracy of three different RSW failure criteria proposed by Lin [162], *Lee* [163], *and Song and Huh* [165] *for (a) SPCUD spot welds, (b) SPRC340R spot welds, and (c) DP590 spot welds under combined shear-tensile loading* [165]. *(d) and (e) show interpolation of failure contour for stitch-type and O-type laser welds made of CR340*

material subjected to combined shear-tensile loading. It is observed that a transition in failure mode alters the trends related to the load-bearing capacity of the laser welds [166].

2.6 General Remarks

As highlighted throughout this chapter, although a preliminary understanding exists of mechanical performance and failure characteristics of 3G-AHSS spot welds under traditional TS and CT tests, no validated methodology exists on accurate quantification of RSW performance indices such as load bearing capacity or energy absorption capability of 3G-AHSS spot welded joints under more complex loading conditions such as combined shear-tensile and tensile-bending loading conditions. Existing studies on shear-tensile combined loading of spot welds primarily focus on designing custom fixtures that minimize joint rotation throughout the tests and do not necessarily account for the actual loading path of the spot welds up to rupture. Regarding failure under bending-dominated loading conditions, a minimal amount of data exists on the behavior of 3G-AHSS spot welds under various ratios of tensile-bending loading conditions. A better treatment of the extracted properties of spot welds under shear-tensile loading and tensile-bending loading can be attained by coupling the tests with digital image correlation (DIC) and accounting for the deformation of the coupons and rotation of the nugget. Furthermore, conflicting data exists in terms of the most accurate force-based failure criteria that can be implemented in FEA to predict the failure of spot-welded connections. Acquiring more strength data points at intermediate loading conditions other than the two extremes of shear-dominated and tensile-dominated loading characterized by TS and CT tests will allow for assessing the existing criteria in various loading conditions. Lastly, the literature does not explore the sequential failure of 3G-AHSS spot weld groups under tensile-bending loading conditions. Characterizing the *in-situ* failure mechanism of multiple spot welds will highlight the critical failure initiation regions. Once this knowledge is obtained, further steps can be taken, such as *in-situ* process schedule modification to improve local properties of spot welds, improve the mechanical performance of the joints, and ultimately, facilitate the application of 3G-AHSS spot welds in future automotive BIW components.

3 Chapter 3: Spot Weld Process Development and Baseline Characterizations[1]

3.1 Overview

No unified sets of welding parameters exist within the literature that follow the recommendations of the AWS D8.9 standard for spot welding of 3G-AHSS sheets. Most of the existing literature on spot welding of 3G-AHSS focuses on studying different phenomena such as liquid metal embrittlement and its mitigation [167], halo ring formation, and its annihilation [67], liquation cracking, and post-weld heat treatment schedules [168]. These studies typically manipulate the welding schedule to locally modify the microstructure of critical cracking or failure initiation regions. There exists a demand to produce defect-free spot welds and optimize the process parameters according to the suggestions of commonly implemented standards such as AWS D8.9 for automotive spot-welding applications. Furthermore, conflicting data exists regarding the hardness characteristics of various 3G-AHSS RSW sub-regions and the influence of BM strength on joint properties. In this chapter, optimized welding current values were determined with respect to AWS D8.9 welding schedule recommendations by performing TS and CT mechanical tests. Using the optimized welding settings, the microstructure, and microhardness characteristics of the optimized spot welds were investigated.

3.2 Background

3G-AHSS are candidates for vehicle structural components since they address automotive industry requirements through their favorable balance of strength and ductility [4], [5]. The enhanced properties of 3G-AHSS are attributed to the simultaneous existence of martensite and RA as constituents of their microstructure. Within their microstructure, martensite provides strength to the steel, while RA imparts ductility by accommodating strain through the TRIP mechanism [170]. These steels are commonly joined during BIW assembly using the RSW process, the predominant method of sheet metal joining in the automotive industry [171].

[1] This chapter is composed of a published research paper as outlined in the statement of contributions. Shojaee M, Midawi ARH, Barber B, Ghassemi-Armaki H, Worswick M, Biro E. Mechanical properties and failure behavior of resistance spot welded third-generation advanced high strength steels. J Manuf Process 2021;65:364–72. https://doi.org/10.1016/j.jmapro.2021.03.047.

The weldability of 3G-AHSS is an inevitable area of concern that governs their applicability in the automotive industry [55]. During RSW, the complex initial microstructure of 3G-AHSS will be transformed within the FZ and profoundly altered in the HAZ owing to the thermal cycle the BM undergoes. The resulting microstructures can affect the mechanical performance and failure behavior of welded connections and thereby compromise the integrity and durability of the vehicle structure [172,173]. Hence, it is imperative to optimize the RSW process parameters to achieve acceptable strength and energy absorption values within 3G-AHSS joints.

One intriguing 3G-AHSS class is Q&P steels. Although the Q&P process was first proposed by Speer *et al.* in 2003 [24], the literature reveals that only a limited number of studies have investigated the mechanical properties and failure behavior of RSW joints within Q&P steels. Liu *et al.* [71] have compared the effects of single and double-pulse RSW processes on the mechanical properties of 3G-980 steels and found that the application of a higher secondary current improves joint tensile shear strength and promotes partial pullout failure mode. They also related the failure of the spot welds to the presence of liquation cracks within the partially melted zones of the weldments. Luo *et al.* [174] established an FEA model to predict the failure mode of 3G-980 resistance spot welds and obtained the constitutive relationship of its FZ. As for other welding processes, Guo *et al.* [175] and Li *et al.* [176] examined the mechanical properties of a fiber laser welded 980 MPa strength 3G steel. HAZ softening was observed in both studies due to martensite tempering; however, these studies reported that the softened zone did not affect the tensile strength of the joints. It is worth noting that the HAZ softening phenomenon has been reported for friction stir welding of Q&P-980 as well [177]. In the case of the RSW process, although HAZ softening is widely acknowledged to occur for other types of AHSS such as in DP steels [178], [171], diverging opinions exist regarding the existence and cause of this phenomenon for 3G-AHSS steels. For instance, while Wang *et al.* [70] reported an approximately 34 HV drop in the hardness of the sub-critical HAZ compared to the BM of 3G-980 RSW joints, Lei and Pan [74] did not observe a softened HAZ during RSW of this particular steel. Other than this uncertainty regarding the existence of HAZ softening for 3G-AHSS RSW joints, the effect of 3G-AHSS base material strength on RSW strength, fracture energy, and failure behavior is yet to be understood since no study has yet evaluated and compared these parameters between two different grades of 3G-AHSS. This comparison appears important since increasing material strength is an attractive approach to accomplish the weight targets of the auto industry, especially in applications in which high load-

bearing capacity is required. Therefore, it is important to evaluate how RSW properties change as the material strength increases for 3G-AHSS.

The current work aims to provide a better understanding of the mechanical properties and failure behavior of RSW joints from two 3G-AHSS grades with strengths of 980 and 1180 MPa, designated in this paper as 3G-980 and 3G-1180, respectively. Welding process robustness was evaluated by developing weldability lobes for both materials. This was followed by conducting TS and CT mechanical tests to assess weld strength and energy absorption capability for different nugget sizes.

3.3 Materials and Methods

3.3.1 As-received Materials

The materials selected for this research are two grades of Q&P 3G-AHSS received from Auto/Steel Partnership (ASP), referred to as 3G-980 and 3G-1180, with the numerical designation representing the UTS values of 980 MPa and 1180 MPa, respectively. Both materials were uncoated in the as-received condition, had a nominal thickness of 1.4 mm, and their chemical compositions are listed in Table 3.1. The carbon equivalent of the investigated steels was calculated using the formula proposed by Yurioka *et al.* [179].

Table 3.1. Chemical composition of the investigated 3G-AHSS. Reported values are in wt.%.

Material	C	Mn	Si	Cr+Mo+V	Cu+Ni	Fe	C_{eq}
3G-980	0.21	2.11	1.49	0.02	<0.01	Bal.	0.64
3G-1180	0.17	2.52	1.59	0.28	<0.02	Bal.	0.70

Figure 3.1 (a) and (b) are scanning electron micrographs of the as-received materials showing microstructures comprising ferrite, martensite, and RA. The existence of RA was confirmed using electron backscattered diffraction (EBSD) phase maps, shown in Figure 3.1 (c) and (d). The phase maps revealed 4.1% and 3.8% RA in the 3G-980 and 3G-1180 microstructures, respectively. Figure 3.1 (e)- (h) demonstrates the macro segregation of Mn and Si as the major alloying elements of the selected 3G-AHSS.

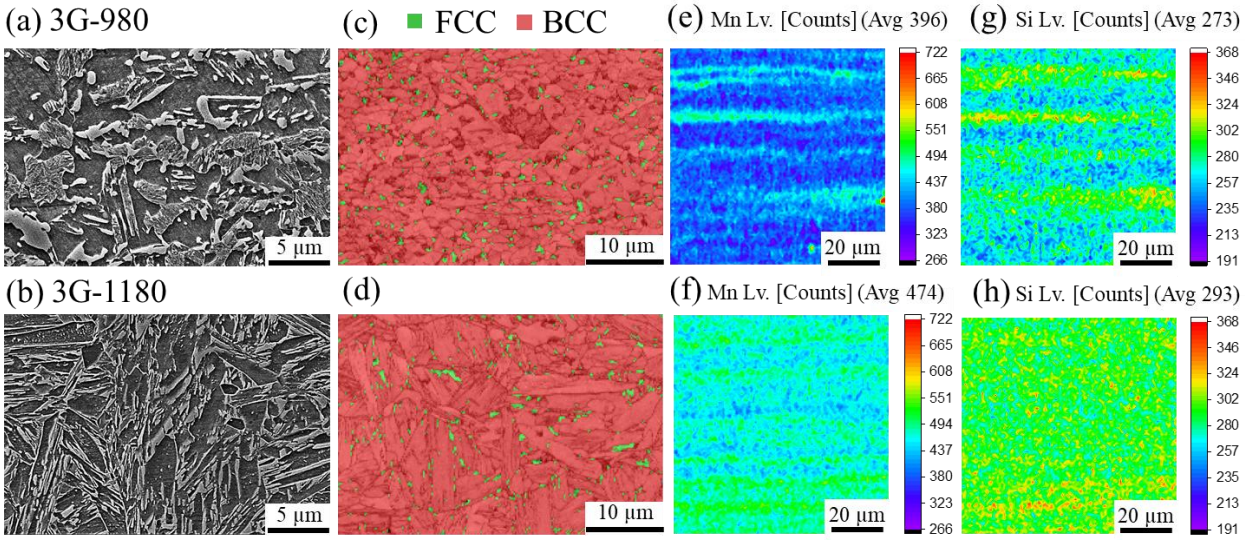


Figure 3.1. (a) and (b) scanning electron micrographs; (c) and (d) phase maps showing the body-centered cubic (BCC) and face-centered cubic structures in different colors; (e)- (h) Mn and Si elemental distribution maps of the investigated 3G-980 and 3G-1180 base materials.

The BM properties were quantified in the rolling direction of the steel sheets using rectangular tension test specimens according to the ASTM-E8 standard tensile testing procedure [180]. BM uniaxial tensile tests were conducted on a universal servo-electric 100-kN MTS Criterion frame at a constant crosshead speed of 1 mm/min. Strain values were measured via stereoscopic DIC techniques with a 50 mm virtual extensometer (see Figure 3.2). Average tensile properties were extracted from the resulting stress-strain curves and the corresponding values are reported in Table 3.2.

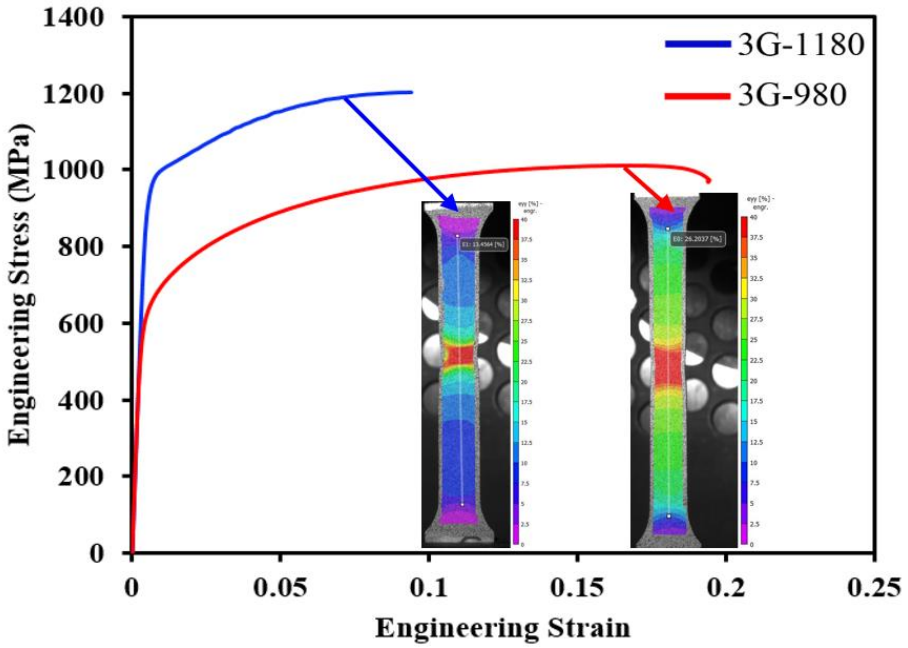


Figure 3.2. Representative engineering stress-strain curves for as-received 3G-980 and 3G-1180 materials in the rolling direction.

Table 3.2. Average tensile properties of the investigated steels in the rolling direction.

Material	YS [MPa]	UTS [MPa]	TE [%]	UE [%]	n
3G-980	616 ± 14	1013 ± 13	19.9 ± 0.5	16.8 ± 0.5	0.17
3G-1180	967 ± 7	1181 ± 19	11.8 ± 0.6	8.1 ± 0.3	0.09

YS, yield strength; UTS, ultimate tensile strength; TE, total elongation; UE, uniform elongation; n, hardening exponent; 0.2% offset method was used to calculate YS.

3.3.2 Resistance Spot Welding

A medium-frequency direct current (MFDC) RSW FANUC robot (model 2000ic) equipped with a Honda C-type spot welding gun and a Rexroth Bosch weld controller was used for resistance spot welding of the investigated 3G-AHSS. RWMA (Resistance Welder Manufacturer's Association) [181] Group A, Class II, Cu-Cr domed electrodes with a dressed face diameter of 7 mm were used which were water-cooled with a flow rate of 6 L. min^{-1}. RSW welding parameters were chosen from the AWS D8.9 standard [23] and their values are schematically shown in Figure 3.3. Based on the thickness and strength of the selected materials, AWS D8.9 [35] recommends a double-pulse welding schedule with a total welding duration of 20 cycles (≈334 ms). It should be noted that a total welding time of 418 and 250 ms (25 percent above and below the recommended welding time by AWS standard) was also utilized for developing the weldability lobes. However,

334 ms welding time was used for all mechanical testing and characterizations. An electrode stabilization procedure was conducted prior to fabricating TS and CT specimens as per recommendations of AWS D8.9 to minimize the dynamic behavior of the new pair of electrodes. For each of the three experimented total welding times, the welding current was varied between 6.5 kA to 10 kA to allow attaining a minimum weld size (MWS) of $4\sqrt{t} = 4.73$ mm up to electrode face diameter weld size (FDWS) of 7 mm. The occurrence of expulsion at high welding currents was confirmed based on the SEP 1220 standard [182]. The nugget sizes of the welds related to the lobes were measured after revealing the welds through chisel testing and the reported nugget diameters are averages of the largest and smallest weld diameters.

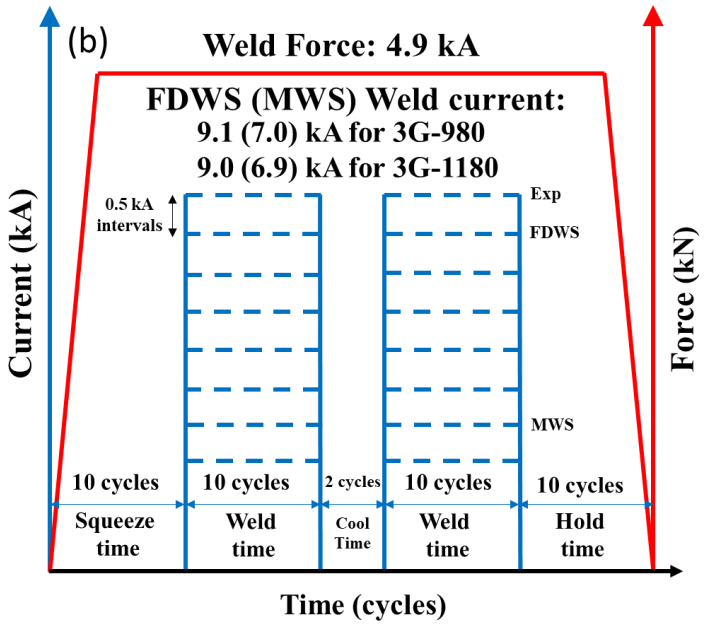


Figure 3.3. Schematic representation of double pulse RSW schedule opted in this research program. Welding current was varied from below undersized welds up to expulsion region. The highlighted welding currents correspond to FDWS and MWS conditions.

3.3.3 Tensile Shear and Cross Tensile Mechanical Tests

TS and CT tests were implemented to characterize the tensile shear strength (TSS) and cross tensile strength (CTS) of the investigated joints after the RSW process. Tests were performed on an MTS frame universal tester with a maximum capacity of 100 kN at a constant crosshead speed of 10 mm/ min. Mechanical testing specimens were prepared from the undersized nugget size region (below MWS), up to the expulsion region in 500 A increments. The lap-shear and cross-tension specimen geometries and dimensions are shown schematically in Figure 3.4. Shims

of the same thickness as the tested material were used for all TSS specimens to maintain alignment and minimize sheet bending. Two parameters were extracted from the load-displacement curves to evaluate the mechanical performance of the weld in each welding condition: peak load and area under the curve up to the peak load. The latter was integrated digitally as specified by AWS D8.1 [26]. All data points used from the mechanical results represent an average of five test repetitions and the error bars show 95 % confidence interval values. Lastly, the failure modes of tested specimens were determined by visual examination of the fractured surfaces.

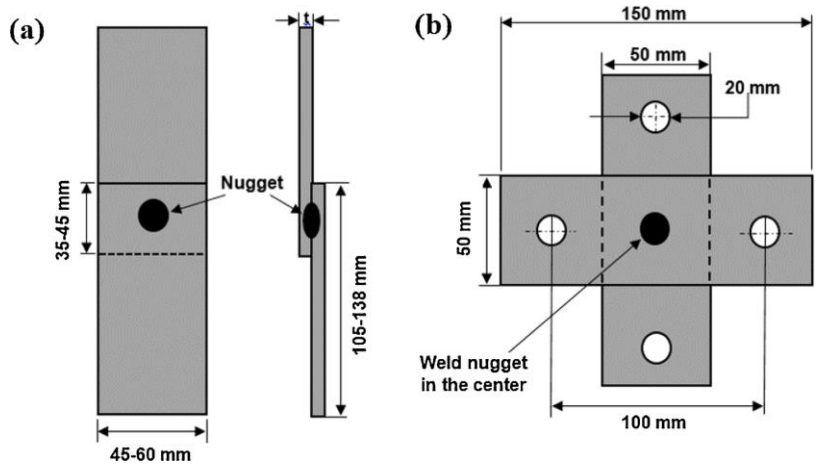


Figure 3.4. Schematic representation of (a) tensile shear and (b) cross tensile test specimens.

3.3.4 Microstructural Characterization

Samples were cut through the centerline of the welds and were prepared for microstructural observation following conventional procedures, *i.e.* mounting in conductive epoxy resin, grinding with SiC sandpapers up to 1200 grit, polishing with 1 μm diamond compound, and etching with 2% Nital (2% HNO3 + 98 % ethanol). Microstructures were characterized using optical microscopy (OM) and field emission scanning electron microscopy (FESEM, UltraZeiss) techniques. Microhardness maps were plotted for welds with a nugget size of 7 mm using a Clemex CMT automated hardness tester with a Vickers indenter according to ASTM E384 [25]. A load of 500 g and a dwell time of 15 s were used to create the microhardness maps. The horizontal and vertical distance between indents was 200 μm to prevent interaction from the strain fields of adjacent indents.

3.4 Results and Discussions

3.4.1 Spot Weldability Lobes

The weld-lobes of the investigated steels are shown in Figure 3.5 for three different welding times: 250, 334, and 417 ms in 0.1 kA current increments. As shown, the lobes divide the welding current/time domain into three regions: First, the undersized weld region due to insufficient heat input. Second, the area to the right of the expulsion limit where molten nugget extends past the corona bond due to excessive heat input, and lastly, the area within which an acceptable nugget size and therefore appropriate joint strength is achieved, which is located between the MWS and expulsion line. Welding currents up to 7 kA and 6.8 kA resulted in undersized welds for 3G-980 and 3G-1180, and the expulsion occurred at 9.3 kA and 9.1 kA, respectively, for total welding time of 334 ms. The nugget diameters reported in Figure 3.5 (a) were measured according to AWS D8.1 standard by opening the welds through chisel testing. Figure 3.5 (b) shows the weldability lobes constructed for three different total welding times to establish the operational window where acceptable welds are achieved. It was noted that both MWS and expulsion are attained at lower welding currents for 3G-1180 compared to the 3G-980 material which implies a slightly higher resistivity, and heat generation rate for the 3G-1180 material. It is known that alloys with higher resistivity require lower currents to be welded than those that are better conductors of electricity but are also more susceptible to expulsion, leading to narrower welding current ranges. The broader range for the 3G-980 is attributed to the lower carbon equivalent of the steel since lower carbon equivalent is associated with lower electrical resistivity and therefore, lower overall heat input [74], [183], [184]. The welding range in all cases exceeds the MWS value by a relatively large margin (above 2 kA) without experiencing expulsion for both materials.

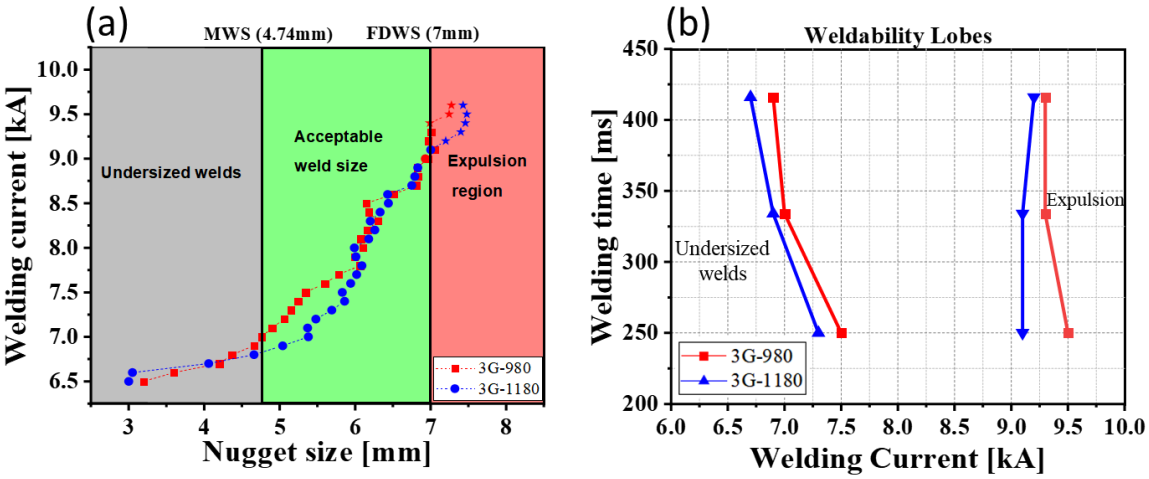


Figure 3.5. (a) Current range curve of the investigated steels for 334 ms welding time, and (b) weldability lobes for 3 total welding times: 250, 334, and 417 ms (MWS, Minimum Weld Size; FDWS, Face Diameter Weld Size of 7 mm).

3.4.2 Spot Weld Optimization by TS and CT tests

Figure 3.6 plots the load-displacement curves for different welding currents from which the TSS values can be determined. Weld strength increased with increasing welding current, except for the 3G-980 expulsion case. All welds made with welding currents between 6.5 and 8.5 kA failed in an IF mode. However, as the current exceeded 9 kA, the failure mode changed to PO and P-PO modes, as identified by the withdrawal of the weld nugget from one sheet. All the welds exhibiting IF exhibited brittle-type load-displacement response recognized by the sharp decrease in weld stress after passing the peak load. On the other hand, the PO load-displacement curves are distinguishable by their much higher displacement values during testing. In this failure mode, the load-displacement curves have a long tail which corresponds to the continued tearing of the nugget circumference and BM. Surpassing the expulsion limit causes the failure mode to revert to IF for both steels. Within the expulsion region, a notable difference was observed between the load-carrying capacities of the two steels. It is evident that for 3G-980, the peak load within the expulsion region is lower than specimens welded just below the expulsion limit (9 and 9.5 kA welding currents). The decrease in peak load was accompanied by a significant decrease in the displacement to failure.

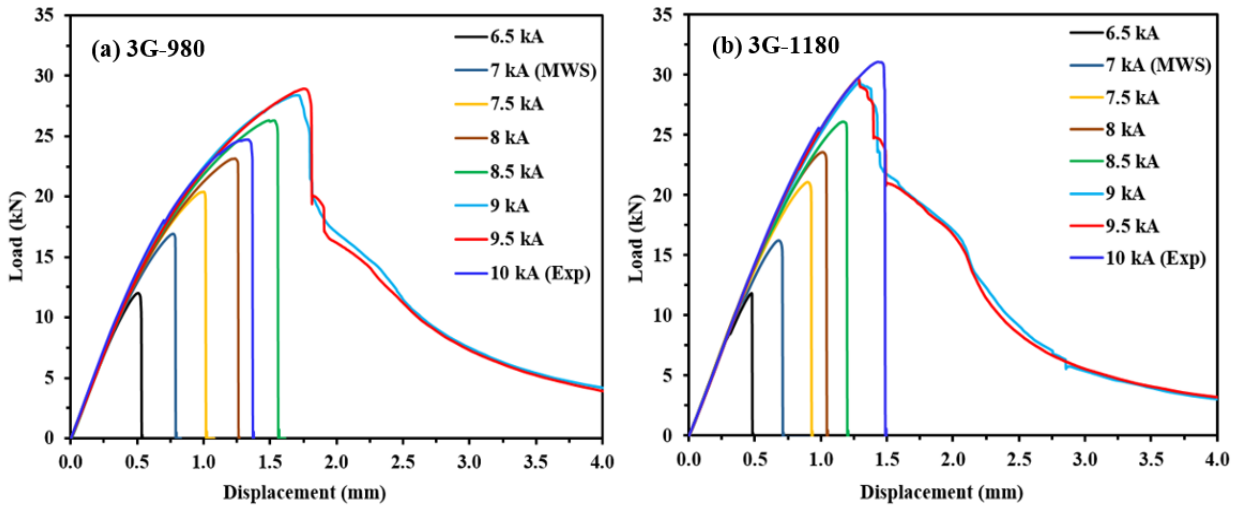


Figure 3.6. Representative load-displacement curves for (a) 3G-980 and (b) 3G-1180 resistance spot welds during lap-shear tests of different welding currents.

The load-displacement curves from cross-tension tests of different welding currents are shown in Figure 3.7. Like the TSS tests, it has been determined that with increasing current, the strength of the joints increased during cross-tensile loading. But, in contrast to the TSS load-displacement curves, displacement values are much higher until the failure in this test. The higher displacement is due to the extension bending of the base material during the CTS test. It also should be noted that the jagged nature of these curves is due to the slippage of CTS coupons within the testing fixture during testing. In the case of the 3G-980 specimens, all welds with nugget diameters exceeding the MWS value exhibited PO/P-PO failure modes. However, the MWS criterion does not predict the PO failure mode for 3G-1180 as the PO failure mode was observed for nuggets exceeding 6 mm in size.

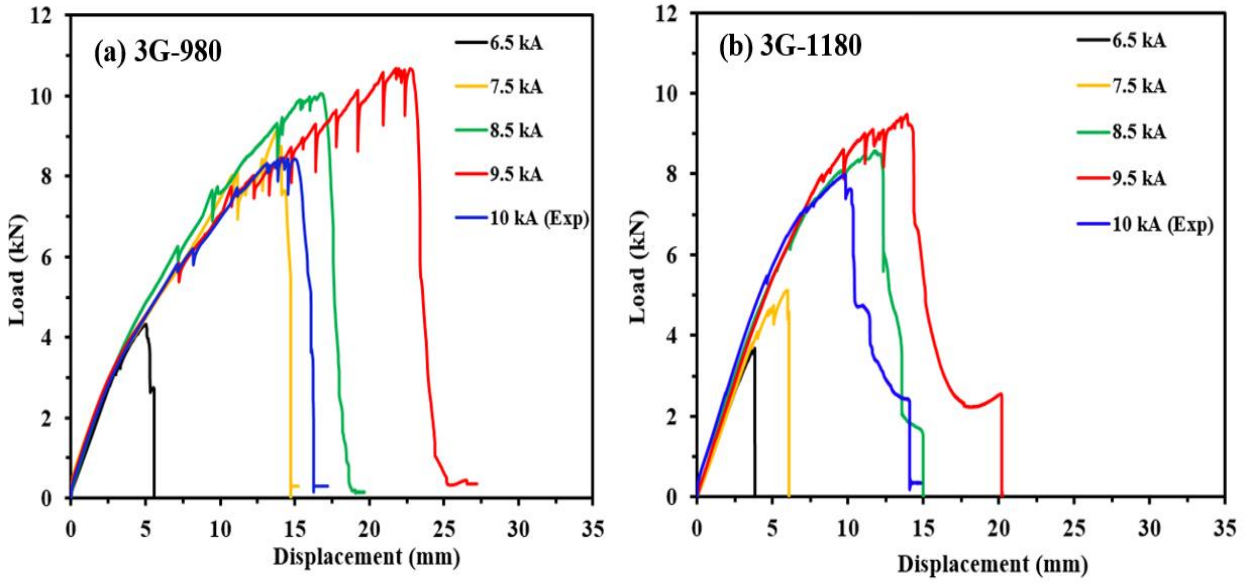


Figure 3.7. Load-displacement characteristics of (a) 3G-980 and (b) 3G-1180 resistance spot welds during cross tension tests.

Figure 3.8 summarizes the changes in load-bearing capacities (peak load) for all experimented welding currents during TS and CT mechanical tests. The MWS, expulsion points, and observed failure modes have also been shown on these graphs. It is seen that in the case of TS tests (Figure 3.8 (a)), all samples welded up to 8.5 kA welding currents failed in IF mode. The 8.5 kA welding current results in nugget diameters that are approximately 2 mm above the minimum nugget diameter of 4.73 mm requirement. This indicates that the $4\sqrt{t}$ criterion does not guarantee PO failures in 3G-AHSS spot welds. According to Pouranvari *et al.*, the driving force for IF during the TS test is shear stresses at the sheet/sheet interface [14]. Therefore, an increase in nugget size, which decreases the experienced stresses at the notch region, is the primary reason for increased strength as welding current increases from the undersized region. Testing the specimens that were welded with currents above 8.5 kA resulted in PO/P-PO failure of the samples. The increased tendency for PO/P-PO failures at higher welding currents is related to the increase in nugget diameter and rotation of coupons as testing continues, which forms tensile stresses around the nugget periphery, promoting through-thickness crack propagation, and hence, PO/P-PO failures. It is observed that welding currents within the expulsion region caused inconsistencies in attained strengths and should be avoided.

As for the changes of strength during CT tests, a similar increasing trend in load-bearing capacity is observed up to a welding current of 9 kA for both steels. However, the transition between IF and PO/P-PO failure modes occurred sooner in CT tests: between 6.5 kA and 7 kA for 3G-980, and between 7.5 kA and 8 kA for 3G-1180. The sooner transition between failures in CT test is related to the higher shear stresses experienced in the nugget circumference (i.e., BM/HAZ) related to the geometry of the CT test and load application direction. When the shear stresses experienced by the weld circumference exceed the fracture shear stress of the material, the spot welds fail under PO mode in CT tests. Similar to the TS results, expulsion had a detrimental effect on the load-carrying capacity of CT tests which could be related to the higher electrode indentation creating more stress concentration regions, wider HAZ, and material loss as seen in Figure 3.8 (b).

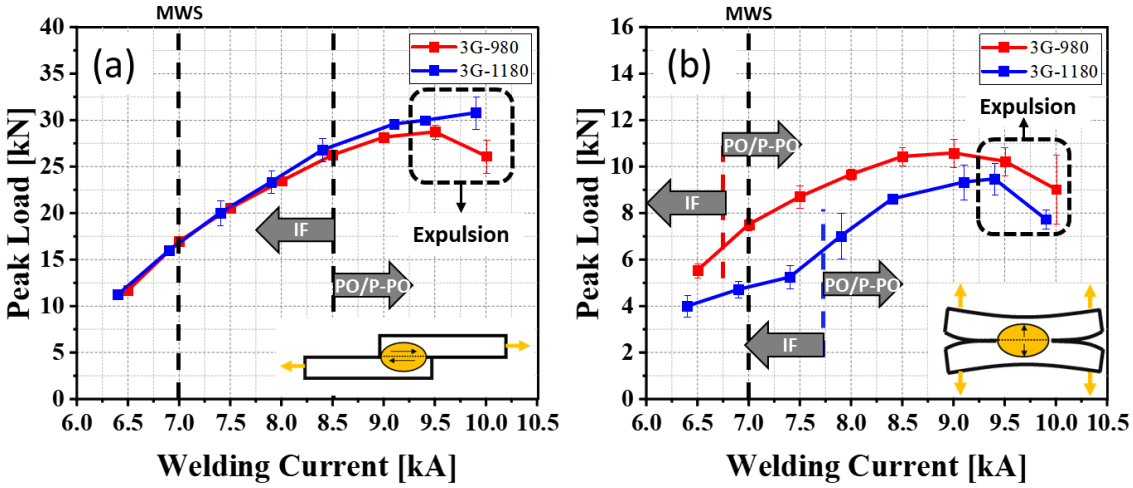


Figure 3.8. Effect of welding current on load-bearing capacity during (a) tensile shear, and (b) cross tension mechanical tests of 3G-980 and 3G-1180 spot welds.

According to the presented results from TS and CT mechanical tests, a welding current of 9.1 and 9.0 kA were selected as the optimized welding current resulting in the highest strength for 3G-980 and 3G-1180 spot-welded joints, respectively. These welding conditions will be referred to as FDWS from here onwards. Sub-optimal welding conditions that meet the MWS requirement of AWS standard are also considered for comparison purposes. Microstructural evolution and microhardness distribution of the selected welding conditions were investigated which are discussed in the following sections.

3.4.3 Optimized (FDWS) and Sub-optimal (MWS) Weld Conditions

Welding currents of 9.1 and 9.0 kA were selected for 3G-980 and 3G-1180 to avoid the probabilistic nature of the expulsion phenomenon and at the same time attain optimum mechanical properties by maximizing nugget diameter. This is because nugget diameter has been widely recognized to be the most important factor affecting resistance spot welds' mechanical properties [14]. A welding current of 7.0 kA and 6.9 kA were used for MWS conditions with 4.7 mm nugget diameters. The dynamic resistance profiles of the investigated steels after 334 ms of welding time for both the optimized FDWS and sub-optimal MWS conditions have been shown in Figure 3.9 (a). From a general perspective, these profiles can be divided into two stages: stage I where the resistance initially increases rapidly. This is due to the heating effect as current begins to flow into the specimens, causing voltage build-up before asperity breakdown. Thereafter during stage II, heat generation and softening occur at the sheet-sheet interface and the resistance drops due to the pronounced effect of asperity collapse and an increase in the contact area between the sheets and the electrodes. As shown the 3G-1180 exhibits higher overall resistance compared to the 3G-980. This can be associated with the higher alloying content of the 3G-1180 steel as mentioned earlier by its higher carbon equivalent value compared to the 3G-980 steel. Moreover, these curves illustrate the higher nugget growth rate in the 3G-980 steel during welding. This is because while the β point, representing the starting point of nugget growth, is reached at a shorter welding time in the 3G-1180 steel, the final nugget size for both steels is the same. Therefore, the 7 mm nugget size was formed at a shorter period for 3G-980 compared to the 3G-1180. By having the instantaneous values of resistance and current, the generated power can be calculated as shown in Figure 3.9 (b). As expected, the generated power during welding was higher for the case of 3G-1180. The higher power generation results in more accumulated energy during the welding of 3G-1180. As shown in Figure 3.9 (c), for a nugget size of 7 mm the accumulated heat difference between the two investigated steels maximizes at 167.9 J for the FDWS case and 80 J for the MWS condition.

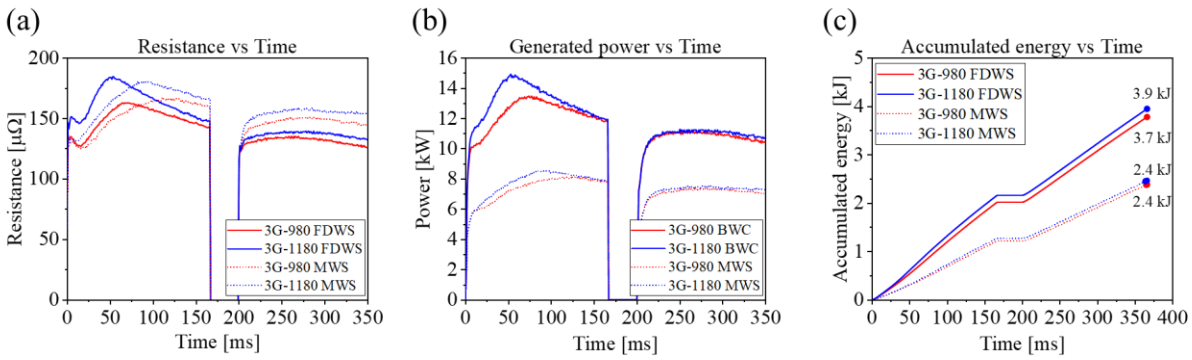


Figure 3.9. (a) Nugget sizes and dynamic resistance profiles, (b) generated power, and (c) accumulated energy during the RSW process of the investigated steels.

3.4.4 Microstructural Evolution of the Welds

The cross-sectional view of the FDWS and MWS spot welds for 3G-980 and 3G-1180 are shown in Figure 3.10. According to the most conventional classification of the joint, the cross-sectional view is divided into three areas: FZ at the center of the weld, the outer HAZ, and the BM unaffected by the heat input. Generally, the microstructure is coarse within the FZ and becomes finer towards the BM.

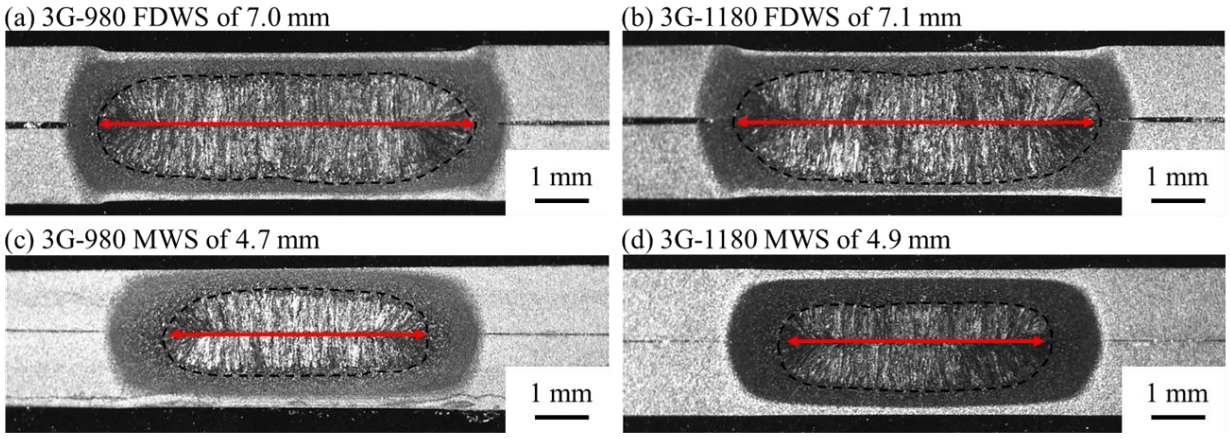


Figure 3.10. Optical images of RSW cross sections for (a) and (b) electrode face diameter weld size (FDWS), (c) and (d) minimum allowable weld size (MWS) illustrating the FZ diameters.

Figure 3.11 (a) shows the correlation between the peak temperatures experienced and the approximate location of each of the FZ and HAZ sub-regions on a Fe-C phase diagram along with the possible metallurgical transformations occurring in each region. As for the BMs, a complex microstructure containing martensite, tempered martensite, ferrite, and retained austenite was observed for both steels. However, the volume fraction of these phases was different between the two steels. The microstructure within the FZ of both 3G-AHSS spot welds consisted of coarse lath

martensite with a columnar grain growth towards the weld centerline. The critical cooling rate for the martensitic transformation of the investigated steels was estimated at 46.7 Ks^{-1} and 26.9 Ks^{-1} for 3G-980 and 3G-1180, respectively, using the equation proposed by Easterling *et al.* [185]. The rapid solidification within a few cycles during RSW [14] noticeably increases the degree of constitutional supercooling and causes dendritic growth morphologies within the FZ [62]. The non-equilibrium solidification within FZ could lead to partitioning/segregation of alloying elements such as carbon and phosphorous, as reported in previous works on RSW of Q&P steels [79,168]. It has recently been proposed that if the selected welding schedule results in the boundary of FZ/HAZ remaining stationary for a prolonged time, severe partitioning/segregation can result in the formation of a locally softened zone referred to as the "halo ring" [150]. Signs of the halo ring were not revealed in the observed metallographies around the FZ periphery after following the double pulse welding schedule recommended by AWS standards.

Optical micrographs along with higher magnification SEM images of HAZ sub-zones have also been shown in Figure 3.11. Owing to the weld cycle thermal gradient, the HAZ experiences a range of possible microstructural evolutions and metallurgical transformations. The CGHAZ contains large equiaxed packets of martensite related to the austenitic growth of this region during welding followed by rapid cooling. The driving force for austenitic growth in the adjacent region (FGHAZ) is lower, because of the lower peak temperature experienced, resulting in the formation of fine martensitic packets. In ICHAZ, partial transformation of martensite to austenite and nucleation of new ferrite grains occurs. Lastly, the temperature regime experienced in SCHAZ is suitable for tempering of available martensite. It is noted that whether softening occurs in SCHAZ depended on the fraction of pre-existing martensite in the BM microstructure.

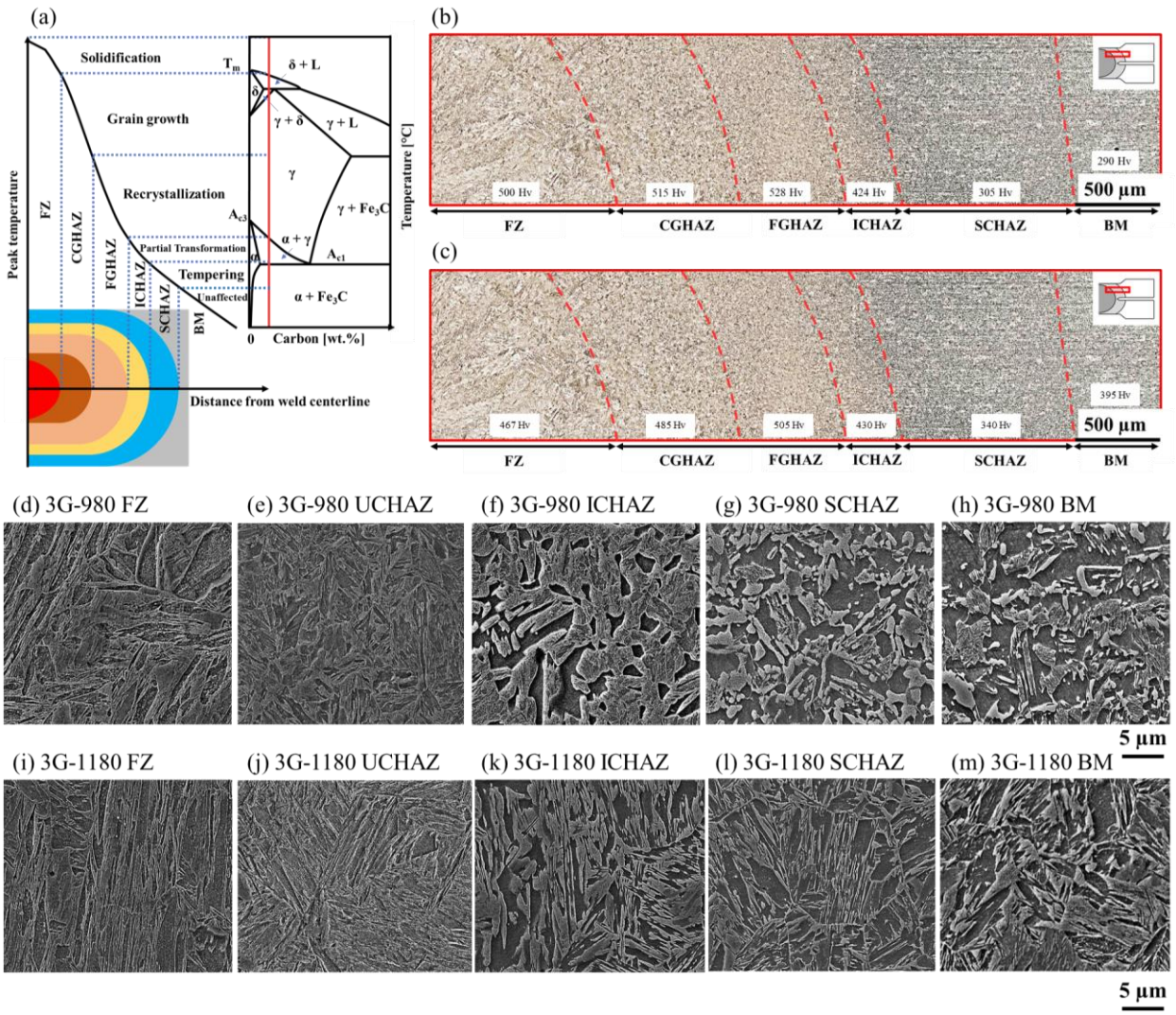


Figure 3.11. (a) Sub-division of different RSW regions with their respective peak temperatures shown on Fe-C equilibrium phase diagram; (b) and (c) show optical micrographs of all the corresponding regions along with their average microhardness values for 3G-980 and 3G-1180 spot-welded joints. (d)-(m) high magnification scanning electron microscope (SEM) images of spot welds indicating the RSW sub-regions for 3G-980, and 3G-1180.

The metallurgical transformations occurring in different RSW sub-regions are typically correlated with variations in local hardness. Figure 3.12 shows the Vickers microhardness maps of the 3G-980 and 3G-1180 FDWS RSW cross-sections, covering all sub-regions shown earlier in Figure 3.11. The average hardness of the BM was 290 and 395 Hv for 3G-980 and 3G-1180, respectively. The higher hardness of the 3G-1180 AHSS is associated with a higher volume fraction of hard phases such as martensite and bainite compared to the BM of 3G-980 material. The average FZ hardness for 3G-980 and 3G-1180 steels was respectively 1.75 and 1.25 times higher than that of the BMs. The microhardness traverses showed that the average FZ hardness of

3G-980 is 7% harder than the FZ of 3G-1180 (500 Hv vs 467 Hv). The hardenability of each FZ is believed to be influenced by the initial BM chemistry. Interestingly, the softer steel (3G-980) has shown higher hardenability within the FZ compared to 3G-1180. This increased hardness is associated with the higher carbon percentage of the 3G-980 which increases the hardness of the martensite [186]. However, it should be noted that the hardenability of both steels is sufficient for a fully martensitic microstructure within the FZ. The hardness of the UCHAZ (FGHAZ and CGHAZ) was found to be higher than the hardness of respective FZ. Investigations by Song *et al.* [187] showed that electrode collapse in the shoulder region of the welds is associated with higher thermal contact area and higher heat extraction rate which can be correlated to the observed increased hardness in the UCHAZ.

The hardness of the 3G-1180 SCHAZ was 12% lower than that of the BM (HAZ softening), whereas the SCHAZ in 3G-980 spot welds experienced a 5% increase in hardness (HAZ secondary hardening). The softening in the SCHAZ of the 3G-1180 spot welds is attributed to the decomposition of primary martensite available in the BM to ferrite and coarse carbides (martensite tempering) [26]. The lower volume fraction of primary martensite available in the 3G-980 BM and the formation of fine plate-shaped M_2C carbides were found responsible for secondary hardening in SCHAZ of 3G-980 spot welds by Ramachandran *et al.* [66,188]. The degree of HAZ softening was dependent on the initial fraction of primary martensite in the BM microstructures [189], [52]. The 3G-1180 possesses a higher fraction of martensite compared to the 3G-980 meaning more martensite was available to be tempered during the welding procedure. Meanwhile, although tempering of martensite occurred for the available primary martensite in the microstructure of the 3G-980 steel, this softening effect may have been balanced by the secondary hardening effect due to the transformation of pre-existing cementite within the tempered martensite in the base material structure [66]. As a result, no noticeable softening or hardening in the SCHAZ of the 3G-980 steel was observed. Explaining the mechanism resulting in softening or hardening in different regions of 3G-AHSS spot welds requires further investigation. More details about secondary hardening behavior of SCHAZ in bainite-containing DP AHSS has been examined in detail by Saha *et al.* [66].

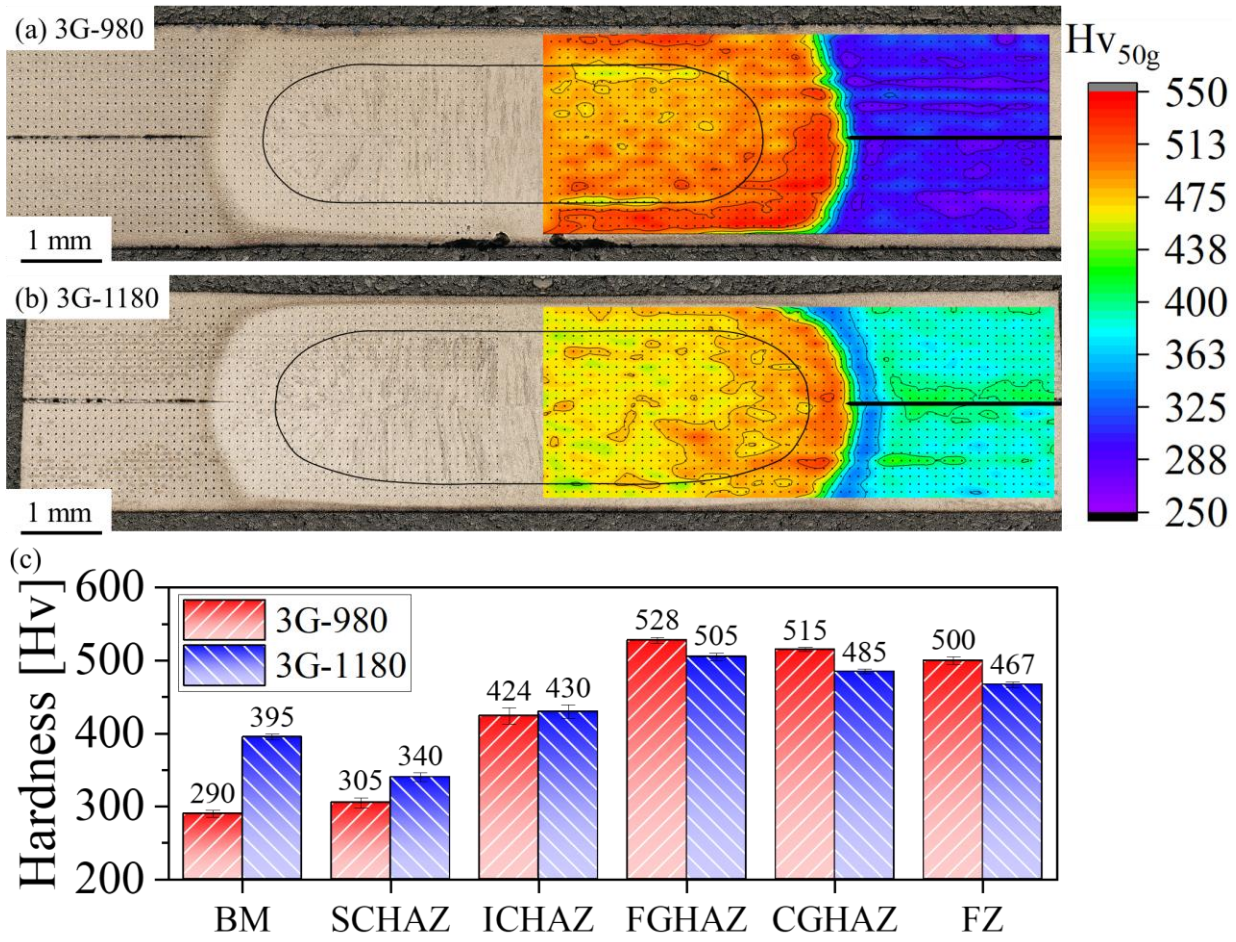


Figure 3.12 Microhardness maps for (a) 3G-980 and (b) 3G-1180 resistance spot welds superimposed on the optical micrographs of the corresponding FDWS RSW cross sections. (c) Average hardness values of RSW sub-regions (error bars are 95% confidence intervals).

3.4.5 Summary

In this chapter, RSW process robustness was assessed by developing current range curves and weldability lobes for two grades of 3G-AHSS, namely 3G-980 and 3G-1180. While both steels offer acceptable weldability range, the 3G-980 steel displayed a wider weldability window, due to the lower carbon equivalent of that steel. Industry-standard TS and CT mechanical tests were performed on spot welds with nugget diameters varying from the undersized region up to within the expulsion region. TSS values up to 28.7 kN for 3G-980 and 30.8 kN for 3G-1180 were recorded. Also, CTS values of 10.4 kN and 9.3kN were measured for 3G-980 and 3G-1180 respectively. Unified sets of RSW process parameters, termed FDWS and MWS, corresponding to optimal and sub-optimal welding conditions were selected based on the results of the mechanical tests for further analysis in subsequent chapters. The criteria for selecting process parameters were

based on the recommendations of the AWS D8.9 standard and the attainment of defect/expulsion-free spot welds. Also in this chapter, microstructural evolution and microhardness distribution of the optimized welding conditions were characterized. Microhardness measurements revealed average hardnesses of 290 Hv and 395 Hv for the BMs and a hardness of 500 Hv and 467 Hv in the FZ for the 3G-980 and 3G-1180 steels, respectively. The high hardness value in the FZ is associated with the formation of martensite in this region. As for HAZ, while the SCHAZ experienced a 7% secondary hardening in the case of 3G-980, a 12% hardness drop, relative to that of the BM, was observed in the SCHAZ area for 3G-1180 due to more pronounced martensite tempering.

4 Chapter 4: Combined Shear-tensile Loading of Spot Welds via KS-II tests[2]

4.1 Overview

Resistance spot-welded joints undergo complex loading conditions in service [14,190]. A safe and reliable migration from previous generations of AHSS to 3G-AHSS within the vehicle BIW, among other requirements, demands the establishment of the relationship between mechanical properties and failure characteristics of 3G-AHSS RSW upon different loading conditions; and calibration of reliable failure criteria capable of accurately predicting the onset of failure for such joints for use in crash safety simulation. Combined shear-tensile loading of spot welds is a common loading type that spot welds can experience during vehicle crash events. Characterization of spot weld mechanical performance indices under combined shear tensile loading, such as shear and tensile load bearing capacity components, and energy absorption is accompanied by unique challenges due to coupon rotation, and/or slippage. This study utilized a new fixture based on the Arcan apparatus coupled with the DIC technique to track the instantaneous orientation of the KS-II coupons. This way, the actual proportion of shear and tensile components of force applied to the nugget, instead of the nominal ratio at the beginning of the tests, could be quantified experimentally. A novel triangulation method was proposed to minimize the influence of coupon slippage and deformation at regions away from the nugget on calculated absorbed energy. The more precise absorbed energy calculation was achieved by changing the displacement reference point from the crosshead to a local measurement between coupon halves. Energy absorption capabilities of the spot welds were calculated by separately tracking the deformation of the nugget in the shear and tensile directions. It was observed that within the tensile-dominated loading orientations (45° to 90°) pullout failures of 3G-980 spot welds exhibit much higher post-failure energy absorption capabilities than the RSW of 3G-1180. The propagation of the formed cracks

[2] This chapter is composed of a published research paper as outlined in the statement of contributions. **Shojaee M**, Tolton C, Midawi ARH, Butcher C, Ghassemi-Armaki H, Worswick M, Biro E. Influence of loading orientation on mechanical properties of spot welds. Int J Mech Sci 2022;224:107327. https://doi.org/10.1016/j.ijmecsci.2022.107327.

into the FZ was found responsible for the relatively inferior energy absorption capability of 3G-1180 joints.

4.2 Background

The mechanical performance of spot welds varies drastically depending on the base metals being joined, the welding process parameters, and the nature of loading. There has been considerable past research concerning the influence of material-related parameters such as initial microstructure [191], surface condition [45,192], coating type [193], and process-related parameters like welding current [194], time [195,196], and force [197] on the attained AHSS RSW mechanical and metallurgical characteristics. The stress-state experienced by spot welds during a specific mechanical test is also a major contributor to the load-bearing capacity and energy absorption capability of spot welds [198]. In this regard, industry-standard TS and CT mechanical tests are commonly performed [93,199]. Liu *et al.* [71] showed that resistance spot-welded Q&P 3G-AHSS, exhibit very different strengths and energy absorption capabilities between shear-dominated and tensile-dominated loading conditions using TS and CT tests, respectively. While Liu *et al.* reported liquation cracking and P segregation at the partially melted zone as the mechanism responsible for their observed failure behavior during TS and CT tests, Ramachandran *et al.* [79] considered the formation of a carbon-depleted and locally softened zone at the boundary of the nugget, as the crack initiation region during CT tests of 3G-AHSS spot welds. Chen *et al.* [200] improved the mechanical properties of Q&P 3G-AHSS spot welds, as measured using TS and CT tests, by applying post-weld tempering pulses as well.

At present, understanding the relationship between mechanical properties and failure behavior of 3G-AHSS RSW requires performing numerous unidirectional mechanical tests to span the range of representative loading conditions an RSW component may see in service. Other than the conventional TS and CT tests, a thorough understanding of the response of the weldment to a combination of shear and tensile loading (or mixed loading mode) is necessary since, as identified by Lin *et al.* [162], spot welds in structural components often fail under such combined loading conditions. To this end, more complex testing geometries have been utilized with the intent of characterizing the mechanical properties of spot welds under different proportions of shear and tensile loads. The KS-II mechanical test, in which two formed U-channels are welded at the center of the mating surfaces and pulled at different orientations, is suitable for imposing different combinations of shear/tensile load to the spot weld.

One issue that arises during the combined loading of spot welds is the deviation of the loading path from the intended initial proportion between shear and tensile loads due to unwanted rotation and/or deformation of the coupons during the tests. Virtually all previous combined loading investigations performed utilizing the Arcan apparatus fixture have overlooked the significant effect of loading path and coupon rotation on the extracted spot weld performance indices such as energy absorption capability [105,110,111,201]. The issue of coupon deformation and rotation/slippage has only received limited attention recently. Pandya *et al.* [91] used orientation plates to ensure alignment of the coupons and still acknowledged the occurrence of rotation during combined loading of dual-phase (DP) spot welds. Song and Huh [165] attempted to minimize coupon rotation by designing a custom pin-joint fixture and adding six extra spot welds to prevent excessive bending of the region surrounding the investigated spot-weld. Previous efforts have primarily focused on minimizing coupon rotation during combined loading tests, while not necessarily quantifying the rotation during the experiment. It is anticipated that the rotation would be even more significant in testing higher-strength 3G-AHSS. Therefore, the influence of coupon rotation on the measured mechanical properties should be accurately quantified during experiments. The coupon deformation and rotation data can then be used for more accurate extraction of spot weld performance indices and precise prediction of spot weld failure by calibrating reliable spot weld failure criteria.

No study has yet concentrated on correlating the alterations in mechanical properties, more specifically strength and energy absorption capability, to failure modes during the KS-II testing methodology, particularly for 3G-AHSS spot-welded joints. Moreover, the rather different gripping and geometry of KS-II specimens, compared to standard spot weld mechanical tests, can create new challenges in extracting the spot weld mechanical properties. A validated methodology in extracting spot weld performance indices during KS-II mechanical testing can significantly improve the accuracy of experiment-based failure criteria used within the automotive industry.

The current study characterizes the changes in failure mode and mechanical properties, specifically strength and energy absorption, in 3G-AHSS RSW joints as the ratio of applied shear and tensile components of force varies. To this end, KS-II tests were performed in eight different orientations to span the range of combined shear and tensile load ratios. The changes in mechanical properties were correlated to the changes in failure modes and crack initiation regions which

originated from variations in microstructural and microhardness characteristics of the investigated joints as well as different loading orientations. A novel methodology was developed that assisted with instantaneous measurement of the nugget orientation and the accurate calculation of nugget center point displacement throughout the tests. As a final aspect of this study, the current KS-II results are compared to standard TS and CT test results of a previous study [135] to identify and understand differences in measured weld performance between these testing methodologies.

4.3 Materials and Methods

In this section, the details of the investigated steel and the experimental methods applied are outlined. The utilized RSW process parameters are presented; followed by an introduction to the KS-II testing methodology and designed fixture components. The developed triangulation method for more accurate extraction of spot weld performance indices such as absorbed energy is explained. Lastly, the procedure for performing interrupted mechanical tests, and microstructural analysis are described. This section also lays the foundation for the subsequent description of the results from the KS-II mechanical tests given in section 4.4.

4.3.1 As-received Materials

The same 3G-980 and 3G-1180 AHSS, as introduced in Chapter 3 were used in this study. More details about the investigated materials can be found in section 3.3.1.

4.3.2 Resistance Spot Welding

An MFDC RSW robot equipped with a C-type welding gun and a Rexroth Bosch weld controller with a BOS 6000 operating interface was used in this study, as described in the previous chapter. RWMA, group A, class II, Cu-Cr domed electrodes with a flat face diameter of 7 mm were used for welding. A water flow rate of 6 L/min was maintained for electrode cooling. The optimized RSW welding schedule and parameters were selected following the AWS D8.9 standard [35]. The FDWS was 7 mm for both steels, as determined by process optimization of the same two steels explained in Chapter 3. The selected welding currents along with other RSW process parameters are shown in Table 4.1.

Table 4.1. Resistance spot welding process parameters.

Material	Electrode force [kN]	Squeeze time [ms]	Total weld time [ms]	Hold time [ms]	Number of pulses	Cooling between pulses [ms]	Weld current [kA]
3G-980	4.9	167	334	167	2	34	9.1
3G-1180	4.9	167	334	167	2	34	9.0

4.3.3 KS-II Testing

Figure 4.1 (a) shows a welded KS-II sample geometry with the RSW nugget at the center point between the two coupons. The loading orientation (θ) is defined as the angle between the load application line and the mating line between the two coupons as shown in Figure 4.1 (b). Experiments were conducted in eight different loading orientations (θ = 0°, 10°, 15°, 30°, 45°, 60°, 75°, and 90°). The loading orientations from 0° to 30° are referred to as shear-dominated loading orientations, and the tests performed between 60° and 90° are referred to as tensile-dominated loading orientations. It is possible to decompose the applied load into two perpendicular shear and tensile components with respect to the local *s*-*t* axis introduced for each loading orientation. In all experimental orientations, the *s*-axis is parallel to the mating line between the two coupons, representing the shear direction, and the *t*-axis is perpendicular to the mating line, corresponding to the weld tensile loading direction. The respective shear and tensile force components, $\vec{F}_s$ and $\vec{F}_n$, are related to the measured force at the load cell, $\vec{F}_{Load\ cell}$, as:

$$\left|\vec{F}_n\right| = \left|\vec{F}_{Load\ cell}\right| \times sin(\theta)\ ;\ \left|\vec{F}_s\right| = \left|\vec{F}_{Load\ cell}\right| \times cos(\theta) \qquad (4.1)$$

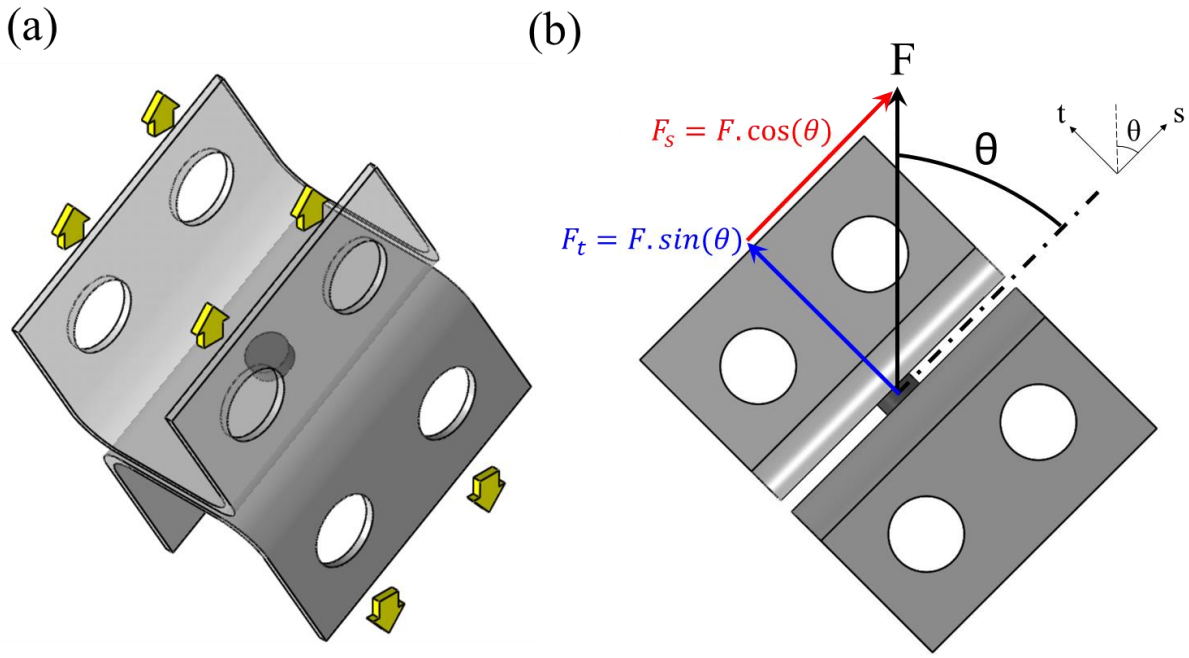


Figure 4.1. Schematic representation of a welded KS-II specimen suitable for applying a combined loading mode to the spot weld; (b) the load F applied to the spot weld at the angle θ can be resolved into tensile and shear components.

The KS-II coupon geometry and dimensions are shown in Figure 4.2 (a). A pre-existing fixture developed by Anderson *et al.* [202], based on the approach used by Wierzbicki *et al.* [203] for performing so-called butterfly fracture tests, was modified for KS-II testing in this study. A schematic drawing of a spot-welded KS-II specimen ready for testing is shown in Figure 4.2 (b). The modified fixture and its components are shown in Figure 4.2 (c) and (d). The KS-II fixture consisted of a pair of KS-II holder assemblies. The KS-II specimen is attached to the holder assembly via spacers. Upon clamping the KS-II specimens within the fixture, the frame assembly is loaded in tension via two pins, one attached to the upper movable actuator and the other fixed to the stationary bolster of a 100 kN servo-hydraulic displacement-controlled tensile machine. The KS-II specimen is bolted to two adaptors, labeled as the KS-II spacers and highlighted in green in the figure, which are, in turn, bolted to the KS-II holder. The holder can be mounted in various orientations at 5° increments to accommodate the range of intended loading orientations. Inside the KS-II spacer, there are removable inserts fabricated using A2 tool steel, hardened to 58 HRC, with diamond knurled surface patterns to minimize coupon rotation during tests. During assembly, the bolts connecting the KS-II specimen to the fixture assembly were consistently tightened to 45 Nm using a torque wrench. The custom fixture assembly was mounted on a 100 kN servo-

hydraulic displacement-controlled test frame as shown in Figure 4.2 (e) and (f). All KS-II tests were performed at a constant crosshead speed of 10 mm/min at ambient temperature.

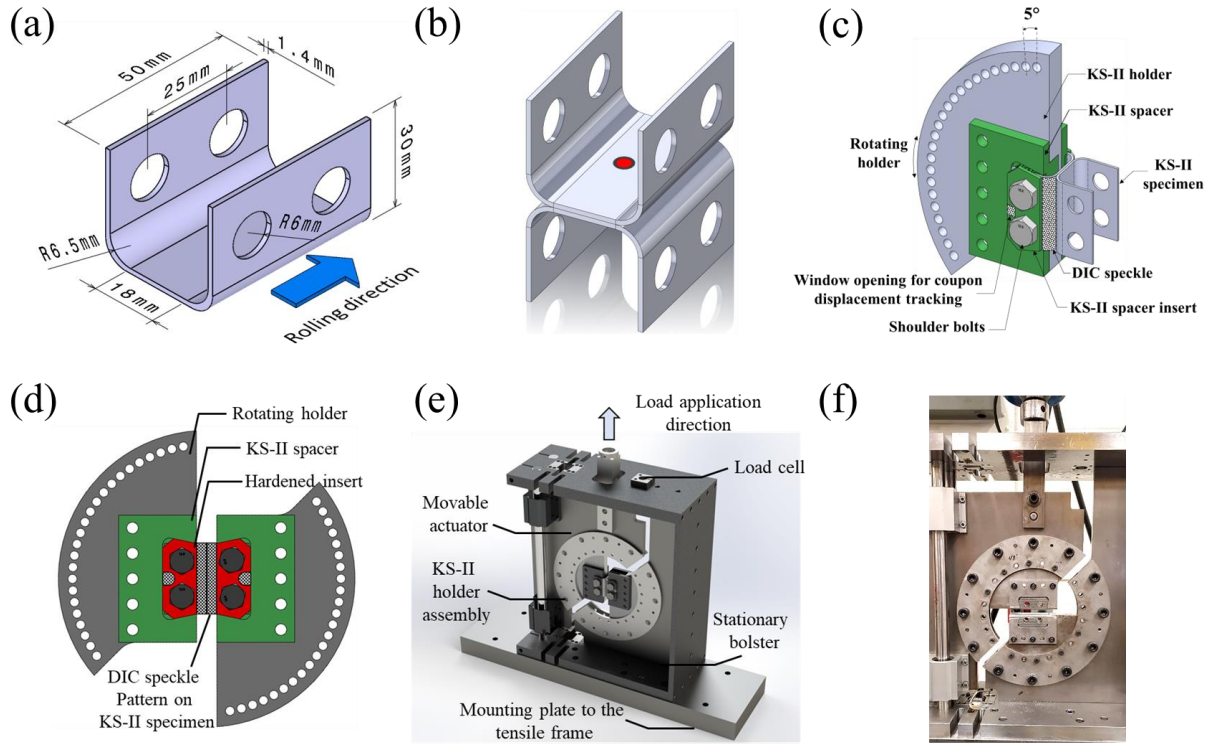


Figure 4.2. Schematic representation of (a) KS-II coupon geometry and dimensions, (b) welded KS-II specimen, (c) and (d) KS-II specimen mounted on the KS-II holder ready for testing (orientation shown corresponds to a KS-II test at 0º); (e) and (f) computer-aided design (CAD) drawing and manufactured KS-II fixture assembly mounted on the tensile frame (orientation shown corresponds to a KS-II test at 90º).

The force values were extracted from the data recorded using a custom LabVIEW program interfaced with an MTS FlexTest SE controller. The crosshead displacements were recorded for tests in all loading orientations as well. By rotating the holders, it was possible to achieve Mode I opening ($\theta = 90°$), Mode II shearing ($\theta = 0°$), and mixed mode loading orientations ($\theta = 10°$, 15°, 30°, 45°, 60°, and 75°). The schematic in Figure. 4.3 shows the shear and tensile components of forces acting on the spot welds in different orientations of the KS-II tests. The KS-II tests were intended to load the spot weld in shear (0° loading orientation), and incrementally add the tensile component of the force until 90° loading orientation. It is noted that the frictional effect from the vertical bar in the assembly along the horizontal direction was not considered in this study. Future work should consider the influence of unwanted horizontal forces during the KS-II tests.

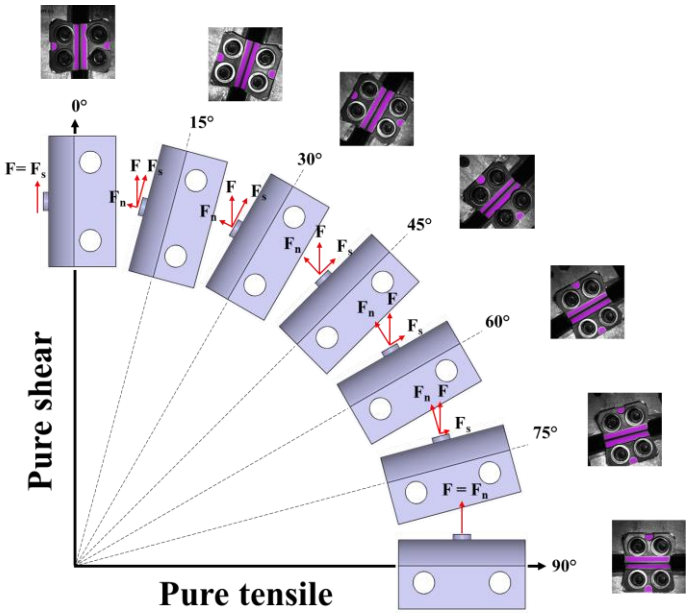


Figure. 4.3 Schematic representation of different KS-II loading orientations showing the shear and tensile components of force acting on the spot welds. (Loading in 10° orientation not shown for clarity)

4.3.4 Digital Image Correlation

The displacements of regions of interest on the exposed surface of KS-II specimens during testing (speckled regions in Figure 4.2 (c) and (d)) were recorded separately using the three-dimensional DIC technique. Details about the DIC apparatus and data analysis methods are outlined in Table 4.2. Varying imaging frequencies (frame rate) were selected for different orientations of the KS-II tests to ensure the acquisition of at least 500 images prior to the complete detachment of the two KS-II coupon halves.

Table 4.2. Summary of DIC parameters for KS-II tests.

DIC hardware parameters	DIC analysis parameters
Camera manufacturer, model, image scale: Point Gray Research, GZL-CL-41C6M-C, 0.005 mm/pixel	**DIC software package, manufacturer:** Vic 3D R9.1, Correlated Solutions
Lens manufacturer, model, focal length: Schneider, Aspherical IF, 75 mm	**Subset size:** 21 pixels
Field of view (FOV): 90 mm × 90 mm	**Step size:** 7 pixels
Stand-off distance (SOD): 60 cm	**Strain filter size:** 5
Frame rate: 24 to 45 frames/second	**Subset weights:** Gaussian-center weighted
Speckling technique, size: Paint spray, 0.2 mm	**Strain filter weights:** Gaussian-90% center-weighted

Two parameters are extracted from the KS-II tests to assess spot weld mechanical performance: (i) peak-load which is representative of joint strength, and (ii) absorbed energy until full failure. While the peak-load values were extracted directly from the data acquisition system, the procedure to calculate the energy absorption of the weldments during KS-II tests is described in the following section. All plotted values for peak-load and energy absorption capability of the weldments are an average of at least five test repetitions and the presented error bars show 95% confidence intervals. Lastly, it should be noted that this study compares the current KS-II results at 0° and 90° loading orientation with standard TS and CT mechanical tests performed in Chapter 3.

4.3.4.1 Absorbed Energy Calculation

The energy absorption capability of a weldment is defined as the area underneath the load-displacement curve up to F_{max} according to the AWS D8.1 standard. The area under the load-displacement graph after the peak-load is often neglected due to the inconsistent nature of the unloading regime. Recent work by Tolton [126] has demonstrated that the energy absorption during unloading can contribute significantly to the total energy absorption and is important to consider in the calibration of weld models. Therefore, the energy absorbed after surpassing the peak-load has also been calculated for all loading orientations in this study to compare the total

energy absorption capability and to highlight how the tendency for severe plastic deformation and rotation of the nugget (e.g. during PO failure) changes between the two investigated steels as the loading orientation changes.

One question that arises while constructing the load-displacement curves of the KS-II tests and calculating the absorbed energy from those curves is the determination of the most appropriate location(s) to measure the displacement. A commonly adopted approach to determine the energy dissipation of the welded connection during failure of the KS-II sample is simply to integrate the measured load versus load-point displacement response where the load-point displacement would correspond to the actuator or crosshead displacement of the tensile frame. Unfortunately, such an approach will include energy dissipation contributions due to the deflection of the coupon away from the weld nugget, deflection of the test frame, and any slippage of the coupon within the grips, for example.

An example of rotation/slippage during a KS-II test at 0° loading orientation can be seen by comparing the first and final frames of the DIC footage in Figure 4.4. One reason for the rotation/slippage is the high hardness of these ultra-high-strength steel samples which makes gripping difficult. The slippage occurs primarily during the early stages of loading and ceases once the clearance holes in the samples contact the shoulder bolts. Despite preventive measures such as high clamping force between the KS-II coupons and the knurled inserts, the KS-II footage revealed slippage and rotation of the coupons especially for the shear-dominated loading orientations (0° to 30°). However, the slippage reduced significantly as the loading orientation increased and became virtually negligible at the 75° and 90° loading orientations. Similar behavior in terms of rotation/slippage of coupons during mechanical testing of RSW joints has been reported by Pandya *et al.* [91] who developed a new experimental apparatus for combined loading of DP AHSS spot welds. However, the designed experimental device did not allow for quantification of the amount of rotation/slippage. In the current work, techniques were developed to minimize the influence of slippage and deformation away from the nugget in the determination of the nugget energy dissipation during the failure of spot-welded KS-II coupons, as outlined in the following.

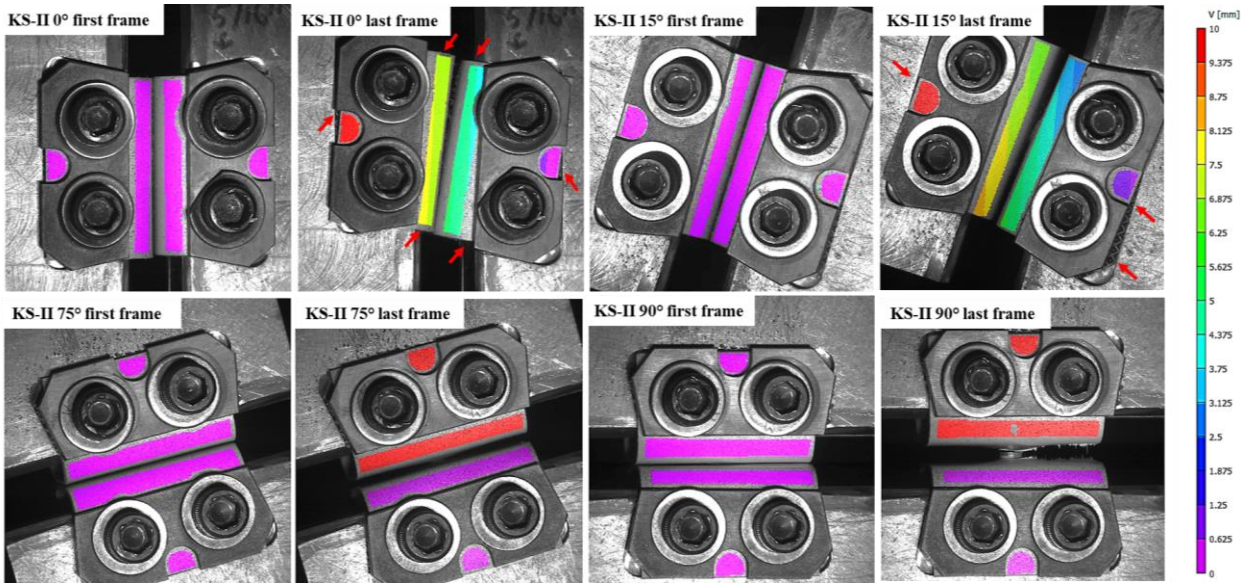


Figure 4.4. Comparison of first and last DIC frames of KS-II tests performed at 0° and 90° loading orientations for 3G-980 samples. Slippage and rotation of coupons within the fixture were difficult to prevent, especially at lower loading angles. The contour levels represent the vertical displacement within the region of interest.

To account for coupon rotation and minimize the effect of energy dissipation due to slippage and deformation away from the nugget on the nugget energy absorption calculation, a novel triangulation technique was developed to track the approximate location of the nugget center point on each side of the KS-II sample. Two triangles are constructed, one on each side of the KS-II sample denoted $C_0C_1C_2$ and $C_3C_4C_5$ (Figure 4.5 (a)). The current positions of vertices C_0-C_5 are tracked by the DIC system for each image during the tests. Before running the tests, the initial position of the weld nugget is assumed at the mid-point between the two triangles (red cross in Figure 4.5 (b)). During testing, the applied load forces the two halves of the KS-II sample apart, and this displacement is tracked by updating the new positions of the vertices and calculating the relative displacement of the nugget center point on either side of the coupons. The rationale behind using relative displacement between two nugget center points was to better account for the local relative displacement of the two coupon halves during the tests. The calculated relative displacement is assumed to correspond to deformation across the weld itself. The calculated displacement is most accurate in situations where nugget detachment from the BM, and thereafter severe out-of-plane rotation of the nugget does not occur. In comparison to the standard TS and CT tests, the KS-II fixturing provides more coupon rigidity and stiffness that limits the amount of rotation, especially during shear-dominated loading scenarios. Furthermore, rotation of the

coupons (triangles) can be calculated and used to update the current orientation of the weld line (green lines in Figure 4.5 (b)) and the local *s-t* coordinates which, in turn, is used to break the applied load into shear and normal components (F_s and F_t, respectively) acting on the weld. The displacement across the weld is also broken into components, δ_s, and δ_t, as illustrated in Figure 4.5 (c). The nugget displacement (d) will be referred to as the "projected nugget displacement" from here onwards.

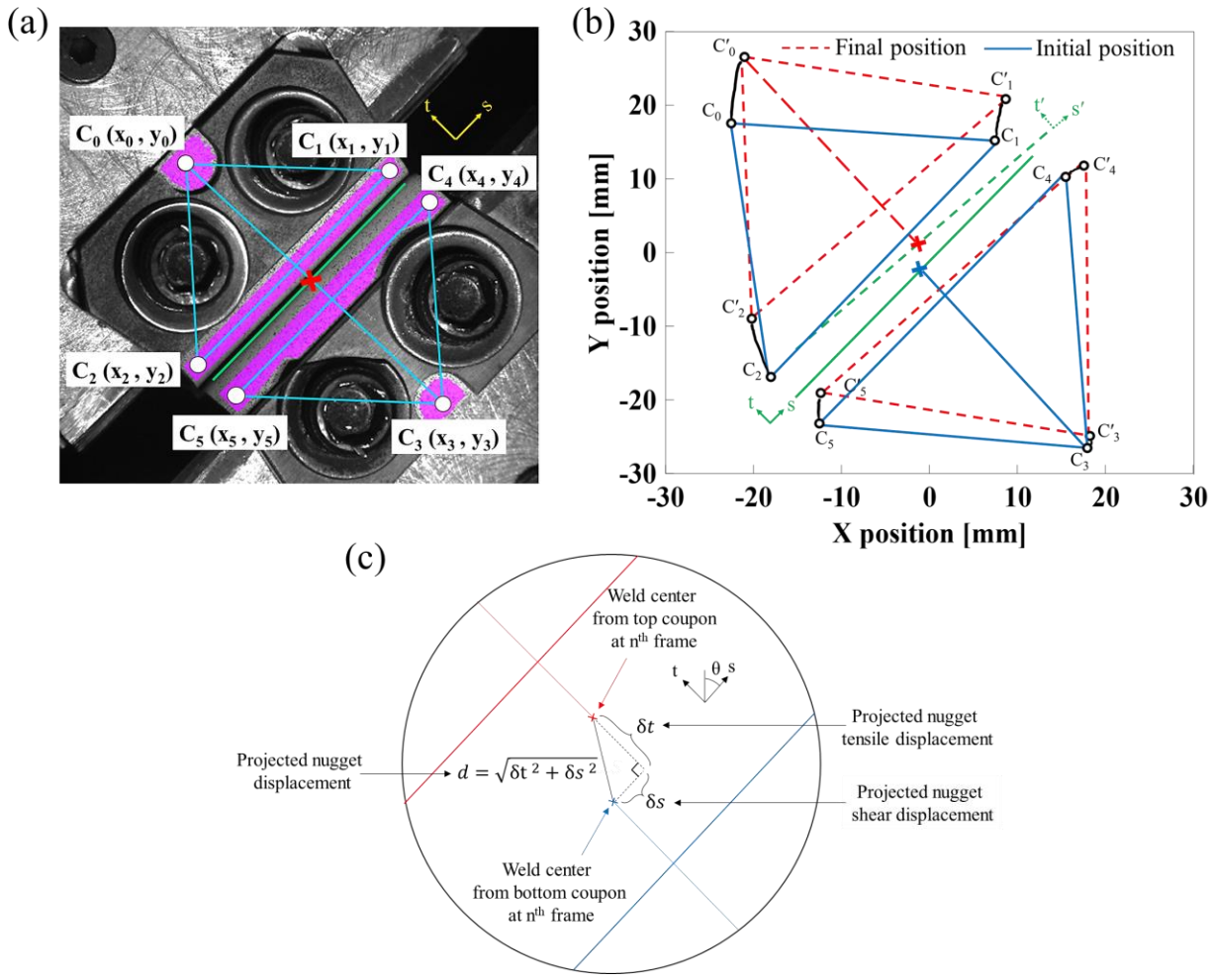


Figure 4.5. (a) Triangulation method implemented to locate weld center (red cross) before performing a KS-II test at 45° for 3G-980, (b) displacement and rotation of extracted pixels between first and last frame of the same test, and (c) detailed view of the nugget center point and measuring its projected locations in local s-t coordinate system during a test.

After determining the shear and tensile components of force, and shear and tensile components of projected nugget displacement for all frames of the tested orientations, the energy

absorption capability of the weldments was calculated by separately integrating the work done along the shear and tensile directions according to Equations (10) and (11).

$$E^{\delta s} = \int F_s . d\delta s \tag{4.2}$$

$$E^{\delta t} = \int F_t . d\delta t \tag{4.3}$$

in which $E^{\delta s}$ and $E^{\delta t}$ are energy dissipation due to the shear and tensile deformation of the nugget, F_s and F_t are shear and tensile components of applied force along their respective rotated *s* and *t* axes, and lastly, δs and δt are the relative nugget displacements along the *s*- and *t*-axes. The total energy absorption values were calculated using Equation (12).

$$E_{total} = E^{\delta s} + E^{\delta t} \tag{4.4}$$

Using this approach, the energy associated with the deformation of the weld itself can be calculated without introducing the previously mentioned energy dissipation associated with slippage of the grips and the test frame elastic energy. E_{total}, $E^{\delta s}$, and $E^{\delta t}$ values are reported as the summation of dissipated energy up to peak ($E_{up}, E_{up}^{\delta s}, E_{up}^{\delta t}$), and after peak ($E_{ap}, E_{ap}^{\delta s}, E_{ap}^{\delta t}$) of their corresponding curves. Figure 4.6 summarizes the steps taken to calculate the total energy absorption value (E_{total}) of a spot weld from the measured KS-II data. The data shown in the figure corresponds to that acquired for a 3G-980 spot weld at a 30° loading orientation. This procedure was followed for all the reported absorbed energy data in this study.

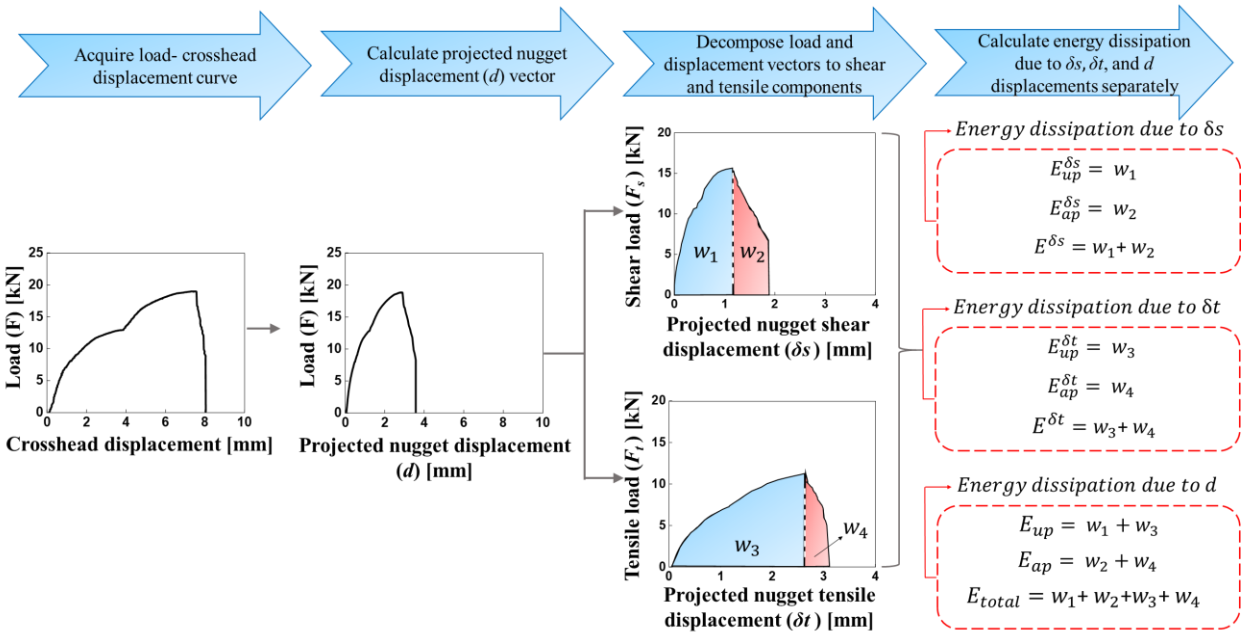


Figure 4.6. Summary of procedure to calculate total energy absorption capability (E_{total}) of a spot weld after performing a KS-II test. The data shown corresponds to a 3G-980 spot weld tested at 30° loading orientation.

The results of the combined loading KS-II tests are presented using the "projected nugget displacement" output from the developed triangular analysis method. The triangulation method projects the global displacements onto a local *s-t* coordinate system that is aligned with the spot weld nugget. The locations of the DIC points tracked by the triangular analysis method (shown in Figure 4.5) were selected to be relatively far away from the spot weld nugget and as close to the fixture as possible to reduce the effect that coupon deformation may have on the tracking. One concern during the extraction of KS-II coupon displacement values was the possible influence of coupon deformation on the extracted C_0 to C_5 displacement measures. To understand whether KS-II coupon deformation affects the recorded displacements, strain values were measured by treating the three vertices on each coupon as a triangular finite element. The calculations revealed negligible strain on the KS-II regions of interest and therefore no meaningful correlation could be established between coupon deformation and its influence on the tracked displacements, supporting the assumption that deformation is limited to the weld region. An example of such strain measurement is shown in Figure 4.7 (a) for the extreme case of a KS-II test at 0° with the highest load-bearing capacity for which the strain level is seen to remain at an average of 1×10^{-5} for ε_{xx} and ε_{yy}, and -1×10^{-5} for ε_{xy}. The same check was repeated for triangular elements of 45°

and 90° loading orientations and even smaller strain components, on the order of $1x10^{-5}$, were calculated (an example of lower strain values is shown in Figure 4.7 (c) for the 45° loading orientation case). Therefore, it was determined that coupon deformation will not have a measurable effect on the coupon DIC tracking. Note that the out-of-plane displacements (in the *r*-direction, perpendicular to both *s*- and *t*-directions) of the tracked DIC points were observed to be an order of magnitude less than the in-plane measurements (*s*- and *t*-directions) for all loading orientations and could also be neglected in the tracking analysis. It is noted that the z-displacement for 0° loading orientation was the highest relative to the other tested orientations and became significantly smaller at tensile-dominated loading orientations.

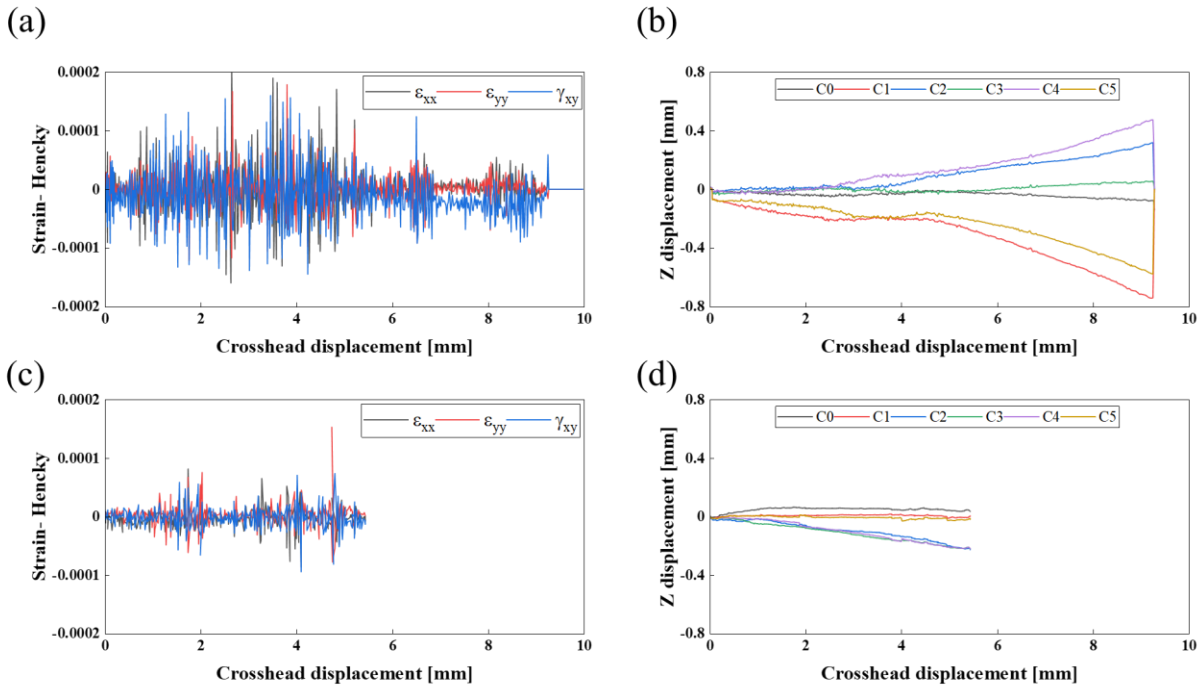


Figure 4.7. (a) and (c) Negligible value of strain components in triangular element C0C1C2 throughout a KS-II test at 0° and 45° loading orientations, respectively. (b) and (d) show the evolution of Z displacement related to points C0-C5 throughout the same KS-II test at 0° and 45° loading orientations. The Z displacement is an order of magnitude smaller than the in-plane displacement.

4.3.5 Fracture Analysis by Interrupted Tests

To assess the fracture initiation sites and propagation paths for different loading orientations, interrupted KS-II tests were performed. In the cases of expected IF, the interrupted specimens were pulled up to approximately 90 percent of the measured failure load for each loading orientation.

For cases in which PO or P-PO was the expected failure mode, the tests were interrupted immediately after reaching the peak-load value. The failure modes (IF, PO, or P-PO) were determined by visual examination of the as-tested samples. It is worth noting that while AWS D8.1M recognizes eight different failure modes associated with RSW, only failure modes 1 (PO), 5 (P-PO), and 7 (IF) from AWS D8.1M failure categories, were observed and reported accordingly in this study.

4.4 Results and Discussions

4.4.1 Spot Weld Loading Histories

Figure 4.8 (a) compares the load-crosshead displacement, and load-projected nugget displacement of a 3G-980 KS-II specimen tested at 45° loading orientation. As illustrated, the load-displacement curve corresponding to the output of the developed triangulation method exhibits lower levels of displacement. The reduced displacement of the load-projected nugget displacement curve is attributed to the reduced influence of slippage, occurring between points c and e, and the minimized effect of coupon displacement at regions away from the nugget on the nugget displacement calculation. To clarify how the developed method accounts for asymmetrical deformation between the two coupon halves, snapshots of the triangles at locations b-f on the load-displacement curve have been plotted in Figure 4.8 (b) to (f). A comparison between the initial and current position of the two coupons at different stages of the test revealed that the deformation between coupon halves is asymmetrical as the test continues. At point c in the load-crosshead displacement curve, a local load drop was measured by the load cell which is a characteristic of coupon slippage. However, it is observed that the slippage does not necessarily result in displacement of the nugget, and therefore, the nugget displacement caused by slippage is minimized in the developed method. Figure 4.8 (c) and (d) illustrate how the slippage resulted in changes in the triangle orientations. Interestingly, between points e and f, almost all the displacement corresponds to the top coupon.

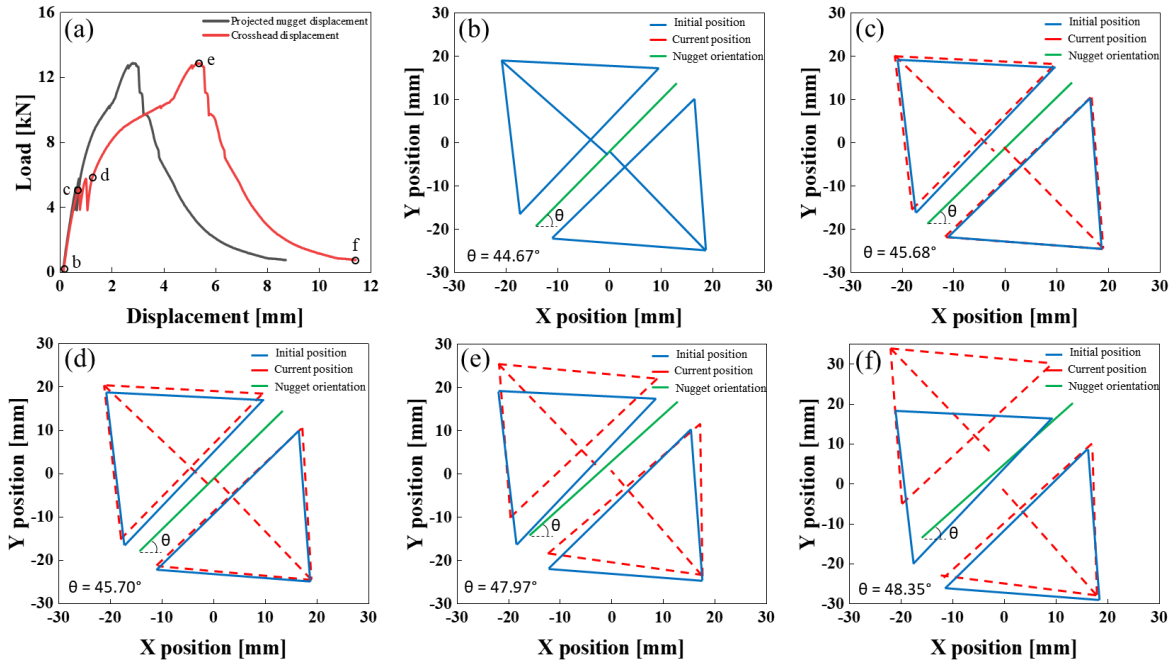


Figure 4.8. (a) Comparison between load-crosshead and load-projected nugget displacement characteristics of a spot-welded 3G-980 KS-II test at 45° loading orientation. (b)-(f) Correspond to the vertices' current locations at points highlighted on the load-crosshead displacement curve in (a).

The effect of KS-II loading orientation on the resultant load-projected nugget displacement response is shown in Figure 4.9 (a) for three selected loading angles: pure shear loading (0°), an equal proportion of shear, and tensile components (45°); and pure tensile loading (90°). As can be seen, the load-displacement characteristics are greatly affected by sample orientation. In the case of the 0° tests, sudden failure of the weldments occurs, as evidenced by the sharp decrease in strength after reaching the peak-load value. However, by adding a tensile component to the applied force, more ductile failures were observed, albeit at lower loads. One advantage of the developed triangulation method is the approximation of the nugget orientation, deduced from the instantaneous slope of the line containing the nugget central region at its middle point, as demonstrated for a 3G-980 KS-II test at 45° in Figure 4.8. Changes in the slope of this line throughout the tests imply deviation of the loading path acting on the spot weld from the intended nominal path. Representative loading histories for experimented orientations have been plotted for both materials in Figure 4.9 (b). It is demonstrated that, due to the rotation of the nugget, the ratio between F_s and F_t continuously deviates from the initial ratio, especially within the shear-dominated loading orientations. This deviation is a maximum at 0° loading orientation, with 8°

and 6° rotation on average for 3G-980 and 3G-1180 joints, respectively, and diminishes to less than 0.1° rotation, from the 75° loading orientation and beyond for both steels. Such alterations in loading paths have only been predicted by finite element models in the past, as shown in the studies by Song and Huh [165] and, Burget and Sommer [204].

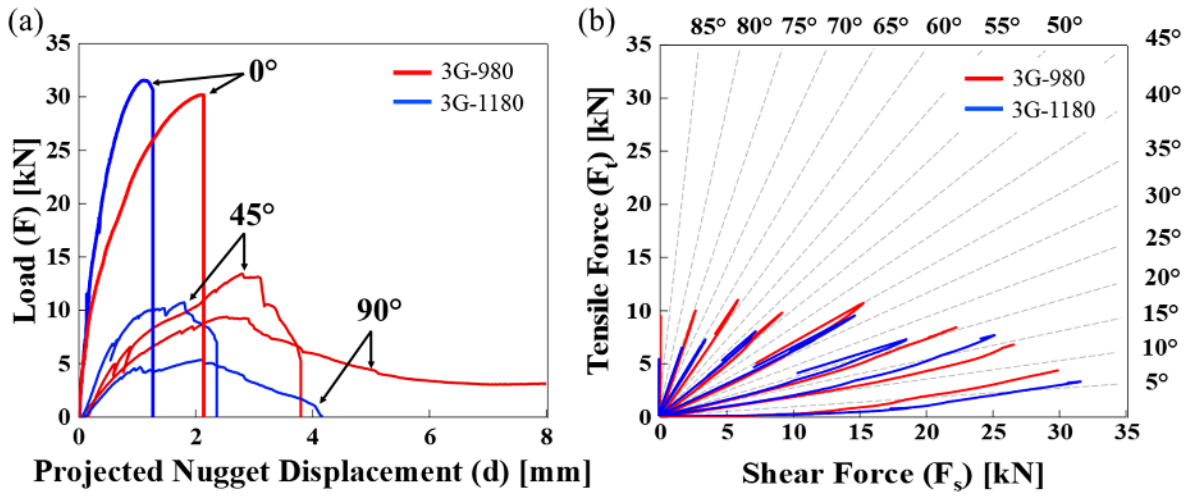


Figure 4.9. (a) Effect of loading orientation on load-projected nugget displacement characteristics of 3G-980 and 3G-1180 resistance spot welds for three selected KS-II tests; (b) loading path acting on the spot welds at various loading orientations.

4.4.2 Failure Modes

Figure 4.10 outlines the final failure modes observed during the KS-II mechanical tests at different orientations for both investigated steels. While the 3G-980 steel does not exhibit a P-PO failure until the 30° orientation, a loading orientation of 10° was enough to promote this type of failure for the 3G-1180 steel. Moreover, the 3G-980 spot welds maintain a high plug ratio (plug ratio > 0.75), measured as shown schematically in Figure 4.11 (a), for all the cases after 30° loading orientation. However, not only were the 3G-1180 welds not able to form full nugget PO or P-PO failures with as high plug ratios, but their plug ratio values declined noticeably by increasing the KS-II loading angle (Figure 4.11 (b)). The decreasing trend in the plug ratio of 3G-1180 resistance spot welds at loading angles after 45° is evident in Figure 4.10 as well in which the ratio of average PO diameter over average FZ diameter declines as loading orientation increases.

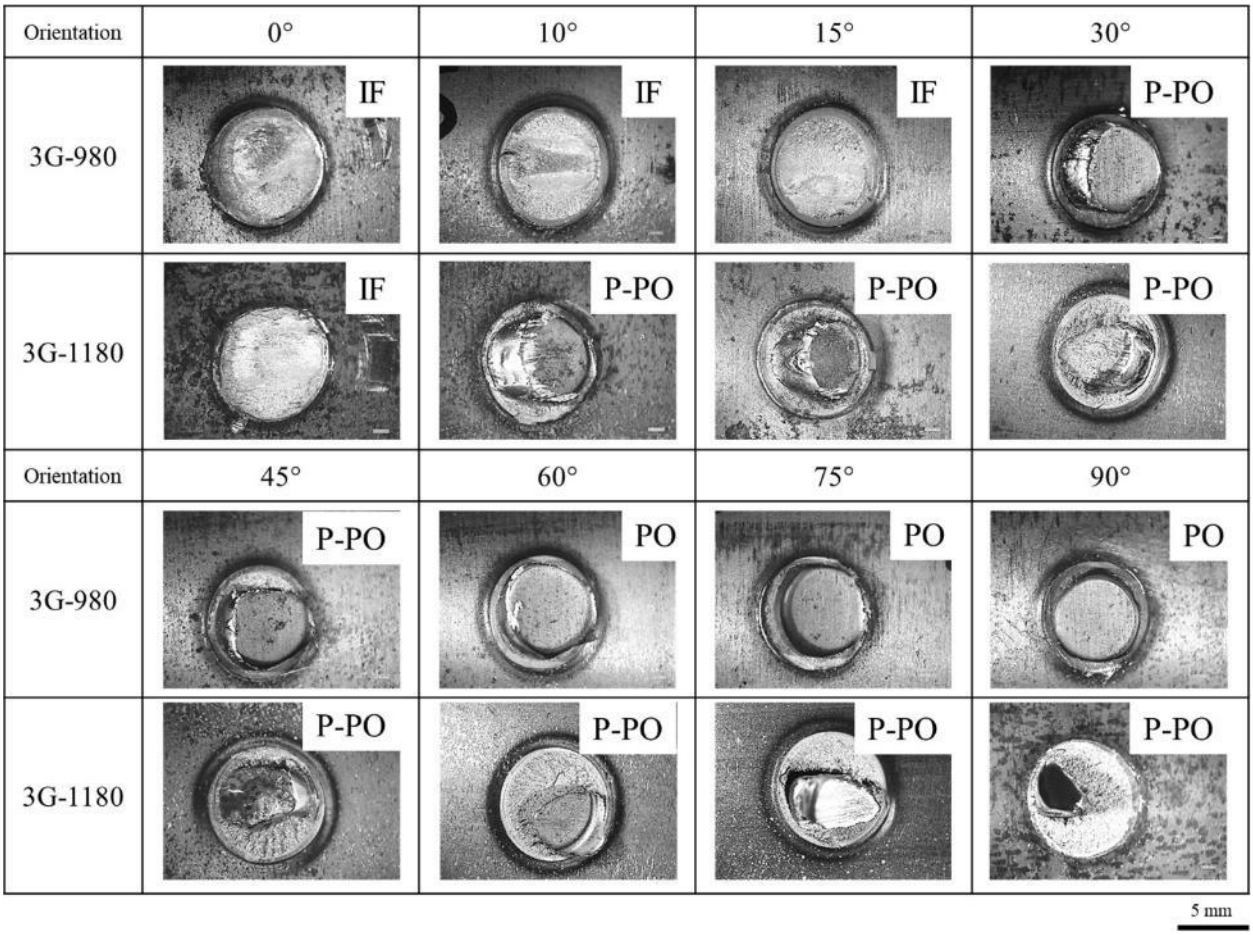


Figure 4.10. Effect of loading orientation on the final fracture surface of 3G-980 and 3G-1180 resistance spot welds after KS-II tests at different loading orientations.

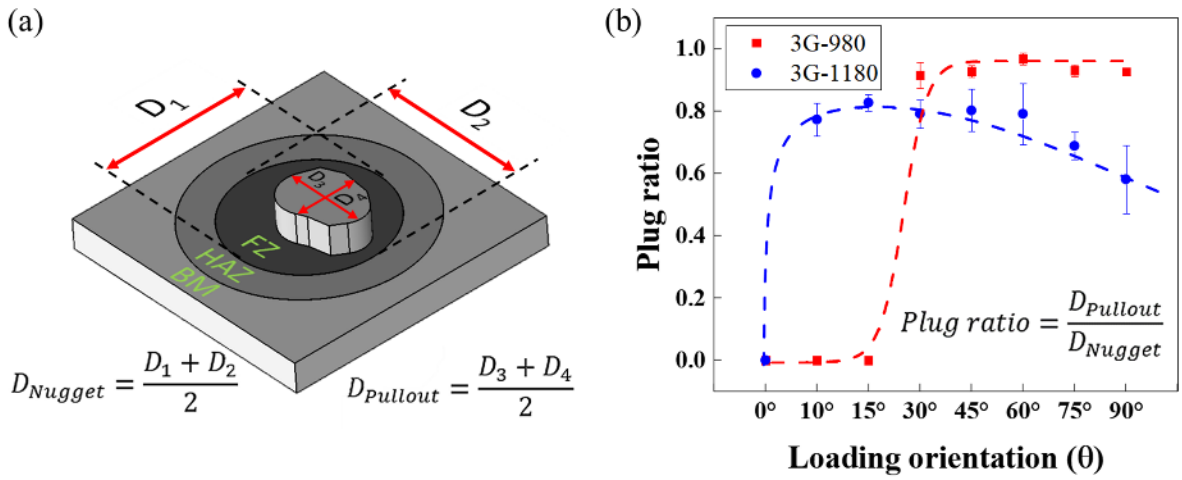


Figure 4.11. (a) Schematic illustration of a partial pullout failure surface along with the average measurements of the nugget diameter (D_{Nugget}) and pullout diameter ($D_{Pullout}$), (b) changes of plug ratio during different loading orientations of KS-II tests.

4.4.3 Failure Path Characterization by Interrupted Tests

Interrupted KS-II mechanical tests were performed at four different loading orientations (0°, 10°, 60°, and 90°) to investigate failure initiation sites, propagation paths, and to explore the mechanism leading to the earlier transition from IF to P-PO failure in 3G-1180 spot welds compared to the 3G-980 spot welds (10° vs 30°, respectively, as shown in Figure 4.10).

The cross-section of the interrupted KS-II specimens tested at the 0° and 10° orientations are shown in Figure 4.12 for both steels. In the case of the 3G-980, strain localization occurs at the notch area, leading to the initiation of cracks that propagated towards the FZ producing IF in both the 0° and 10° loading directions (Figure 4.12 (a) and (g)). The high sustained load at the 0° loading orientation (as shown earlier in Figure 4.12) can be correlated to the IF for both steels which is identified by the propagation of fracture through the FZ. It is well-known that the driving force for this type of failure is the shear stress concentration at the fusion boundary at the sheet/sheet interface (weld notch) and the stress in this region is a function of the nugget area in the sheet/sheet plane as discussed by Pouranvari *et al.* [205]. Therefore, the relatively large nugget formed due to the chosen welding condition (FDWS of 7mm), accompanied by the high hardness value of the fully martensitic FZ, required a high load to promote crack propagation into the FZ and, hence, the high strength of the weldments. As for the 3G-1180 interrupted tests, higher magnification images of 3G-1180 at 0° show the tendency for a PO failure due to the formation and propagation

of the cracks into the SCHAZ (Figure 4.12 (f)). However, the final failure was IF because of the low growth rate of the cracks within the SCHAZ. Comparison between the partially propagated cracks in Figures 15 (e) and (f) indicate the competing nature of IF and PO failure modes as discussed by Dancette *et al.* [206]. The low crack growth rate in the 3G-1180 SCHAZ at the 0° orientation is compensated for by adding the tensile component of force at the 10° loading orientation. As shown in Figure 4.12 (j), the dominant failure mode changed from IF at 0° to P-PO at 10° as the tensile component of force increased. It is clear from Figure 4.12 (d) and (j) that the active failure mode for the 3G-1180 RSW joints at shear-dominated loading angles was dependent on the competition between crack growth rates in two different microstructures: FZ and SCHAZ. Based upon the results of the interrupted tests, while shear stresses at the FZ promoted the IF mode, even a small amount of tensile component during loading was sufficient to change the crack propagation towards the through-thickness direction, leading to P-PO failure at 10° orientation for 3G-1180 spot welds for example. Therefore, a lower magnitude of tensile stress within the SCHAZ was required for through-thickness diversion of the cracks initiated at the notch region in the 3G-1180 spot welds compared to the 3G-980 spot welds.

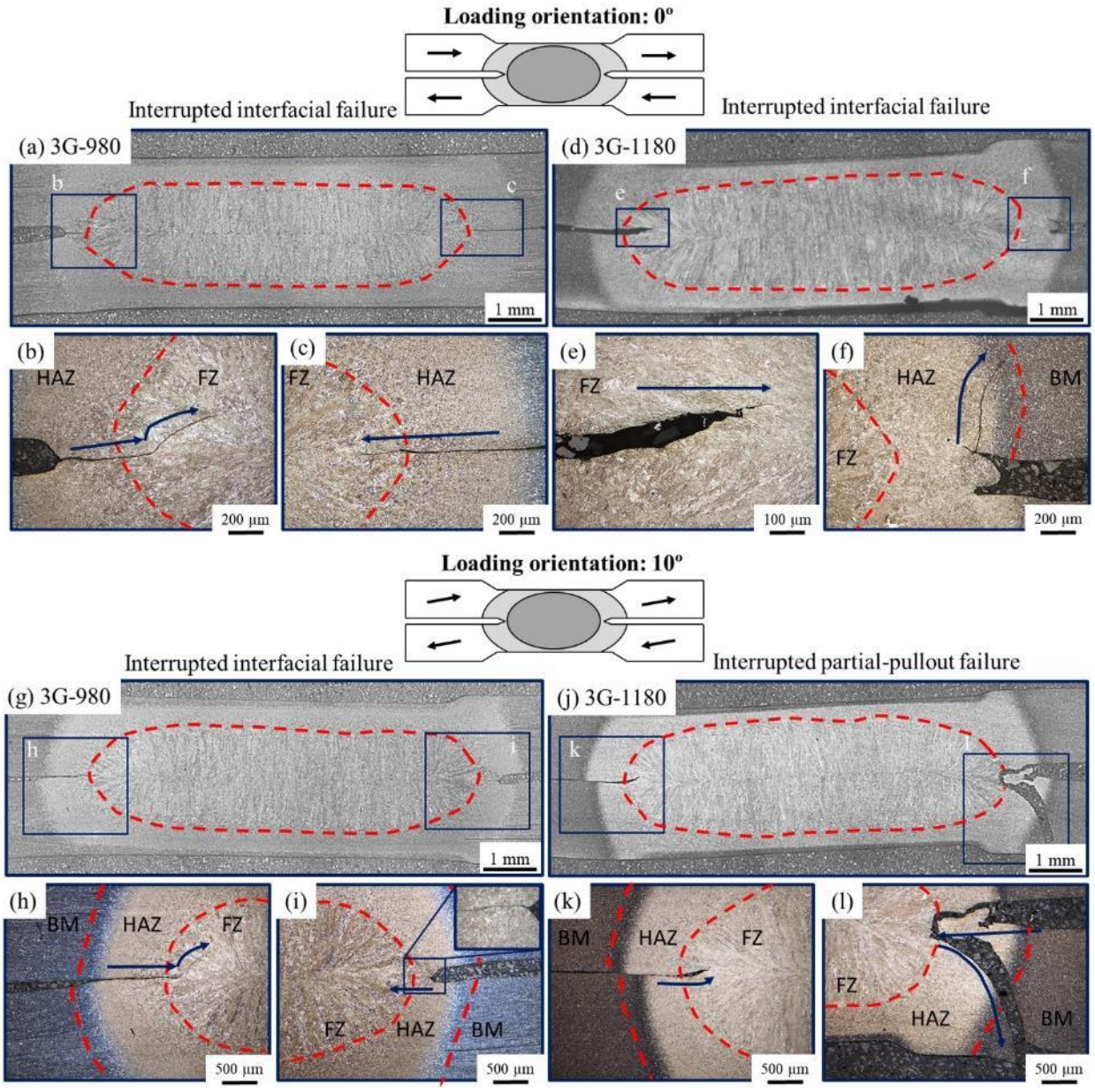


Figure 4.12. (a) and (d) overall macrographs of interrupted KS-II tests for 3G-980 and 3G-1180 tested at 0° loading orientation; (g) and (j) overall macrographs of interrupted KS-II tests for 3G-980 and 3G-1180 tested at 10° loading orientation. Other images show the magnified micrographs of the highlighted regions within the macrographs.

As the loading angle increased in the interrupted KS-II tests (60° and 90°), the failure mode of 3G-980 RSW weldments changed to P-PO and then full nugget PO (Figure 4.13 (a) and (g)). The cracks initiated from the notch region and either propagated slightly into the FZ or immediately up to the sheet/sheet interface due to the dominant tensile component of the force in these orientations. The notch region has been extensively reported as a geometrically favorable

location for failure initiation of ultra high strength steels [52]. Therefore, the microstructure immediately in front of the notch area will have a decisive influence on the propagation of the cracks that are formed. The reason for early through-thickness crack propagation can be elucidated based on the hardness maps provided in Figure 3.12. The maps reveal higher hardness at the UCHAZ and FZ boundary region of 3G-980 spot welds as compared with the FZ interior which accounts for the lower resistance to crack propagation leading to high plug ratios in tensile-dominated loading conditions. Recently, Song *et al.* reported electrode collapse as the reason for the higher cooling rate in the FZ boundary and UCHAZ region [187]. The occurrence of P or S segregation at the FZ boundary has also been reported as the mechanism responsible for the higher hardness of the FZ boundary for 3G-AHSS spot welds [79]. As failure continued, the emerging cracks on the surface grew around the nugget leading to P-PO and PO failures with high plug ratios in tensile-dominated loading conditions. As for 3G-1180, the same decreasing trend in plug ratio, as shown earlier in Figure 4.11 (b), was observed during the interrupted mechanical tests at orientations where tensile forces were dominating. The lower plug ratio of 3G-1180 at KS-II orientations from 45° to 90°, implies that, following initiation, the propagation of cracks towards the hard and brittle FZ was more energetically favorable compared to strain localization in the softened SCHAZ.

The higher tendency of the initiated cracks to propagate into the FZ of the 3G-1180 welds, as shown in Figure 4.13 (d) and (j), could be related to the lower fracture toughness of the region immediately in front of the notch region and less pronounced strength difference between the FZ and BM of the 3G-1180 weldments compared to the 3G-980 welds. In-depth characterization of fracture toughness for the FZ of 3G-AHSS has been the focus of a recent study by Chabok *et al.* [144]. It is also noted that the martensite formed in the FZ of the 3G-980 and 3G-1180 welds can exhibit different characteristics based on the initial chemical composition of the as-received steels, especially C, Mn, and Si content which are discussed in more details in Chapter 6. Upon propagation of the cracks into the FZ, the tendency for through-thickness propagation still existed as shown by the diversion of the cracks from within the FZ towards the faying surface.

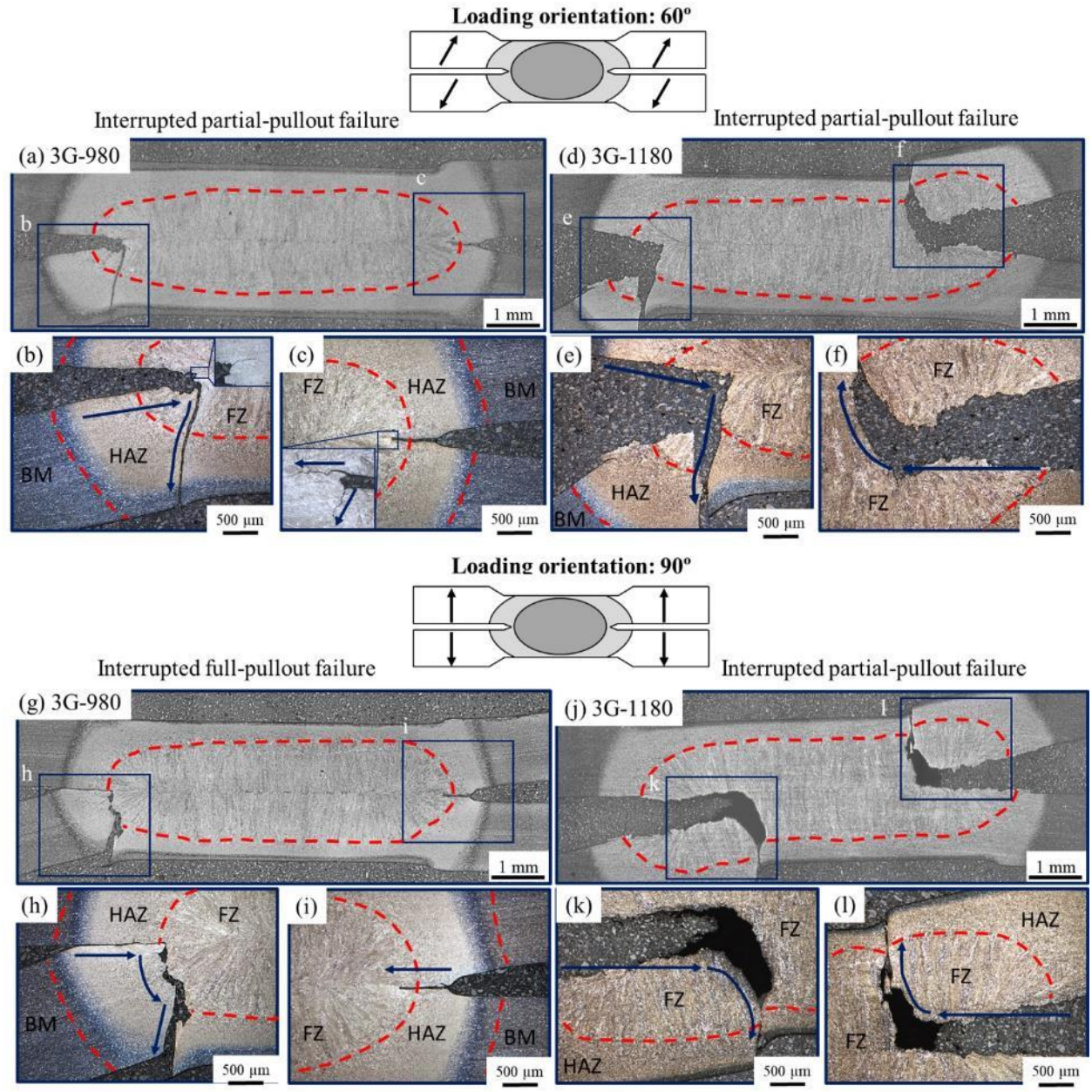


Figure 4.13. (a) and (d) overall macrographs of interrupted KS-II tests for 3G-980 and 3G-1180 tested at 60° loading orientation; (g) and (j) overall macrographs of interrupted KS-II tests for 3G-980 and 3G-1180 tested at 90° loading orientation. Other images show the magnified micrographs of the highlighted regions within the macrographs.

Overall, a comparison of the interrupted mechanical test results reveals that in the cases of the 3G-1180 RSW joints, active competition between crack propagation towards the FZ and/or the softened SCHAZ dictated the dominant failure mode at orientations for which shear forces were dominating (Figure 4.12 (d) and (j)). On the other hand, a consistent propagation of formed cracks

into the FZ, rather than the softened zone, was noted in orientations with the dominant tensile loading component (Figure 4.13 (d) and (j)). These observations indicated that the softened HAZ in the SCHAZ of 3G-1180 RSW joints did not influence failure initiation at loading angles for which tensile forces were dominant. As for the 3G-980 weldments, IF occurred until 15° loading orientation (Figure 4.12 (a) and (g)), and thereafter, a consistent PO or P-PO with a high plug ratio was noted throughout the rest of KS-II orientations (4.12 (a) and (g)). Therefore, it can be stated that the interrupted tests reveal a higher susceptibility for the FZ of 3G-1180 to crack propagation during KS-II tests with dominant tensile loading orientation compared to the FZ of 3G-980. This observation could be attributed to the differences in morphology of the formed martensite within the two FZs which is discussed in more detail in Chapter 6.

4.4.4 Energy Absorption Capability

The effect of loading orientation during the KS-II tests on E_{total} of the 3G-980 and 3G-1180 spot welds is shown in Figure 4.14 (a) and (b) respectively. To facilitate the correlation of E_{total} with the previously discussed failure characteristics, the failure modes in each loading orientation are included. As can be seen in Figure 4.14, E_{up} decreases as the loading orientation angle increases from 0° to 90° for welds in both steels. The decreasing trend of E_{up} can be related to the decreasing RSW strength as the loading angle approaches 90°. Throughout all the tested orientations, the 3G-980 spot welds exhibited higher E_{up} (*i.e.*, before failure initiation).

In contrast to the changes in E_{up} in Figure 4.14 (a) and (b), the value of E_{ap} increases as a function of loading orientation for welds in both steels. Such an observation indicates a higher tendency for rotation and deformation of the material surrounding the nugget as the tensile component of the force increases. As can also be seen, an extremely limited capacity in E_{ap} was evident for both steels at low angle loading orientations, especially from 0° to 15° orientations denoting limited post-failure plastic deformation. Interestingly, at the higher loading angles of 75° and 90°, the post-failure energy absorption (E_{ap}) exceeded the E_{up}, which supports the assertion by Tolton [126] and O'Keeffe [125] that it is important to account for energy dissipation during unloading in the numerical simulation of spot welds.

While the same overall trends are observed for the E_{up} and E_{ap} for both steels, two rather different trends are noticeable in terms of E_{total} (grey bar charts in Figure 4.14 (a) and (b)), between the two investigated spot welds. A decreasing trend in E_{total} was observed for the 0° to

15° orientations for the 3G-980 spot welds. This observation can be correlated to the IF mode of the 3G-980 weldments that were reported earlier within this region. Therefore, it appears that the addition of the tensile component of the applied force negatively influenced the energy absorption capability of weldments that failed in an IF mode. The added tensile component made it easier for cracks that initiated during loading to propagate through the epitaxial structure of the FZ. However, the magnitude of the tensile component was not high enough to promote P-PO or PO failure by strain localization within the BM or the hardened SCHAZ of 3G-980 spot welds. Thereafter, the declining trend of 3G-980 E_{total} until 15° altered as the failure mode changed to the P-PO and PO mode for which the E_{total} increased smoothly throughout the rest of the loading orientations (30° to 90°). This observation can be attributed to the PO or P-PO failure modes of the 3G-980 weldments for loading orientations of 30° to 90° with a slight increase in plug ratio.

As for the 3G-1180 spot welds, a declining trend was observed for the E_{total} as the loading angle increased up to 90° (Figure 4.14 (b)). Interestingly, the highest E_{total} was observed for the IF at 0° loading orientation. Thereafter, the P-PO failures with a relatively high plug ratio (specifically 10°, 15°, and 30° loading orientations) also exhibited E_{total} values close to that of IF mode. However, a reduction in E_{total} was noted as the plug ratio of the P-PO weldments decreased (45° to 90° loading orientations). Although the increase of E_{ap} was able to compensate for the loss in E_{up} for 3G-980 steel as the loading orientation increased, this was not the case for the 3G-1180 steel. This observation indicates that IF of the 3G-1180 spot welds should not always be considered an inferior failure and that IF could be advantageous since this failure mode resulted in 20% to 35% higher E_{total} than the P-PO failure modes. Therefore, based on the presented results in Figure 4.14 (a) and (b), while PO and P-PO failures with high plug ratios resulted in a comparable total energy absorption capability as with the IFs, the P-PO failures with relatively low plug ratios were found detrimental to the energy absorption capability of 3G-AHSS RSW weldments in KS-II mechanical test. Reduction in E_{total} of 3G-1180 spot welds can be attributed to their inability to form a full nugget PO failure mode in the KS-II testing geometry.

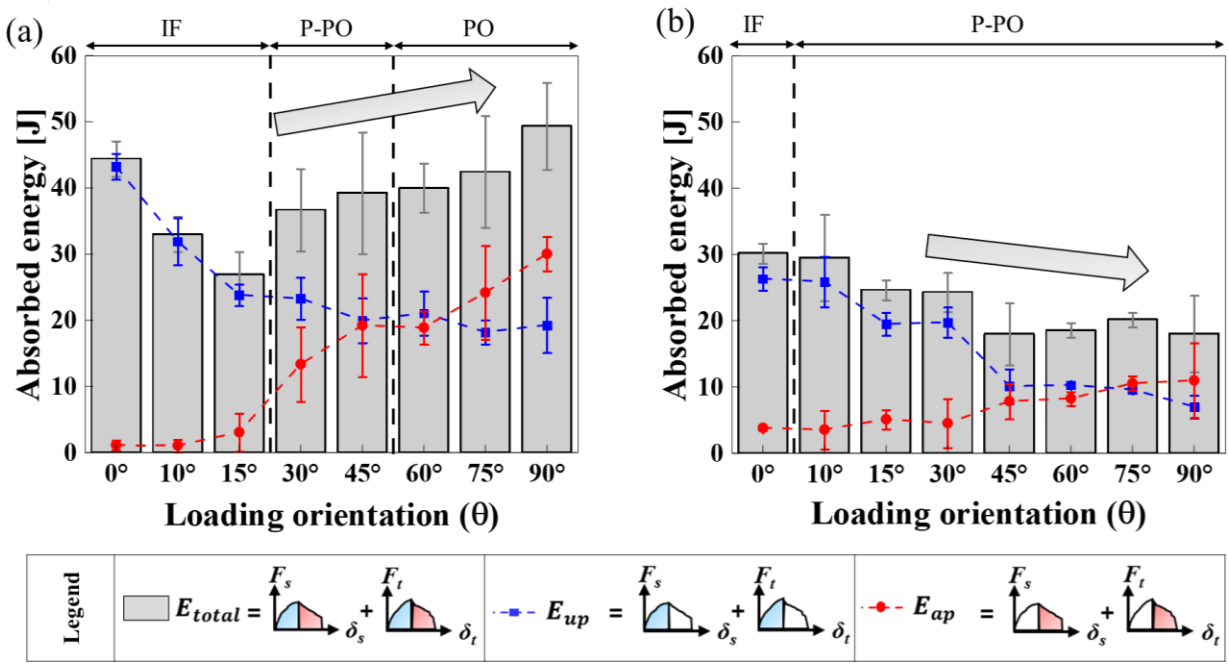


Figure 4.14. The effect of loading orientation on total energy absorption capability (E_{total}) of (a) 3G-980, and (b) 3G-1180 resistance spot welds during KS-II tests.

The E_{total} of the spot welds, plotted in Figure 4.14, can be presented as the summation of $E^{\delta s}$, and $E^{\delta t}$ which have been plotted for both materials and all experimented orientations in Figure 4.15 and Figure 4.16 respectively. As expected, $E^{\delta s}$ decreased while $E^{\delta t}$ increased as the loading orientation approached 90° for both materials. Moreover, the rotation of the coupons during the tests changed the proportion between energy dissipation due to shear and tensile deformation of the coupon from its initial ratio at the beginning of the tests, particularly for lower loading orientations. For example, at 45° loading orientation, where $E^{\delta s}$ and $E^{\delta t}$ should theoretically be equal, a higher contribution of $E^{\delta t}$ was noticed for both steels. Interestingly, it appears that the earlier transition of crack propagation path in 3G-1180 RSW compared to 3G-980 has resulted in a sudden increase in total $E^{\delta t}$ value between 0° to 10° loading orientations. A comparison of Figure 4.16 (a) and (b) can further clarify the decreasing trend of 3G-1180 E_{total} in Figure 4.14 (b). The incapability of 3G-1180 RSW in withstanding deformation of the nugget in the tensile direction can be elucidated by the virtually stagnated value of $E^{\delta t}$ from 10° loading orientation onwards (Figure 4.16 (b)). Propagation of the formed cracks during tensile-dominated mechanical tests into the brittle FZ of 3G-1180 spot welds resulted in a less ductile post-failure response of the weldment, and hence decreasing trend in 3G-1180 E_{total}. Whereas for the 3G-980

spot welds, propagation of the cracks around the nugget periphery led to a much higher $E_{ap}^{\delta t}$ in Figure 4.16 (a), and hence, increasing trend of 3G-980 E_{total} in Figure 4.14 (a).

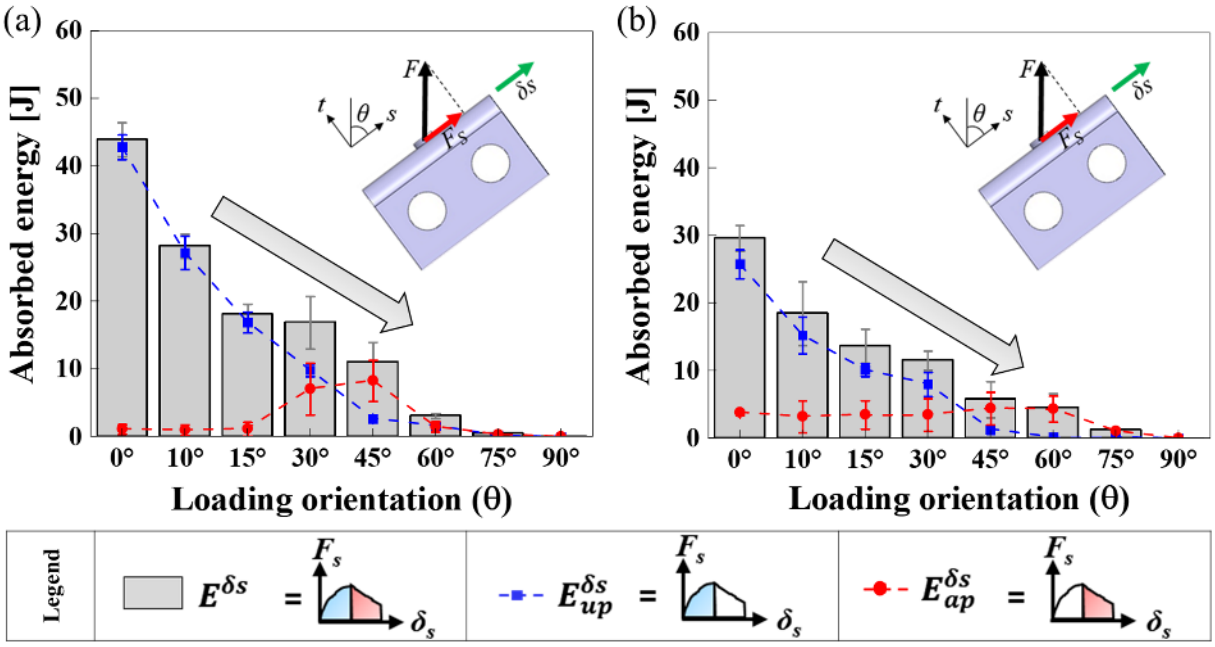


Figure 4.15. The effect of loading orientation on energy absorption capability due to shear displacement of projected nugget ($E^{\delta s}$) for (a) 3G-980, and (b) 3G-1180 resistance spot welds during KS-II tests.

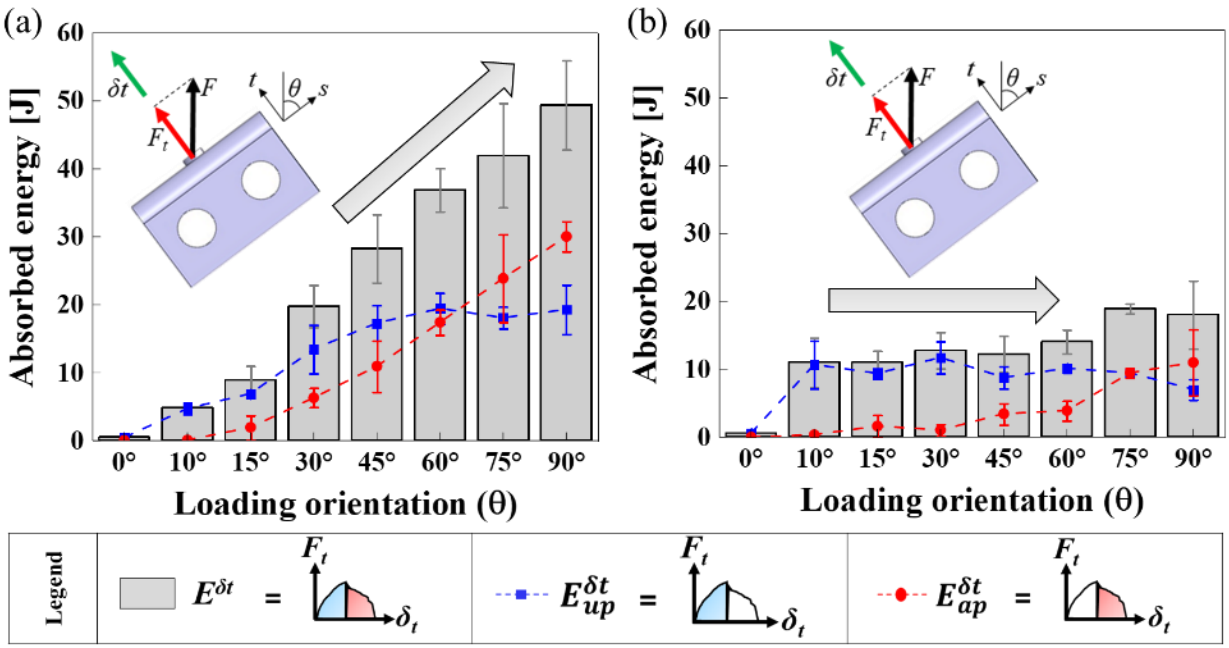


Figure 4.16. The effect of loading orientation on energy absorption capability due to tensile displacement of projected nugget ($E^{\delta t}$) for (a) 3G-980, and (b) 3G-1180 resistance spot welds during KS-II tests.

4.4.5 Comparison of KS-II with TS and CT tests

Industry-standard TS and CT experiments were performed on spot-welded connections of the two investigated base materials according to AWS D8.9 instructions, as outlined earlier in section 3.4.2. The results of these experiments are compared to the current KS-II experiments at 0° and 90° loading orientations, the corresponding load orientations, to contrast the measures of spot weld performance. Figure 4.17 (a) and (b) show the acquired load-displacement curves from the KS-II 0° and TS tests for the 3G-980 and 3G-1180 joints, respectively. Three load-displacement curves are plotted for the KS-II tests, including the load-crosshead response from the test frame, load-C0 displacement (location of point C0 was shown in Figure 4.5 (a)), as well as the load-projected nugget displacement. The crosshead displacements are much higher, which is attributed to the test frame compliance and, more significantly, the slippage of KS-II coupons within the gripped region by the knurled inserts. The vertical displacement of point C0 and crosshead match quite well which demonstrates that the crosshead displacement is dominated by the coupon displacement due to slip/rotation and does not necessarily represent the deformation of the spot weld. Interestingly, the local load-projected nugget displacement response is very close to that measured in the TS experiment, lending credence to the DIC-based measure of nugget displacement introduced in this work. The difference within the unloading regimes of the TS and KS-II at 0° loading orientation is related to the difference in the failure modes. The occurrence of PO or P-PO failures within shear-dominated loading orientations of the KS-II tests requires sufficient development of tensile stresses in the through-thickness direction around the nugget periphery. The higher rigidity and stiffness of the KS-II coupons and the utilized fixturing, compared to TS coupons, did not allow enough rotation for the rapid development of such tensile stresses (as shown earlier in Figure 4.12 (f)). Therefore, IF was observed at KS-II 0° loading orientation. On the other hand, the TS coupon did not constrain the joint as much which led to higher coupon and spot weld rotation and hence, PO failure with an elongated unloading tail of the load-displacement curve.

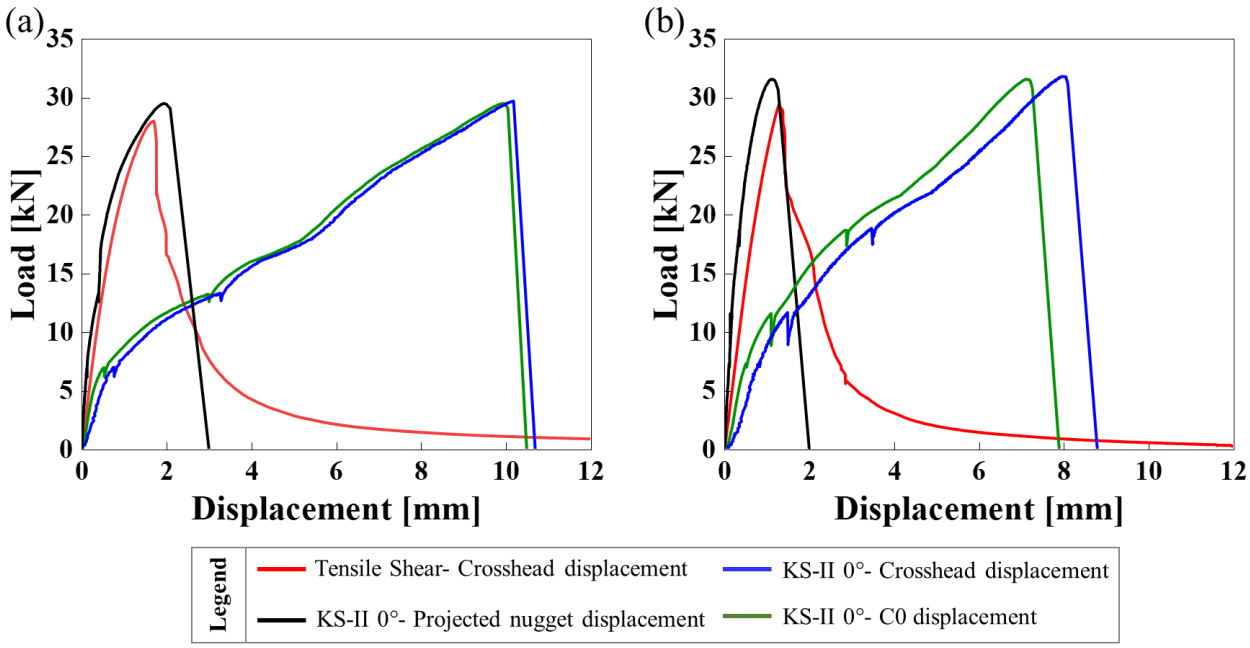


Figure 4.17. Comparison between load-displacement responses of tensile shear and KS-II tests at 0° loading orientation for (a) 3G-980 and (b) 3G-1180 resistance spot welds.

Figure 4.18 (a) and (b) show the measured load-displacement data from the KS-II 90° and cross-tension tests for the 3G-980 and 3G-1180 spot welds, respectively. The load-crosshead displacement and load-projected nugget displacement for the KS-II 90° tests are in close agreement, largely since there was very little slippage at this loading orientation. As shown in Figure 4.18 (a), a minor slippage has been recorded by the load cell at the beginning of the KS-II 90° load-crosshead displacement curve. The DIC footage revealed that this slippage did not occur at the coupon level. It is believed that this slippage is related to the pin connecting the KS-II fixture to the tensile frame not being fully engaged at the beginning of the test. The load-projected nugget displacement curve shows that the developed method was able to effectively eliminate the influence of such sources of slippage as well. The KS-II 90° response is seen to be much stiffer than the cross-tension experiment. The larger compliance in the cross-tension experiment can be attributed to the long arms used to grip the cross-tension weldment such that much of the displacement is due to bending of the BM whereas the KS-II specimen was more constrained, not allowing for as much BM deformation. It is noteworthy that the discrepancy between displacement values acquired from the crosshead and projected nugget of KS-II tests was most noticeable at shear-dominated loading orientations, with the most severe slippage, and this discrepancy reduced

continuously as loading orientation approached tensile-dominated orientations with negligible slippage.

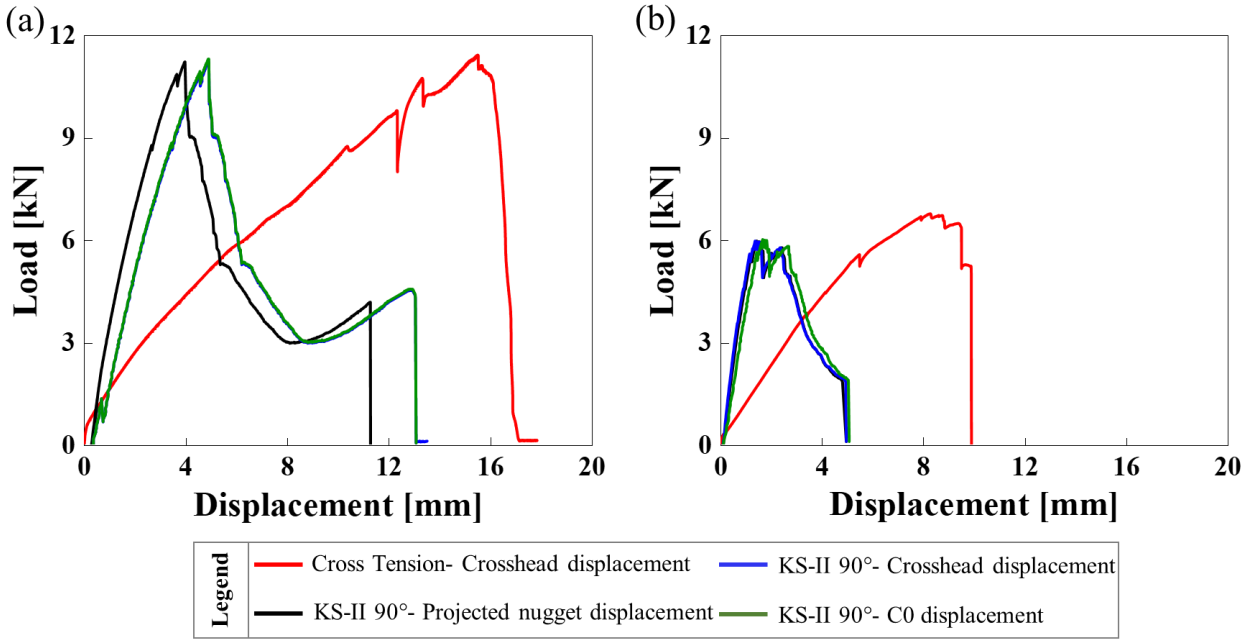


Figure 4.18. Comparison between load-displacement responses of cross-tension and KS-II tests at 90° loading orientation for (a) 3G-980 and (b) 3G-1180 resistance spot welds.

Comparison of the peak-loads from the two sets of experiments shows good agreement between the peak-loads for the corresponding load orientations. The peak-loads in the KS-II 0° experiments were within 3% and 4% of the corresponding TS strength values for 3G-980 and 3G-1180 on average. In addition, the peak-loads in the KS-II 90° experiments were, on average, within 5% and 9% of the peak-loads in the cross-tension experiments for 3G-980 and 3G-1180, respectively. Thus, despite the significant differences in compliance between the various experiments, the failure loads were in good accord. The absorbed energy in the experiments is typically calculated as the integral of the crosshead load- displacement. Rather than using this global response, a better measure of energy absorbed by the weld, as opposed to the surrounding parent metal or test frame or dissipated through slippage in the grip, can be obtained using the local displacement measure (the projected nugget displacement) introduced in the current work.

4.5 Summary

Mechanical properties and failure behavior of RSW joints from two grades of 3G-AHSS, namely 3G-980 and 3G-1180, were characterized by performing combined/mixed loading KS-II mechanical tests. DIC analysis revealed that there was a non-negligible level of coupon rotation

and slippage within the KS-II testing fixture, most notably for tests within the shear-dominated loading orientations. To obtain a more precise quantification of spot weld performance indices, a novel triangulation method, coupled with DIC-based imaging was proposed. The proposed procedure calculates the relative displacement of two projected points between the two KS-II coupon halves, representing the displacement of nugget center points throughout the tests.

The developed technique for projected nugget displacement provided three advantages. First, quantification of the instantaneous ratio between shear and tensile loads throughout the tests resulted in the more accurate calibration of a force-based failure criterion. Typically, the nominal ratio between shear and tensile components of force, at the beginning of the tests, is used for finding failure strengths at different orientations, whereas the developed procedure accounts for the actual orientation of the nugget at the failure point. Second, it was shown that local calculation of the energy absorbed by a joint during a KS-II test based on the integral of the load versus projected nugget displacement provides a better quantification of the energy dissipated by the weld region, as opposed to energy calculation based on the integral of the load versus crosshead displacement. The latter includes energy dissipated by the frame compliance, base metal deformation at regions away from the weld, and slippage within the grip. Lastly, the proposed method provided the possibility of calculating the energy dissipation by deformation of the nugget in the shear and tensile directions independently.

A comprehensive correlation between failure behavior and mechanical performance of the spot welds was provided for different load orientations. The 3G-1180 spot welds exhibited an earlier transition from IF to P-PO compared to the 3G-980 spot welds as the loading orientation increased (10° vs 30°). The earlier transition in dominant failure mode for the 3G-1180 spot welds was attributed to the existence of a softened region in the SCHAZ which facilitated the propagation of the cracks (following initiation at the weld notch) towards the through-thickness direction.

As the loading orientation approached 90°, corresponding to pure tensile loading, the E_{total} of 3G-980 spot welds exhibited an increasing trend, whereas E_{total} declined for 3G-1180 joints. The lower E_{total} of the 3G-1180 spot welds, specifically within tensile-dominated loading orientations, was related to their inability to form a full nugget PO failure mode and the tendency of the formed cracks to propagate into the FZ leading to P-PO failures with low plug ratios. It was observed that propagation of the cracks into the FZ of the 3G-1180 spot welds limited their capability to absorb

energy by deforming in the tensile direction. In contrast, propagation of the cracks around the weld periphery substantially improved the post-failure energy absorption capability of 3G-980 joints, as evidenced by their continuously increasing $E_{ap}^{\delta t}$value from 45° to 90° loading orientation.

5 Experimental Characterization of Load-based Fracture Models for 3G-AHSS Resistance Spot Welds in Shear-tensile and Tensile-bending Loading Conditions[3]

5.1 Overview

Failure of resistance spot welds in computer-aided engineering models can be based upon criteria that incorporate test data obtained in various loading conditions including different proportions of tensile, shear, and moment loads. The decomposition of the critical load into its respective shear, tensile, and bending moment components is influenced by the rigid body motion during their corresponding mechanical tests. Continuous tracking of the weld orientation and the deformed coupons is required to accurately determine the load components at the onset of failure. A comprehensive experimental investigation was performed to characterize the critical failure load components in combined loading using various orientations of KS-II tests and a range of CP coupon geometries. Mechanical testing was coupled with DIC to systematically evaluate empirical force-based failure models for resistance spot welds of two grades of 3G-AHSS with optimal and suboptimal FZ diameters, referred to as FDWS and MWS conditions, respectively. New analysis methodologies using DIC were developed to account for rotation and deformation of the joint in the determination of the shear, normal, and bending moments acting on the spot-welded joints. The CP test results for both steels revealed a non-convex experimental fracture locus in bending-tension loading cases. The conventional assumption of a convex failure locus from Seeger's force-based criteria overestimated the critical bending moment strength between 7% and 66%. Results indicated that changes in the operative failure mechanism from pullout/partial-pullout to interfacial can expand the fracture loci within the shear-tensile loading mixities. Improved alternative functional forms for the weld failure models were proposed and contrasted with conventional models that assume convexity.

[3] This chapter is composed of a published research paper as outlined in the statement of contributions. **M. Shojaee**, Tolton C, Midawi ARH, Zhang T, Ghassemi-Armaki H, Worswick M, Butcher C, Biro E, An experimental methodology to characterize load-based fracture models of third generation advanced high strength steel resistance spot welds, Int. J. Adv. Manuf. Technol. (2024) 1–23. https://doi.org/10.1007/s00170-024-13438-6.

5.2 Background

Resistance spot welds used in automotive body parts are subjected to complex external loading types such as tensile forces, shear forces, bending forces, and their combinations. As explained in section 2.5.3, various force-based fracture criteria considering the aforementioned loading types have been proposed that try to predict the failure of spot welds under complex loading conditions. Load-based fracture models for spot welded joints made of conventional grades of AHSS are typically assessed in shear-tensile loading conditions [115,165]. Virtually no study has focused on calibration of RSW experimental failure loci in tensile-bending loading of spot welds which is characterized by CP mechanical tests.

The geometry adopted in the CP test can significantly affect the results in terms of load-bearing capacity and failure mode by changing the severity of bending [15,113]. The RSW CP test typically involves joining two L-shaped coupons with a spot weld on the horizontal flange region. During this test, the weld is subjected to normal tensile stress and bending stress due to the offset between the loading axis and spot weld. Calibration of the RSW failure loci in bending-dominated loading conditions has received limited attention in the available literature due to challenges in determining bending moment using CP tests. Complexity arises from the opening of the lower arms and the deformation of the unconstrained vertical arms that do not necessarily remain straight throughout the CP test [207]. It is common to idealize the CP test and use a constant moment arm which can overestimate the bending moments, as recently reported by Xu *et al.* [115]. However, with the adoption of DIC, a more rigorous treatment of the CP test can be developed to account for the deformation of the coupon, and better estimate the bending moment, and tensile loads applied to the weld.

RSW failure loci are commonly calibrated in combined shear-tensile loading. Wung [157] proposed the initial form of RSW failure criterion using TS and CT tests. A more advanced form of RSW failure criterion was proposed by Lin *et al*. [162] that accounted for combined shear and tensile test data obtained from KS-II tests. The KS-II test provides a more favorable boundary condition to characterize weld failure due to the constraint imposed upon the weld in contrast to lap shear tests that can have significant rotation. The calibration of RSW failure models in shear-tensile loading typically assumes the orientation of the coupon is fixed even though coupon rotation can be significant in shear-dominated conditions [120,126,158]. Song [165], and Langrand [111] demonstrated how deformation-induced rotations of the weld can lead to major discrepancies

between the measured and predicted failure strengths using Lin's failure criterion [102]. The issue of coupon deformation and rotation was acknowledged by Pandya *et al.* [91] during the combined loading of a 1G-AHSS spot weld using a modified cross-tension fixture that utilized orientation plates to minimize deviation from the intended loading path. Therefore, the construction of a reliable RSW failure locus in shear/tensile loading conditions demands the decomposition of KS-II failure loads into shear and tensile strength components based on the orientation of the nugget at the onset of failure initiation as opposed to the orientation at the start of the test.

In this study, the validity of existing force-based RSW failure models was evaluated by performing CP and KS-II mechanical tests of resistance spot welds under bending-dominated and mixed shear-tensile loading conditions, respectively. Optimized and suboptimal RSW currents were considered to recognize how changing the FZ diameter affects the shape and size of the failure loci. Novel procedures were developed using DIC techniques to improve the characterization of the RSW failure load components by quantifying the orientation of the coupons during the test. The results highlight deficiencies of existing RSW failure models, especially in bending-dominated loading cases where large discrepancies were observed in the shape of the experimental failure locus compared to the convex shape predicted by existing empirical functions. Modified RSW failure functional forms were proposed to accurately predict the failure of 3G-AHSS spot-welded connections in bending-dominated as well as combined shear and tension loading cases.

5.3 Materials and Methods

5.3.1 As-received Materials

The same 3G-980 and 3G-1180 AHSS, as introduced in Chapter 3 was used in this study. More details about the investigated materials can be found in section 3.3.1.

5.3.2 Resistance Spot Welding

RSW was carried out using the same MFDC welder equipped with a Rexroth Bosch weld controller as described earlier in Chapter 3. 7 mm flat Cu-Cr dome-shaped electrodes were used for spot welding throughout this study. The electrodes were continuously cooled via 20°C water with a nominal flow rate of 6 L/min. RSW process parameters were selected based on the recommendations of the AWS D8.9 standard [35] and their values are outlined in Table 5.1. To investigate the influence of nugget size on the size of the failure loci, two different nugget

diameters were produced for each of the investigated materials: an optimized electrode FDWS of 7 mm and a sub-optimal MWS of $4\sqrt{t} \approx 4.7$ mm.

Table 5.1. Resistance spot welding process parameters used in this study.

Material	Squeeze time [ms]	Number of pulses	Weld time for each pulse [ms]	Cool time between pulses [ms]	Hold time [ms]	FDWS Welding current [kA]	MWS Welding current [kA]
3G-980	167	2	167	33	167	9.1	7.0
3G-1180	167	2	167	33	167	9.0	6.9

MWS, minimum weld size ($4\sqrt{t} \approx 4.7$ mm FZ diameter); FDWS, electrode face diameter weld size (≈ 7.0 mm FZ diameter).

RSW cross sections were prepared for OM following conventional metallographic procedures *i.e.*, rough grinding, fine polishing up to 1 μm polishing diamond paste, and etching with 2% Nital solution. A Keyence VHX digital microscope was used for the FZ diameter measurement of different welding schemes.

5.3.3 Digital image correlation

All CP and KS-II mechanical tests were coupled with stereoscopic digital image correlation analysis for accurate tracking of coupon displacement. A random black-and-white speckle pattern was created in regions of interest for tracking the displacement fields. The DIC system was equipped with a pair of GZL-CL-41C6M-C camera models from Point Grey Research with a 0.005 mm/pixel image scale. VIC 3D R9.1 software from Correlated Solutions was used for the post-processing. A subset size, step size, and strain filter size of 21 pixels, 7 pixels, and 5, respectively, were selected. The weighting of subsets was based on the default Gaussian weight option and a 90% center-weighted Gaussian strain filter was used. The VSG [208] was 49 pixels (0.245 mm).

5.3.4 CP tests to characterize combined bending and tensile loading

CP tests were performed to characterize failure in combined bending and normal loading cases. Three CP coupon geometries (shown in Figure 5.1) with different initial bending moment arms were considered to achieve different proportions of applied bending moment and tensile loads on the spot welds. The initial bending moment arm is defined as the distance between the center of sheet thickness at the grip (vertical flange) and the projected center of the FZ along the bottom

arm (initially horizontal flange region of the CP coupon). It is noted that this assumption is expected to underestimate the moment arm length after the peak load as cracks propagate through the weld (IF) or around its periphery during PO failure, for example. CP tests were repeated at least 3 times for each welding schedule and geometry. The respective vertical and horizontal arms of the coupon, *h*, and *d* (as defined in Figure 5.1 (c)) were measured individually prior to each test and the average measurements along with the corresponding 95% confidence intervals are outlined in Table 5.2 for all CP geometries and experimented RSW schemes.

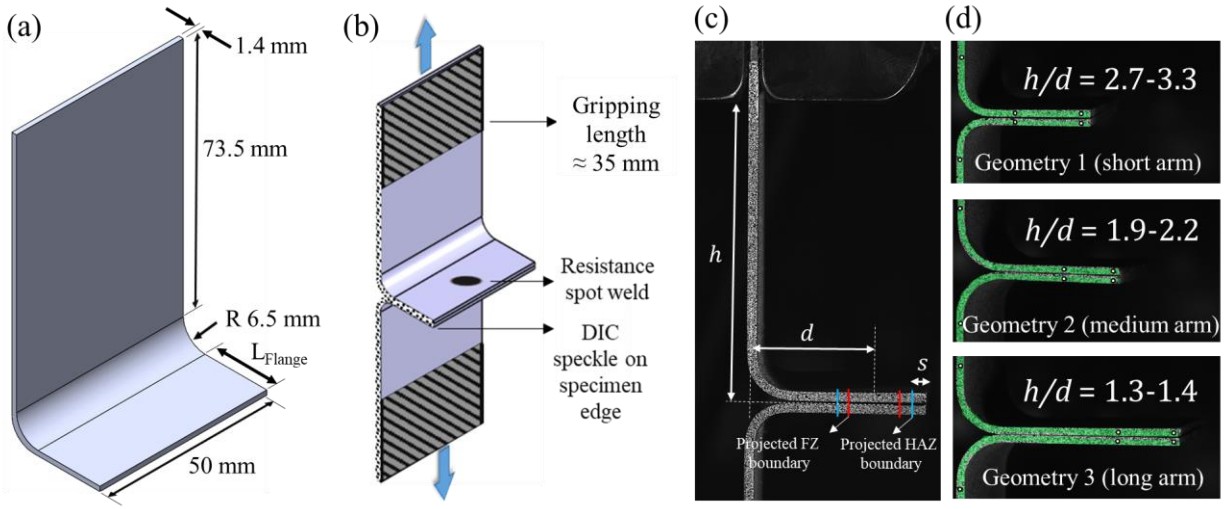


Figure 5.1. Schematic representation of (a) CP coupon geometry and dimensions, (b) welded CP specimen showing the speckled region of interest; (c) "h" is the vertical distance from the grip to the centerline of two sheets; "d" is the horizontal distance from mid-thickness of the sheet at the grip to projected FZ boundary; "s" is the over-hang distance after the spot weld on the horizontal flange; (d) three different CP geometries with various horizontal flange lengths (L_{Flange}) were considered. Dimensions L_{Flange}, h, d, and s are outlined in Table 3 for all three experimented CP geometries.

Table 5.2. Summary of average horizontal flange length (L_{Flange}), initial bending moment arm on the horizontal arm "d", initial bending moment arm on the vertical arm "h", and free over-hang distance (s) for 3 different CP coupon geometries and 4 different welding schemes investigated in this study. Errors are 95% confidence interval values.

Welding condition	**Geometry 1 (short arm)**				**Geometry 2 (medium arm)**				**Geometry 3 (long arm)**			
	L_{Flange} [mm]	d [mm]	h [mm]	s [mm]	L_{Flange} [mm]	d [mm]	h [mm]	s [mm]	L_{Flange} [mm]	d [mm]	h [mm]	s [mm]
3G-980 FDWS	19.5	12.8 ± 1.2	42	6.0 ± 2.1	25	22.1 ± 0.1	42.5	4.5 ± 0.8	32	31.4 ± 0.3	41	4.9 ± 0.9
3G-980 MWS	19.5	15.4 ± 1.2	42	7.2 ± 1.8	25	21.2 ± 0.1	42.5	5.0 ± 0.6	32	31.4 ± 0.5	42	4.5 ± 0.5
3G-1180 FDWS	19.5	13.2 ± 0.8	42.5	6.3 ± 1.5	25	20.4 ± 0.2	42.5	4.6 ± 0.7	32	31.3 ± 0.2	42	4.8 ± 0.7
3G-1180 MWS	19.5	13.4 ± 1.6	42	6.8 ± 1.9	25	19.3 ± 0.2	42.5	5.1 ± 0.3	32	30.4 ± 0.1	42.5	5.0 ± 0.6

In this section, a novel methodology for the CP test is proposed that exploits the DIC measurements to account for the deformation and rotation of the arms that affect the evolution of the bending moment, and tensile loads. As an example, the deformation and rotation of the CP coupons are shown in Figure 5.2 for the 3G-980 FDWS short arm geometry at the initial, peak load, and final frames.

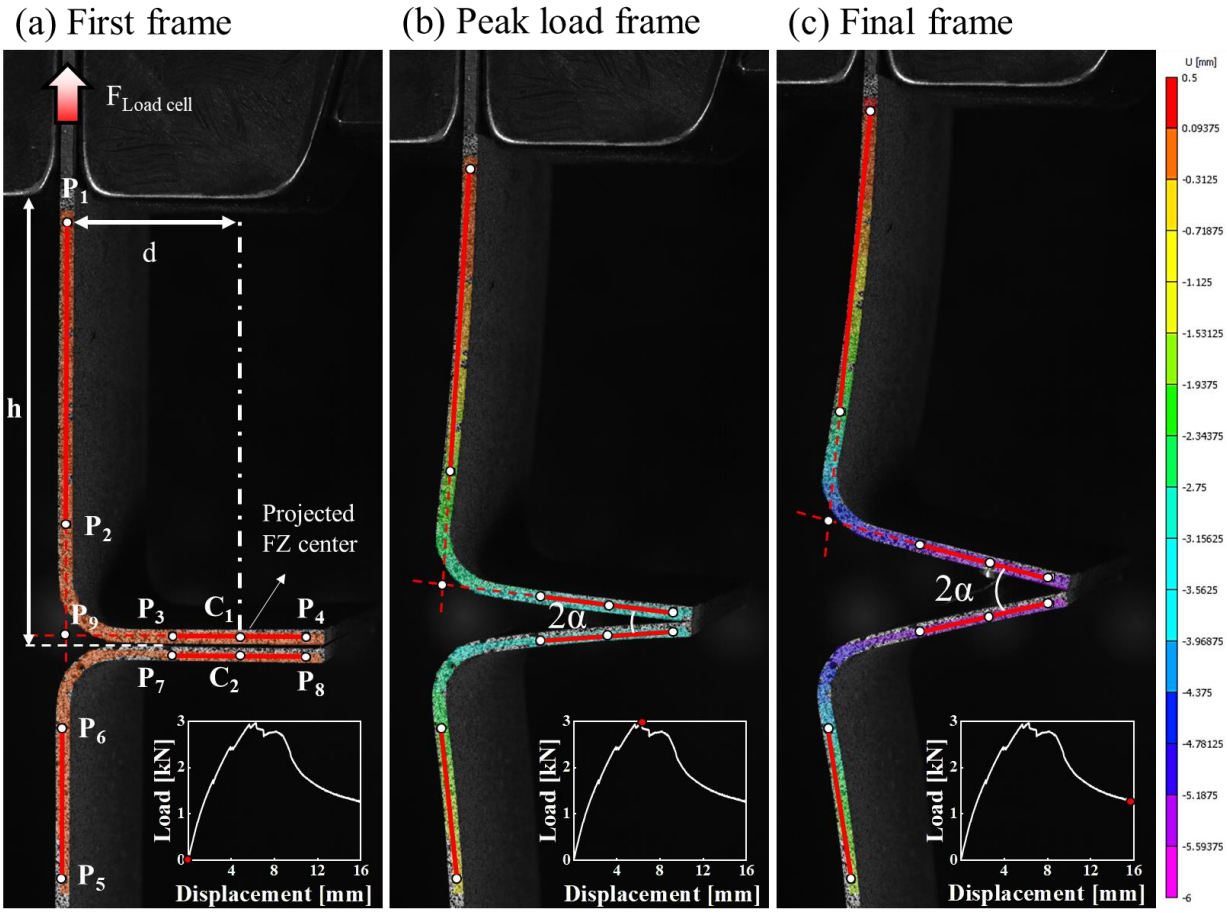


Figure 5.2. Comparison between (a) first, (b) peak load, and (c) final frame of a short arm (geometry 1) 3G-980 FDWS CP test. Figures highlight the deformation of the coupons and the continuous reduction of the effective bending moment arm acting on the projected FZ center throughout the test. The color contour U shows horizontal displacement within the region of interest.

A static equilibrium analysis was conducted on the CP coupons to estimate the evolution of bending moment, and tensile force acting on the RSW throughout the tests. The coupon is assumed to be constructed of four rigid beams defined by eight point inspectors (P_1-P_8) that construct four position vectors $\overrightarrow{p_1p_2}$, $\overrightarrow{p_3p_4}$, $\overrightarrow{p_5p_6}$, and $\overrightarrow{p_7p_8}$. Inspectors P_3, P_4, P_7, and P_8 were placed at the edges of the projected RSW FZ, whereas inspectors C_1 and C_2 were placed at the center of the projected FZ. The intersection of vectors $\overrightarrow{p_1p_2}$ and $\overrightarrow{p_3p_4}$ is referred to as point P_9. A schematic representation of the undeformed and deformed CP coupon, along with the location of point inspectors can be seen in Figure 5.3 (a) and (b), respectively.

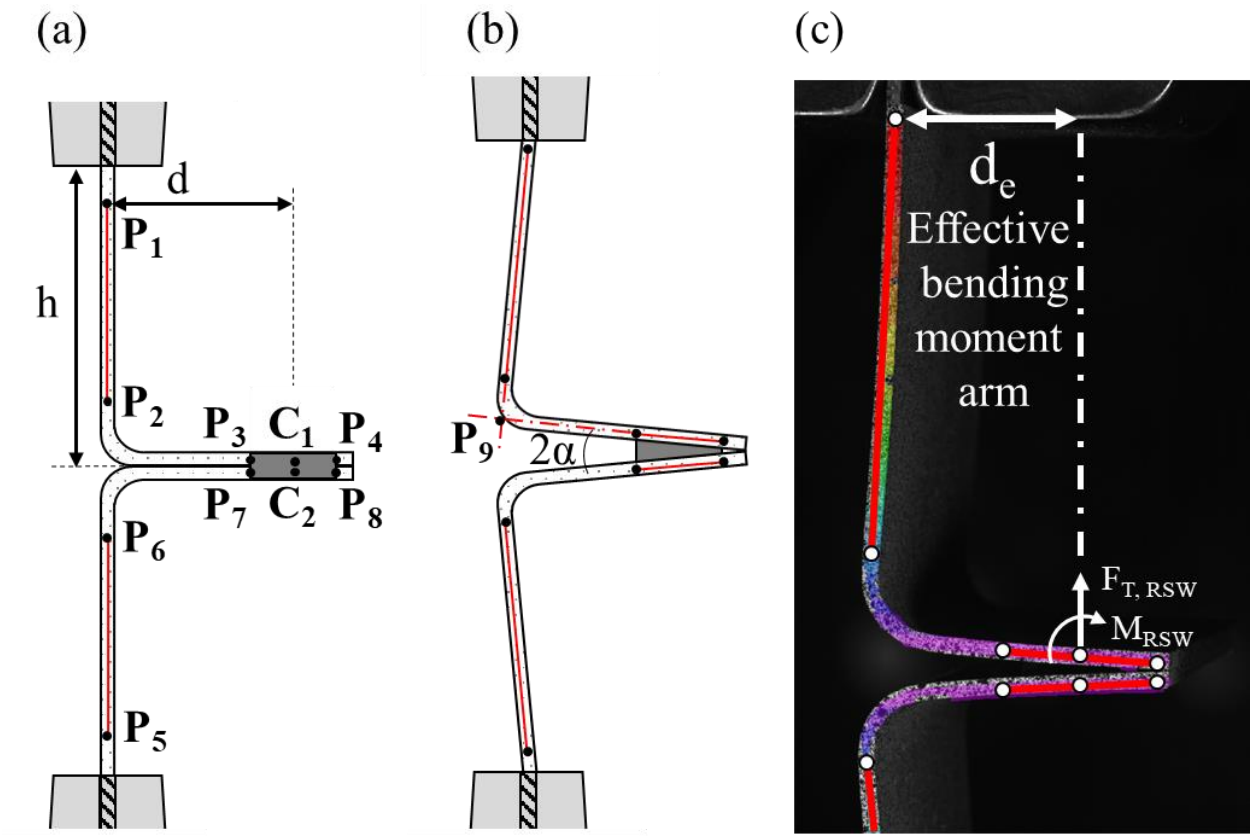


Figure 5.3. Schematic drawing showing the configuration of the CP specimen (a) at the beginning of the test, and (b) n^{th} frame after starting the test. (c) Forces and moments acting at the center of the spot weld.

The total opening angle, 2α, is determined by the dot product:

$$\cos(2\alpha) = \frac{\overrightarrow{p_3p_4} \cdot \overrightarrow{p_7p_8}}{|\overrightarrow{p_3p_4}||\overrightarrow{p_7p_8}|} \tag{5.1}$$

The tensile force applied to the center of the spot weld is equal to the recordings of the vertical load cell ($\vec{F}_{T,RSW} = \vec{F}_{Load\ cell}$). The effective bending moment arm ($\vec{d}_e$) is defined as the instantaneous horizontal distance between inspector P_1 at the mid-thickness of the upper arm at the grip and inspector C_1 located at the projected center of the spot weld. The bending moment imposed upon the weld, $\vec{M}_{RSW}$, can be defined using the tensile force applied to the center of spot weld ($\vec{F}_{T,RSW}$) and the effective moment arm, $\vec{d}_e$:

$$\vec{M}_{RSW} = \vec{d}_e \times \vec{F}_{T,RSW} \tag{5.2}$$

It is noted that any compressive contact between the lower arms due to the overhang distance, *s*, has been ignored. The overhang distance should be minimized with distances between 4.5-7.2 mm in the present study as outlined in Table 5.2.

Representative examples of the evolution of parameters $\vec{d}_e$, α, $\vec{M}_{RSW}$, and $\vec{F}_{T,\,RSW}$ have been summarized for a 3G-980 FDWS and 3G-980 MWS geometry 1 (short arm) CP test. Figure 5.4 (a) illustrates how the effective bending moment arm decreased by 34% and 76% from the beginning of a 3G-980 FDWS short arm CP test up to the peak load, and final frame, respectively. It was observed that the bending arm reduces at a higher rate after the critical peak load point, as highlighted by the steeper slope of the red arrow in Figure 5.4 (a) after the peak load point. The higher reduction rate in the bending moment arm can be correlated with the detachment of an RSW leg during PO failure of the FDWS condition, which facilitates out-of-plane rotation of the nugget during the unloading stage of the test. In the case of the 3G-980 MWS short arm CP test, as shown in Figure *5.4* (c), changes in the effective bending arm were less severe with a 13% reduction until peak load by the end of the test. The alteration in the bending arm is less significant in the MWS condition due to the limited deformation of the coupons prior to full separation in IF mode. The observed trends clearly highlight the need to consider the evolution of the bending moment during CP tests for the accurate generation of fracture models. Alteration of the forces and moments effective on the spot weld for the same 3G-980 FDWS and 3G-980 MWS short arm CP tests are shown in Figure *5.4* (b) and (d), respectively. The corresponding critical bending, and normal force values at the onset of separation, defined by the peak load, were determined for all tests, and the values were used to evaluate the existing RSW failure prediction models in tensile load-bending moment conditions outlined in section 5.4.3.

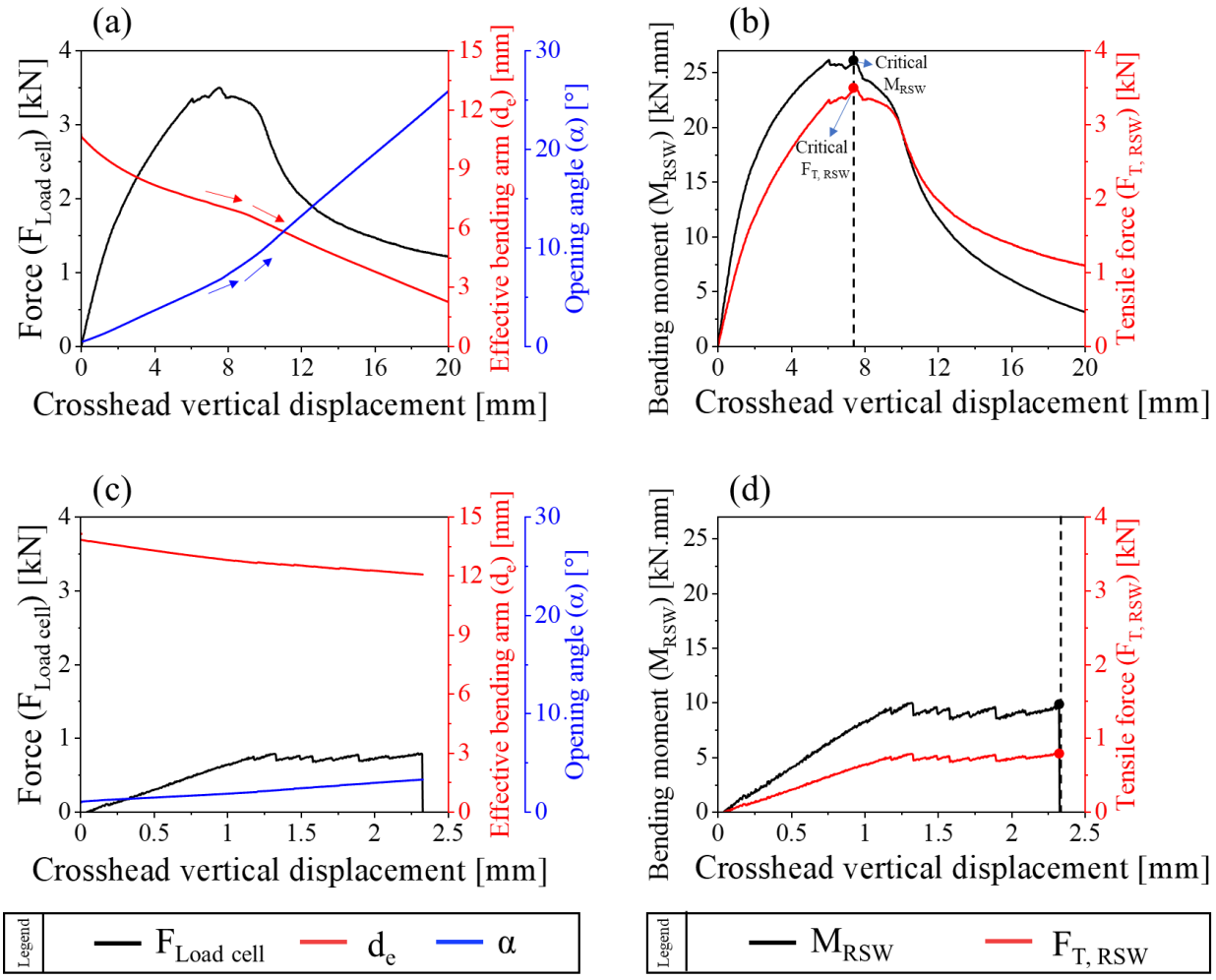


Figure 5.4. Representative evolution of effective bending moment arm (d_e), opening angle (α), bending moment (M_{RSW}), and tensile force ($F_{T,\ RSW}$) applied to the projected RSW FZ throughout (a) and (b) 3G-980 FDWS, and (c) and (d), 3G-980 MWS geometry 1 (short arm) CP tests.

Upon determining the evolution of load components, the tensile energy absorption capacity of the spot weld ($E_{T,\ RSW}$) is calculated as:

$$E_{T,RSW} = \int F_{T,RSW} . \delta t_{C1-C2} \tag{5.3}$$

where $\delta t_{C1\text{-}C2}$ is the relative vertical displacement of the projected FZ center, tracked via the displacement field of inspectors C_1 and C_2. The vertical crosshead displacement does not accurately reflect the displacement of the nugget on the bottom horizontal flange region, as evidenced by the arm deformations and nugget rotation shown in Figure 5.2. Therefore, the evolution of $F_{T,\ RSW}$ parameters were plotted against the local relative displacements at the projected centers of the FZ on the upper and lower CP coupons, rather than the global crosshead

vertical displacement. Considering the local displacement field minimizes the influence of deformations occurring at regions away from the spot weld on the subsequent $E_{T,\,RSW}$ calculations. The moment energy ($E_{M,\,RSW}$) due to the rotation of the nugget (opening angle δα) is defined as:

$$E_{M,RSW} = \int M_{RSW}.\,\delta\alpha \qquad (5.4)$$

The total joint absorbed energy ($E_{Total,\,RSW}$) is defined as the sum of $E_{T,\,RSW}$, and $E_{M,\,RSW}$. $E_{Total,\,RSW}$ were compared against global energy dissipation values (E_{Global}) calculated from the area under crosshead vertical displacements- $F_{Load\ cell}$ plots.

For the sake of simplicity and applicability of the results to the automotive industry, the CP post-processing methodology presented in this section assumes horizontal alignment of the nugget, which is especially important up to the peak load frame of the tests. In reality, slight rotation of the nugget can occur up to the peak load frame which can develop unwanted shear load components throughout the CP tests. A detailed equilibrium force analysis is provided in Appendix A which tracks the actual orientation of the nuggets throughout the tests and does not assume their horizontal alignment. Results indicated minimal variations in critical $\vec{M}_{RSW}$ and $\vec{F}_{T,RSW}$ at the onset of failure while accounting for the actual orientation of the nugget compared with the horizontally aligned nugget assumption.

5.3.5 KS-II tests to characterize combined shear and tensile loading

In this study, KS-II tests for MWS conditions were performed in 8 orientations to obtain a broad range of shear-tensile loading ratios. The KS-II test results for the FDWS condition were reported in Chapter 4 and are used to contrast with the current MWS condition. The testing methodology for MWS KS-II tests was similar to the FDWS KS-II tests discussed in section 4.3.3. A brief overview of the KS-II and the triangulation methodology is provided in the following. More comprehensive details about the KS-II testing fixture and the implemented triangulation methodology to account for nugget orientation can be found in Chapter 4.

Figure 5.5 shows the first and final images related to the displacement fields that were tracked for a KS-II test at 10° loading orientation. DIC circle inspector tools with a 2.5 mm diameter were used to report the displacement in the KS-II tests. The location of the point and circular inspectors is shown in Figure 5.5 as well. The opening windows in the KS-II inserts, where C_0 and C_3 inspectors are located, were machined to account for any asymmetric deformation of

the two coupon halves. The displacement of point C_0 was shown in Chapter 4 to accurately represent the crosshead displacement.

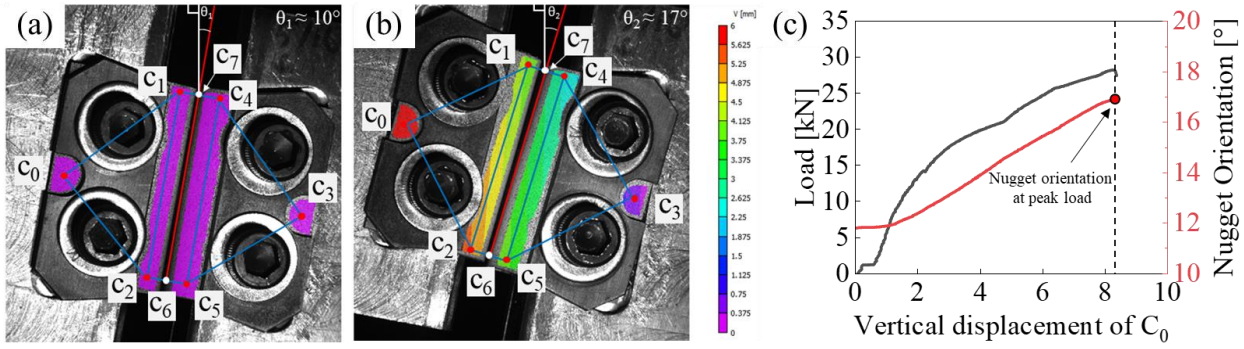


Figure 5.5. Comparison between (a) first and (b) final frame of a KS-II test at 10° loading orientation. The color contour V represents vertical displacement within the region of interest. (c) load- displacement and nugget orientation plot of the same test shows the instantaneous orientation of the nugget throughout the test.

Examining the KS-II DIC images revealed a non-negligible amount of slippage throughout some of the KS-II tests, especially in the shear-dominated orientations of 0°, 10°, 15°, and 30°. Most of the slippage occurs at the coupon level due to the clearance holes not being completely engaged with the KS-II holder at the beginning of the tests. Any slippage or induced rotation of the KS-II specimen within the grip must be accounted for to correctly resolve the shear and tensile force components. For example, Figure 5.5 (a) and (b) demonstrate how a KS-II specimen, with an approximate initial 10° loading orientation, rotates by approximately 7° before full detachment (failure) of the coupon by the end of the test. The methodology for approximation of the actual nugget orientation consisted of using 6 circular point inspectors within the DIC region of interest to form two triangles, the vertices of which track the non-symmetric orientation of each coupon half independently. In this approach, points C_6 and C_7 construct a line between the two KS-II coupon halves that contain the nugget, and the instantaneous slope of this line is updated as the current orientation of the nugget.

5.4 Results and Discussions

5.4.1 CP Mechanical Test Results

Representative evolution of parameters $F_{T,\,RSW}$, and M_{RSW} during testing three geometries of CP specimens have been illustrated for different welding schemes in Figure 5.6. Results revealed that the spot welds fail under a combination of bending moments and tensile-dominated forces in the CP testing geometry. The initial bending arm (d) was increased between 188% to 213% from

the short arm geometry to the long arm geometry of various welding schemes. On average, the increase in the initial bending arm resulted in a 215% and 233% increase in displacement-to-failure of 3G-980 and 3G-1180 FDWS test conditions, respectively. The increase of the average failure displacement was 80% and 53%, for 3G-980 and 3G-1180 MWS conditions, respectively. The larger increase in the displacement to failure of the FDWS conditions with larger bending arms is attributed to a transition to a PO failure mode with a larger rotation of the nugget in contrast to the MWS conditions with IF. Furthermore, the long arm conditions exhibited increased plastic deformation of the flange.

The applied force and displacement-to-failure provide limited insight into the performance of the weld in the CP test. The severity of the applied bending moment is a function of the geometry and its evolution during the test. Therefore, the evolution of the bending moment and tensile forces were plotted against their corresponding displacements/rotations for the different CP coupon geometries. Subsequently, the load-bearing capacity and energy absorption capability of the welds are calculated independently in tensile and bending conditions.

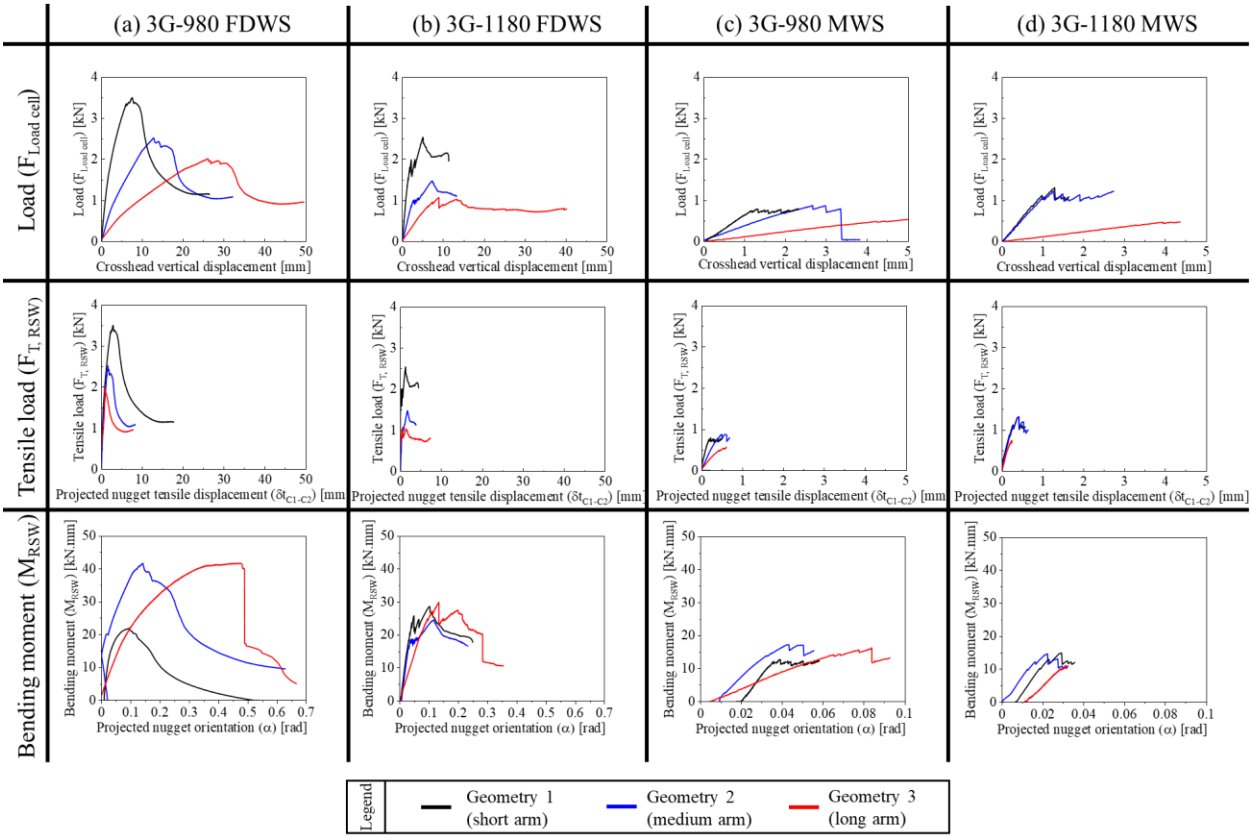


Figure 5.6. Representative plots showing the evolution of $F_{Load\ cell}$, $F_{T,\ RSW}$, and M_{RSW} during testing of three different CP geometries of (a) 3G-980 FDWS, (b) 3G-1180 FDWS, (c) 3G-980 MWS, and (d) 3G-1180 MWS welding schemes.

The average critical $F_{T,\ RSW}$, and M_{RSW} applied to the projected center of the RSW FZ for all CP geometries and welding schemes are shown in Figure 5.7. As expected, a decreasing trend in terms of peak load was observed with increasing moment arm length. The suboptimal MWS welds' strength was found to be more sensitive to changes in the CP coupon geometry as their average strength decreased between 40% to 65% from geometry 1 (short arm) to geometry 3 (long arm) for 3G-980 and 3G-1180, respectively, compared to a 39% to 41% drop in average peak load for 3G-980 and 3G-1180 FDWS weld conditions. Changing the CP geometry from short arm to long arm consistently resulted in a higher average critical M_{RSW} value. The increase in critical M_{RSW} from short-arm to long-arm geometry was 39% and 49% for 3G-980 FDWS and 3G-1180 FDWS, on average. The increase in M_{RSW} of MWS conditions was calculated at 42% and 10% for 3G-980 and 3G-1180, respectively. It is noted that an idealized assumption of a constant bending arm throughout CP tests would have resulted in consistent over-estimation of the critical M_{RSW} values

between 74%-138% for FDWS conditions, and between 6%-46% over-estimation for MWS conditions.

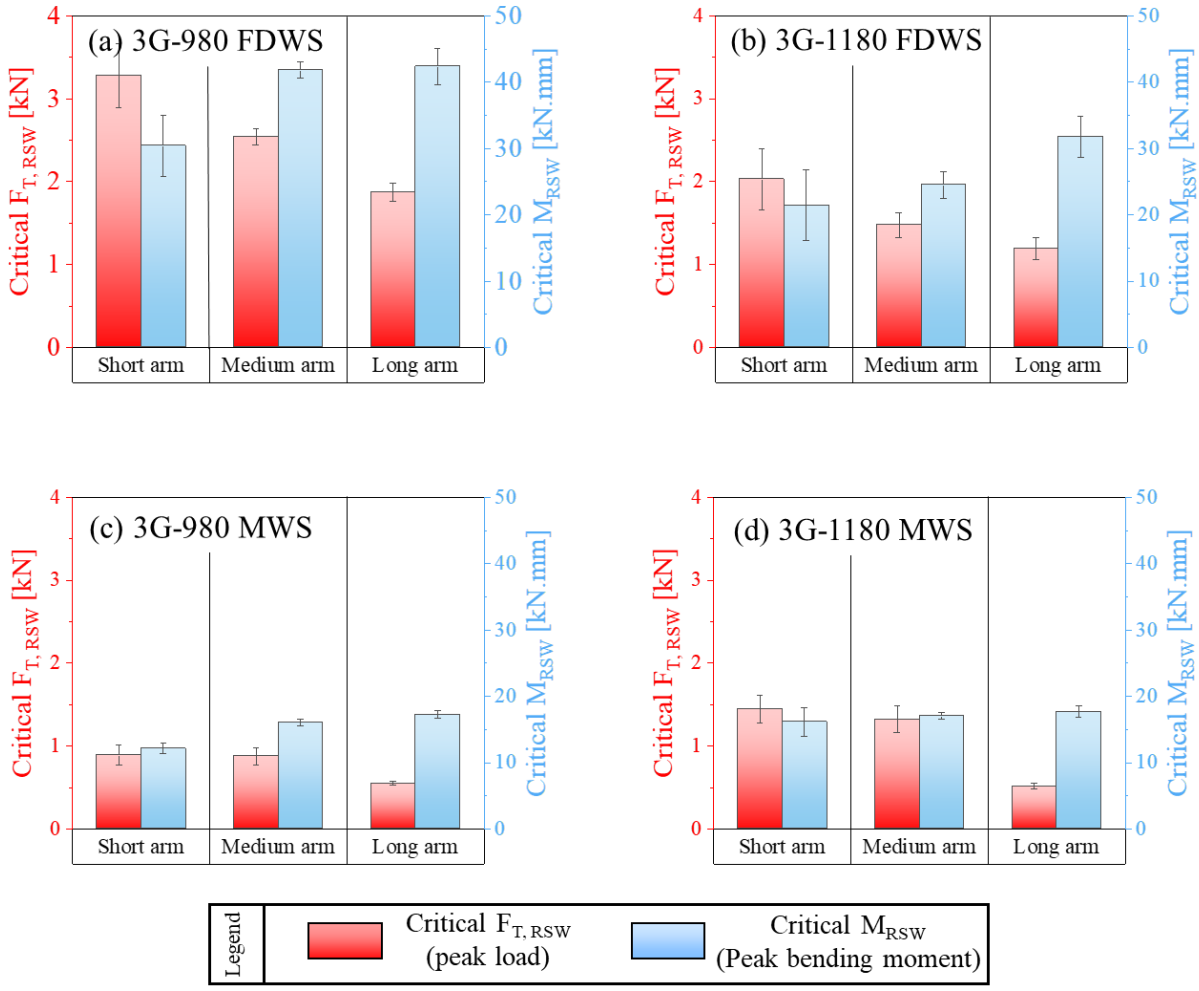


Figure 5.7. Influence of CP coupon geometry on average critical $F_{T, RSW}$, and M_{RSW} applied to the projected center of the RSW FZ for (a) 3G-980 FDWS, (b) 3G-1180 FDWS, (c) 3G-980 MWS, and (d) 3G-1180 MWS welding conditions.

The alteration in $E_{T, RSW}$, $E_{M, RSW}$, $E_{Total, RSW}$, and E_{Global} due to changes in initial bending arm length is summarized in Figure 5.8. It is interesting to note that the $E_{Total, RSW}$ was relatively unchanged with the change from short to long arm with an 8.1% and 4.5% increase on average for 3G-980 and 3G-1180 FDWS cases. Although the total energy absorption capacity of the joints remained nearly the same, the $E_{T, RSW}/E_{Total, RSW}$ ratio decreased from 69.5% to 35.4% for 3G-980 FDWS, and from 62.6% to 45.1% for 3G-1180 FDWS cases. At the same time, increasing the bending arm from short arm to long arm geometry inc reased the $E_{M, RSW}/E_{Total, RSW}$ ratio from 30.5%

to 64.6% for 3G-980 FDWS, and from 37.4% to 54.9% for 3G-1180 FDWS condition. The $E_{Total,\ RSW}$ calculations for MWS conditions revealed much more limited energy absorption capabilities as evidenced by the smaller scales in Figure 5.8 (c) and (d). The larger variation in MWS $E_{Total,\ RSW}$ is attributed to a few tests having P-PO failure modes with small plug ratios. Unlike the FDWS conditions, increasing the initial bending arm in MWS welding schemes did not result in a consistently higher $E_{M,\ RSW}/E_{Total,\ RSW}$ ratio.

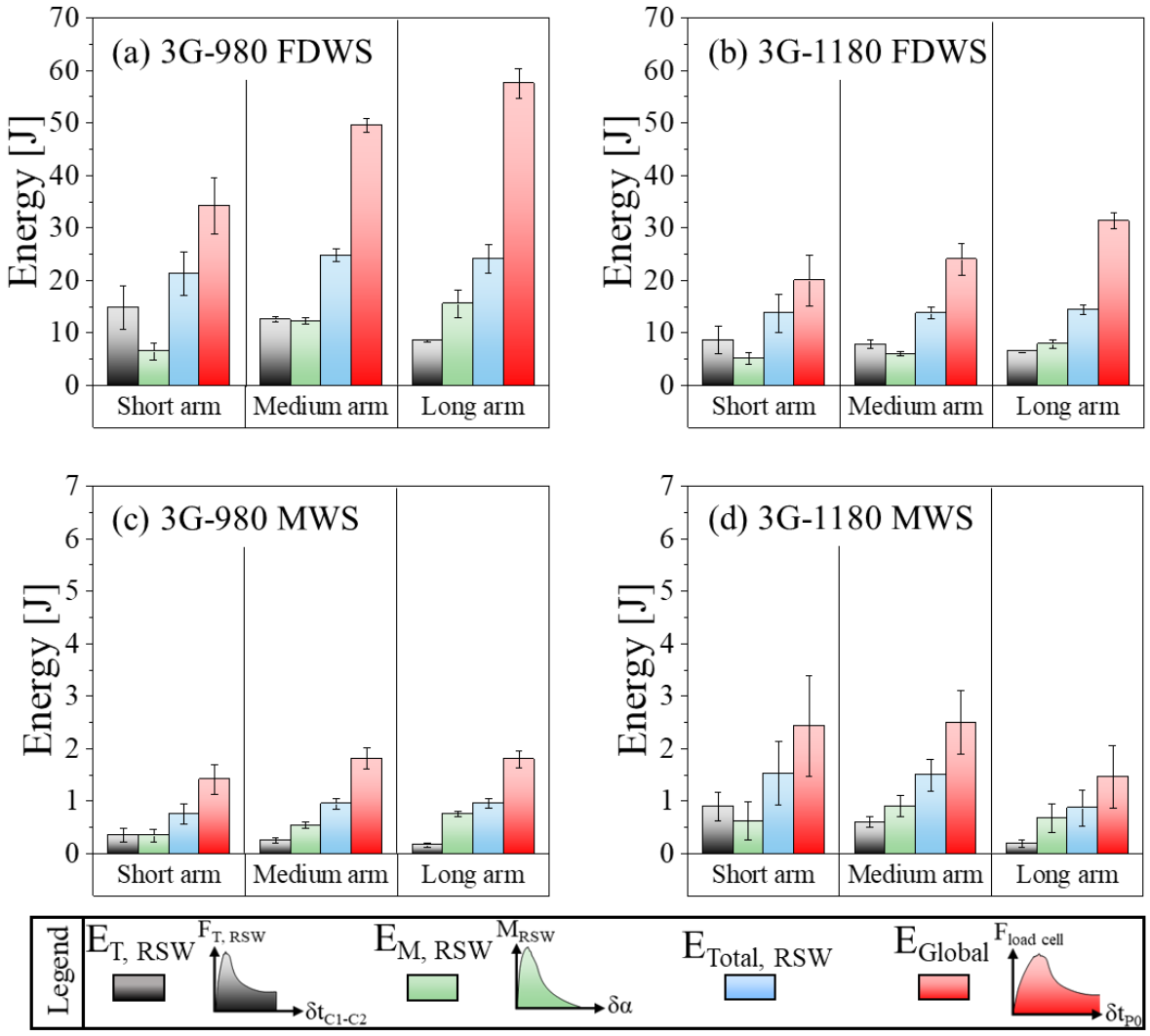


Figure 5.8. Influence of CP coupon geometry on average $E_{T,\ RSW}$, $E_{M,\ RSW}$, $E_{Total,\ RSW}$ of the projected center of the RSW FZ, and E_{Global} for (a) 3G-980 FDWS, (b) 3G-1180 FDWS, (c) 3G-980 MWS, and (d) 3G-1180 MWS welding conditions.

Changes in the effective bending arm (d_e) from the beginning of the test ($d_e=d$) until the peak load frame of the tests were measured according to the procedure outlined in section 5.3.4 and is summarized in Figure 5.9. The reduction in d_e was most noticeable for high heat input FDWS cases. More specifically, the 3G-980 and 3G-1180 FDWS exhibited between 26%-28%, and 16%-22% reduction in d_e, respectively, throughout the three CP geometries. The higher reduction in the bending arm of 3G-980 FDWS could be explained by the higher ductility of the as-received steel as well as the tougher behavior of the welds. As an example, representative fracture surfaces along with the cross-sectional view of the short arm FDWS conditions are shown for both investigated materials in Figure 5.10. The failure was accompanied by crack initiation and propagation in both materials. While the cracks initiated at the notch tip area on the side closer to the loading axis for both steels, two distinctly different propagation paths were observed between the 3G-980 and 3G-1180 spot welds. In the case of the 3G-980 welds, the cracks immediately grew outwards from the notch and towards the BM region with ductile failure behavior and the development of a neck in the failed joint leg (Figure 5.10 (a)). After going through the sheet thickness and reaching the faying surface, the cracks grew around the nugget circumference, leaving both the FZ and HAZ intact after full failure. However, in the case of the 3G-1180 (Figure 5.10 (b)), the cracks rapidly propagated halfway into the FZ, after which the propagation direction switched away from the faying surface. Finite element modeling by Pawar *et al.* [209] revealed full nugget PO failure of spot welds can accommodate more plastic deformation of the coupons. Therefore, other than the difference in the ductility of the tested 3G-AHSS, the observed failure mechanisms are also believed to be a contributing factor for a more severe reduction in the effective bending arm of the 3G-980 FDWS CP tests as compared to the 3G-1180 FDWS tests. Reduction of d_e for various CP geometries of 3G-980 MWS and 3G-1180 MWS conditions was between 7%-11%, and 7%-16%, respectively. The differences in the reduction of d_e between the two 3G-AHSS MWS spot welds were determined to be statistically insignificant, which can be correlated with their similar IF behavior in most of the tests.

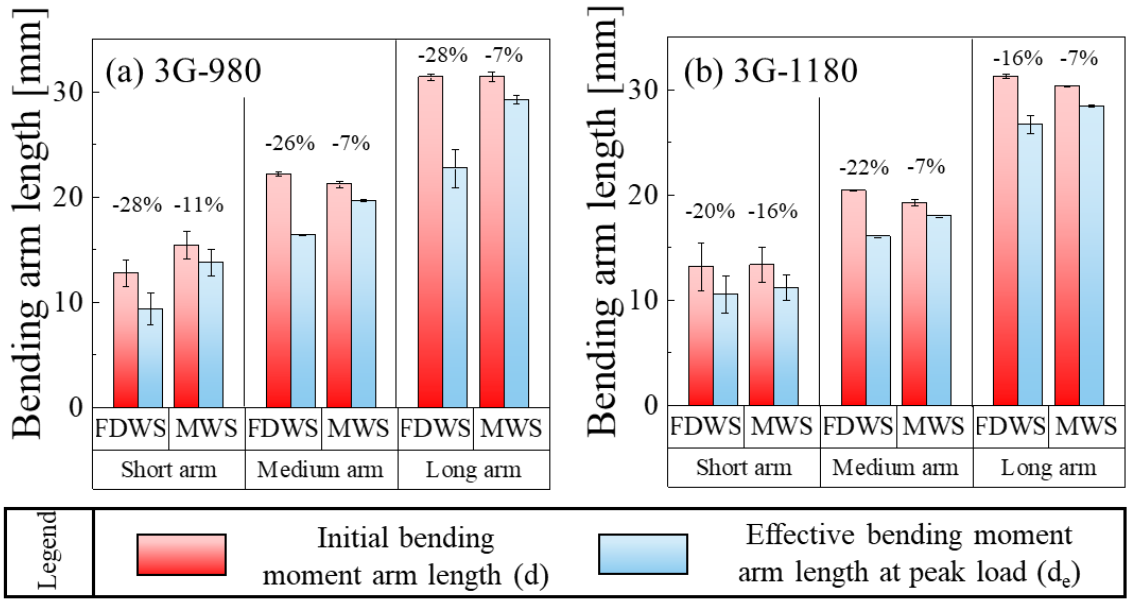


Figure 5.9. Changes in effective bending moment arm from the beginning of the tests up to the peak load frame of (a) 3G-980, and (b) 3G-1180 CP tests with various geometries and welding schemes.

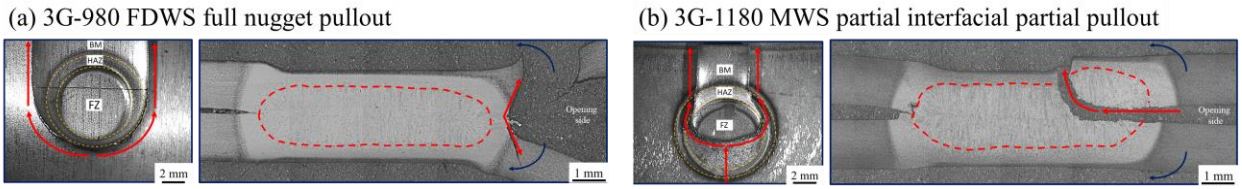


Figure 5.10. Representative failure behavior of CP geometry 1 (short arm) tests for (a) 3G-980 FDWS and (b) 3G-1180 FDWS conditions.

5.4.2 KS-II Mechanical Test Results

Figure 5.11 (a) and (b) show representative measured load-displacement curves for each of the FDWS loading orientations. The area under the load-displacement curves is typically used as a quality index reflecting the energy absorption capability of the joints. It is observed that the spot welds exhibit much higher strength for shear-dominated loading orientations with limited energy absorption after reaching the peak load value, taken as the onset of failure, as demonstrated by the abrupt unloading response. In contrast, the tests performed under tensile-dominated loading orientations exhibit relatively lower strength values, however, their post-failure energy absorption represents a higher proportion of the total energy absorption, as evidenced by the elongated unloading tails of the corresponding curves. The same overall trends were also observed in the MWS condition as shown in Figure 5.11 (c) and (d).

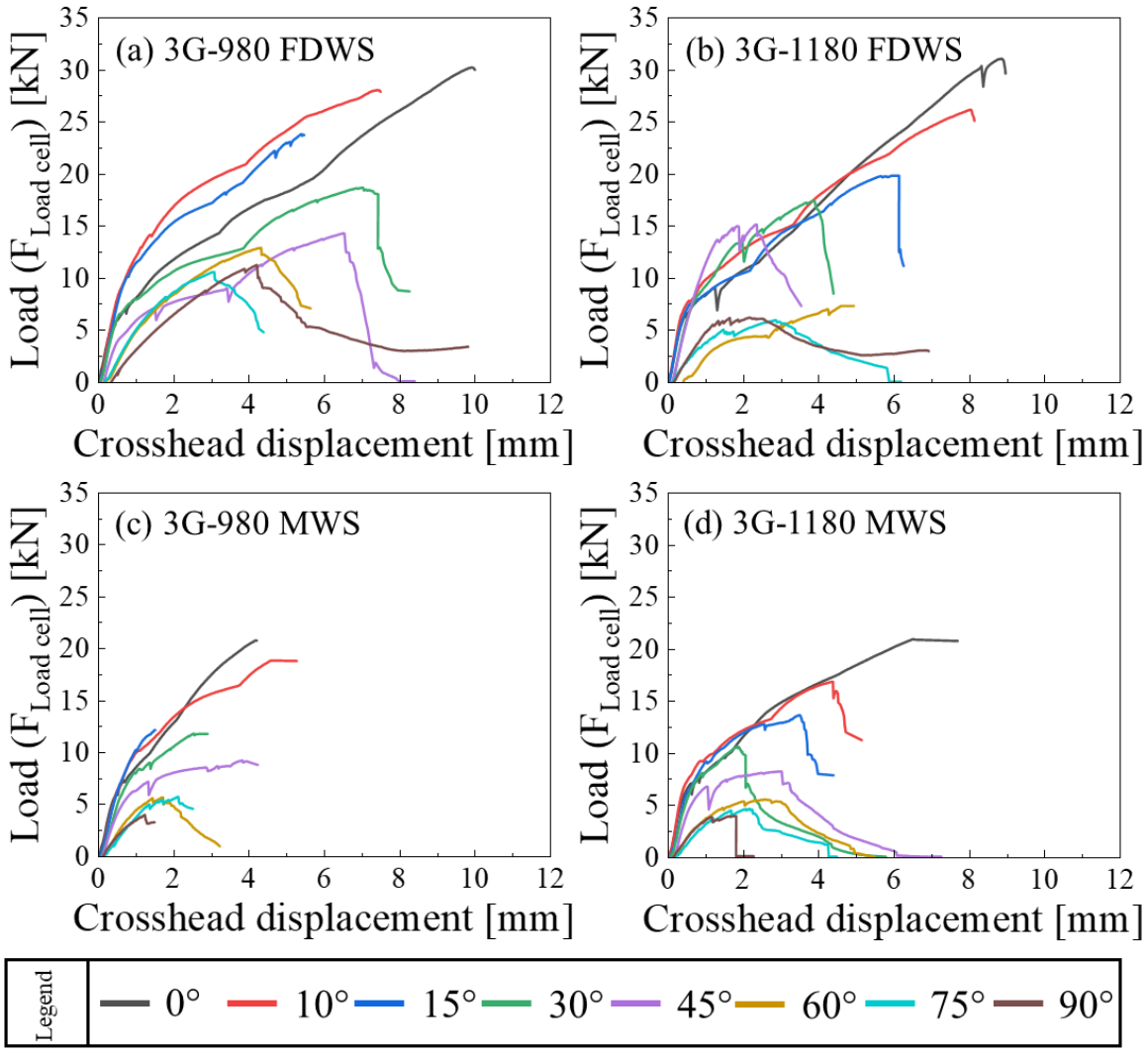


Figure 5.11. Representative KS-II load-crosshead displacement plots for different loading orientations of (a) 3G-980 FDWS, (b) 3G-1180 FDWS, (c) 3G-980 MWS, and (d) 3G-1180 MWS conditions.

The peak load values from each of the tests were extracted for different loading orientations and the corresponding values are plotted in Figure 5.12 (a) and (b) for FDWS and MWS conditions, respectively. The decreasing trend as loading orientation changes from shear loading (0°) to tensile loading (90°) is related to changes in the stress state at the nugget periphery. In summary, the load-carrying capacity of 3G-980 and 3G-1180 spot welds decreased by 65% and 81% for the FDWS, and 79% and 78% for MWS conditions as the loading orientation changed from 0° to 90°.

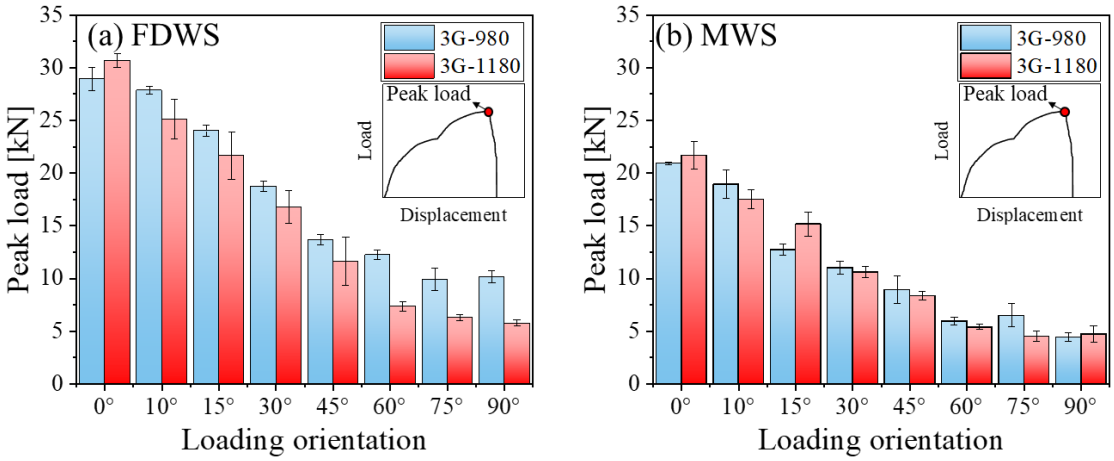


Figure 5.12. Influence of KS-II loading orientation on peak load of (a) FDWS and (b) MWS welding schemes.

Although the nominal orientation of the nugget is commonly used to calculate the shear and tensile force components [105,109,156], the DIC displacement measurements revealed rotations that must be considered. Figure 5.13 (a) summarizes the procedure that was followed for the calculation of the final nugget orientation at the peak load value throughout all performed KS-II loading orientations. As expected, rotations are minimal in tensile-dominant loading orientations (45°-90°). In contrast to uniaxial tension, rotations are unavoidable due to the induced moment in the shear-dominant loading cases. The induced coupon rotation leads to an evolution of the shear and tensile loading components that must be considered in the construction of the RSW failure loci in shear-tensile loading.

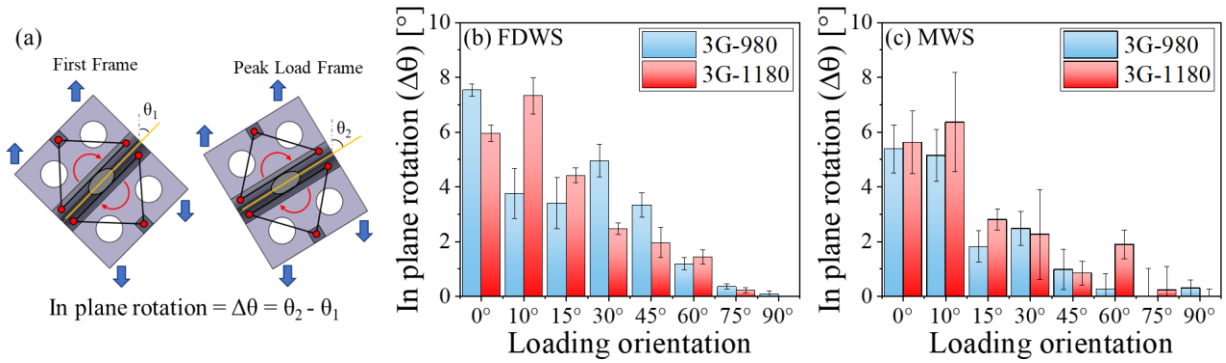


Figure 5.13. (a) Summary of procedure for calculating in-plane rotation using DIC data (rotation of the coupons is exaggerated for better visualization of changes in θ). In-plane rotation values at peak load frame for (b) FDWS and (c) MWS conditions.

5.4.3 Calibration of RSW Failure Loci

Constructing a load-based failure locus for resistance spot welds requires the decomposition of the critical failure load value into its components at the onset of failure. Identifying the critical failure load in RSW mechanical tests can be challenging due to the weld being hidden and the typically jagged nature of the resultant force-displacement curves. Local strength drops in force-displacement curves are well documented in the literature and are thought to be due to the slipping of coupons/testing fixtures or the formation of cracks that have not reached critical lengths for further growth [14]. Although some studies have shown crack initiation and partial propagation from the intrinsic notch region in between the welded sheets during the strain hardening (loading) region of the load-displacement curves [210], the peak load point is typically considered the critical failure load.

As discussed earlier in section 2.5.3, different models have been proposed to describe the failure behavior of resistance spot welds. The phenomenological functions of Lee *et al.* (f^{L}, Equation 2.7) [101], Seeger *et al.* (f^{S}, Equation 2.8) [120], and song and Huh (f^{SH}, Equation 2.9) [165] are among the most commonly implemented failure criteria to describe the quasi-static RSW failure locus in tensile-shear loading cases. These three models were calibrated and the corresponding calibrated failure loci in shear-tensile loading conditions are shown in Figure 5.14 (a) and (b) for 3G-980 and 3G-1180 spot welds, respectively.

It is noted that the final orientations of the nuggets at the onset of failure, acquired from the output of the triangulation methodology, were used to decompose the strength values into shear and tensile force components in Figure 5.14 (a) and (b). Considering the final orientation of the nugget when decomposing the strength value at peak load point can lead to more realistic calibration of strength-based spot weld failure criteria. considering the final orientation of the nuggets changes the location of the data points, especially for shear-dominated loading orientations with the most severe coupon rotations. To be more specific, considering the rotation of the nugget throughout the tests moves the corresponding nominal strength data point in each loading orientation to a lower average shear force component and higher average tensile force component.

According to Figure 5.14 (a) and (b), Seeger's two-dimensional model with its two shape exponents as variables, provided the best agreement with the experimental data with an average of between 0.2% to 3.5% over-prediction error. Figure 5.14 (c) outlines the average error of different

model predictions compared to the experimental failure load components upon using the triangular KS-II analysis. It is observed that the Song and Huh model underestimates the failure strength of the investigated 3G-AHSS spot welds between 9.2% and 22.3% on average for all orientations. The average error of under-predictions drops to between 0.4% and 3.7% for Lee's model. It appears the quadratic constraint of f^{L} and f^{SH} models is overly restrictive with poor predictions in combined shear and tensile loading. Consequently, the more flexible f^{S} model is selected as a basis for comparison and further analysis of the existing RSW loci failure predictions.

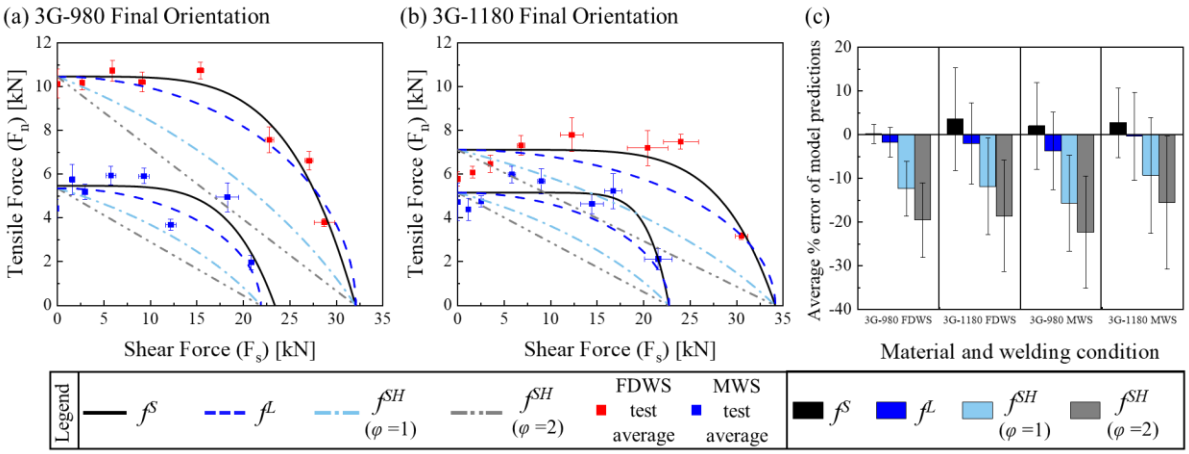


Figure 5.14. Comparison between different RSW failure criteria along with the experimental KS-II data points, decomposed according to their final orientations, for (a) 3G-980 and (b) 3G-1180 spot welds (all shown calibrated models correspond to the final orientation data points upon using the DIC triangular analysis); (c) average error of predictions corresponding to different models calibrated in (a) and (b).

The three-dimensional form of Seeger's failure criteria has been rewritten in Equation 5.5 which accounts for failure under bending-dominated loading [211]. Failure is predicted to occur when f^{S} exceeds unity, corresponding to loading outside of the failure surface.

$$f^{S} = \left[\frac{F_s}{S_S}\right]^{a} + \left[\frac{F_n}{S_N}\right]^{b} + \left[\frac{M_b}{S_B}\right]^{c} \leq 1; \qquad (5.5)$$

where S_B is the critical bending moment applied to the spot weld at the onset of failure during CP tests. Wang *et al.* [86] proposed determining S_B by assuming the polynomial-based failure surface as:

$$S_B = \frac{F_{Max\ CP} \times d}{\sqrt{1-\left(\frac{F_{Max\ CP}}{F_{Max\ KS-II\ 90^{\circ}}}\right)^2}} \qquad (5.6)$$

where $F_{Max,\ CP,}$ and $F_{Max,\ KS\text{-}II\ 90°}$ are the maximum load-bearing capacities in CP and KS-II at 90° tests, respectively, and d is the initial bending moment arm of a single CP geometry. The appropriate value of c in Equation 5.5 cannot be determined with a single CP geometry and is conventionally assumed that c = 2 [120,161]. The predicted three-dimensional failure surfaces of Seeger in Equation 5.5 with the value of S_B determined from Equation 5.6 based on peak load data from the short arm CP geometry are shown in Figure 5.15. The calibrated force-based failure strengths and exponents have been summarized in Table 5.3.

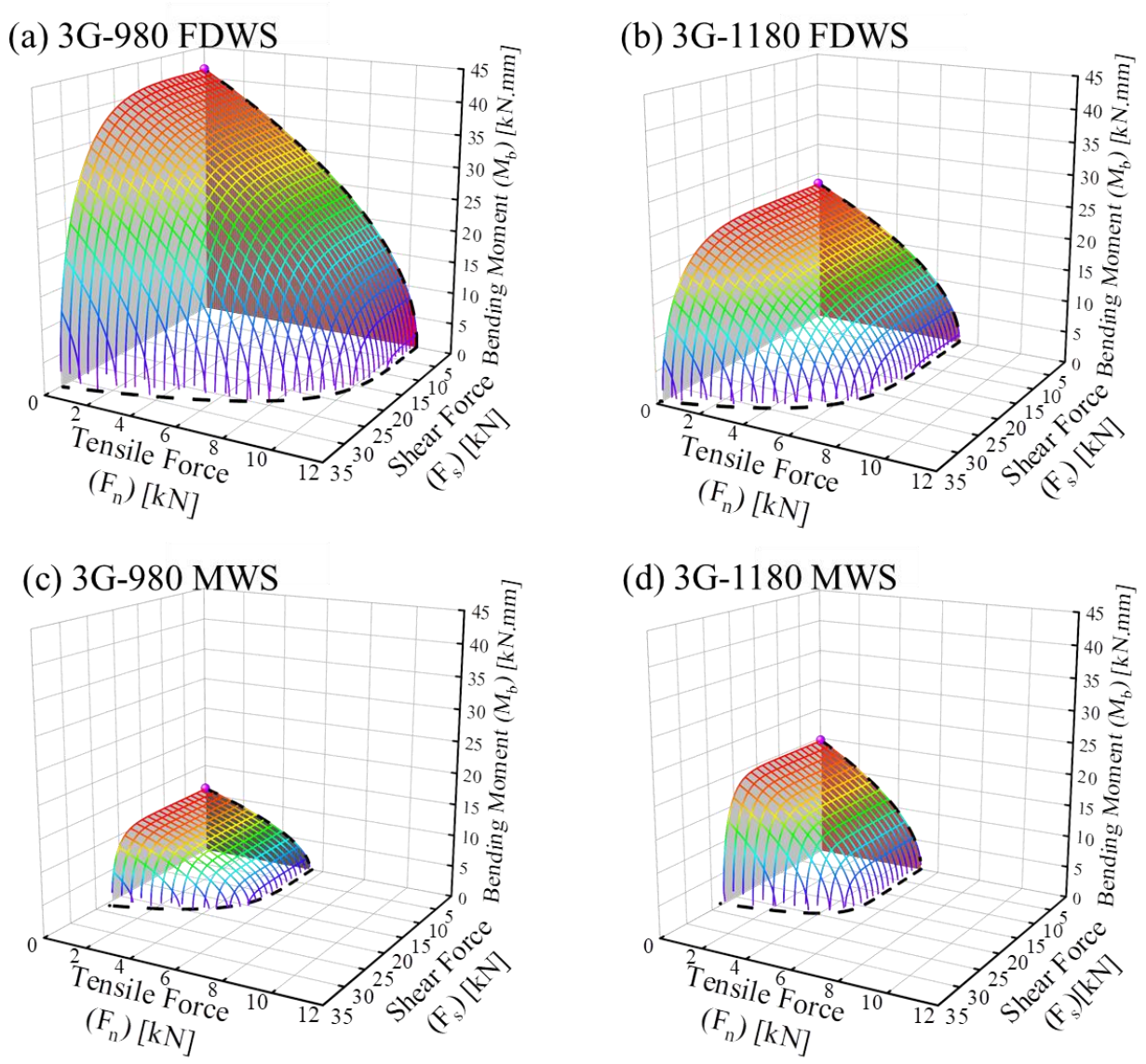


Figure 5.15. Three-dimensional RSW failure surfaces calibrated using Equation 5.5 and Equation 5.6 according to the final orientation of the KS-II coupons following the DIC triangular analysis and short arm CP tests for (a) 3G-980 FDWS, (b) 3G-1180 FDWS, (c) 3G-980 MWS, and (d) 3G-1180 MWS welding schemes.

Table 5.3. Summary of calibrated force-based RSW failure model parameters for Seeger's three-dimensional criteria including failure strengths and exponents.

Calibrated equation $f^S = \left[\frac{F_s}{S_S}\right]^a + \left[\frac{F_n}{S_N}\right]^b + \left[\frac{M_b}{S_B}\right]^c = 1$						
Material and corresponding RSW scheme	Average shear strength (S_s) [kN]	Average tensile strength (S_N) [kN]	Average bending strength (S_B) [kN.mm]	Calibrated exponents		
				a	b	c
3G-980 FDWS	32.071	10.458	41.407	4.67	1.00	2
3G-1180 FDWS	34.160	7.116	23.359	6.00	1.00	2
3G-980 MWS	21.877	5.361	11.021	10.00	1.00	2
3G-1180 MWS	22.743	5.159	19.699	10.00	1.00	2

The following two sections focus on assessing the accuracy of failure strength predictions from Seeger's model shown in Figure 5.15. More specifically, the experimentally acquired failure data, summarized in sections 5.3.4 and 5.3.5, are contrasted with Seeger's model in shear-tensile and tensile-bending loading conditions (dashed black lines in Figure 5.15). Suitable alternative functional forms are proposed that can be implemented in finite element analysis for a more accurate RSW failure prediction accuracy.

5.4.3.1 Evaluating RSW failure models in tensile-bending loading conditions

The critical tensile strengths ($F_{T,\,RSW}$) and bending moments (M_{RSW}) at the onset of failure are summarized in Figure 5.16 for each CP test geometry. As shown in this figure, increasing the bending moment arm in FDWS conditions effectively induced a higher ratio of $\frac{M_{RSW}}{F_{T,RSW}}$. However, due to the IF mode with limited deformation up to the onset of failure, increasing the bending moment arm was not effective in the consistent attainment of a higher $\frac{M_{RSW}}{F_{T,RSW}}$ ratio for MWS welding schemes.

Two different approaches were adopted to calibrate Seeger's proposed failure loci in tensile-bending conditions shown in Figure 5.16. The first approach included the traditional assumption of c=2 and S_B calculated from Equation 5.6 (as shown earlier in Figure 5.15). Calibration using

this approach reveals a convex failure locus that poorly predicts the overall trend of critical tensile strengths and bending moments. As an example, at any given average experimental tensile strength of the medium arm CP specimens, Seeger's failure surface, calibrated using the conventional approach consistently under-predicted failure bending moments by 10.5% for 3G-980 FDWS, 10.3% for 3G-1180 FDWS, 48.8% for 3G-980 MWS, and 14.1% for 3G-1180 MWS. Alternatively, the Seeger model was calibrated using the failure data from all three CP geometries. While using multiple CP failure data points increased the overall accuracy of the predictions in combined tension and bending, the tensile strength of the joints was under-predicted by a large margin. Specifically, the tensile strengths were under-predicted by 46.5% for 3G-980 FDWS, 48.3% for 3G-1180 FDWS, 66.2% for 3G-980 MWS, and 45.2% for 3G-1180 MWS conditions.

An exponential functional form is proposed to better predict the failure of spot welds in tensile-bending loading conditions. The calibrated parameters corresponding to the proposed functional form are outlined in Table 5.4. The proposed failure loci, compared to the loci proposed by Seeger, predict pure bending strengths that are 57% and 94% higher for 3G-980 FDWS and 3G-1180 FDWS conditions, respectively. The predicted bending strengths are 116% and 4% higher for 3G-980 MWS and 3G-1180 MWS conditions, respectively, in comparison to the bending strengths calculated from Equation 5.6. Characterizing the failure of the spot welds at relatively small bending moments (<10 kN.mm for FDWS and <5 kN.mm for MWS conditions) required initial bending arms smaller than 7 mm. Attempts for fabrication of such CP coupons were unsuccessful due to cracking of the 3G-AHSS at low bending radii and welding limitations associated with the geometry of the utilized RSW C gun.

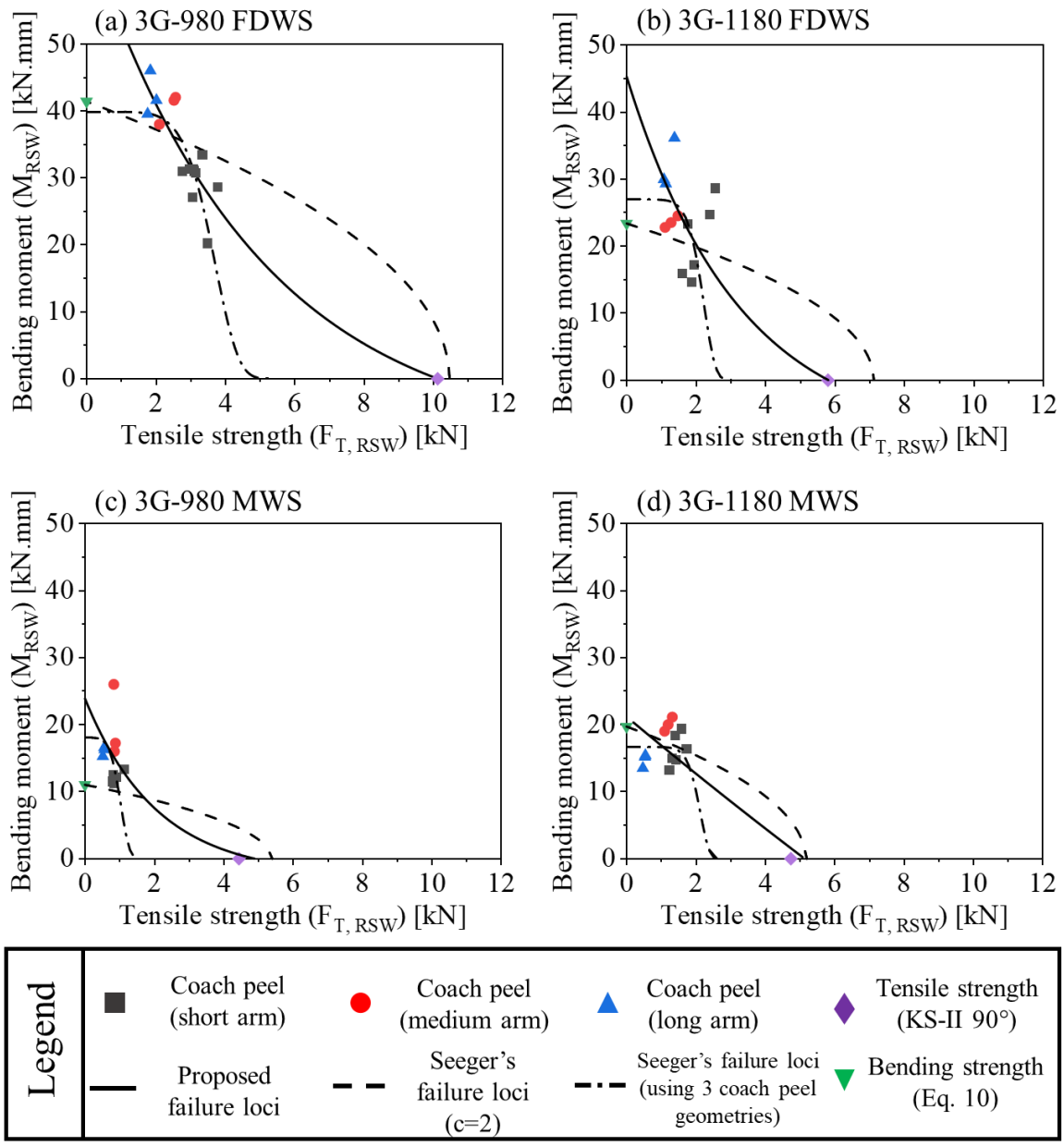


Figure 5.16. Comparison between failure predictions of proposed and Seeger's RSW failure loci in tensile-bending dominated conditions for (a) 3G-980 FDWS, (b) 3G-1180 FDWS, (c) 3G-980 MWS, and (d) 3G-1180 MWS conditions. The developed shear strength component is not shown.

Table 5.4. Summary of calibrated parameters for the proposed force-based RSW failure model in tensile-bending conditions.

Calibrated equation $M_b = A_1 \times e^{(-\frac{F_n}{t_1})} + M_{b0}$			
Material and corresponding RSW scheme	A_1	t_1	M_{b0}
3G-980 FDWS	76.242	4.891	-9.623
3G-1180 FDWS	54.234	3.230	-8.969
3G-980 MWS	26.353	2.073	-2.481
3G-1180 MWS	230.830	53.388	-209.651

5.4.3.2 Evaluating RSW Failure Models in Tensile-shear Loading Conditions

The failure loci of the investigated 3G-AHSS in shear-tensile loading conditions are reported for both the "nominal" and "final" orientations. The nominal condition assumes that there is no rotation of the weld, which is valid for tensile-dominated loading but not for shear-dominated orientations. The final condition refers to critical load components determined from the final weld orientation measured using the DIC triangulation method at the peak load frame of the KS-II tests.

The failure loci, shown in Figure 5.17, were calibrated using Equation 5.5 for both the nominal and final KS-II orientation conditions. The (R^2) values can be seen to reduce when considering the final orientation of the coupons which is associated with the non-linearity in the shear-dominated loading orientations. According to Figure 5.17, both investigated materials exhibited relatively similar failure contour profiles in the MWS condition which could be correlated with their similar failure behavior. Most KS-II tests in the MWS condition failed either interfacially, identified via propagation of a crack through the FZ, or in P-PO mode resulting in a small plug PO area. On the other hand, differences were observed in the FDWS failure contours between the 3G-980 and 3G-1180 spot welds. Specifically, within the tensile-dominated loading orientations the 3G-980 FDWS conditions exhibited between 50 to 65% higher load-bearing capacity on average than the 3G-1180 FDWS spot welds. It was observed that the majority of the tested 3G-980 FDWS joints within the tensile-dominated loading orientations failed in a full nugget PO manner. In contrast, the 3G-1180 FDWS joints typically failed in P-PO mode with a smaller plug area. A representative failure behavior of 3G-980 and 3G-1180 spot welds in the

FDWS condition has been shown in Figure 5.18. The differences in the local mechanical properties (such as toughness) in regions of crack initiation and propagation between the two steels are thought to be responsible for the observed discrepancy in load-bearing capacity, especially within the tensile-dominated loading orientations.

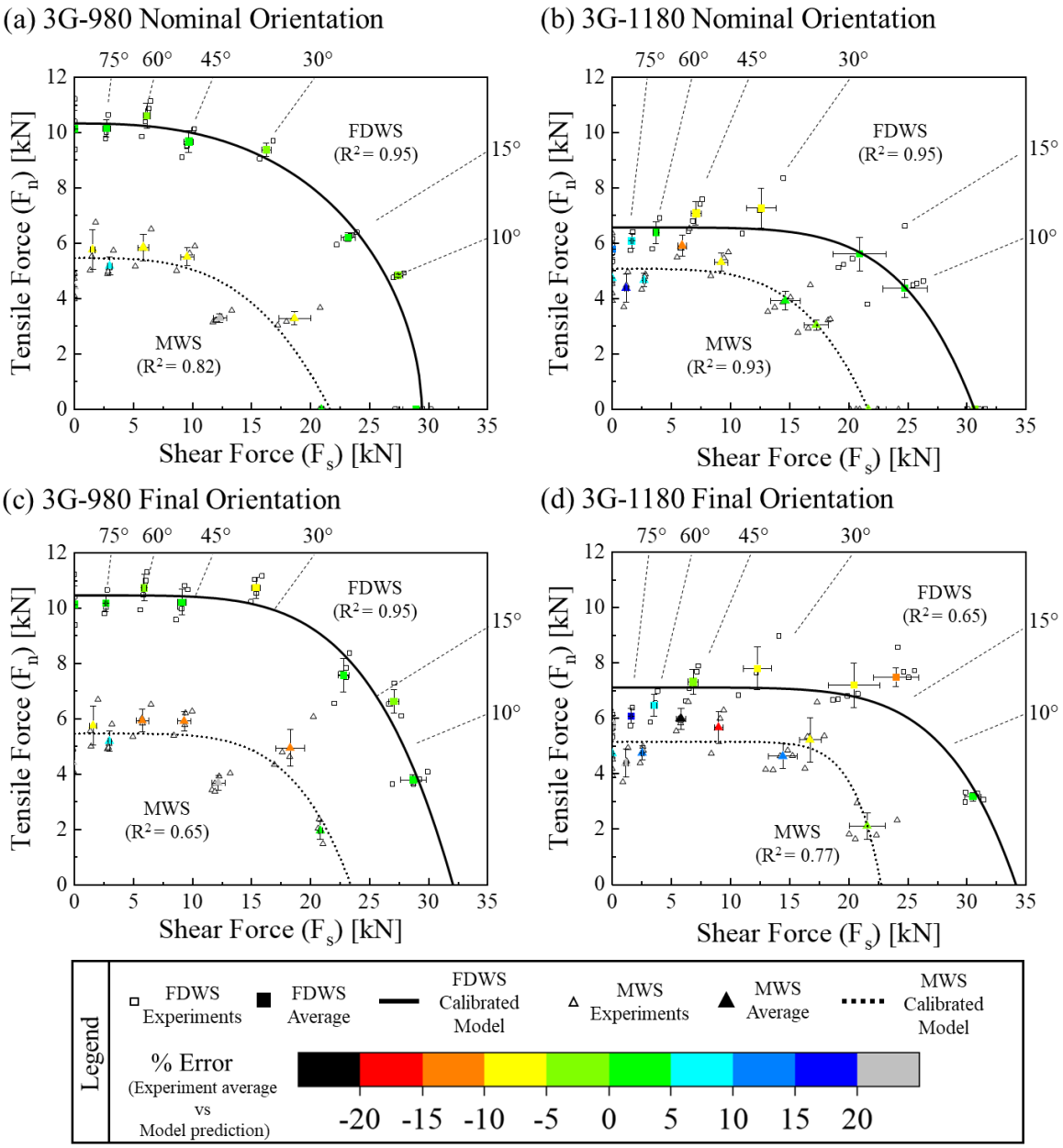


Figure 5.17. Seeger's failure loci in shear-tensile loading conditions while considering (a) and (b) the nominal orientation of the 3G-980 and 3G-1180 KS-II coupons; (c) and (d) final orientation of the 3G-980 and 3G-1180 KS-II coupons measured using DIC analysis. The hollow scattered symbols represent the individual data points attained from each test repetition, while the solid symbols show the average values at each loading orientation. The color scale represents the %

error of calibrated model predictions compared to the experimental average at each loading orientation.

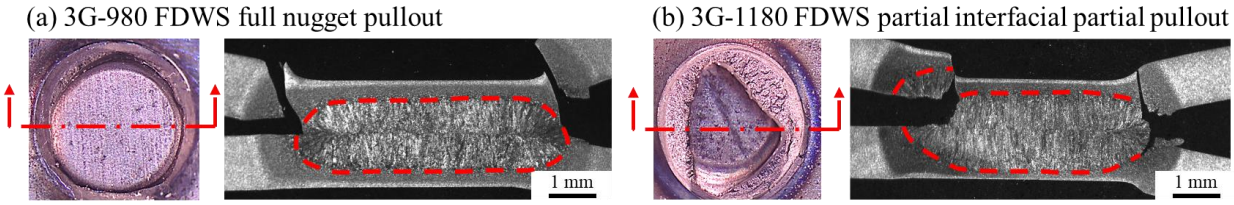


Figure 5.18. Representative failure behavior of (a) 3G-980 and (b) 3G-1180 FDWS conditions within the tensile-dominated KS-II loading orientations. The shown micrographs correspond to KS-II tests performed at θ=60° loading orientation.

All calibrated RSW failure loci shown in Figure 5.17 approach the tensile force (vertical) axis in an orthogonal direction. However, a close examination of the attained final data points reveals expansion of the failure loci in different combined load mixities, specifically within the tensile-dominated region (from 45° to 90° loading orientations). While limited data exists within the literature for the combined loading of spot welds, a similar overall trend of failure data is reported for the combined loading of laser welded high strength low alloy (HSLA) steels [166] and toughened structural adhesives [212]. An empirical and idealized failure model in the form of an exponential function is proposed which can better capture the overall trend of experimental data points and reduce the discrepancies between experimental measurements and model predictions. The calibrated exponential model and its coefficients are shown in Figure 5.19 (a) and (b), and Table 5.5, respectively. Alternatively, two independent functional forms can be utilized to reduce the percent errors related to Seeger's model within the tensile-dominated region. The calibrated loci shown in Figure 5.19 (c) and (d) use Seeger's model for capturing the extreme non-linearity within the IF region, whereas a modified version of the power law is calibrated within the PO/P-PO failure regions. The empirical modified power law is as follows:

$$f = \frac{k(m+F_S)^n}{F_n} = 1 \qquad (5.7)$$

where *k*, *m*, and *n* are the load coefficient, an additive term for vertical axis offset, and load hardening exponent, respectively. The calibrated parameters for these two functions have been summarized in Table 5.6.

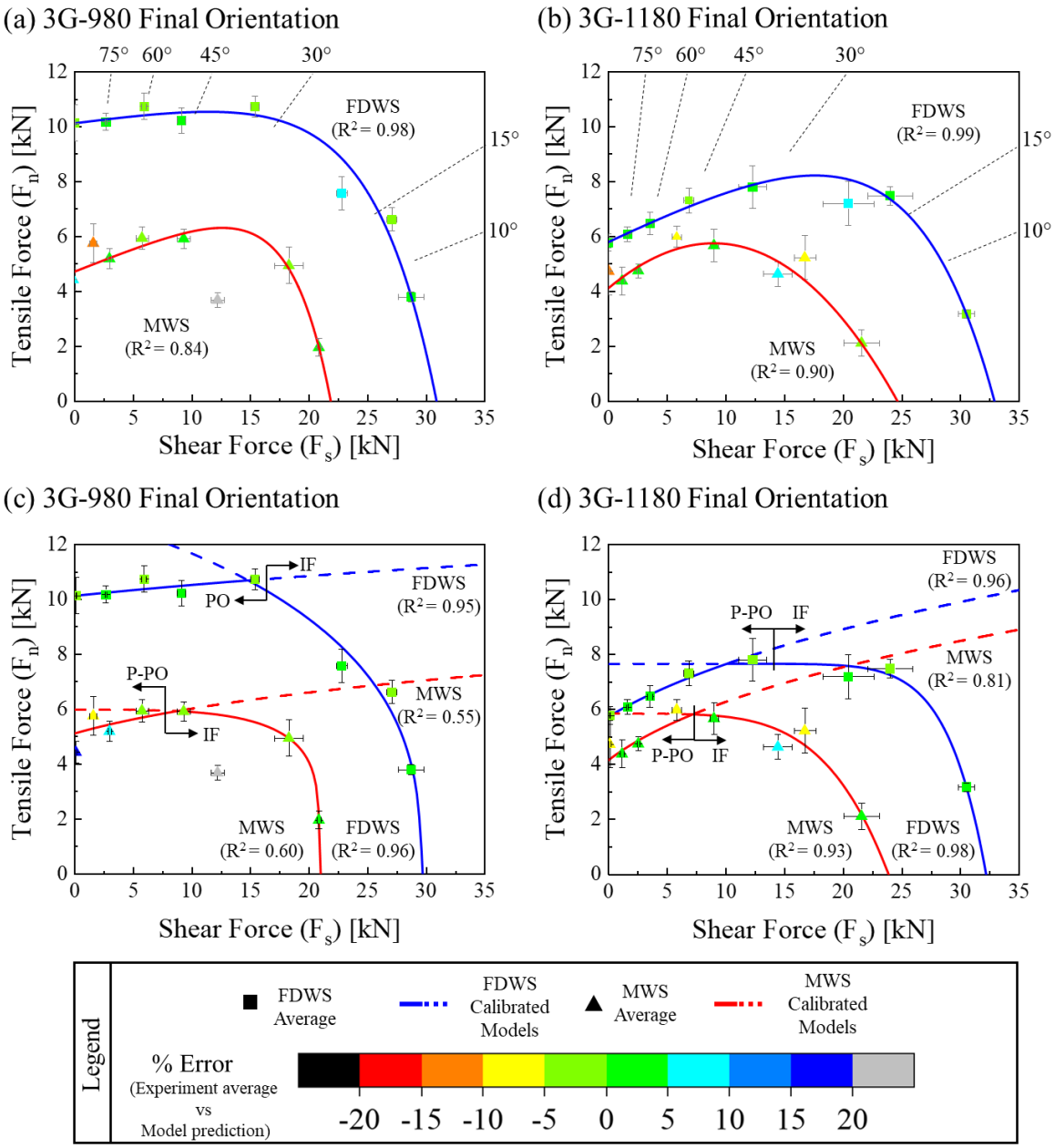


Figure 5.19. Proposed failure loci in shear-tensile loading conditions while considering the final orientation of the 3G-980 and 3G-1180 KS-II coupons measured using DIC analysis. (a) and (b) show an exponential function with six calibrated coefficients; (c) and (d) show two different functional forms of failure loci before and after the failure transition points. Seeger's model was used within the IF region whereas a modified version of the power law equation was used within the PO or P-PO regions. The color scale represents the % error of calibrated model predictions compared to the experimental average at each loading orientation (IF, interfacial failure; PO, pullout failure; P-PO, partial pullout failure).

Table 5.5. Summary of calibrated parameters for an ideal exponential RSW failure model with six coefficients (based on final orientation KS-II data points).

Material and corresponding RSW scheme	**Calibrated equation:** $\boldsymbol{f = \frac{F_n}{F_{n0}} - \left[A_1 e^{\frac{F_s - F_{s0}}{t_1}} - A_2 e^{\frac{F_s - F_{s0}}{t_2}}\right] \frac{1}{F_{n0}} = 1}$					
	A_1	A_2	F_{s0}	F_{n0}	t_1	t_2
3G-980 FDWS	-0.008	264.71	-9.21	-255.12	5.47	4206.76
3G-1180 FDWS	-1.31E-5	132.23	-68.22	-140.57	7.33	664.59
3G-980 MWS	-2.03E-7	192.48	-40.01	-194.55	3.52	1150.40
3G-1180 MWS	-0.09	2.58	-946.87	-607.21	99.69	143.62

Table 5.6. Summary of calibrated parameters for two RSW failure models valid before and after failure transitions (based on final orientation KS-II data points).

Material and corresponding RSW scheme	$\boldsymbol{f = \frac{k(m + F_s)^n}{F_n} = 1}$			$\boldsymbol{f = \left[\frac{F_s}{S_S}\right]^a + \left[\frac{F_n}{S_N}\right]^b = 1}$			
	k	m	n	S_S	S_N	a	b
3G-980 FDWS	5.60	37.61	0.16	30.10	14	1.29	2.62
3G-1180 FDWS	2.88	7.54	0.34	32.18	7.66	10	1
3G-980 MWS	3.09	9.40	0.22	20.85	5.98	3.65	5.05
3G-1180 MWS	2.49	4.37	0.34	23.88	5.84	4.58	1

The modified RSW failure loci shown in Figure 5.16 and Figure 5.19, for tensile-bending and tensile-shear loading conditions, respectively, can be input directly into FEA models such as LS-DYNA's *MAT_100_DA weld material model which is considered a direct enhancement of the *MAT_100 weld material model because it accounts for the failure of spot welds under bending-dominated forces as well as shear and tensile forces. Further characterization of the shear-bending dominated loading cases with different bending arm lengths comparable to the spacing of spot-welded connections in multi-weld components can lead to additional improvements in current RSW failure prediction procedures.

5.5 Summary

In this study, the force-based RSW failure loci for two grades of 3G-AHSS were developed in shear-tensile and tensile-bending loading conditions. To observe the influence of nugget diameter on the size and general shape of the failure loci, different RSW process parameters were selected to produce different nugget sizes, referred to as FDWS and MWS, with high and low heat inputs, respectively. Comparison between several existing force-based RSW failure criteria revealed that the equation suggested by Seeger *et al.* [120] has the highest flexibility in capturing

the experimental trends specifically in shear-tension loading conditions characterized by KS-II tests with an average over-prediction error between 0.2% and 3.5% for various loading orientations. The criterion proposed by Song and Huh [165] was found the most conservative in the prediction of 3G-AHSS RSW failure in the same loading condition with between 9.2% and 22.3 under-predictions for various shear-tension loading conditions. Experimental shear and tensile failure load components of the KS-II tests revealed expansion of the failure locus as the shear component of applied force increased within the tensile-dominated loading orientations. Changes in the dominant failure mechanism of spot welds from PO/P-PO to IF were found responsible for such trends. None of the existing force-based RSW failure criteria were found capable of predicting such experimental behaviors. Suitable alternative functional forms were proposed to accurately capture the expansion/contraction of the failure loci in tensile-dominated loading orientations.

Assessing the validity of predictions by Seeger's failure loci in tension-bending conditions necessitated performing CP tests with different initial bending moment arm lengths. Novel DIC-based methodologies were developed to account for the severe coupon deformation and the effective bending arm reduction. Bending moments and load components throughout the tests were plotted against local projected nugget orientation and displacements, respectively, which allowed for the precise calculation of critical moments and load components applied to the projected RSW at the onset of failure. Results indicated that doubling the initial bending arm of the CP coupons from short arm to long arm geometry reduces the critical tensile forces ($F_{T,\,RSW}$) applied to the spot weld between 38.3% and 64.3% whereas the effective bending moment (M_{RSW}) at the onset of failure increases between 32.1% and 53.5% for the weld conditions considered. The FDWS conditions exhibited consistent total energy absorption capabilities ($E_{Total,\,RSW}$) as the bending arm increased. While the $E_{Total,\,RSW}$ remained virtually unchanged as the CP geometry changed in FDWS cases, the ratio of $E_{T,\,RSW}/\,E_{Total,\,RSW}$ decreased by 34.1% and 17.5% for 3G-980 and 3G-1180 FDWS conditions. Meanwhile, the $E_{M,\,RSW}/\,E_{Total,\,RSW}$ ratio increased by 34.1% and 34.7% upon changing the CP geometry from short arm to long arm for 3G-980 and 3G-1180 FDWS conditions, respectively. CP test results revealed an exponentially decreasing failure loci between the bending moment and normal force in contrast to the assumed convex relationship of Seeger's model. The Seeger RSW failure loci over-predicted the critical M_{RSW} of the short-arm geometry up to 66.1%. An exponential functional form was proposed and calibrated that successfully

addresses the deficiencies in the prediction accuracy of spot weld failure in tension-bending loading cases.

6 Characterization of Weld Group Failure under Predominantly Tensile-bending Loading[4]

6.1 Overview

The mechanical properties and failure behavior of groups of resistance spot welds made from two grades of third generation advanced high strength steels (3G-980 and 3G-1180) were investigated using two partially joined hat channel rails, which were separated under tensile-bending loading conditions. The component tests revealed 2.3% higher strength and 13% higher energy absorption for the 3G-980 weld-groups compared with the 3G-1180 weld-groups. Sequential joint failure occurred along the flanges, and deformation of the channels throughout the component tests were recorded using synchronized optical and thermal cameras. Channels made from 3G-980 showed more severe plastic deformation of the sidewalls and flanges (channel collapse) than those made from 3G-1180. More deformation of the 3G-980 channels increased the time before the initiation of the failure of the first weld by 25 s, on average. Moreover, welds along the flange of 3G-980 components failed predominantly in a ductile PO manner with average crack propagation lengths and tear-out areas that were 25% and 49% higher, respectively, compared with the predominantly brittle P-PO failures of 3G-1180 weld-groups. The combination of higher plastic work due to channel deformation, delayed joint failure, and ductile failure mode was responsible for the superior mechanical performance of 3G-980 weld-groups. A novel testing methodology comprising two half-sectioned spot welds on L-shaped coupons was proposed to observe the strain localization, failure initiation sub-regions, and failure propagation paths under tensile-bending loading conditions similar to the weld-group tests. While failure consistently initiated in front of the intrinsic notch in all the welds, the formed cracks propagated in two distinct manners. In the case of 3G-980 welds, the formed cracks deviated away from the faying interface and grew through the UCHAZ equiaxed grains, whereas, for 3G-1180 joints, the cracks propagated into the epitaxial structure of the FZ. Metallurgical characterizations for understanding the lower

[4] This chapter is composed of an under-review research paper as outlined in the statement of contributions. **Shojaee M**, Betiku O.T, Tolton C, Midawi ARH, Ramachandran D, Zhang T, Ghasssemi-Armaki H, Worswick M, Butcher C, Biro E. Investigating the mechanical properties and failure behavior of groups of resistance spot welds under tensile-bending loading conditions (under review).

susceptibility of 3G-980 FZ to cracking revealed 9.6% finer prior austenite grain size and 10% higher density of geometrically necessary dislocations at the FZ edge of 3G-980 joints as compared with that of 3G-1180. The combination of finer grains and higher dislocation density resulted in the formation of martensitic structures with 13% higher local yield strength than that of the 3G-1180 joints, effectively inhibiting crack propagation through the 3G-980 FZ.

6.2 Background

Automotive structural components rarely contain a single spot weld. Hence, it is critical to understand how sequential failure of spot welds affects BIW crash performance. As Schneider et al. [211] highlighted, single spot welds' energy absorption capability can significantly differ from that of weld-groups due to possible energy absorption contributions from BM plastic work and load-sharing between multiple joints. Caiman mode I test, developed by Okeeffe *et al.* [213], is used to characterize failure propagation along spot weld-groups under tensile-bending loading conditions.

This study investigates the mechanical performance and progression of failure under quasi-static tensile-bending loading of Caiman components manufactured from two grades of 3G-AHSS, 3G-980, and 3G-1180. Due to difficulty detecting the onset of individual weld failure from acquired load-displacement datasets, all Caiman tests were coupled with optical and thermal imaging techniques to track the progression of individual weld failure using thermal spikes associated with the plastic work of individual weld failure. Nonetheless, it was impossible to observe the initial stages of weld failure and track differences in crack propagation paths between the two steels because welds were hidden from the exterior. Hence, a modified version of the CP test with two half-sectioned spot welds was proposed for *in-situ* observation of strain localization regions during the initial stages of multiple RSW failures under tensile-bending loading conditions similar to the Caiman component tests. Weld failure analysis from the Caiman and DHCP tests consistently showed PO failures with plug ratios greater than unity for 3G-980 and P-PO failures with relatively lower plug ratios for 3G-1180 joints. To explain the observed differences in failure behavior of the investigated 3G-AHSS spot welds, suitable characterization techniques were utilized to characterize different mechanical and metallurgical aspects of the failure initiation regions, such as local properties of failure initiation sites, including YS, toughness, prior austenite grain sizes (PAGS), and dislocation densities. Results from this study clarify the mechanical

performance, critical failure initiation sites, and failure mechanisms as groups of resistance spot welds made of 3G-AHSS progressively fail under tensile-bending loading conditions.

6.3 Materials and Methods

6.3.1 As-received Materials

The same 3G-980 and 3G-1180 AHSS, as introduced in Chapter 3, were used in this study. More details about the investigated materials can be found in section 3.3.1.

6.3.2 Resistance Spot Welding

RSW was carried out using the same MFDC welder equipped with a Rexroth Bosch weld controller as described earlier in Chapter 3. 7 mm flat Cu-Cr dome-shaped electrodes were used for spot welding throughout this study. The electrodes were continuously cooled via 20°C water with a nominal flow rate of 6 L/min. Optimized RSW process parameters were selected based on the recommendations of the AWS D8.9 standard [35], and their values are outlined in Table 5.1.

Table 6.1. Summary of resistance spot welding process parameters used in this study.

Material	Squeeze time [ms]	Number of pulses	Weld time for each pulse [ms]	Cool time between pulses [ms]	Hold time [ms]	FDWS Welding current [kA]
3G-980	167	2	167	33	167	9.1
3G-1180	167	2	167	33	167	9.0

FDWS, electrode face diameter weld size (≈ 7.0 mm FZ diameter).

6.3.3 Caiman Mode I Mechanical Test

The Caiman mode I component test, developed by O'Keeffe [125], investigated the failure behavior of spot weld groups under predominantly tensile-bending loading conditions as two partially spot-welded hat channel rails separate. The Caiman mode I coupon geometry is shown in Figure 6.1 (a), which consists of a hat cross-section with flanges on both sides. Blanks were laser trimmed and formed to shape using tooling that consisted of a die, binder, and a punch (more details on the forming of the channels can be found elsewhere [125]). Two hat channels were joined together using 13 equally distanced resistance spot welds along part of the length of each flange, as shown in Figure 6.1 (b). A weld pitch of 26 mm was adopted to avoid shunting effects. The fixtures implemented to mount the Caiman specimen on the tensile frame are shown in Figure 6.1 (c), where two sets of inner and outer bosses clamp the ends of the unwelded portion of the hat

channels, which are mounted within the tensile frame using custom-designed clevises. The bottom clevis is clamped in the grips of the tensile frame and stays stationary throughout the tests, whereas the top clevis is threaded into the crosshead and moves up at a rate of 50 $mm.min^{-1}$. It is noted that the strain rate of the component tests were not the same as the single spot weld characterization techniques reported in previous chapters of this work. The inconsistency in strain rate values may lead to errors if finite element works are to be performed in future. The Caiman samples were tested on an MTS model 45 servo-electric universal tester equipped with a 100 kN load cell. The tests were terminated after a total crosshead displacement of 250 mm (~5 min test run time). The Caiman tests were repeated three times for each investigated 3G-AHSS to ensure the acquired load-displacement data and RSW failure responses were repeatable. The Caiman experiments were recorded using a pair of optical Point Grey Research GRAS-50S5M-C 5.0 MP cameras, providing side-view images of the experiments at a rate of 5 frames per second. A pair of Telops-IR-2K thermal cameras were also used to provide thermal images from the top and bottom of the components (Figure 6.1 (d) and (e)). Post-processing of thermal photos was carried out using RevealIR software.

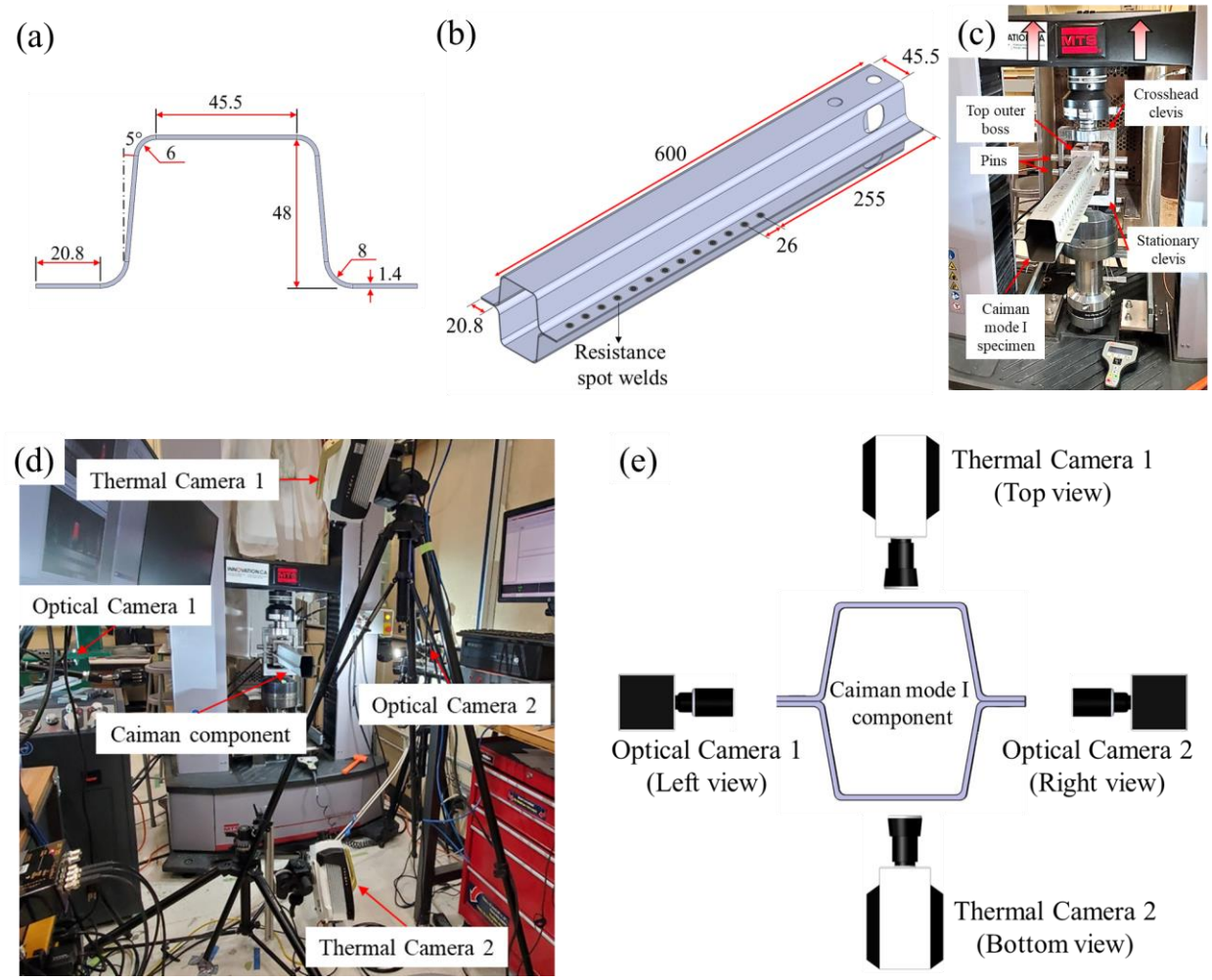


Figure 6.1. (a) Hat channel cross-section and (b) resistance spot-welded Caiman mode I component geometry and dimensions (all dimensions are in mm); (c) Caiman component installed on the MTS tensile frame using a fixture consisting of clevises, pins, inner and outer bosses (inner bosses not visible). (d) and (e) show the location of cameras to record optical and thermal images throughout the tests.

6.3.4 Double-half CP (DHCP) Mechanical Test

Tolton *et al.* [214] correlated thermal spikes on the Caiman mode I components flange to individual spot weld failure during quasi-static tensile loading of the specimens. However, Tolton *et al.* [213] and O'Keeffe [126] indicated that a detailed understanding of RSW failure mechanisms was impossible due to the critical failure initiation sites hidden from the exterior. Mohamadizadeh *et al.* [127] proposed a double-half weld testing geometry, allowing *in-situ* observation of damage evolution during shear and tensile loading of spot welds. In this work, a similar approach is used to develop a modified version of the CP coupon [115] with two half-sectioned resistance spot welds on the flange that allow *in-situ* observation of the initial stages of spot weld failure under

tensile/bending-dominated loading conditions (See Figure 6.2). It is important to note that the spot weld loading in the CP test is similar to that experienced during Caiman mode I test. Spot welds were cut along the centerline to create direct access to the weld cross-section for strain measurement using DIC analysis. Two Point Grey Research GZL-CL-41C6M-C cameras were placed at the front and back of the specimen (Figure 6.2 (d) and (e)) to ensure capturing the failure initiation and propagation path of both spot welds. The DHCP tests were conducted using a standard Shimadzu tensile frame with a crosshead velocity of 10 $mm.min^{-1}$. Reference double full section CP tests were also conducted for both materials, which could be compared against the DHCP tests. DHCP Tests were repeated five times for each material to ensure repeatability of the observed failure behaviors. For the DIC imaging, a random black-and-white speckle pattern was created on the sectioned surface of the welds. Post-processing of test footage included full-field Hencky (logarithmic) strain measurements using Vic2D software. Table 6.2 outlines the adopted DIC post-processing parameters.

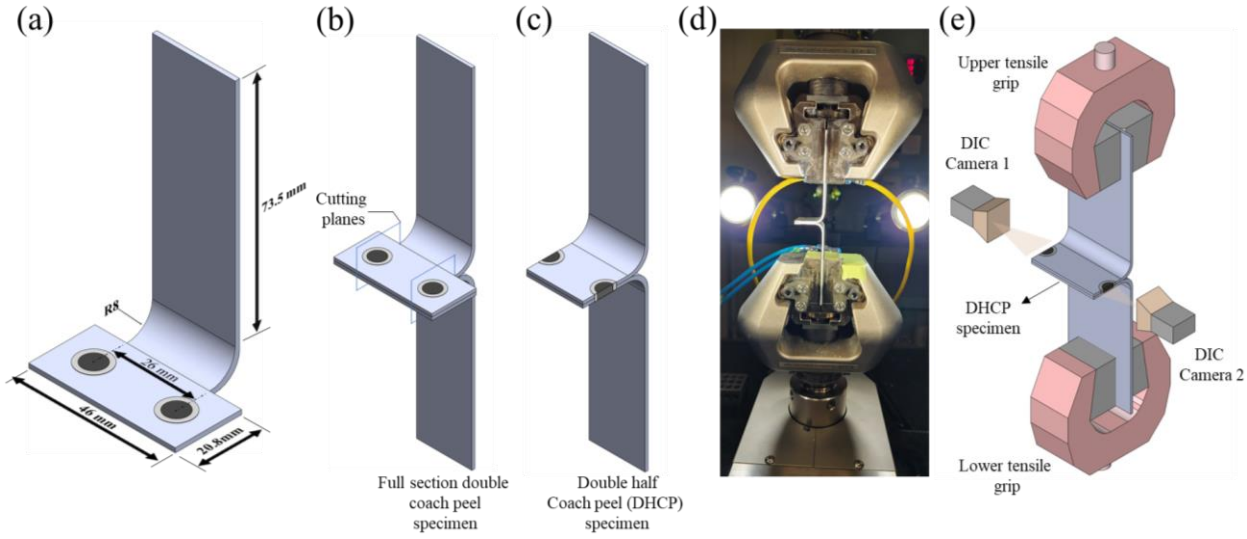


Figure 6.2. (a) DHCP coupon geometry and dimensions, including the location of spot welds; (b) DHCP specimen before sectioning the two spot welds; (c) DHCP specimen after sectioning the spot welds through their centerlines; (d) DHCP specimen installed on a tensile frame; (e) all DHCP tests were accompanied with DIC technique for in-situ strain measurement. The schematic shows the placement of the DIC cameras.

Table 6.2. Summary of DIC post-processing parameters.

Software package	VIC 2D v7 from Correlated Solutions
Subset size	21 pixels
Step size	7 pixels
Strain filter size	5
Subset weights	Gaussian center-weighted
Strain filter weights	Gaussian-90% center-weighted
Virtual strain gauge	49 pixels (0.245 mm)

6.3.5 Metallurgical and Mechanical Characterizations

Resistance spot-welded samples were sectioned through the centerline and prepared for microstructural observation using standard metallography procedures. The sample preparation procedure included mounting in conductive resin, coarse and fine grinding with SiC pads, polishing up to 1 μm finish using a diamond paste, and etching with 2% Nital solution (98% Ethanol + 2% Nitric acid). A Keyence optical microscope was used for microstructural observation, depth mapping, and nugget size measurement. A field emission scanning electron microscope at an accelerating voltage of 20 kV was used for the fractography of the failed joints.

Electron backscatter diffraction (EBSD) was used for microstructural characterization and measuring the prior austenite grain (PAG) sizes of the RSW failure initiation sites. Conventional sample preparation techniques were used, followed by a final vibratory polishing step. Pattern acquisition was carried out at a 0.5 μm step size. The PAGs were revealed using the Kurdjumov-Sachs (K-S) orientation relationship in ARPGE software [215].

A Nanovea-M1 instrumented indenter was used to estimate the local yield strength of various regions for the investigated 3G-AHSS spot welds according to the procedure outlined by Midawi *et al.* [216]. Upon attainment of the characteristic S-shaped load-displacement curves of various RSW sub-regions, the yield strength was calculated according to Equation 6.1:

$$\delta_y = \frac{F_S}{3.28 \times \pi \times a^2} \qquad 6.1)$$

where δ_y is the yield strength, a is the radius of the indenter, and F_S is the force corresponding to the highest plastic strain at the edges of the indenter before material pileup. The value of F_S can be identified by constructing a tangent to the resultant load-displacement curve. This technique has been adopted to determine the yield strength of various regions in resistance spot welds of dual-

phase (DP) AHSS [140], gas metal arc welded X80 pipelines [217], and interstitial free (IF) steel brazed beads [218]. A nearly flat indenter with a diameter of 50 μm and a peak load of 15 N was used for indenting different RSW sub-regions. The indenter approach speed, contact load, loading rate, and unloading rate were adjusted to 3 μm/min, 20 mN, 30 N/min, and 30 N/min, respectively. At least ten indents were made in each RSW sub-zone, and the reported yield strength error bars are 95% confidence intervals.

6.4 Results

6.4.1 DHCP Test Results

DHCP tests were performed on the investigated FDWS 3G-AHSS spot welds to pinpoint the critical failure initiation sub-regions and visualize the strain localization as two adjacent half spot welds fail under predominantly tensile and bending loads, similar to loads experienced during the Caiman mode I test. Results from Chapter 5 established that the mechanical performance of resistance spot welds under tensile-bending loading conditions is a function of geometry and BM ductility. Hence, a comparable weld pitch and initial bending arm were selected between the DHCP and Caiman components. Figure 6.3 illustrates the representative load-displacement response and major strain (e_1) distributions of the 3G-980 spot weld cross section during DHCP testing. Figure 6.4 shows the same data for a representative 3G-1180 DHCP test.

The peak load measured from the DHCP tests was 2.84 ± 0.32 kN and 2.05 ± 0.19 kN for the 3G-980 and 3G-1180 FDWS spot welds, respectively. The stepped unloading response of the load-displacement curves is due to the two spot welds not failing simultaneously. In the case of the 3G-980, it is observed that failure of the first weld is initiated via strain localization in front of the notch region (FGHAZ) (Figure 6.3 (b) and (c)) followed by crack propagation away from the faying interface and towards the yielded joint leg in the BM (Figure 6.3 (d)). A similar failure path was observed from the second weld approximately 12 s after the first weld failure initiated (Figure 6.3 (g)). Upon detachment of one RSW leg, the spot welds started more severe out-of-plane rotation, and BM tear-out occurred due to the unbalanced loading of the parent sheets (Figure 6.3 (h) and (i)). As for the cross section of 3G-1180 spot welds, the first weld failed persistently in IF mode (Figure 6.3 (e)), identified via propagation of the formed cracks into the FZ followed by P-PO failure of the second spot weld with strain localization in front of the notch and FZ boundary (Figure 6.3 (g) and (h)). A critical difference between the sequential PO failure of the 3G-980 joint versus the P-PO failure of the 3G-1180 joints was the percentage of strength loss after the

occurrence of the first failure. The average strength loss from the first weld failure was 10.5% ± 1.2% versus 36.6% ± 10.5% for PO of 3G-980 and IF of 3G-1180 DHCP tests, respectively. Another noticeable difference between the DHCP tests of 3G-980 and 3G-1180 was related to displacement to failure (total rupture). On average, the displacement to failure of DHCP tests was 23.4% higher for 3G-980 specimens (26.5 mm for 3G-980 vs 21.5 mm for 3G-1180). The higher displacement of DHCP tests for 3G-980 is related to the higher ductility of the material and their PO failure. The lower displacement to failure of 3G-1180 spot welds can also be elucidated via the lower opening angle between the faying surfaces at the onset of the first weld failure.

Load displacement response of the CP tests with two full-section welds (without cutting the two welds in half) are also included in Figure 6.3 and Figure 6.4 using dashed red lines. On average, the full-section CP tests exhibited 26.5% and 16.2% higher strengths for 3G-980 and 3G-1180 specimens compared to the corresponding DHCP tests. The lower strength of the half-sectioned welds is associated with the lower load-bearing area of the joints. Lower displacement to failure of the DHCP tests is primarily attributed to the shorter crack propagation path during the failure of half-sectioned joints.

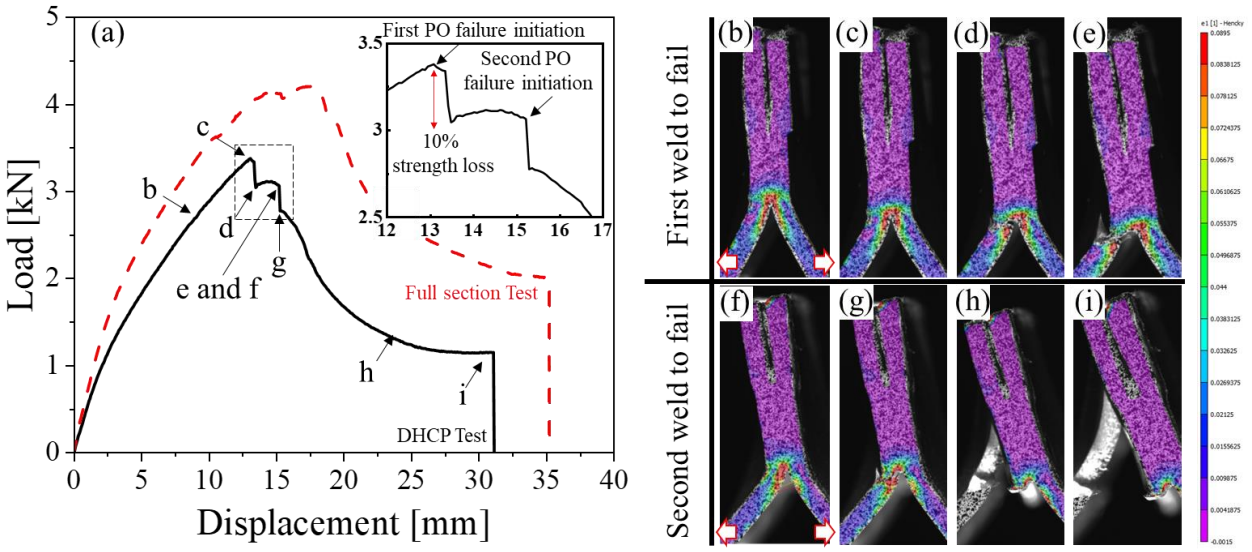


Figure 6.3. (a) Representative load-displacement characteristics of the 3G-980 DHCP test with a magnified inset highlighting the strength loss after the first PO failure. Full section double coach peel test's load-displacement response is also included for comparison. (b-e) show the distribution of major principal strain (e_1) for the cross-section of the first half weld to fail at different crosshead displacements. (f) to (i) show the distribution of e_1 at different crosshead intervals for the second half weld failure. DIC strain maps highlight a higher susceptibility of failure through yielded BM of the 3G-980 spot welds during combined tensile-bending loading.

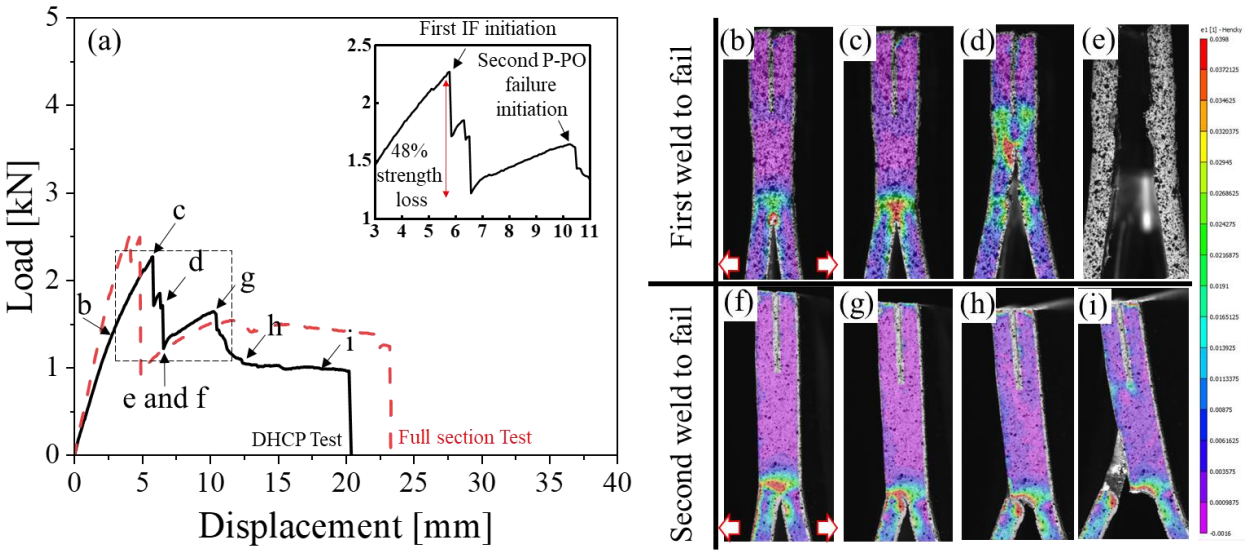


Figure 6.4. (a) Representative load-displacement characteristics of the 3G-1180 DHCP test with a magnified inset highlighting the strength loss after the first IF. Full section double coach peel test's load-displacement response is also included for comparison. (b-e) show the distribution of major principal strain (e_1) for the first half weld cross-section to fail at different crosshead displacements. (f) to (i) show the distribution of e_1 at different crosshead intervals for second half weld failure. DIC strain maps highlight a higher failure susceptibility through the FZ of the 3G-1180 spot welds during combined tensile-bending loading.

Figure 6.5 (a) and (b) highlight differences in the extent of parent metals' plastic deformation during DHCP tests of 3G-980 and 3G-1180 spot welds. Images illustrate a three-time higher opening angle for the loaded side of the 3G-980 half joints compared with the opening angle of the 3G-1180 DHCP tests. Strain contours in these images also indicated that a more severe reduction in the effective bending arm on the 3G-980 joints leads to strain localization in the BM region, away from the FZ. Interestingly, the cross-sectional view of the 3G-980 failed joint, shown in Figure 6.5 (c), revealed necking in the BM region resulted from plastic flow in the parent metal up to the UTS value. The higher strains in the necking region are further validated by the more than three times higher strain levels of 3G-980 joints (maximum e1 value of 10.96% for 3G-980 vs 3.47% for 3G-1180 DHCP tests), leading to further plastic flow in the 3G-980 BM. On the other hand, the stiffer 3G-1180 parent metal more effectively maintained the initial geometrical configuration, with an opening angle of approximately a third of that of 3G-980 DHCP tests. Strain contours indicate negligible strain levels in the BM of the 3G-1180 half joints. Strain localization and failure consistently occurred inside the FZ of 3G-1180 DHCP joints.

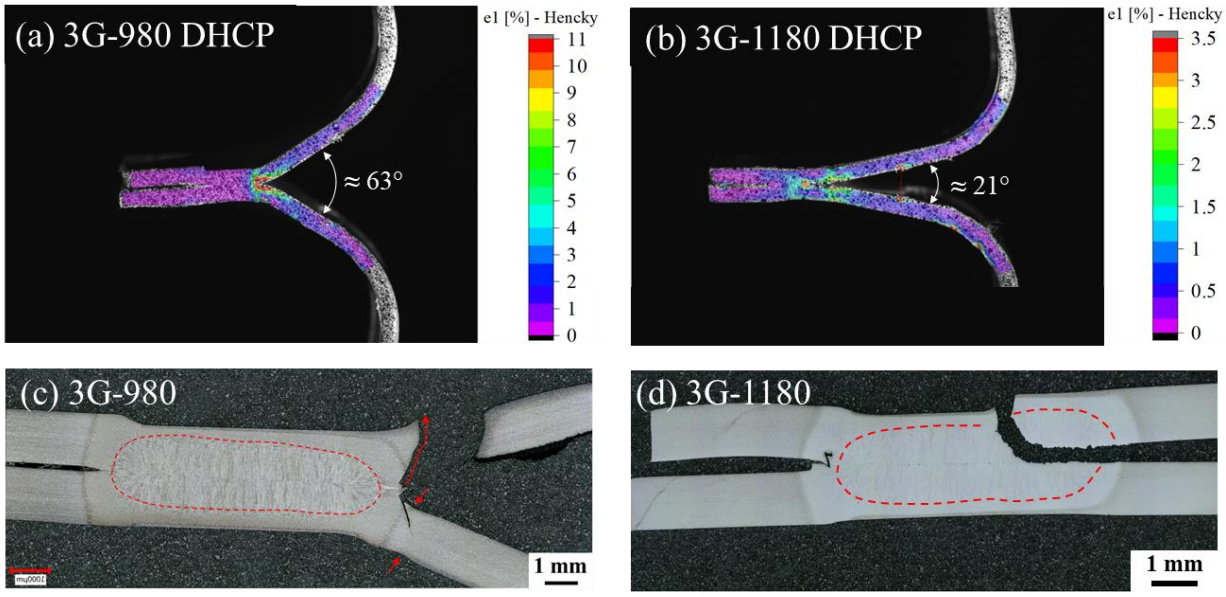


Figure 6.5. Differences in opening angle of the parent metals for (a) 3G-980 and (b) 3G-1180 DHCP tests. (c) and (d) illustrate a representative cross-sectional view of the failed joints after the DHCP tests.

6.4.2 Caiman Test Results

6.4.2.1 Global Load-displacement Response and Failure Sequence Tracking

The resultant load-crosshead displacement curves typically characterize spot welds' strength and energy absorption capability. The load-displacement curves for typical single spot weld characterization techniques show an upward loading trend to a peak load, identified as the weld strength, and unloading upon failure initiation. The unloading stage of the load-displacement curves (after peak load) can be smooth or abrupt depending on the failure type (PO/P-PO vs. IF). The Caiman weld groups tested in this study show a rather different load-displacement shape, as shown in Figure 6.6 (a) and (b), with a characteristic sequential unloading associated with the failure of multiple welds as the test continues. Figure 6.6 (d-h) and (j-n) correspond to optical images from the left view of the components taken at different crosshead displacements. On average, strength, energy up to peak load, and total energy absorption values for the 3G-980 specimens were 2.3%, 13%, and 9.2% higher, respectively, than those measured from the tests on the 3G-1180 weld groups.

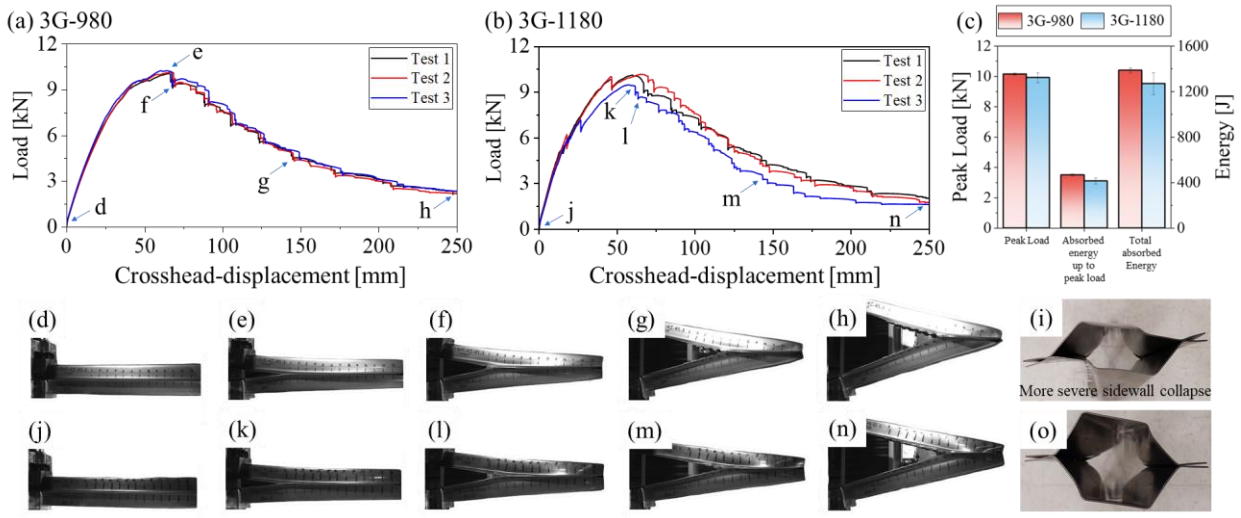


Figure 6.6. (a) and (b) experimental quasi-static load- crosshead displacement characteristics, and (c) summary of peak load and absorbed energy of the Caiman mode I component tests. (d)-(h) and (j)- (n) left side view of the components at different crosshead-displacement intervals highlighted in (a) and (b). (i) and (o) top view of the components after 250 mm crosshead displacement comparing the sidewall and channel plastic deformation between the investigated 3G-AHSS Caiman components.

Figure 6.7 and Figure 6.8 show snapshots from the thermal videos at different displacements for representative 3G-980 and 3G-1180 Caiman tests, respectively. Thermal images in these figures show radiometric temperature increase due to plastic deformation heat dissipation associated with joint failure and flange deformation at different crosshead displacements. These tests were performed at quasi-static strain rates, allowing enough time for the dissipation of the generated heat to the surrounding environment. Hence, the low-temperature spike (4-5 °C) compared with more than 30 °C thermal spike of high strain rate (dynamic) Caiman tests reported by Tolton *et al.* [125]. Comparing the thermal images of quasi-static Caiman tests by Tolton *et al.* [125] on fully martensitic USIBOR® 1500 and 3G-AHSS of current study provided a means to contrast strain energy dissipation throughout the deforming channels. In the case of Caiman components made of fully martensitic USIBOR® 1500, thermal spikes were concentrated around the vicinity of spot welds on the flanges. However, thermal profile line scans in Figure 6.7 and Figure 6.8 exhibited temperature increase both at the location of spot welds and the surrounding flange material which is indicative of the more ductile 3G-AHSS BM plastic deformation throughout the tests and channel collapse (Figure 6.7 (f) and Figure 6.8 (f)).

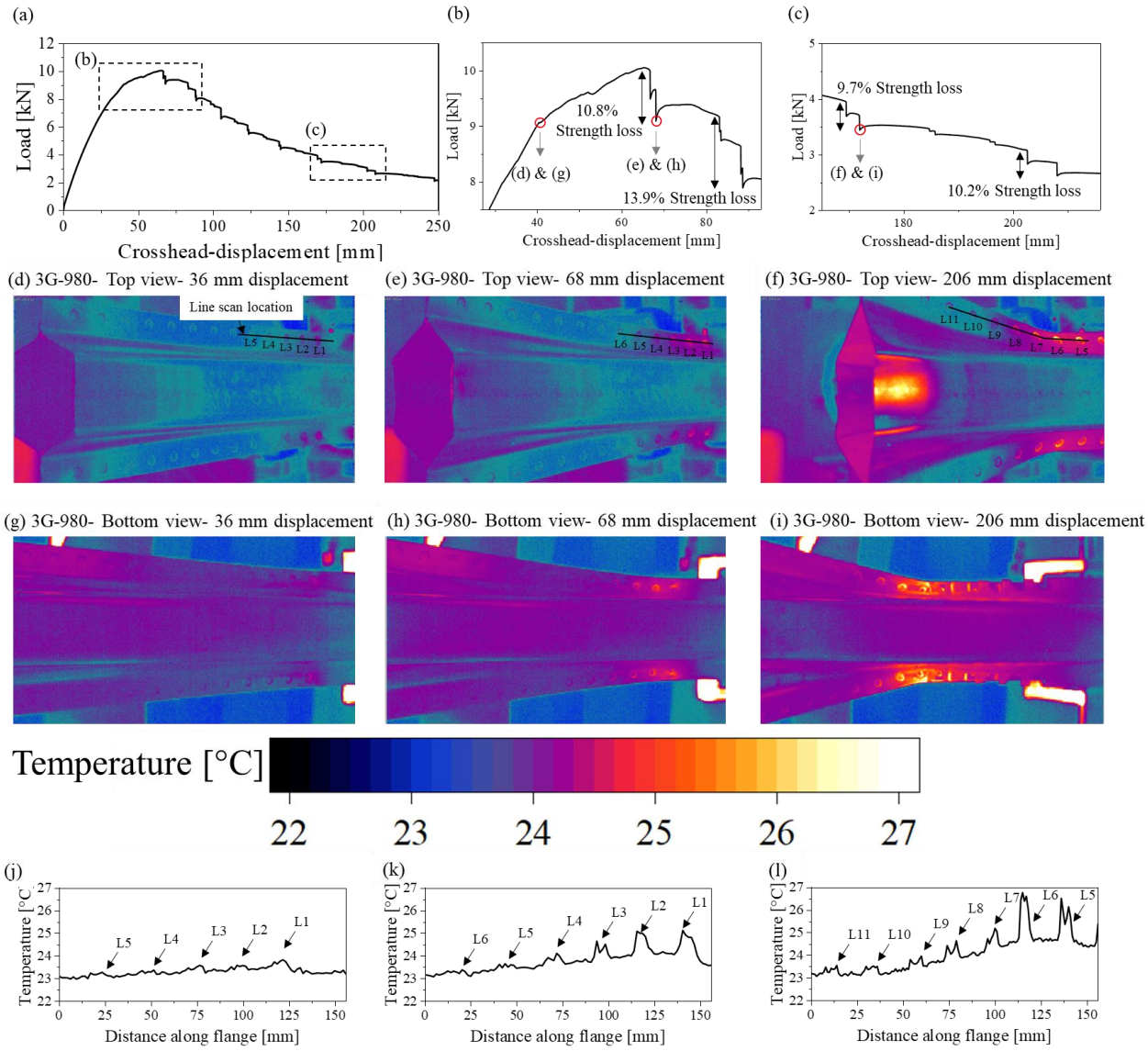


Figure 6.7. (a) Load- displacement of a 3G-980 quasi-static Caiman mode I test; (b) and (c) show a magnified view of (a) at different displacement intervals. (d)-(i) top and bottom view thermal images of the same test highlighting heat generation associated with weld failure and flange/channel deformation and tearing. (j)-(l) are temperature line scans from top view thermal images shown in (d)-(f).

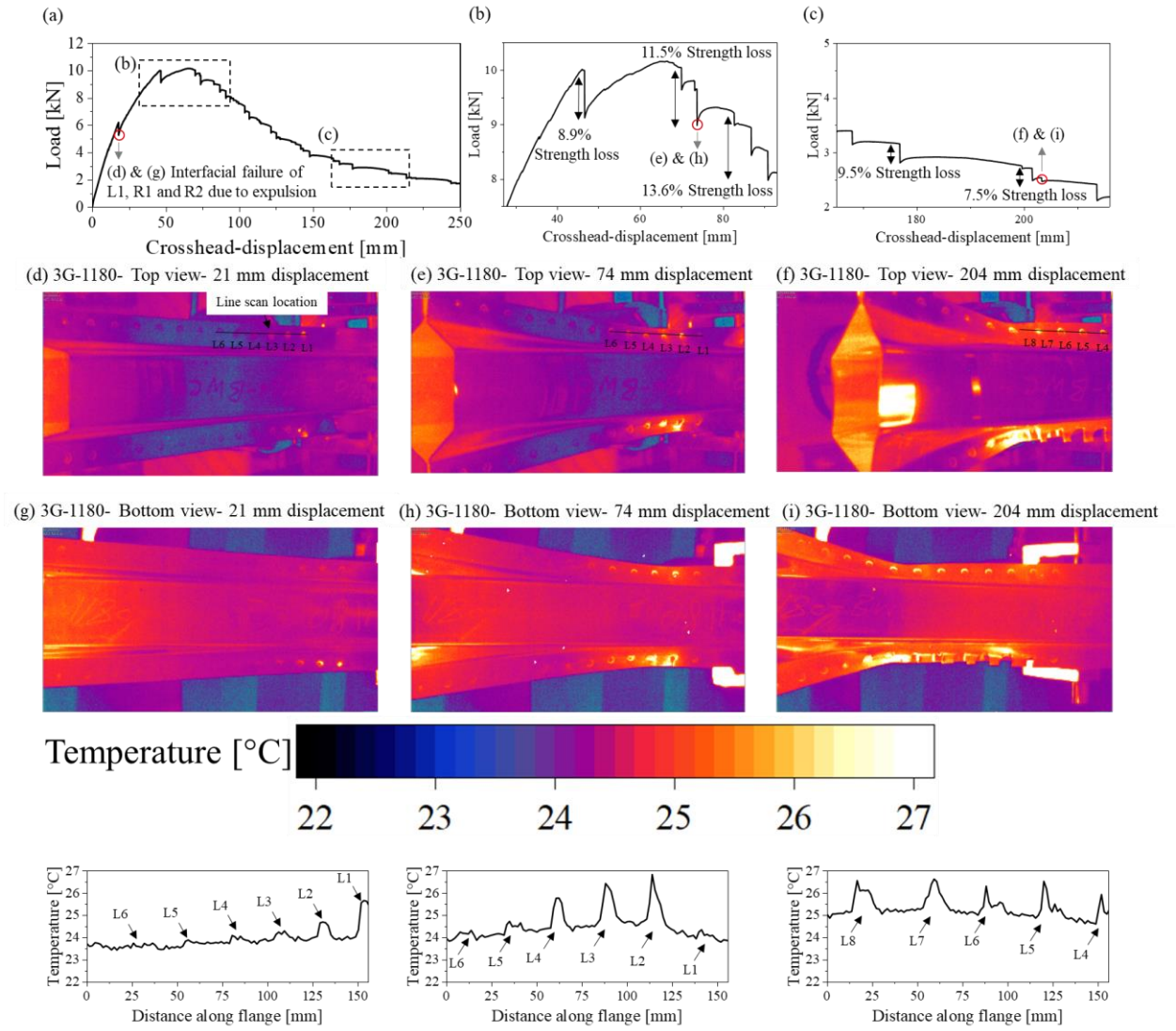


Figure 6.8. (a) Load- displacement of a 3G-1180 quasi-static Caiman mode I test. (b) and (c) show a magnified view of (a) at different displacement intervals. (d)-(i) top and bottom view thermal images of the same test highlighting heat generation associated with weld failure and flange/channel deformation and tearing. (j)-(l) are temperature line scans from top view thermal images shown in (d)-(f).

The strength losses recorded in the Caiman tests were muted compared to those of the DHCP tests, which implies the failure of multiple welds in the Caiman channels. The load drops in the acquired Caiman load-crosshead displacement response could correspond to simultaneous failure of spot welds on both flanges, sequential failure of spot welds on the left and right flange, or, in a few cases, simultaneous failure of multiple welds on one side of the flange. These possibilities complicated distinguishing individual joint failure along the weld group and comparing the failure rate among the two investigated components merely from the acquired load-

displacement responses. Alternatively, the thermal images were synchronized with the recorded load-displacement histories, which assisted in determining crosshead displacement corresponding to individual weld failure.

The spot weld failure propagation rate through the weld-groups was compared by plotting the "crack" opening length as a function of crosshead displacement in Figure 6.9. Although both weld groups exhibited similar failure rates, evidenced via comparable slopes of the opening length plots, the 3G-1180 weld-group initiated failure earlier and consistently showed higher opening lengths at any given crosshead displacement than the 3G-980 weld groups. The superior energy absorption of 3G-980 Caiman assemblies in comparison with the 3G-1180 Caiman tests is partly related to the higher amount of plastic work dissipated due to more severe deformation of the 3G-980 sidewalls and flanges (as depicted in Figure 6.6 (i)). According to the side view images in Figure 6.6, the end of 3G-980 rails starts collapsing earlier, which reduces the effective load on the spot welds [214]. Another factor contributing to the superior energy absorption of 3G-980 weld groups is their more favorable failure mode, as discussed below.

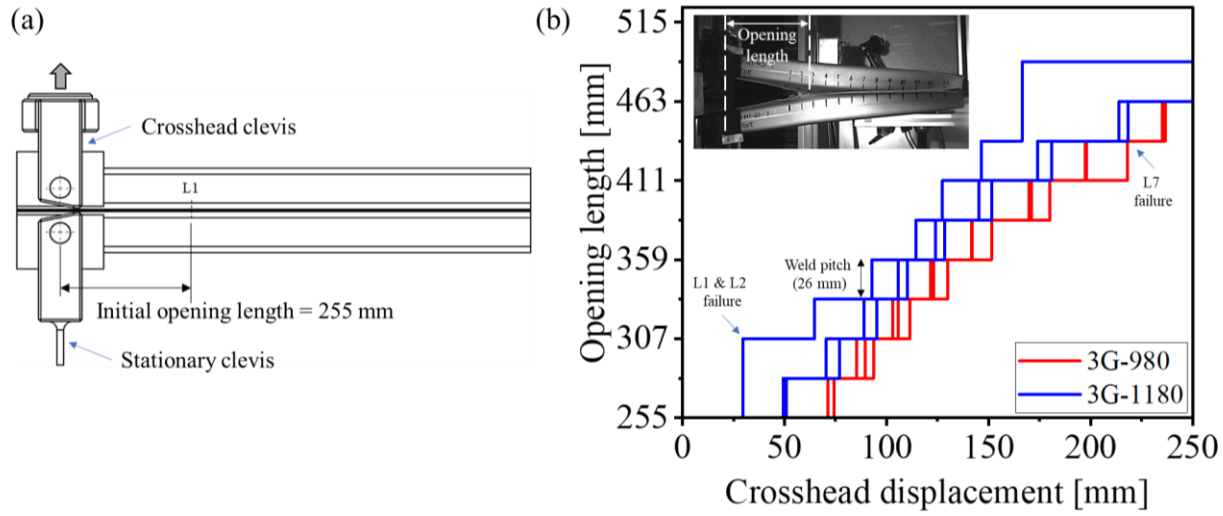


Figure 6.9. (a) the "crack" opening length is defined as the instantaneous distance from the central axis of the stationary clevis until the last failed spot weld. (b) Comparison between the Caiman component "opening length" at different crosshead displacements. Individual weld failure was determined using a combination of thermal videos and optical images. The data shown corresponds to three Caiman test repetitions of each investigated 3G-AHSS.

6.4.2.2 Failure Behavior and Fractography of Caiman Weld Groups

Examinations of the Caiman mode I test revealed consistent PO failure with plug ratios greater than unity for 3G-980 spot welds, as illustrated in Figure 6.10 (a). Failure was initiated in

front of the notch (within UCHAZ) due to stress concentration (Figure 6.10 (c)) and propagated away from the faying interface (Figure 6.10 (d)). Thereafter, the crack propagated around the nugget periphery, followed by BM tearing (Figure 6.10 (e) and (f)), resulting in a joint failure with a plug ratio greater than unity. It is noted that BM tearing was also noticed in the tensile-bending loading conditions outlined earlier in Chapter 5, which is believed to be caused by the eccentric loading of the nugget. No IF was observed for 3G-980 weld groups, even for joints where expulsion of molten metal occurred during welding.

In the case of the 3G-1180 spot welds (Figure 6.10 (b)), although failure initiates from the UCHAZ where the notch existed, cracks propagated inside the epitaxial structure of the FZ. Next, the cracks were redirected to the sheet surface (Figure 6.10 (g) and (h)), and lastly, BM tear-out occurred (Figure 6.10 (i) and (j)). Overall, the 3G-1180 joints exhibited a higher tendency to fail either interfacially (in the case of joints accompanied with expulsion) or in a P-PO manner, resulting in a relatively lower plug ratio than failed joints from the 3G-980 weld groups.

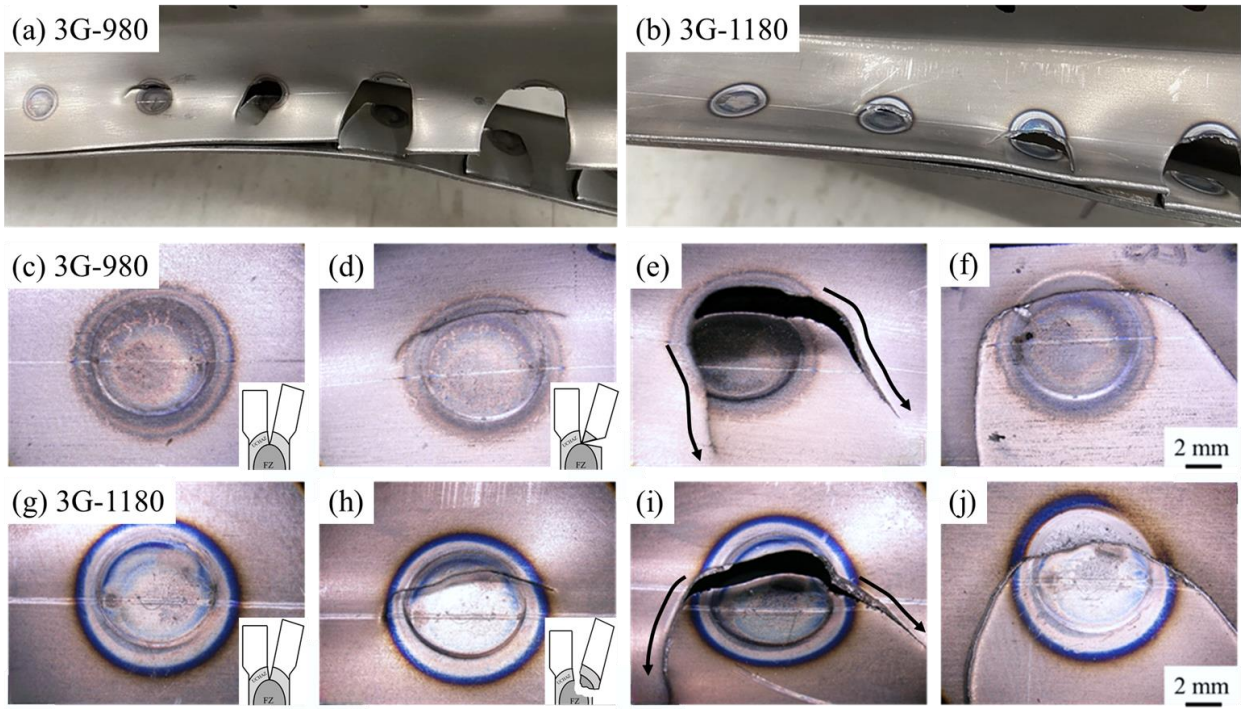


Figure 6.10. Failure behavior of spot welds after quasi-static Caiman mode I mechanical tests for (a) 3G-980 and (b) 3G-1180 spot welds. (c-j) show a detailed view of the spot welds in (a) and (b). (k) and (l) are cross-sectional views of spot welds shown in (f) and (j), respectively.

The micrographs shown in Figure 6.11 (a) and (d) demonstrate the crack initiation and propagation paths from a cross-sectional point of view. Figure 6.11 (a) illustrates severe plastic deformation level, as evidenced by the high opening angle between the failed and intact joint leg. On the other hand, Figure 6.11 (d) highlighted a fast fracture response with low deformation of the parent metal surrounding the 3G-1180 joint. Figure 6.11 also depicts inverse pole figure (IPF) maps of the failure initiation sites and crack propagation directions after the Caiman mode I test. In the case of IPF maps shown in Figure 6.11 (b) for the 3G-980 failed joint, it was observed that the columnar solidified structure of the FZ edge effectively resisted cracking in the tensile-bending loading mode of the Caiman tests. As shown in Figure 6.11 (c), failure proceeded through the equixed grains of UCHAZ. As for the 3G-1180 failed joints, Figure 6.11 (e) shows transgranular crack propagation through the UCHAZ and FZ structure with comparatively less jagged propagation, indicating lower energy absorption throughout the failure sequence than the 3G-980 welds.

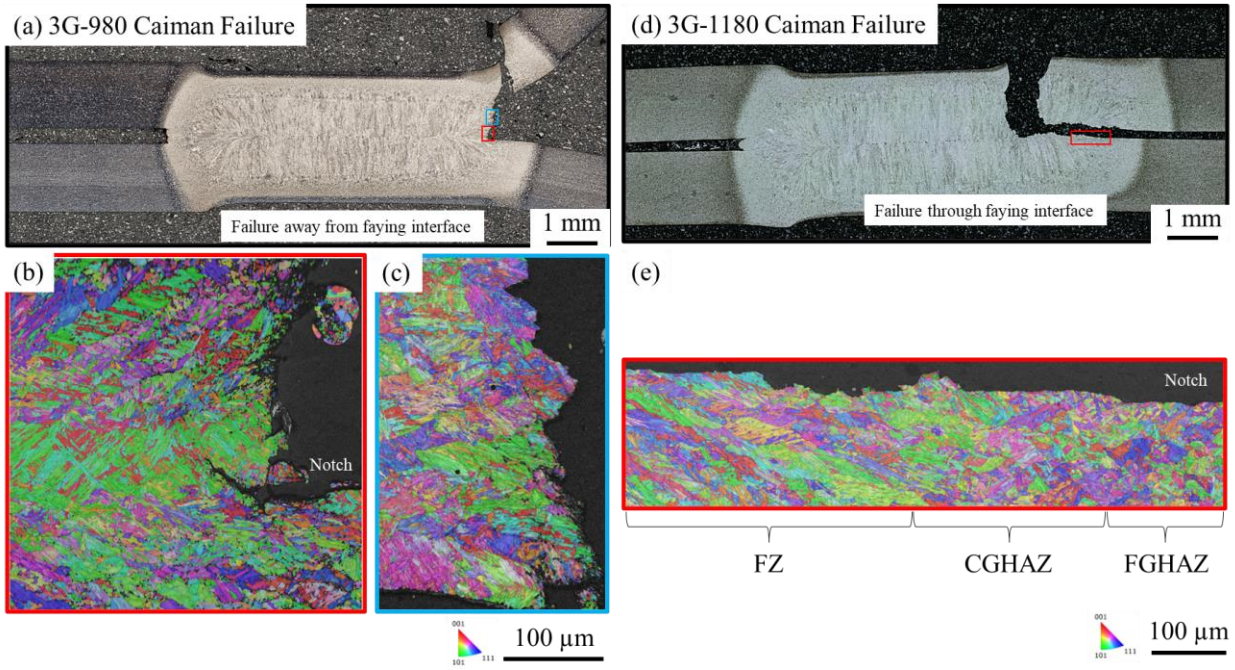


Figure 6.11. (a) and (d) cross-sectional view of spot welds shown in Figure 6.14 (f) and (j), respectively. (b-c) and (e) show inverse pole figure EBSD scans of the failure initiation regions and crack propagation paths after the Caiman mode I test.

Figure 6.12 shows three-dimensional depth maps and the fracture morphology of both materials' last failed joints from the Caiman flanges. The fracture morphology of the failed

weldments indicated a ductile fracture for 3G-980 spot welds, as evidenced by elongated dimples formed from microvoid coalescence (Figure 6.12 (b-e)). The 3G-1180 failed joint exhibited a predominantly fast fracture mechanism, as evidenced via the quasi-cleavage facets, and a relatively smaller portion of failure in ductile mode (Figure 6.12 (g-j)).

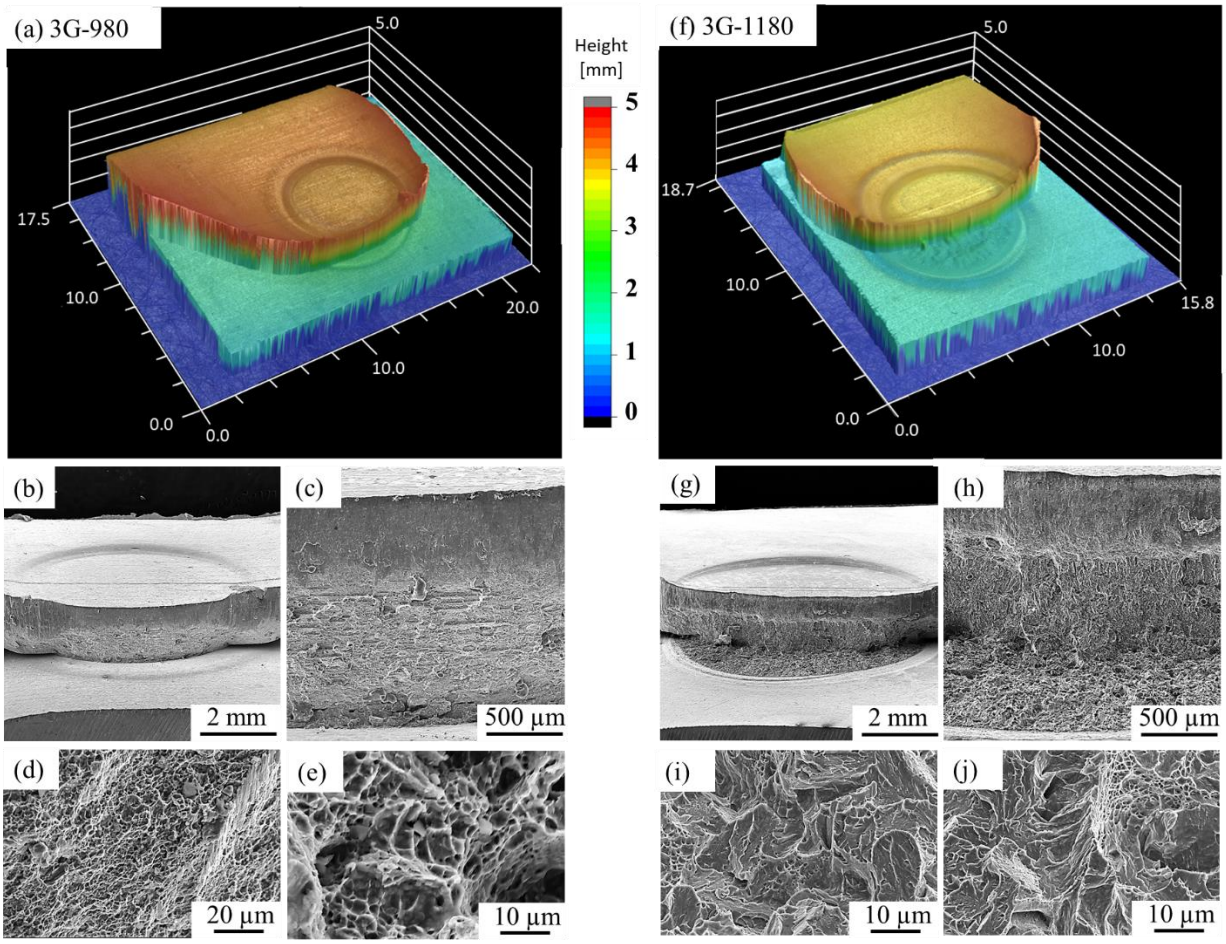


Figure 6.12. (a) and (f) Three-dimensional depth maps of the failed 3G-980 and 3G-1180 spot welds shown previously in Figure 14 (f) and (j), respectively, upon performing Caiman mode I quasi-static tests. (b)-(e) and (g)-(j) show scanning electron microscope fractography images of failed interfaces at different magnifications.

The plug ratio of failed spot welds, defined as the ratio between the diameters of the pullout region and the nugget, are higher than unity in all cases due to large BM tear-out regions. The moment arm that exists between the loading axis and the weld nugget forces one side of the spot welds on the flanges to undergo concentrated tensile stresses due to the resultant bending moments while the opposite side experiences relatively lower tensile stresses. The BM tear-outs observed

in Figure 6.10 (f) and (j) are comparable to the failure mechanism during coach peel testing of single spot welds, as outlined by Pouranvari *et al.* [113].

Instrumented indentation experiments were conducted to quantify the local yield strength of different RSW sub-regions and compare them against each other for both considered 3G-AHSS spot welds. Figure 6.13 (a) and (b) show representative load-displacement indentation curves for each RSW sub-region of 3G-980 and 3G-1180, respectively. Variation in the displacements shows significant alteration of the local mechanical properties, which is representative of the rather large changes in local microstructures. A strong correlation exists between the average hardness values of various subregions shown in Figure 3.12 (c) and the local yield strength averages outlined in Figure 6.13 (c). The lowest RSW yield strengths corresponded to the softened SCHAZ of 3G-1180 and BM of 3G-980. Although the failure is always initiated within the UCHAZ region (as shown via DIC strain maps in Figure 6.3 and Figure 6.4 earlier) due to the high-stress concentration at the notch, the yielding of the 3G-980, BM redirected the formed cracks away from the FZ edge. However, the higher structural rigidity of the 3G-1180 channels compared to 3G-980 channels retarded strain localization in the weakest 3G-1180 RSW sub-region (SCHAZ) with brittle crack propagation through the FZ. Results indicated that the yield strengths of UCHAZ and FZ of 3G-980 are 13.4% and 9.8% higher than those of 3G-1180 joints, respectively. The higher local hardness and YS of the FZ edge for 3G-980 joints are related to the microstructural features in this zone, described in detail below.

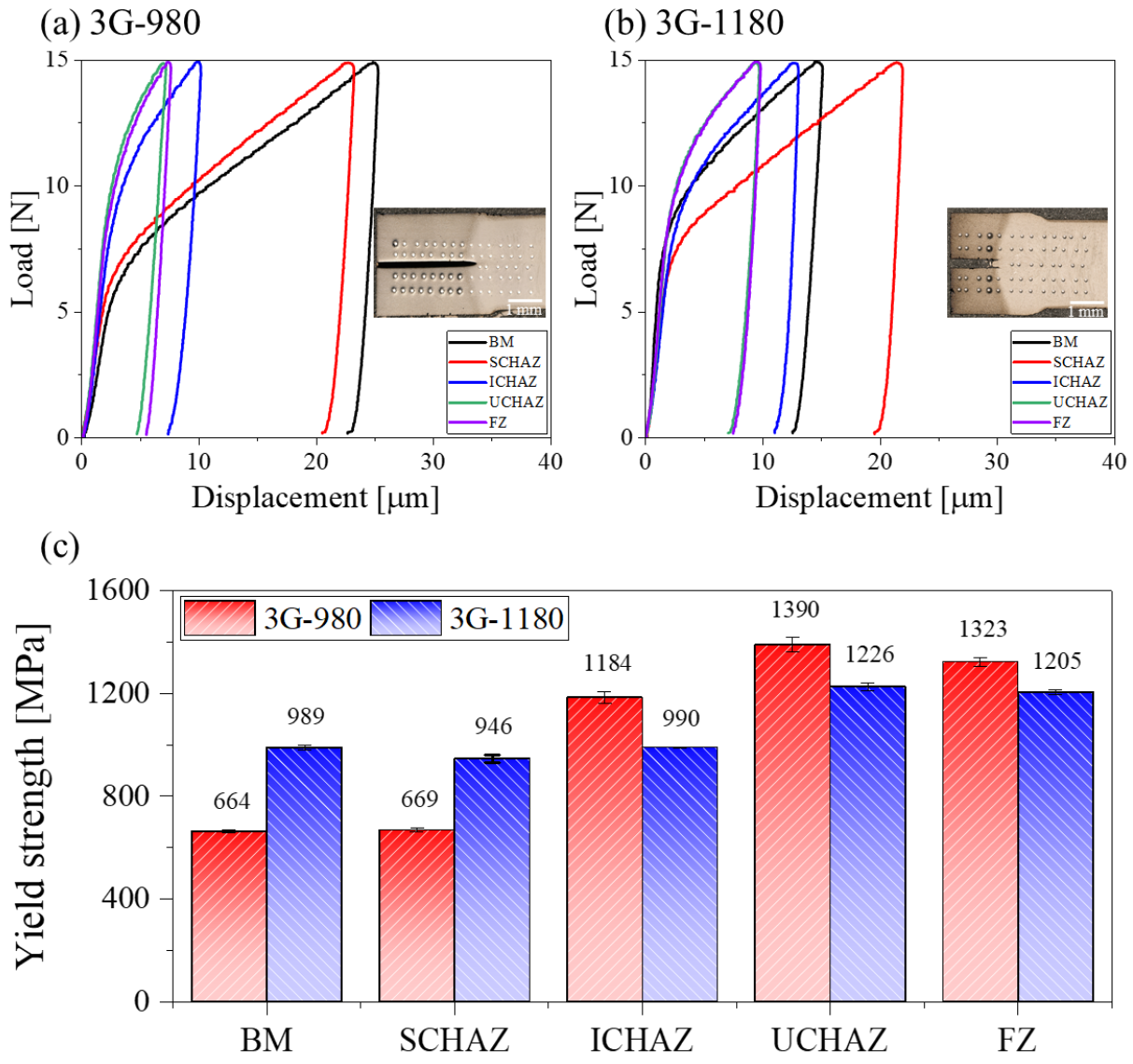


Figure 6.13. Representative load-displacement curves were obtained through instrumented indentation tests for various sub-regions of (a) 3G-980 and (b) 3G-1180 resistance spot welds. (c) Summary of yield strengths calculated using Equation 6.1 for different RSW sub-zones.

6.5 Discussions

The 3G-980 RSW joints exhibited superior mechanical properties, specifically higher load bearing capacity, energy absorption capability, and plug ratios, in comparison with the 3G-1180 joints upon sequential failure of the welds under tensile-bending dominated loading conditions of the Caiman and DHCP tests. Both parent metals ductility and metallurgical factors related to the FZ edge of the investigated spot welds are believed to be responsible for the higher susceptibility of full nugget PO failure behavior in the 3G-980 joints as well as P-PO failure of 3G-1180 joints

with relatively smaller plug ratios under tensile-bending loading modes. By contrasting the results reported in Figure 6.7 and Figure 6.8 as well as the thermal maps during Caiman testing of PHS-1500 components reported by Tolton *et al*. [125], it can be concluded that the ductility of parent metals involved in the Caiman tests exerts an influence on the dissipation of plastic work and energy absorption capability of the components. The influence of parent metal ductility on the energy absorption capability of Caiman components is such that more ductile parent metals (3G-980) lead to increased deformation of joint legs (improved energy absorption) and lower spot weld failure propagation rates (as shown by the synchronized failure tracking in Figure 6.9). Whereas, in the case of less ductile parent metals (3G-1180), thermal spikes are more concentrated in the vicinity of the joints with less pronounced plastic work associated with BM deformation, leading to a more limited energy absorption capacity. An in-depth analysis of the influence of BM ductility and its effect on joint energy absorption capability was provided in Chapter 5. Interestingly, BM plastic deformation occurred to an extent that led to necking in DHCP tests of 3G-980 tests. Necking of BM was not observed in the failure of the 3G-980 Caiman specimen due to load sharing and failure of multiple welds simultaneously. The following section compares the local mechanical and metallurgical properties of the investigated spot welds' FZ edge.

6.5.1 Correlation Between Failure Behavior and Local Mechanical/Metallurgical Characteristics of the Joints

Characterization related to the hardness of FZs, representative of strength, and YS, which quantifies the resistance to the onset of plastic deformation, revealed a 7.5% stronger martensitic lath structure at the FZ edge and 9.8% higher YS values for the FZ of 3G-980 compared to that of 3G-1180. In terms of FZ's other local properties, Midawi *et al.* [219] extracted tensile coupons directly from the RSW FZ of the same lots of materials and reported plastic work values of 178.78 MJ/m^3 and 117.32 MJ/m^3 for 3G-980 and 3G-1180 FZs, respectively. Plastic work is considered a measure of mechanical deformation energy per unit of volume before fracture. In this regard, the lath martensite formed in 3G-980 FZ edge exhibits 52% higher toughness than the FZ edge of 3G-1180 joints. These observations are in line with the observed crack propagation paths, where the martensitic lath structures of 3G-980 joints in front of the notch exhibited more resistance to plastic deformation, while regions away from the nugget, such as the BM with 51% lower yield strength, plastically deformed (as demonstrated by the strain maps related to the DHCP tests shown in Figure 6.3) under tensile-bending loading conditions. The continuation of

deformation in the 3G-980 joint leg resulted in the formation of a localized neck, which provided a more energetically favorable crack path. This led to strain localization and failure through the BM and high tear-out areas, with superior mechanical properties of the DHCP tests compared to the corresponding 3G-1180 test results. A rather straightforward index commonly used in the literature to predict the failure location of spot welds is the relative hardness ratio between the FZ and BM [129,133,138]. Experimental and finite element analysis by Ghatei-Kalashami *et al.* [90] and Zhang *et al.* [139,140] showed that a higher FZ/BM hardness mismatch (higher difference in the local mechanical properties of the FZ and BM) leads to failure initiation within the HAZ, whereas a lower FZ/BM hardness ratio can result in failure initiation closer to the FZ as is the case in this study.

The differences in local mechanical performance of martensite formed in 3G-980 and 3G-1180 sub-regions can be explained by four cooperative mechanisms: solid solution strengthening, boundary strengthening (Hall-Petch strengthening), dislocation strengthening, and precipitation strengthening. Quantifying strength contribution due to carbide precipitation in lath martensitic structures requires extensive transmission electron microscopy to calculate the volume fraction and mean diameter of carbides, which was out of the scope of current work. Since no tempering occurred in the FZ of investigated joints (as evidenced via SEM micrographs shown earlier in Figure 3.11), precipitation hardening is not believed to significantly strengthen the YS of as-quenched martensite formed from the RSW thermal cycles employed in this study [220]. According to Galindo [221], the YS of as-quenched lath martensitic microstructures ($\sigma_{Mart\ Yield}$) can be estimated as a summation of the strengthening contribution from the rest of the aforementioned mechanisms using the following equation:

$$\sigma_{Mart\ Yield} = \sigma_0 + \sum_i (\beta_i^2 x_i)^{1/2} + \frac{300}{\sqrt{d_{Block}}} + 0.25 M \mu b \sqrt{\rho_{Lath}} \qquad (6.2)$$

where the first term of this equation is the lattice frictional stress of pure iron for both studied joints ($\sigma_0 = 50$ MPa) [222]. The second term quantifies the contribution of strengthening due to substitutional solute atoms where x_i is the atomic fraction of element *i*, and β_i is a strengthening coefficient parameter specific to each solute alloying element [223]. A summary of β_i values is provided by Galindo [221] for the substitutional alloying elements considered here (Mn, Si, Ni, Cr, Mo). The higher alloying content of 3G-1180 AHSS (as outlined in Table 3.1) results in 18.5%

higher contribution of solid solution strengthening mechanism on the $\sigma_{Mart\ Yield}$ values (73.5 MPa for 3G-980 joints vs 87.0 MPa for 3G-1180 joints).

The third term in Equation (6.2) accounts for the strengthening effect due to hierarchical martensitic boundaries, including martensite PAG, packets, blocks, and laths. Block width (d_{Block}), due to its relatively smaller length scale, has been reported as the most effective barrier against dislocation motion and is considered the major sub-structure that controls the boundary strengthening of martensite [224]. Nadimi *et al.* [225] proposed the following linear regression model based on the carbon content of different grades of spot-welded AHSS to estimate the d_{Block} value:

$$d_{Block}^{-1/2} = 1.373[C\%] + 0.395 \qquad (6.3)$$

Equation (6.3) predicts d_{Block} values of 2.07 µm and 2.51 µm for the 3G-980 and 3G-1180 compositions, respectively, which lead to a 10% higher contribution of grain boundary strengthening mechanism on the overall martensite yield strength of 3G-980 joints (208.3 MPa for 3G-980 joints vs 189.7 MPa for 3G-1180 joints). To further confirm the higher contribution of the boundary strengthening mechanism on the yield strength of martensitic structures in 3G-980 joints, the FZ edge was scanned via the EBSD technique for both investigated joints. The resulting inverse pole figures and reconstructed PAG maps are shown in Figure 6.14. According to Betiku *et al*. [226], equiaxed grains in front of the notch of spot welds pose more resistance to crack propagation than columnar grains. In this regard, a similar columnar morphology was observed for the PAG of both FZs. However, 25% smaller aspect ratios were measured for the PAG of 3G-980 FZ, on average, in comparison with the aspect ratio of PAG for 3G-1180 FZ (134 µm average grain size with an average aspect ratio of 4.1 for 3G-980 FZ vs. 179 µm average grain size with an average aspect ratio of 5.5 for 3G-1180 FZ). The more refined PAGS in the FZ edge of 3G-980 enhances the local boundary strengthening, which follows the Hall-Petch equation. Zhang *et al.* [227] showed that the improvement of local mechanical properties due to a decrease in average PAG size within martensitic structures is typically associated with the reduction of the martensite packet size and block width, as predicted from (6.3) to be the case for 3G-980.

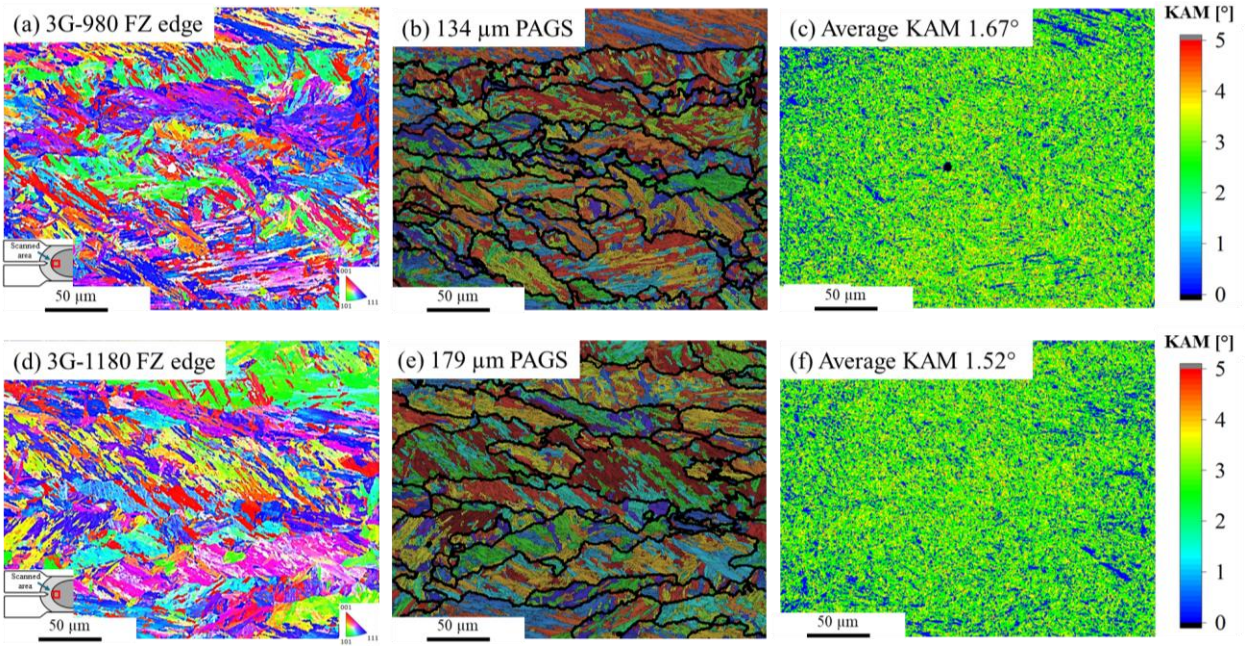


Figure 6.14. Inverse pole figure (IPF) maps at the edge of the FZ for (a) 3G-980 and (d) 3G-1180 spot welds; reconstructed maps showing PAGB represented with the black lines in the FZ edge of (b) 3G-980 and (e) 3G-1180 joints; Kernel average misorientation (KAM) maps at the edge of the FZ for (c) 3G-980 and (f) 3G-1180 joints.

The last term in Equation 6.2 (also known as the Taylor equation) accounts for the strengthening due to the segregation of interstitial carbon atoms at martensite lath boundaries and the formation of Cottrell atmospheres around dislocations. In the last term of Equation 6.2, M is the Taylor orientation factor (M = 3), μ is the elastic isotropic shear modulus (μ = 80 GPa) of lath martensite, b is the magnitude of the Burgers vector in BCC structures (b = 0.286 nm), and ρ_{Lath} is the dislocation density [221,225]. The Kernel average misorientation (KAM) values, as a qualitative measurement of local strain distribution with respect to the neighboring points in the FZ edge of spot welds, are plotted in Figure 6.14 (c) and (f) for 3G-980 and 3G-1180 FZ edges, respectively. The average value from KAM distribution graphs is related to the geometrically necessary dislocation density (ρ_{Lath}) by the following equation [82]:

$$\rho_{Lath} = \frac{2KAM_{avg}}{|\overrightarrow{b}|.u} \qquad (6.4)$$

where KAM_{avg} is the average misorientation angle (1.67° and 1.52 for 3G-980 and 3G-1180 FZ edges, respectively), and u is the step size of the EBSD scan. Using Equation 6.4 results in ρ_{Lath} values of 2.33×10^{16} m^{-2} and 2.12×10^{16} m^{-2} for 3G-980 and 3G-1180 FZ edges, respectively. The

10% smaller ρ_{Lath} is the primary reason for the softer FZ edge 3G-1180, as shown in the microhardness plots earlier in Chapter 3 (Figure 3.12). Using the Taylor equation to quantify the contribution of the dislocation strengthening mechanism on the overall martensite yield strength predicts a 15.5% higher dislocation strengthening effect for 3G-980 FZ edge (766 MPa for FZ of 3G-980 joints vs 664 MPa for FZ of 3G-1180 joints). Higher dislocation density at the FZ of 3G-980 is primarily attributed to its higher carbon content. According to studies by Morito *et al.* [228] and Martin *et al.* [229], two mechanisms explain the higher dislocation density in martensite lath of Fe-C alloys with higher interstitial carbon content. First, higher plastic strain accommodation in prior austenite grain before the martensitic transformation, and second, lower M_s temperature in steels with higher carbon content, which, in turn, minimizes the amount of auto-tempering after martensitic transformation. The resulting higher dislocations in PAGs increase the energy barrier for the migration of lath boundaries. Table 6.3 outlines different indices calculated for the 3G-980 and 3G-1180 FZ edge from the EBSD scans and theoretical calculations explained in this section.

Table 6.3. Summary of calculated indices from FZ edge EBSD maps of investigated spot welds.

RSW Material	PAGS [µm]	Aspect Ratio	Block width [µm]	KAM	ρ_{Lath} [m^{-2}]
3G-980	134	4.1	2.07	1.67	2.33×10^{16}
3G-1180	179	5.5	2.51	1.52	2.12×10^{16}

A summary of the contribution from each of the theoretical lath martensite strengthening mechanisms explained above and their percentage difference with experimented FZ edge yield strength values from the instrumented indentation tests are provided in Table 6.4. The approximately 17% discrepancy between theoretical and experimental martensite yield strength measurements are associated with not accounting for precipitation strengthening, and autotempering, as well as some of the underlying assumptions of Equation 6.2, *i.e.*, assuming full segregation of carbon to lath boundaries, negligence of other compositional, cooling rate, and M_s effects. Interestingly, the discrepancy between theoretical and experimented yield strength values was approximately similar, indicative of unaccounted factors being consistent for both joints. Nonetheless, both Equation 6.2 and experimental measurements predict higher plastic deformation

resistance for the FZ edge of the 3G-980 spot welds, which aligns with the observed failure behaviors from Caiman and DHCP tests.

Table 6.4. Summary of contributions from various strengthening mechanisms on yield strength of martensite formed in resistance spot welds of 3G-980 and 3G-1180. % difference refers to the comparison between the sum of theoretical yield strength values and yield strength measurements from instrumented indentations shown in Figure 17.

Material	Lattice frictional stress [MPa]	Solid solution strengthening [MPa]	Boundary strengthening [MPa]	Dislocation strengthening [MPa]	Yield strength (theoretical) [MPA]	% difference from the experiment
3G-980 FZ edge	50	73.5	208.3	766.0	1097.8	-17.0 %
3G-1180 FZ edge	50	87.0	189.7	664.0	990.7	-17.8 %

Various techniques can be implemented to improve the local mechanical properties of FZ edge in the case of 3G-1180 spot welds and increase their energy absorption capability under tensile-bending loading conditions. Examples of these techniques include the implementation of weld schedules that temper the as-quenched martensite formed within the FZ of spot welds in the current study [210] or using *in-situ* post-weld heat treatment (PWHT) schedules that promote the formation of equiaxed martensite PAG morphology at the FZ edge [226]. In this regard, the former technique improves the contribution of the precipitation strengthening mechanism on the overall local properties, whereas the PWHT schedules can enhance the contribution of boundary strengthening on local joint properties.

6.6 Summary

This study investigated the mechanical performance of 3G-AHSS spot welded groups under tensile-bending loading of Caiman and DHCP tests. The Caiman weld-group tests revealed 13% higher energy absorption capability for the 3G-980 weld-groups after 250 mm of crosshead displacement, as well as a smoother unloading behavior upon sequential failure of the 3G-980 joints, compared with the 3G-1180 weld-groups. It was shown that both geometrical factors and the failure behavior of the joints contribute to the observed differences. In summary, the more severe reduction in the effective bending moment arm of 3G-980 channels throughout the Caiman

tests resulted in a 25 s delay, on average, for the onset of first joint failure compared to the 3G-1180 Caiman weld-group tests. Furthermore, 3G-980 weld-groups failed predominantly in ductile PO mode with crack propagation lengths and tear-out areas that were 25% and 49% higher than the brittle P-PO failure of 3G-1180 weld-groups.

Due to the difficulty in coupling the Caiman tests with DIC, a modified version of the CP test with two sectioned spot welds on the flange region, referred to as the DHCP test, was proposed that allowed in-situ visualization of strain localization and crack propagation paths during tensile-bending loading of two sectioned spot welds. Results indicated strain localization in front of the intrinsic notch, within the UCHAZ, for both investigated joints followed by two distinct failure propagation paths: the 3G-980 joint failure proceeded via ductile yielding and formation of a neck in the BM due to up to 63° opening angle of the flanges at the onset of failure, which redirected the crack at the notch away from the faying interface and resulted in PO failures with high plug ratios. On the other hand, the 3G-1180 failure included a fast fracture mechanism towards the epitaxial structure of the FZ, resulting in relatively lower plug ratios. The 3G-1180 DHCP samples exhibited a maximum of 21° flange opening angle at the peak load frame, which maintained the bending moment on the joint FZ more effectively than the 3G-980 samples. Comparison of the failures between Caiman and DHCP weld failures of the 3G-1180 showed less severe strength loss upon sequential failure of joints on the Caiman weld-groups (on average, 10.2% strength loss after each joint failure of the Caiman tests vs 48% strength loss for DHCP tests). This observation demonstrated that the failure of spot welds in Caiman tests is dominated by load-sharing among multiple spot welds.

Aside from the geometrical factors that changed the joint's stress state, the FZ edge's metallurgical characteristics also influenced the failure behavior of the investigated joints under tensile-bending loading conditions. Mechanical characterizations indicated a 9.8% higher yield strength for the as-quenched martensite formed in the FZ edge of 3G-980 spot welds. The higher yield strength of the martensitic lath structure of 3G-980 more effectively resisted plastic deformation of the FZ edge, leading to earlier yielding of BM and diverting the formed cracks from the notch away from the faying interface. The contribution of various strengthening mechanisms to the yield strength of the martensitic structure of the FZ edge was quantified. It was noted that dislocation strengthening has the most prominent effect on the overall martensite yield

values (67%-70% of the overall strength). In this regard, the higher carbon content of the 3G-980 material resulted in higher straining of the lattice and, ultimately, 10% higher dislocation density at the FZ edge of the 3G-980 spot welds, as evidenced by the KAM maps.

7 Conclusions and Future Recommendations

7.1 Conclusions

This research program focused on evaluating the mechanical behavior of resistance spot welds composed of two grades of 3G-AHSS under different loading conditions: combined shear-tensile in KS-II tests, tensile-bending in CP tests, and sequential spot weld failure during tensile-bending loading in weld-group tests. For the first time, it was shown how the effects of factors such as nugget orientation and plastic deformation far from the joint region affected spot weld performance metrics, such as load components at failure and total energy absorption capacity. Using KS-II and CP tests in conjunction with the DIC technique, this research adopted the projected nugget as the displacement reference point, enabling precise quantification of shear, tensile, and bending energy absorption capabilities and assessing the accuracy of existing force-based RSW failure criteria. The research expanded the understanding of single spot weld characterization techniques to multi-weld components (specifically the Caiman sample), revealing that the ductility of the parent metal and the local mechanical properties of the FZ edge are the two primary factors determining the overall mechanical performance of the weld-groups. The following are the major conclusions drawn from this study:

1. The failure criterion by Seeger et al. [117] accurately predicts the failure of 3G-AHSS spot welds under shear-tension loading conditions, with an average over-prediction error ranging from 0.2% to 3.5%, but it cannot be extended to bending conditions. In bending, Seeger's criteria significantly overestimated the critical bending strength of the joints, with errors reaching up to 66.1%. The failure surface is not convex in bend-dominated loading as postulated by the Seeger model. To address this limitation, alternative mathematical formulations were proposed to improve predictive accuracy for RSW under tension-bending loading scenarios.
2. The conventional approach of measuring the energy absorption capability of spot welded joints using the integral of load-crosshead displacement is overestimated. The boundary conditions, rigid body motion, and evolution of load components and moment arms must be considered in the dissipated energy calculations. This study developed new DIC-based techniques to compensate for such testing artifacts. Calculating the energy absorption capability of spot welds using the local projected nugget as the displacement reference point effectively minimized the influence of plastic deformation in regions away from the joint on E_{Total}. The

post-processing of CP mechanical tests was significantly improved by accounting for the substantial effect of bending moment arm reduction throughout the tests, a consequence of the inadequate boundary conditions applied to the CP specimens. The proposed CP analysis systematically calculated the critical bending moments and load components applied to the projected nugget at the onset of failure under tensile-bending conditions, providing a more accurate assessment of the mechanical performance of the spot welds in comparison with existing methodologies.

3. The present study clarified the effect of key parameters (*i.e.*, steel strength, and RSW welding current) on the RSW mechanical response. The joints were characterized under a low compliance testing specimen (the KS-II coupon), reducing the effect of deformations and peel loading on the extracted mechanical performance metrics under various ratios of shear and tensile load components.
4. The current study highlighted the importance of accounting for the post-failure energy dissipation upon performing mechanical tests. Specifically, the correlation between the components of energy absorption capability ($E^{\delta t}$ and $E^{\delta s}$), and the failure behavior of KS-II specimens revealed that propagation of cracks into the epitaxial structure of the 3G-1180 FZ (P-PO failures), as compared with crack propagation away from the faying interface (PO failure) of 3G-980 joints, limits the post-failure energy absorption capability ($E_{ap}^{\delta t}\ and\ E_{ap}^{\delta s}$), especially in tensile-dominated loading orientations of the KS-II tests.
5. The energy absorption of the RSW joints and the rate of failure propagation along the flanges of Caiman components were controlled by the degree to which the parent metal participated in plastic work dissipation and the failure mode of the joints.
6. For the first time, in-situ observation of strain localization during tensile-bending loading of spot welds was made possible using a novel DHCP testing methodology. The combination of higher parent metal ductility and superior local mechanical properties of FZ edge for 3G-980 joints, compared with that of 3G-1180 joints, led to favorable ductile PO failure with higher crack propagation lengths and plug ratios.

7.2 Areas of Future Research and Recommendations

This study showed that developing strength-based failure criteria, while accounting for the geometry of the coupon and joint at the onset of failure, is a viable approach for predicting failure of spot welds from 3G-AHSS. Influence of torsional moments, and subsequent manufacturing

steps, after joining of the components such as paint baking, were not considered in this study. While the present study provided a detailed understanding of the mechanical performance of 3G-AHSS spot welds under KS-II, CP, and Caiman mode I tests, further research is necessary to focus on the following aspects:

1. The experimentally-developed force-based failure criteria in this thesis should be incorporated into commonly used finite element models such as LSDYNA's *MAT_100/*MAT_Spotweld elasto-plastic material model and potentially improve the accuracy of failure predictions from such industrial weld models. Meso-scale finite element models can also be used in conjunction with empirical and experimental analysis to quantify the force/moment components applied to the nugget in various loading modes, similar to the ones investigated in this research program.
2. Further study on various grades of AHSS is required to confirm the exponentially decreasing trend of RSW failure loci in bending dominated loading conditions using the procedures developed in this research program.
3. Other than shear loads, tensile loads, and bending moments, torsional moments are another type of loading mode spot welds may experience in service. A limited number of studies from the literature have focused on characterizing the mechanical performance of spot-welded connections under torsional moments [86][230]. The torsional characterization methodology in such studies can be readily improved by providing a better-defined boundary condition and coupling the tests with DIC. Currently, limited knowledge exists within the literature regarding the extent of influence that torsional moments have at the onset of spot weld failure under various loading conditions.
4. Future work should consider constraining the free end of the Caiman rails to prevent sidewall collapse. It was shown that channel plastic deformation retards weld failure, particularly for the more ductile 3G-980 material. Interpretation of results from current Caiman mode I tests revealed a strong dependency of the energy absorption capability of the Caiman tests on the geometry of the channels throughout the tests along with joint failure behavior. Inner and outer bosses should be mounted, especially at the free end of the Caiman channels to isolate and facilitate understanding of the effect of joint failure mode during sequential unloading of spot welds under tensile-bending loading conditions.

The bosses can act as stiffeners of the hat channels and minimize the channel collapse throughout the tests.

5. Results from this research program highlighted higher susceptibility of 3G-1180 FZ edge, compared with that of 3G-980 joints to cracking during various loading conditions of the spot welds. Different techniques including in-situ PWHT cycles, as suggested by Betiku *et al.* [226], can be implemented that locally alter the morphology of the PAG from columnar to equiaxed. Developing an RSW process map that promotes such microstructural alterations at the joints' FZ edge can hinder failure and impose more resistance to crack propagation towards the FZ.
6. Fabrication of BIW components typically involves joining coated steels to protect the matrix from corrosion followed by a paint-baking process, which is a curing procedure performed at elevated temperatures (approximately 180 °C for 20-30 minutes) to harden the adhesives and the painted layers. These manufacturing steps can alter the mechanical performance of joints as investigated in the bare and un-baked conditions of the current research program. It has been shown that the formation of intermetallic layers with high resistivity during coating can narrow down the weldability lobes, and also the occurrence of liquid metal embrittlement cracks in critical sub-regions can cause premature failures under varying loading modes [231]. The influence of the coating and paint baking cycle on the mechanical performance of 3G-AHSS spot welds under complex loading conditions, as investigated in this study, remains unexplored within the literature and is recommended for future work.

References

[1] J. Poschmann, V. Bach, M. Finkbeiner, Deriving decarbonization targets and pathways – A case study for the automotive industry, J. Clean. Prod. 409 (2023) 137256. https://doi.org/10.1016/J.JCLEPRO.2023.137256.

[2] S.A. SHAHEEN, T.E. LIPMAN, REDUCING GREENHOUSE EMISSIONS AND FUEL CONSUMPTION: Sustainable Approaches for Surface Transportation, IATSS Res. 31 (2007) 6–20. https://doi.org/10.1016/S0386-1112(14)60179-5.

[3] L. Alfaseeh, R. Tu, B. Farooq, M. Hatzopoulou, Greenhouse gas emission prediction on road network using deep sequence learning, Transp. Res. Part D Transp. Environ. 88 (2020) 102593. https://doi.org/10.1016/j.trd.2020.102593.

[4] J. Zielinski, R. Andreucci, N. Rajagopalan, C.B. Aktas, Prospects for meeting the corporate average fuel economy standards in the U.S., Resour. Conserv. Recycl. 136 (2018) 466–472. https://doi.org/10.1016/j.resconrec.2018.03.026.

[5] B. Schoettle, M. Sivak, A comparison of CAFE standards and actual CAFE performance of new light-duty vehicles, (2013). http://deepblue.lib.umich.edu/handle/2027.42/100179 (accessed October 2, 2021).

[6] B. Figueredo, D.C. Ramachandran, A. Macwan, E. Biro, Failure behavior and mechanical properties in the resistance spot welding of quenched and partitioned (Q&P) steels, Weld. World. 65 (2021) 2359–2369. https://doi.org/10.1007/S40194-021-01179-Z/FIGURES/12.

[7] F. Czerwinski, Current trends in automotive lightweighting strategies and materials, Materials (Basel). 14 (2021). https://doi.org/10.3390/ma14216631.

[8] P. Sun, R. Bisschop, H. Niu, X. Huang, A Review of Battery Fires in Electric Vehicles, Springer US, 2020. https://doi.org/10.1007/s10694-019-00944-3.

[9] M. Ghosh, K. Kumar, R.S. Mishra, Friction stir lap welded advanced high strength steels: Microstructure and mechanical properties, Mater. Sci. Eng. A. 528 (2011) 8111–8119. https://doi.org/10.1016/J.MSEA.2011.06.087.

[10] C. Lesch, N. Kwiaton, F.K.-S. research international, undefined 2017, Advanced high strength steels (AHSS) for automotive applications− tailored properties by smart microstructural adjustments, Wiley Online Libr. 88 (2017). https://doi.org/10.1002/srin.201700210.

[11] Z.H. Cai, H. Ding, R.D.K. Misra, Z.Y. Ying, Austenite stability and deformation behavior

in a cold-rolled transformation-induced plasticity steel with medium manganese content, Acta Mater. 84 (2015) 229–236. https://doi.org/10.1016/J.ACTAMAT.2014.10.052.

[12] J. Han, Y.K. Lee, The effects of the heating rate on the reverse transformation mechanism and the phase stability of reverted austenite in medium Mn steels, Acta Mater. 67 (2014) 354–361. https://doi.org/10.1016/J.ACTAMAT.2013.12.038.

[13] J. Zhao, Z. Jiang, Thermomechanical processing of advanced high strength steels, Prog. Mater. Sci. 94 (2018) 174–242. https://doi.org/10.1016/j.pmatsci.2018.01.006.

[14] M. Pouranvari, S.P.H. Marashi, Critical review of automotive steels spot welding: Process, structure and properties, Sci. Technol. Weld. Join. 18 (2013) 361–403. https://doi.org/10.1179/1362171813Y.0000000120.

[15] S. Hu, A.S. Haselhuhn, Y. Ma, Y. Li, B.E. Carlson, Z. Lin, Influencing mechanism of inherent aluminum oxide film on coach peel performance of baked Al-Steel RSW, Mater. Des. 197 (2021) 109250. https://doi.org/10.1016/j.matdes.2020.109250.

[16] F. Billur, J. Dykeman, T. Altan, Three generations of advanced high strength steels for automotive applications, Part III, Stamp. J. (2014).

[17] D. Matlock, J. Speer, E. De Moor, P. Gibbs, Recent developments in advanced high strength sheet steels for automotive applications: an overview, Jestech. 15 (2012) 1–12.

[18] H.W. Yen, M. Huang, C.P. Scott, J.R. Yang, Interactions between deformation-induced defects and carbides in a vanadium-containing TWIP steel, Scr. Mater. 66 (2012) 1018–1023. https://doi.org/10.1016/J.SCRIPTAMAT.2012.02.002.

[19] K.G.C. Kim, S. Kim, Gyosung Kim, Development of High Manganese TWIP Steel with 980MPa Tensile Strength, in: Proc. Int. Conf. New Dev. Adv. High-Strength Sheet Steels, Assoc. Iron Steel Technol., 2008.

[20] C.C. Tasan, M. Diehl, D. Yan, M. Bechtold, F. Roters, L. Schemmann, C. Zheng, N. Peranio, D. Ponge, M. Koyama, K. Tsuzaki, D. Raabe, An Overview of Dual-Phase Steels: Advances in Microstructure-Oriented Processing and Micromechanically Guided Design, Annu. Rev. Mater. Res. 45 (2015) 391–431. https://doi.org/10.1146/annurev-matsci-070214-021103.

[21] C. Peng-Heng, A.G. Preban, The effect of ferrite grain size and martensite volume fraction on the tensile properties of dual phase steel, Acta Metall. 33 (1985) 897–903. https://doi.org/10.1016/0001-6160(85)90114-2.

[22] Y.B. Li, D.L. Li, S.A. David, Y.C. Lim, Z. Feng, Microstructures of magnetically assisted dual-phase steel resistance spot welds, Sci. Technol. Weld. Join. 21 (2016) 555–563. https://doi.org/10.1080/13621718.2016.1141493.

[23] I. de Diego-Calderón, I. Sabirov, J.M. Molina-Aldareguia, C. Föjer, R. Thiessen, R.H. Petrov, Microstructural design in quenched and partitioned (Q&P) steels to improve their fracture properties, Mater. Sci. Eng. A. 657 (2016) 136–146. https://doi.org/10.1016/j.msea.2016.01.011.

[24] J. Speer, D.K. Matlock, B.C. De Cooman, J.G. Schroth, Carbon partitioning into austenite after martensite transformation, Acta Mater. 51 (2003) 2611–2622. https://doi.org/10.1016/S1359-6454(03)00059-4.

[25] D.K. Matlock, J.G. Speer, Third generation of AHSS: microstructure design concepts, 2009.

[26] R.S. Tiara Dewi, Muhammad Amir Masruhim, Third Generation of AHSS: Microstructure Design Concepts, 2016.

[27] M. Davenport, Third-generation advanced high-strength steel emerges, Stamp. J. (2017).

[28] M. Soleimani, A. Kalhor, H. Mirzadeh, Transformation-induced plasticity (TRIP) in advanced steels: A review, Mater. Sci. Eng. A. 795 (2020). https://doi.org/10.1016/j.msea.2020.140023.

[29] P.J. Jacques, E. Girault, P. Harlet, F. Delannay, The Developments of Cold-rolled TRIP-assisted Multiphase Steels. Low Silicon TRIP-assisted Multiphase Steels, ISIJ Int. 41 (2001) 1061–1067. https://doi.org/10.2355/ISIJINTERNATIONAL.41.1061.

[30] G.B. Olson, M. Cohen, Kinetics of strain-induced martensitic nucleation, Metall. Trans. A. 6 (1975) 791–795. https://doi.org/10.1007/BF02672301.

[31] P.J. Gibbs, Design considerations for the third generation advanced high strength steel, (2012). https://doi.org/10.17616/R31NJMSY.

[32] Q. Khan, H. Ghassemi-armaki, A.S. Gill, S. Zilincik, F.C.A. Chrysler, A. Hills, A. Gawade, Characterization and Modeling of Spot-Weld Joints with *MAT_100_DA parameter optimization using LS-OPT® , and 3 sheet spot-weld modeling method development in LS-DYNA ®, 15th Int. LS-DYNA® Users Conf. (2018) 1–16.

[33] A.M. Al-Mukhtar, Review of Resistance Spot Welding Sheets: Processes and Failure Mode, Adv. Eng. Forum. 17 (2016) 31–57.

https://doi.org/10.4028/WWW.SCIENTIFIC.NET/AEF.17.31.

[34] M. Kimchi, D.H. Phillips, Resistance Spot Welding: Fundamentals and Applications for the Automotive Industry, Synth. Lect. Mech. Eng. 1 (2017) i–115. https://doi.org/10.2200/S00792ED1V01Y201707MEC005.

[35] American Welding Society, AWS D8.9M:2012 - Test Method for Evaluating the Resistance Spot Welding Behavior of Automotive Sheet Steel Materials, 2012.

[36] M. Batista, V. Furlanetto, S.D. Brandi, Analysis of the behavior of dynamic resistance, electrical energy and force between the electrodes in resistance spot welding using additive manufacturing, Metals (Basel). 10 (2020). https://doi.org/10.3390/met10050690.

[37] Y.J. Xia, Z.W. Su, Y.B. Li, L. Zhou, Y. Shen, Online quantitative evaluation of expulsion in resistance spot welding, J. Manuf. Process. 46 (2019) 34–43. https://doi.org/10.1016/j.jmapro.2019.08.004.

[38] M. Kahn, Spot welding of advanced high strength steels, University of Waterloo, 2007.

[39] American Welding Society, Test Methods for Evaluating the Resistance Spot Welding Behavior of Automotive Sheet Steel (AWS D8.9M:2012), 2012.

[40] ISO 18278-2:2016 - Resistance welding — Weldability — Part 2: Evaluation procedures for weldability in spot welding, (n.d.). https://www.iso.org/standard/52317.html (accessed June 18, 2024).

[41] K. Zhou, L. Cai, Study on effect of electrode force on resistance spot welding process, J. Appl. Phys. 116 (2014). https://doi.org/10.1063/1.4893968.

[42] R. Ikeda, Y. Okita, M. Ono, K. Yasuda, T. Terasaki, Development of advanced resistance spot welding process using control of electrode force and welding current during welding, Weld. Int. 28 (2014) 13–20. https://doi.org/10.1080/09507116.2012.715880.

[43] D. Saha, C. Ji, Y.P.-S. and T. of Welding, undefined 2015, Coating behaviour and nugget formation during resistance welding of hot forming steels, Taylor Fr. 20 (2015) 708–720. https://doi.org/10.1179/1362171815Y.0000000054.

[44] X. Han, C. DiGiovanni, J. McDermid, E. Biro, N.Y. Zhou, Effect of internal oxidation on the weldability of CMnSi steels, Weld. World. 63 (2019) 1633–1639. https://doi.org/10.1007/s40194-019-00798-x.

[45] A. Ghatei Kalashami, X. Han, F. Goodwin, N.Y. Zhou, The influence of modified annealing during the galvanizing process on the resistance spot welding of the CMn1.8Si

advanced high strength steel, Surf. Coatings Technol. 381 (2020) 125181. https://doi.org/10.1016/J.SURFCOAT.2019.125181.

[46] N.J. Den Uijl, S. Smith, Resistance spot welding of advanced high strength steels for the automotive industry, 4th Int. Semin. Adv. Resist. Welding, Wels, Austria. (2006) 30–60.

[47] O. Ighodaro, Effects of Metallic Coatings on Resistance Spot Weldability of Hot Stamping Steel, Thesis. (2017) 1–110. https://uwspace.uwaterloo.ca/handle/10012/11159.

[48] B. Wang, L. Hua, X. Wang, Y. Song, Y. Liu, Effects of electrode tip morphology on resistance spot welding quality of DP590 dual-phase steel, Int. J. Adv. Manuf. Technol. 83 (2016) 1917–1926. https://doi.org/10.1007/s00170-015-7703-0.

[49] H. Wang, Y. Zhang, X. Lai, Effects of cone angle of truncated electrode on heat and mass transfer in resistance spot welding, Int. J. Heat Mass Transf. 90 (2015) 665–677. https://doi.org/10.1016/j.ijheatmasstransfer.2015.07.027.

[50] W. Tong, H. Tao, X. Jiang, N. Zhang, M.P. Marya, L.G. Hector, X.Q. Gayden, Deformation and fracture of miniature tensile bars with resistance-spot-weld microstructures, Metall. Mater. Trans. A Phys. Metall. Mater. Sci. 36 (2005) 2651–2669. https://doi.org/10.1007/s11661-005-0263-4.

[51] M. Pouranvari, S.P.H. Marashi, Failure behavior of three-steel sheets resistance spot welds: Effect of joint design, J. Mater. Eng. Perform. 21 (2012) 1669–1675. https://doi.org/10.1007/s11665-011-0078-y.

[52] M. Tamizi, M. Pouranvari, M. Movahedi, The Role of HAZ Softening on Cross-Tension Mechanical Performance of Martensitic Advanced High Strength Steel Resistance Spot Welds, Metall. Mater. Trans. A Phys. Metall. Mater. Sci. 52 (2021) 655–667. https://doi.org/10.1007/s11661-020-06104-5.

[53] K. Kishore, P. Kumar, G. Mukhopadhyay, Resistance spot weldability of galvannealed and bare DP600 steel, J. Mater. Process. Technol. 271 (2019) 237–248. https://doi.org/10.1016/J.JMATPROTEC.2019.04.005.

[54] The resistance spot welding of high and ultra-high strength steels - TWI, (n.d.). https://www.twi-global.com/technical-knowledge/published-papers/the-resistance-spot-welding-of-high-and-ultra-high-strength-steels-november-2004 (accessed December 4, 2021).

[55] M. Pouranvari, P.H. Marashi, Critical review of automotive steels spot welding: process,

structure and properties, Sci. Technol. Weld. Join. 18 (2013) 361–403. https://doi.org/10.1179/1362171813y.0000000120.

[56] M. Pouranvari, S.P.H. Marashi, Key factors influencing mechanical performance of dual phase steel resistance spot welds, Sci. Technol. Weld. Join. 15 (2010) 149–155. https://doi.org/10.1179/136217109X12590746472535.

[57] V. Vijayan, S.P. Murugan, S.G. Son, Y. Do Park, Shrinkage Void Formation in Resistance Spot Welds: Its Effect on Advanced High-Strength-Steel Weld Strength and Failure Modes, J. Mater. Eng. Perform. 28 (2019) 7514–7526. https://doi.org/10.1007/S11665-019-04465-6.

[58] R.M. Chen, C.Q. Zhang, M. Lou, Y.B. Li, B.E. Carlson, Effect of Al-Si Coating on Weldability of Press-Hardened Steels, J. Mater. Eng. Perform. 29 (2020) 626–636. https://doi.org/10.1007/S11665-020-04555-W.

[59] J.E. Gould, S.P. Khurana, T. Li, Predictions of microstructures when welding automotive advanced high-strength steels, Weld. J. (Miami, Fla). 85 (2006) 111–116.

[60] N.J. Den Uijl, H. Nishibata, S. Smith, T. Okada, T. Van Der Veldt, M. Uchihara, K. Fukui, Prediction of post weld hardness of advanced high strength steels for automotive application using a dedicated carbon equivalent number, Weld. World. 52 (2008) 18–29. https://doi.org/10.1007/BF03266679.

[61] S. Ramadurga, W. Zeng, T. Long, Z. Zhu, P. Scott, X. Jiang, S. Lou, T. Manufacturing, T. Centre, A. Park, C. Cv, A comprehensive review on laser powder bed fusion of steels : Processing , microstructure , defects and control methods , mechanical properties , current challenges and future trends, 75 (2022) 375–414.

[62] S. Kou, Welding Metallurgy, 2nd ed, n.d.

[63] N.T. Williams, J.D. Parker, N.T. Williams, J.D. Parker, Review of resistance spot welding of steel sheets Part 1 Modelling and control of weld nugget formation Review of resistance spot welding of steel sheets Part 1 Modelling and control of weld nugget formation, 6608 (2013). https://doi.org/10.1179/095066004225010523.

[64] F. Badkoobeh, A. Nouri, H. Hassannejad, H. Mostaan, Microstructure and mechanical properties of resistance spot welded dual-phase steels with various silicon contents, Mater. Sci. Eng. A. 790 (2020) 139703. https://doi.org/10.1016/J.MSEA.2020.139703.

[65] T.K. Eller, L. Greve, M. Andres, M. Medricky, H.J.M. Geijselaers, V.T. Meinders, A.H.

Van Den Boogaard, Plasticity and fracture modeling of the heat-affected zone in resistance spot welded tailor hardened boron steel, J. Mater. Process. Technol. 234 (2016) 309–322. https://doi.org/10.1016/J.JMATPROTEC.2016.03.026.

[66] D.C. Saha, S.S. Nayak, E. Biro, A.P. Gerlich, Y. Zhou, Mechanism of Secondary Hardening in Rapid Tempering of Dual-Phase Steel, Metall. Mater. Trans. A Phys. Metall. Mater. Sci. 45 (2014) 6153–6162. https://doi.org/10.1007/s11661-014-2591-8.

[67] D.C. Ramachandran, B. Figueredo, O. Sherepenko, W. Jin, Y.-D. Park, E. Biro, A study on improving the mechanical performance by controlling the halo ring in the Q&P 980 steel resistance spot welds, J. Manuf. Process. 75 (2022) 320–330. https://doi.org/10.1016/J.JMAPRO.2022.01.019.

[68] E.I. Galindo-Nava, P.E.J. Rivera-Díaz-Del-Castillo, Understanding the factors controlling the hardness in martensitic steels, Scr. Mater. 110 (2016) 96–100. https://doi.org/10.1016/j.scriptamat.2015.08.010.

[69] M. Tamizi, M. Pouranvari, M. Movahedi, Welding metallurgy of martensitic advanced high strength steels during resistance spot welding, Sci. Technol. Weld. Join. 22 (2017) 327–335. https://doi.org/10.1080/13621718.2016.1240979.

[70] B. Wang, Q.Q. Duan, G. Yao, J.C. Pang, X.W. Li, L. Wang, Z.F. Zhang, Investigation on fatigue fracture behaviors of spot welded Q&P980 steel, Int. J. Fatigue. 66 (2014) 20–28. https://doi.org/10.1016/j.ijfatigue.2014.03.004.

[71] X.D. Liu, Y.B. Xu, R.D.K. Misra, F. Peng, Y. Wang, Y.B. Du, Mechanical properties in double pulse resistance spot welding of Q&P 980 steel, J. Mater. Process. Technol. 263 (2019) 186–197. https://doi.org/10.1016/j.jmatprotec.2018.08.018.

[72] V. Hernandez, S. Panda, M. Kuntz, Y.Z.-M. Letters, undefined 2010, Nanoindentation and microstructure analysis of resistance spot welded dual phase steel, Elsevier. (n.d.). https://www.sciencedirect.com/science/article/pii/S0167577X09008039 (accessed December 7, 2021).

[73] E. Biro, Heat-Affected Zone Softening Kinetics in Dual-Phase and Martensitic Steels, McMaster University, 2013.

[74] M. Lei, H. Pan, Comparative study of resistance spot welding performance between cold-rolled DP980 and Q & P980 steels, 6 (2012) 2–5.

[75] L. Wang, J.G. Speer, Quenching and Partitioning Steel Heat Treatment, Metallogr.

Microstruct. Anal. 2 (2013) 268–281. https://doi.org/10.1007/s13632-013-0082-8.

[76] E. Biro, J. McDermid, J. Embury, Y.Z.-M. and materials, undefined 2010, Softening kinetics in the subcritical heat-affected zone of dual-phase steel welds, Springer. 41 (2010) 2348–2356. https://doi.org/10.1007/s11661-010-0323-2.

[77] D.C. Saha, I. Chang, Y. Do Park, Heat-affected zone liquation crack on resistance spot welded TWIP steels, Mater. Charact. 93 (2014) 40–51. https://doi.org/10.1016/j.matchar.2014.03.016.

[78] R. Ashiri, H. Mostaan, Y. Do Park, A Phenomenological Study of Weld Discontinuities and Defects in Resistance Spot Welding of Advanced High Strength TRIP Steel, Metall. Mater. Trans. A Phys. Metall. Mater. Sci. 49 (2018) 6161–6172. https://doi.org/10.1007/s11661-018-4900-0.

[79] D.C. Ramachandran, B. Figueredo, O. Sherepenko, W. Jin, Y.-D. Park, E. Biro, A study on improving the mechanical performance by controlling the halo ring in the Q&P 980 steel resistance spot welds, J. Manuf. Process. 75 (2022) 320–330. https://doi.org/10.1016/J.JMAPRO.2022.01.019.

[80] O. Sherepenko, O. Kazemi, P. Rosemann, M. Wilke, T. Halle, S. Jüttner, Transient softening at the fusion boundary of resistance spot welds: A phase field simulation and experimental investigations for al–si-coated 22mnb5, Metals (Basel). 10 (2020). https://doi.org/10.3390/met10010010.

[81] A. Mohamadizadeh, E. Biro, M. Worswick, Failure characterization and meso-scale damage modeling of spot welds in hot-stamped automotive steels using a hardness-mapping approach, Eng. Fract. Mech. 268 (2022) 108506. https://doi.org/10.1016/j.engfracmech.2022.108506.

[82] P. Eftekharimilani, E.M. van der Aa, M.J.M. Hermans, I.M. Richardson, Microstructural characterisation of double pulse resistance spot welded advanced high strength steel, Sci. Technol. Weld. Join. 22 (2017) 545–554. https://doi.org/10.1080/13621718.2016.1274848.

[83] Y. Y-s, S. K-j, C. S-k, H. S-g, K. S-k, M. K-h, Y. Yang, K. Son, S. Cho, S. Hong, S. Kim, K. Mo, Y. ysyang, Effect of residual stress on fatigue strength of resistance spot weldment, Taylor Fr. 6 (2001) 397–401. https://doi.org/10.1179/stw.2001.6.6.397.

[84] S. Donders, M. Brughmans, … L.H.-S. and, undefined 2005, The effect of spot weld

failure on dynamic vehicle performance, Researchgate.Net. (n.d.). https://www.researchgate.net/profile/M-Brughmans/publication/315047614_The_effect_of_Spot_Weld_Failure_on_Dynamic_Vehicle_Performance/links/5ed64d6f299bf1c67d32a6ff/The-effect-of-Spot-Weld-Failure-on-Dynamic-Vehicle-Performance.pdf (accessed December 6, 2021).

[85] M. Enami, M. Farahani, M. Sohrabian, Evaluation of mechanical properties of Resistance Spot Welding and Friction Stir Spot Welding on Aluminium Alloys, Int. Conf. Res. Sci. Eng. (2016).

[86] W. Wang, Q. Zhu, C. Liu, X. Wei, An investigation on the resultant-based failure criterion for resistance spot welding joint in crush test, Int. J. Crashworthiness. 24 (2019) 152–162. https://doi.org/10.1080/13588265.2017.1421012.

[87] (2013) AWS D8.1M. Specification for Automotive Weld Quality-Resistance Spot Welding of Steel., Second ed. American Welding Society (AWS), Miami, Fl, USA, (n.d.).

[88] J.S. Hou, Resistance Spot Welding and In-Process Heat Treatment of Hot Stamped Boron Steel, University of Waterloo, 2016.

[89] Y. Zhang, X. Zhang, J. Guo, S.M. Manladan, Z. Luo, Y. Li, Effects of local stiffness on the spot joints mechanical properties: Comparative study between resistance spot welding and resistance spot clinching joints, J. Manuf. Process. 39 (2019) 93–101. https://doi.org/10.1016/J.JMAPRO.2019.02.018.

[90] A. Ghatei-Kalashami, S. Zhang, M. Shojaee, A.R.H. Midawi, F. Goodwin, N.Y. Zhou, Failure behavior of resistance spot welded advanced high strength steel: The role of surface condition and initial microstructure, J. Mater. Process. Technol. 299 (2021) 117370. https://doi.org/10.1016/j.jmatprotec.2021.117370.

[91] K.S. Pandya, V. Grolleau, C.C. Roth, D. Mohr, Fracture response of resistance spot welded dual phase steel sheets: Experiments and modeling, Int. J. Mech. Sci. 187 (2020) 105869. https://doi.org/10.1016/j.ijmecsci.2020.105869.

[92] P. Russo Spena, M. De Maddis, G. D'Antonio, F. Lombardi, Weldability and monitoring of resistance spot welding of Q&P and TRIP steels, Metals (Basel). 6 (2016). https://doi.org/10.3390/met6110270.

[93] B. Figueredo, D.C. Ramachandran, A. Macwan, E. Biro, Failure behavior and mechanical properties in the resistance spot welding of quenched and partitioned (Q&P) steels, Weld.

World. 65 (2021) 2359–2369. https://doi.org/10.1007/s40194-021-01179-z.

[94] T. Chen, Z. Ling, M. Wang, L. Kong, Effect of post-weld tempering pulse on microstructure and mechanical properties of resistance spot welding of Q&P1180 steel, Mater. Sci. Eng. A. (2021) 142164. https://doi.org/10.1016/J.MSEA.2021.142164.

[95] C. Lee, Y., Wehner, T., Lu, M., Morrissett, T., Pakalnins, E., and Tsai, Test of resistance spot welds under combined tension and shear, in: 1996: p. SMWC VII, Paper C2, 1996.

[96] Y.L. Lee, T.J. Wehner, M.W. Lu, T.W. Morrissett, E. Pakalnins, Ultimate Strength of Resistance Spot Welds Subjected to Combined Tension and Shear, J. Test. Eval. 26 (1998) 213–219. https://doi.org/10.1520/JTE11994J.

[97] M.O. Hahn O., K. Özdem, Experimentelle Bestimmung und rechnerische Vorhersage des Tragverhaltens punktgeschweißter Bauteile aus Stahlblechverbindungen unter Crashbelastung mit Hilfe von Ingenieurkonzepten, FAT/ AVIF A172; Febr. (2004).

[98] H. Ghassemi-Armaki, E. Biro, S. Sadagopan, Advanced characterization of HAZ softening of AHSS for crash modeling, ISIJ Int. 57 (2017) 1451–1460. https://doi.org/10.2355/isijinternational.ISIJINT-2016-649.

[99] S. Patil, H. Lankarani, Characterisation and modelling the strength of EHSS steel grade spot weld for automotive joints and its application for frontal impact load-case, Int. J. Crashworthiness. 24 (2019) 13–23. https://doi.org/10.1080/13588265.2017.1389628.

[100] X. Yang, Y. Xia, Q. Zhou, A simplified FE model for pull-out failure of spot welds, Eng. Fract. Mech. 77 (2010) 1224–1239. https://doi.org/10.1016/j.engfracmech.2010.02.029.

[101] Y. Lee, W. TJ, M. Lu, T. Morrissett, E. Pakalnins, Ultimate strength of resistance spot welds subjected to combined tension and shear, J. Test. Eval. 26 (1998) 213–219. https://www.astm.org/DIGITAL_LIBRARY/JOURNALS/TESTEVAL/PAGES/JTE11994J.htm (accessed January 29, 2022).

[102] S.H. Lin, J. Pan, S.R. Wu, T. Tyan, P. Wung, Failure loads of spot welds under combined opening and shear static loading conditions, Int. J. Solids Struct. 39 (2001) 19–39. https://doi.org/10.1016/S0020-7683(01)00187-1.

[103] S.-H. Lin, J. Pan, S. Wu, T. Tyan, Failure loads of spot weld specimens under impact opening and shear loading conditions, Exp. Mech. 2004 442. 44 (2004) 147–157. https://doi.org/10.1007/BF02428174.

[104] B. Langrand, A. Combescure, Non-linear and failure behaviour of spotwelds: a “global”

finite element and experiments in pure and mixed modes I/II, Int. J. Solids Struct. 41 (2004) 6631–6646. https://doi.org/10.1016/J.IJSOLSTR.2004.06.009.

[105] B. Langrand, E. Markiewicz, Strain-rate dependence in spot welds: Non-linear behaviour and failure in pure and combined modes I/II, Int. J. Impact Eng. 37 (2010) 792–805. https://doi.org/10.1016/J.IJIMPENG.2010.01.004.

[106] J. Song, H.H.-I.J. of M. Sciences, undefined 2011, Failure characterization of spot welds under combined axial–shear loading conditions, Elsevier. (n.d.).

[107] K.S. Pandya, V. Grolleau, C.C. Roth, D. Mohr, Fracture response of resistance spot welded dual phase steel sheets: Experiments and modeling, Int. J. Mech. Sci. 187 (2020) 105869. https://doi.org/10.1016/j.ijmecsci.2020.105869.

[108] J. Song, H.H.-I.J. of M. Sciences, undefined 2011, Failure characterization of spot welds under combined axial–shear loading conditions, Elsevier. (n.d.). https://www.sciencedirect.com/science/article/pii/S0020740311000774 (accessed January 29, 2022).

[109] Y.J. Chao, Ultimate strength and failure mechanism of resistance spot weld subjected to tensile, shear, or combined tensile/shear loads, J. Eng. Mater. Technol. Trans. ASME. 125 (2003) 125–132. https://doi.org/10.1115/1.1555648.

[110] M.E. Barkey, H. Kang, Testing of spot welded coupons in combined tension and shear, Exp. Tech. 23 (1999) 20–22. https://doi.org/10.1111/J.1747-1567.1999.TB01300.X.

[111] B. Langrand, A. Combescure, Non-linear and failure behaviour of spotwelds: a “global” finite element and experiments in pure and mixed modes I/II, Int. J. Solids Struct. 41 (2004) 6631–6646. https://doi.org/10.1016/J.IJSOLSTR.2004.06.009.

[112] A. Arumugam, A. Pramanik, A study of spot weld pull-out failure (PF) mechanism under different loading conditions for stainless steel and mild steel joints, Aust. J. Mech. Eng. 20 (2022) 603–616. https://doi.org/10.1080/14484846.2020.1725348.

[113] M. Pouranvari, S.P.H. Marashi, Failure of resistance spot welds: Tensile shear versus coach peel loading conditions, Ironmak. Steelmak. 39 (2012) 104–111. https://doi.org/10.1179/1743281211Y.0000000066.

[114] A.K. Akela, H. Shashikumar, J.N. Mohapatra, R. Singh, D.S. Kumar, G. Balachandran, The Weldability study of dual phase and transformation induced plasticity automotive steels, Aseestant.Ceon.RsAK Akela, H Shashikumar, JN Mohapatra, R Singh, DS Kumar,

G BalachandranJournal Min. Metall. Sect. B Metall. 2023•aseestant.Ceon.Rs. (2023). https://doi.org/10.2298/JMMB220712014A.

[115] Z. Xu, C. Tian, L. Mao, H. Tian, B. Yi, H. Ling, A mechanical properties and failure mechanism study for resistance spot welded AHSSs under coach-peel and lap-shear loads, Eng. Fract. Mech. 290 (2023) 109474. https://doi.org/10.1016/j.engfracmech.2023.109474.

[116] N. Chen, H.P. Wang, B.E. Carlson, D.R. Sigler, M. Wang, Fracture mechanisms of Al/steel resistance spot welds in coach peel and cross tension testing, J. Mater. Process. Technol. 252 (2018) 348–361. https://doi.org/10.1016/j.jmatprotec.2017.09.035.

[117] C. Tolton, C. O'Keeffe, M. Worswick, P. Penner, C. Yau, S. Malcolm, J. Dykeman, R. Soldaat, W. Bernert, Investigation of Resistance Spot Weld Failure under Shear Loading in Die Quenched UHSS Assemblies, Master's thesis, in: 7th Int. Conf. Hot Sheet Met. Form. High-Performance Steel, 2020.

[118] S. Singh, S., Schmid, G., and Geo, Fatigue testing of jointed sheet material specimens, IIW-Doc. III. (1992) 992–998.

[119] S. Zhang, Approximate stress intensity factors and notch stresses for common spot-welded specimens, Weld. Res. Suppl. 78 (1999) 173-s-179-s.

[120] F. Seeger, M. Feucht, T. Frank, B. Keding, A. Haufe, An Investigation on Spot Weld Modelling for Crash Simulation with LS-DYNA, 4th LS-DYNA User Forum. (2005) 1–12.

[121] Y.P. Yang, J. Gould, W. Peterson, F. Orth, P. Zelenak, W. Al-Fakir, Development of spot weld failure parameters for full vehicle crash modelling, Sci. Technol. Weld. Join. 18 (2013) 222–231. https://doi.org/10.1179/1362171812Y.0000000082.

[122] C. Qian, H. Ghassemi-Armaki, L. Shi, J. Kang, A.S. Haselhuhn, B.E. Carlson, Competing fracture modes in Al-steel resistance spot welded structures: Experimental evaluation and numerical prediction, Int. J. Impact Eng. 185 (2024). https://doi.org/10.1016/j.ijimpeng.2023.104838.

[123] B.& H. Seeger, F., Feucht, M., Frank, T., Keding, An Investigation on Spot Weld Modelling for Crash Simulation with LS-DYNA, in: 4th LS-DYNA User Forum 1–12, 2005.

[124] C. O'Keeffe, J. Imbert-Boyd, M. Worswick, C. Butcher, S. Malcolm, J. Dykeman, P.

Penner, C. Yau, R. Soldaat, W. Bernert, Examination of Mode i Loading on Resistance Spot Weld Groups in Tailored Hot Stampings, Procedia Eng. 197 (2017) 294–303. https://doi.org/10.1016/j.proeng.2017.08.107.

[125] C. O'Keeffe, Investigation of Resistance Spot Weld Failure in Tailored Hot Stamped Assemblies, Master's thesis, University of Waterloo, 2018.

[126] C.J. Tolton, Characterization of Spot Weld Failure within Weld Groups under Predominantly Shear Loading, Master's thesis, University of waterloo, 2020.

[127] A. Mohamadizadeh, · E Biro, · M Worswick, Novel Double-Half Spot Weld Testing Technique For Damage Progress And Failure Analysis Using Digital Image Correlation Techniques, (123AD). https://doi.org/10.1007/s11340-021-00743-4.

[128] D.J. Radakovic, M. Tumuluru, Predicting resistance spot weld failure modes in shear tension tests of advanced high-strength automotive steels, Weld. J. (Miami, Fla). 87 (2008).

[129] M. Pouranvari, Understanding the factors controlling the interfacial failure strength of advanced high-strength steel resistance spot welds: hardness vs. fracture toughness, Sci. Technol. Weld. Join. 23 (2018) 520–526. https://doi.org/10.1080/13621718.2017.1421303.

[130] Y.J. Chao, Failure mode of spot welds: Interfacial vs Pullout, (2003) 133–137.

[131] M.M.H. Abadi, M. Pouranvari, Failure-mode transition in resistance spot welded DP780 advanced high-strength steel: Effect of loading conditions, Mater. Tehnol. 48 (2014) 67–71.

[132] D.J. Radakovic, M. Tumuluru, An evaluation of the cross-tension test of resistance spot welds in high-strength dual-phase steels, Weld. J. 91 (2012).

[133] M. Pouranvari, S.P.H. Marashi, Failure mode transition in AHSS resistance spot welds. Part I. Controlling factors, Mater. Sci. Eng. A. 528 (2011) 8337–8343. https://doi.org/10.1016/j.msea.2011.08.017.

[134] Z. Hardness, Transition in Interfacial Failure Mechanism of Resistance Spot Welds during Tensile – Shear Loading : Role of Fusion, (2023).

[135] M. Shojaee, A.R.H. Midawi, B. Barber, H. Ghassemi-Armaki, M. Worswick, E. Biro, Mechanical properties and failure behavior of resistance spot welded third-generation advanced high strength steels, J. Manuf. Process. 65 (2021) 364–372.

https://doi.org/10.1016/j.jmapro.2021.03.047.

[136] N. Nadimi, R. Yadegari, M. Pouranvari, Resistance Spot Welding of Quenching and Partitioning (Q&P) Third-Generation Advanced High-Strength Steel: Process–Microstructure–Performance, Metall. Mater. Trans. A Phys. Metall. Mater. Sci. 54 (2023) 577–589. https://doi.org/10.1007/s11661-022-06903-y.

[137] M. Pouranvari, H.R. Asgari, S.M. Mosavizadch, P.H. Marashi, M. Goodarzi, Effect of weld nugget size on overload failure mode of resistance spot welds, Sci. Technol. Weld. Join. 12 (2007) 217–225. https://doi.org/10.1179/174329307X164409.

[138] H. Rezayat, S. Babu, H. Ghassemi-Armaki, Effects of Heat Affected Zone Softening Extent on Strength of Advanced High Strength Steels Resistance Spot Weld, 10th Int. Conf. Trends Weld. Res. (2016) 1–6.

[139] S. Zhang, C. DiGiovanni, L. He, N.Y. Zhou, Weld hardness ratio and liquid metal embrittlement crack's detrimental effect on resistant spot weld strength, Sci. Technol. Weld. Join. 26 (2020) 58–67. https://doi.org/10.1080/13621718.2020.1833517.

[140] S. Zhang, A. Ghatei-Kalashami, A.R.H. Midawi, N.Y. Zhou, A Comparison between Hardness-Scaling and Ball-Indentation Techniques on Predicting Stress/Strain Distribution and Failure Behavior of Resistance Spot Welded Advanced High Strength Steel, J. Manuf. Sci. Eng. Trans. ASME. 144 (2022). https://doi.org/10.1115/1.4053730/1134922.

[141] W. Noh, Y. Koh, K. Chung, J.H. Song, M.G. Lee, Influence of dynamic loading on failure behavior of spot welded automotive steel sheets, Int. J. Mech. Sci. 144 (2018) 407–426. https://doi.org/10.1016/J.IJMECSCI.2018.06.009.

[142] R. Chen, M. Lou, Y. Li, B.E. Carlson, A Critical Nugget Size Prediction Model for Al–Si-Coated Press Hardened Steel Resistance Spot Welds, J. Manuf. Sci. Eng. 144 (2022). https://doi.org/10.1115/1.4051680.

[143] A. Chabok, E. van der Aa, Y. Pei, A study on the effect of chemical composition on the microstructural characteristics and mechanical performance of DP1000 resistance spot welds, Mater. Sci. Eng. A. 788 (2020). https://doi.org/10.1016/J.MSEA.2020.139501.

[144] A. Chabok, H. Cao, E. van der Aa, Y. Pei, New insights into the fracture behavior of advanced high strength steel resistance spot welds, J. Mater. Process. Technol. 301 (2022) 117433. https://doi.org/10.1016/J.JMATPROTEC.2021.117433.

[145] Y. Chao, Failure mode of resistance spot welds: interfacial versus pullout, (2003). https://www.sid.ir/paper/596628/fa (accessed May 26, 2024).

[146] X. Sun, E. Stephens, M.K.-W.J.-N. YORK-, undefined 2007, Effects of fusion zone size and failure mode on peak load and energy absorption of advanced high-strength steel spot welds, App.Aws.Org. (n.d.). https://app.aws.org/wj/supplement/WJ_2007_01_s18.pdf (accessed May 26, 2024).

[147] L. Shi, J. Kang, D.R. Sigler, A.S. Haselhuhn, B.E. Carlson, Microstructure and fatigue behavior of novel Multi-Ring Domed resistance spot welds for thin X626-T4 aluminum sheets, Int. J. Fatigue. 119 (2019) 185–194. https://doi.org/10.1016/J.IJFATIGUE.2018.08.022.

[148] Y. Ma, A. Takikawa, J. Nakanishi, K. Doira, T. Shimizu, Y. Lu, N. Ma, Measurement of local material properties and failure analysis of resistance spot welds of advanced high-strength steel sheets, Mater. Des. 201 (2021). https://doi.org/10.1016/J.MATDES.2021.109505.

[149] Y. Ma, Y. Yu, P. Geng, R. Ihara, K. Maeda, R. Suzuki, T. Suga, N. Ma, Fracture modeling of resistance spot welded ultra-high-strength steel considering the effect of liquid metal embrittlement crack, Mater. Des. 210 (2021). https://doi.org/10.1016/J.MATDES.2021.110075.

[150] A. Mohamadizadeh, E. Biro, M. Worswick, Shear band formation at the fusion boundary and failure behaviour of resistance spot welds in ultra-high-strength hot-stamped steel, Sci. Technol. Weld. Join. 25 (2020) 556–563. https://doi.org/10.1080/13621718.2020.1773057.

[151] O. Sherepenko, A. Mohamadizadeh, A. Zvorykina, M. Worswick, E. Biro, S. Jüttner, Determination of resistance spot weld failure path in ultra-high-strength press-hardened steel by control of fusion boundary transient softening, J. Mater. Sci. 56 (2021) 14287–14297. https://doi.org/10.1007/S10853-021-06165-W/FIGURES/10.

[152] A.R.H. Midawi, M. Shojaee, A. Mohamadizadeh, C. Bourque, H. Ghassemi-Aramki, M. Worswick, C. Butcher, E. Biro, A novel technique to measure the local mechanical properties of third generation advanced high strength steel resistance spot welds, Forces Mech. 9 (2022). https://doi.org/10.1016/j.finmec.2022.100150.

[153] M. Shamsujjoha, C.M. Enloe, A.C. Chuang, J.J. Coryell, H. Ghassemi-Armaki,

Mechanisms of paint bake response in resistance spot-welded first and third generation AHSS, Materialia. 15 (2021) 100975. https://doi.org/10.1016/j.mtla.2020.100975.

[154] P. Samadian, L. ten Kortenaar, K. Omer, C. Butcher, M.J. Worswick, Fracture characterization of tailored Usibor® 1500-AS and damage modelling based on a coupled-micromechanical-phenomenological strategy, Eng. Fract. Mech. 223 (2020) 106785. https://doi.org/10.1016/J.ENGFRACMECH.2019.106785.

[155] A.R.H. Midawi, M. Shojaee, A. Mohamadizadeh, C. Bourque, H. Ghassemi-Aramki, M. Worswick, C. Butcher, E. Biro, A novel technique to measure the local mechanical properties of third generation advanced high strength steel resistance spot welds, Forces Mech. 9 (2022). https://doi.org/10.1016/J.FINMEC.2022.100150.

[156] H. Ghassemi-armaki, Q. Khan, A.S. Gill, S. Zilincik, Characterization and Modeling of Spot-Weld Joints in Press Hardening Steels Associated with Softening in Heat Affected Zone, 11th Eur. LS-DYNA Conf. 2017. (2017) 1–13.

[157] P. Wung, A force-based failure criterion for spot weld design, Exp. Mech. 2001 411. 41 (2001) 107–113. https://doi.org/10.1007/BF02323112.

[158] S.-H. Lin, J. Pan, S. Wu, T. Tyan, Failure loads of spot weld specimens under impact opening and shear loading conditions, Exp. Mech. 2004 442. 44 (2004) 147–157. https://doi.org/10.1007/BF02428174.

[159] Livermore Software Technology Corporation, LS-DYNA Keyword User's Manual - Volume II, r:6581, 2015.

[160] Y.J. Chao, Ultimate strength and failure mechanism of resistance spot weld subjected to tensile, shear, or combined tensile/shear loads, J. Eng. Mater. Technol. 125 (2003) 125–132. https://doi.org/10.1115/1.1555648.

[161] J. Lim, J. Ha, C. Oh, Practical Failure Criterion of Spot Weld for Crash Simulation, 10th Eur. LS-DYNA Conf. 2015. (2015) 1–7.

[162] S.H. Lin, J. Pan, T. Tyan, P. Prasad, A general failure criterion for spot welds under combined loading conditions, Int. J. Solids Struct. 40 (2003) 5539–5564. https://doi.org/10.1016/S0020-7683(03)00341-X.

[163] Y. Lee, W. TJ, M. Lu, T. Morrissett, E. Pakalnins, Ultimate strength of resistance spot welds subjected to combined tension and shear, J. Test. Eval. 26 (1998) 213–219.

[164] Q. Khan, H. Ghassemi-armaki, A.S. Gill, S. Zilincik, A. Gawade, Characterization and

Modeling of Spot-Weld Joints with * MAT _ 100 _ DA Parameter Optimization using LS-OPT ® , and 3 Sheet Spot-weld Modeling Method Development in LS-DYNA ®, in: 15th Int. LS-DYNA Users Conf., 2018: pp. 1–16.

[165] J.H. Song, H. Huh, Failure characterization of spot welds under combined axial–shear loading conditions, Int. J. Mech. Sci. 53 (2011) 513–525. https://doi.org/10.1016/J.IJMECSCI.2011.04.008.

[166] J. Ha, H. Huh, Failure characterization of laser welds under combined loading conditions, Int. J. Mech. Sci. 69 (2013) 40–58. https://doi.org/10.1016/j.ijmecsci.2013.01.022.

[167] A.R.H. Midawi, M. Patel, M. Shojaee, K. Pearson, O. Sherepenko, H. Ghassemi-Armaki, E. Biro, Effect of Liquid Metal Embrittlement Indent Cracks on Zinc Coated 3rd Generation AHSS Mechanical Performance, Metals (Basel). 13 (2023) 491. https://doi.org/10.3390/MET13030491.

[168] Y. Zhang, W. Xu, G. Zhang, W. Tao, S. Yang, Mechanical Behavior and Failure Mechanism of Q&P980 Steel During In Situ Post-Weld Heat Treatment (PWHT) Resistance Spot Welding, Metall. Mater. Trans. A Phys. Metall. Mater. Sci. (2022). https://doi.org/10.1007/S11661-021-06546-5.

[169] C. DiGiovanni, E. Biro, N.Y. Zhou, Impact of liquid metal embrittlement cracks on resistance spot weld static strength, Sci. Technol. Weld. Join. 24 (2019) 218–224. https://doi.org/10.1080/13621718.2018.1518363.

[170] E.D.E. Moor, S. Lacroix, A.J. Clarke, J. Penning, J.G. Speer, Effect of Retained Austenite Stabilized via Quench and Partitioning on the Strain Hardening of Martensitic Steels, (n.d.). https://doi.org/10.1007/s11661-008-9609-z.

[171] S.S. Nayak, Y. Zhou, V.H. Baltazar Hernandez, E. Biro, Resistance spot welding of dual-phase steels: Heat affected zone softening and tensile properties, ASM Proc. Int. Conf. Trends Weld. Res. (2013) 641–649.

[172] P. Podržaj, I. Polajnar, J. Diaci, Z. Kariž, Overview of resistance spot welding control, Sci. Technol. Weld. Join. 13 (2008) 215–224. https://doi.org/10.1179/174329308X283893.

[173] J. Messler Robert W., M. Jou, Review of control systems for resistance spot welding: past and current practices and emerging trends, Sci. Technol. Weld. Join. 1 (1996) 1–9. https://doi.org/10.1179/stw.1996.1.1.1.

[174] C. Luo, Y. Zhang, Failure Mode Prediction of Resistance Spot Welded Quenching and Partitioning Steel, MATEC Web Conf. 269 (2019) 03002. https://doi.org/10.1051/matecconf/201926903002.

[175] W. Guo, Z. Wan, P. Peng, Q. Jia, G. Zou, Y. Peng, Microstructure and mechanical properties of fiber laser welded QP980 steel, J. Mater. Process. Technol. 256 (2018) 229–238. https://doi.org/10.1016/j.jmatprotec.2018.02.015.

[176] W. Li, L. Ma, P. Peng, Q. Jia, Z. Wan, Y. Zhu, W. Guo, Microstructural evolution and deformation behavior of fiber laser welded QP980 steel joint, Mater. Sci. Eng. A. 717 (2018) 124–133. https://doi.org/10.1016/j.msea.2018.01.050.

[177] H. Lin, H. Jiang, Y. Wang, S. Tian, Microstructure gradient characteristics and mechanical properties of friction stir welded high strength QP980 steel, Mater. Res. Express. 6 (2019). https://doi.org/10.1088/2053-1591/ab5a92.

[178] M.I. Khan, M.L. Kuntz, Y. Zhou, Effects of weld microstructure on static and impact performance of resistance spot welded joints in advanced high strength steels, Sci. Technol. Weld. Join. 13 (2008) 294–304. https://doi.org/10.1179/174329308X271733.

[179] N. Yurioka, H. Suzuki, S. Ohshita, S. Saito, Determination of Necessary Preheating Temperature in Steel Welding., Weld. J. (Miami, Fla). 62 (1983).

[180] ASTM Standard E8/E8M-13a, "Standard Test Methods for Tension Testing of Metallic Materials," ASTM Int. (2013) 1–27. https://doi.org/10.1520/E0008_E0008M-13A.

[181] Resistance Welding Manufacturing Alliance (RWMA) (2003) Resistance Welding Manual (Revised 4th Edition). American Welding Society (AWS), (n.d.).

[182] Verlag Stahleisen GmbH, Testing and Documentation Guideline for the Joinability of thin sheet of steel - Part 2: Resistance Spot Welding (SEP 1220-2), Düsseldorf, 2011.

[183] U. Bohnenkamp, R. Sandström, G. Grimvall, Electrical resistivity of steels and face-centered-cubic iron, J. Appl. Phys. 92 (2002) 4402–4407. https://doi.org/10.1063/1.1502182.

[184] S. Koley, T. Ray, I. Mohanty, S. Chatterjee, M. Shome, Prediction of electrical resistivity of steel using artificial neural network, Ironmak. Steelmak. 46 (2019) 383–391. https://doi.org/10.1080/03019233.2017.1403109.

[185] K. K.E., Easterling, H., Cerjak, H., Bhadeshia, E., Mathematical Modelling of Weld Phenomena, Inst. Mater. London. (2005) 183–200.

https://doi.org/http://hdl.handle.net/20.500.12708/22735.

[186] G. Krauss, Martensite in steel : strength and structure, 275 (1999) 40–57.

[187] S. Song, M. Shojaee, A.R.H. Midawi, O. Sherepenko, H. Ghassemi-Armaki, E. Biro, Influence of expulsion and heat extraction resulting from changes to electrode force on liquid metal embrittlement during resistance spot welding, J. Mater. Res. Technol. 23 (2023) 1458–1470. https://doi.org/10.1016/J.JMRT.2023.01.093.

[188] D.C. Ramachandran, A.R.H. Midawi, M. Shojaee, O. Sherepenko, H. Ghassemi-Armaki, E. Biro, A comprehensive evaluation of tempering kinetics on 3rd generation advanced high strength steels, Materialia. 26 (2022) 101644. https://doi.org/10.1016/j.mtla.2022.101644.

[189] M. Xia, E. Biro, Z. Tian, Y.N. Zhou, Effects of heat input and martensite on HAZ softening in laser welding of dual phase steels, ISIJ Int. 48 (2008) 809–814. https://doi.org/10.2355/isijinternational.48.809.

[190] P. Fanelli, A. Fino, F. Vivio, Analysis of elastic–plastic behavior and plastic front evaluation in spot welded joints, Int. J. Mech. Sci. 90 (2015) 122–132. https://doi.org/10.1016/J.IJMECSCI.2014.10.013.

[191] A. Ghatei-Kalashami, S. Zhang, M. Shojaee, A.R.H. Midawi, F. Goodwin, N.Y. Zhou, Failure behavior of resistance spot welded advanced high strength steel: The role of surface condition and initial microstructure, J. Mater. Process. Technol. 299 (2022) 117370. https://doi.org/10.1016/J.JMATPROTEC.2021.117370.

[192] A.G. Kalashami, C. DiGiovanni, M.H. Razmpoosh, F. Goodwin, N.Y. Zhou, The Role of Internal Oxides on the Liquid Metal Embrittlement Cracking During Resistance Spot Welding of the Dual Phase Steel, Metall. Mater. Trans. A Phys. Metall. Mater. Sci. 51 (2020) 2180–2191. https://doi.org/10.1007/S11661-020-05702-7.

[193] O.L.R. Ighodaro, E. Biro, Y.N. Zhou, Study and Applications of Dynamic Resistance Profiles During Resistance Spot Welding of Coated Hot-Stamping Steels, Metall. Mater. Trans. A Phys. Metall. Mater. Sci. 48 (2017) 745–758. https://doi.org/10.1007/S11661-016-3899-3.

[194] M. Tamizi, M. Pouranvari, M. Movahedi, The Role of HAZ Softening on Cross-Tension Mechanical Performance of Martensitic Advanced High Strength Steel Resistance Spot Welds, Metall. Mater. Trans. A Phys. Metall. Mater. Sci. 52 (2021) 655–667.

https://doi.org/10.1007/S11661-020-06104-5.

[195] D. Zhao, D. Ren, G. Song, K. Zhao, L. Liu, Z. Zhang, Comparison of mechanical properties and the nugget formation of composite ceramic-centered annular welding and traditional resistance spot welding, Int. J. Mech. Sci. 187 (2020) 105933. https://doi.org/10.1016/J.IJMECSCI.2020.105933.

[196] S. Aslanlar, A. Ogur, U. Ozsarac, E. Ilhan, Welding time effect on mechanical properties of automotive sheets in electrical resistance spot welding, Mater. Des. 29 (2008) 1427–1431. https://doi.org/10.1016/J.MATDES.2007.09.004.

[197] M. Wohner, N. Mitzschke, S. Jüttner, Resistance spot welding with variable electrode force—development and benefit of a force profile to extend the weldability of 22MnB5+AS150, Weld. World. 65 (2021) 105–117. https://doi.org/10.1007/S40194-020-01001-2/FIGURES/18.

[198] F. Xu, G. Sun, G. Li, Q. Li, Failure analysis for resistance spot welding in lap-shear specimens, Int. J. Mech. Sci. 78 (2014) 154–166. https://doi.org/10.1016/J.IJMECSCI.2013.11.011.

[199] C. DiGiovanni, E. Biro, N.Y. Zhou, Impact of liquid metal embrittlement cracks on resistance spot weld static strength, Sci. Technol. Weld. Join. 24 (2019) 218–224. https://doi.org/10.1080/13621718.2018.1518363.

[200] T. Chen, Z. Ling, M. Wang, L. Kong, Effect of post-weld tempering pulse on microstructure and mechanical properties of resistance spot welding of Q&P1180 steel, Mater. Sci. Eng. A. 831 (2022) 142164. https://doi.org/10.1016/J.MSEA.2021.142164.

[201] Y.L. Lee, T.J. Wehner, M.W. Lu, T.W. Morrissett, E. Pakalnins, Ultimate Strength of Resistance Spot Welds Subjected to Combined Tension and Shear, J. Test. Eval. 26 (1998) 213–219. https://doi.org/10.1520/jte11994j.

[202] D. Anderson, C. Butcher, N. Pathak, M.J. Worswick, Failure parameter identification and validation for a dual-phase 780 steel sheet, Int. J. Solids Struct. 124 (2017) 89–107. https://doi.org/10.1016/j.ijsolstr.2017.06.018.

[203] T. Wierzbicki, Y. Bao, Y. Bai, A new experimental technique for constructing a fracture envelope of metals under multi-axial loading, Proc. 2005 SEM Annu. Conf. Expo. Exp. Appl. Mech. (2005) 1295–1303.

[204] S. Burget, S. Sommer, Modeling of deformation and failure behavior of dissimilar

resistance spot welded joints under shear, axial and combined loading conditions, 13th Int. Conf. Fract. 2013, ICF 2013. 2 (2013) 1589–1600.

[205] M. Pouranvari, S.P.H. Marashi, S.M. Mousavizadeh, Failure mode transition and mechanical properties of similar and dissimilar resistance spot welds of DP600 and low carbon steels, Sci. Technol. Weld. Join. 15 (2010) 625–631. https://doi.org/10.1179/136217110X12813393169534.

[206] S. Dancette, D. Fabrègue, V. Massardier, J. Merlin, T. Dupuy, M. Bouzekri, Experimental and modeling investigation of the failure resistance of Advanced High Strength Steels spot welds, Eng. Fract. Mech. 78 (2011) 2259–2272. https://doi.org/10.1016/j.engfracmech.2011.04.013.

[207] S. Hu, A.S. Haselhuhn, Y. Ma, Y. Li, B.E. Carlson, Z. Lin, Influencing mechanism of inherent aluminum oxide film on coach peel performance of baked Al-Steel RSW, Mater. Des. 197 (2021) 109250. https://doi.org/10.1016/J.MATDES.2020.109250.

[208] F. Khameneh, A. Abedini, C. Butcher, Lengthscale effects in optical strain measurement for fracture characterization in simple shear, Int. J. Fract. 232 (2021) 153–180. https://doi.org/10.1007/s10704-021-00598-9.

[209] S. Pawar, A.K. Singh, K.-S. Park, S.-H. Choi, Effect of welding current on the microstructural evolution and lap-shear performance of resistance spot-welded 340BH steel, (2023). https://doi.org/10.1016/j.matchar.2023.113126.

[210] O.T. Betiku, M. Shojaee, O. Sherepenko, A.R.H. Midawi, A.M. Chertov, H. Ghassemi-Armaki, R.G. Maev, E. Biro, Optimizing post-weld performance of press-hardened steel resistance spot welds by controlling fusion zone porosity, Weld. World. 66 (2022) 1733–1746. https://doi.org/10.1007/s40194-022-01332-2.

[211] F. Seeger, G. Michel, M. Blanquet, Investigation of spot weld behavior using detailed modeling technique, 7. LS-DYNA Anwenderforum. (2008) 29–38. https://www.dynamore.ch/de/download/papers/forum08/dokumente/B-I-03.pdf.

[212] B. Watson, M.J. Worswick, D.S. Cronin, Quantification of mixed mode loading and bond line thickness on adhesive joint strength using novel test specimen geometry, Int. J. Adhes. Adhes. 102 (2020) 102682. https://doi.org/10.1016/j.ijadhadh.2020.102682.

[213] C. O'Keeffe, "Experimental determination and computational prediction of load-bearing behavior of spot-welded components made of sheet steel connections under crash loading

with the help of engineering concepts". FAT / AVIF A172, February 2004, University of Waterloo, 2018.

[214] C. Tolton, C. O'Keeffe, A. Mohammadizadeh, J. Imbert, M. Worswick, Investigation of resistance spot weld failure in tailor hot stamped assemblies, Int. J. Impact Eng. 180 (2023) 104677. https://doi.org/10.1016/j.ijimpeng.2023.104677.

[215] C. Cayron, ARPGE: a computer program to automatically reconstruct the parent grains from electron backscatter diffraction data, J. Appl. Crystallogr. 40 (2007) 1183. https://doi.org/10.1107/S0021889807048777.

[216] A.R.H. Midawi, C.H.M. Simha, A.P. Gerlich, Novel techniques for estimating yield strength from loads measured using nearly-flat instrumented indenters, Mater. Sci. Eng. A. 675 (2016) 449–453. https://doi.org/10.1016/j.msea.2016.08.056.

[217] A.R.H. Midawi, C.H.M. Simha, A.P. Gerlich, Assessment of yield strength mismatch in X80 pipeline steel welds using instrumented indentation, (2018). https://doi.org/10.1016/j.ijpvp.2018.09.014.

[218] S. Sarmast-Ghahfarokhi, A.R.H. Midawi, V. Yasnogorodski, M.J. Benoit, Y.N. Zhou, Improvement of the mechanical performance of ZnAlMg coated steel brazed joints through precipitation-based strengthening, (2023). https://doi.org/10.1016/j.msea.2023.145657.

[219] A.R.H. Midawi, M. Shojaee, A. Mohamadizadeh, C. Bourque, H. Ghassemi-Aramki, M. Worswick, C. Butcher, E. Biro, A novel technique to measure the local mechanical properties of third generation advanced high strength steel resistance spot welds, (2022). https://doi.org/10.1016/j.finmec.2022.100150.

[220] D.C. Saha, E. Biro, A.P. Gerlich, Y. Zhou, Effects of tempering mode on the structural changes of martensite, Mater. Sci. Eng. A. 673 (2016) 467–475. https://doi.org/10.1016/j.msea.2016.07.092.

[221] E.I. Galindo-Nava, P.E.J. Rivera-Díaz-Del-Castillo, A model for the microstructure behaviour and strength evolution in lath martensite, Acta Mater. 98 (2015) 81–93. https://doi.org/10.1016/J.ACTAMAT.2015.07.018.

[222] P.E.J. Rivera-Díaz-Del-Castillo, K. Hayashi, E.I. Galindo-Nava, Computational design of nanostructured steels employing irreversible thermodynamics, Mater. Sci. Technol. 29 (2013) 1206–1211. https://doi.org/10.1179/1743284712Y.0000000179.

[223] R.L. Fleischer, Substitutional solution hardening, Acta Metall. 11 (1963) 203–209. https://doi.org/10.1016/0001-6160(63)90213-X.

[224] X. Wei, L. Sun, Z. Zhang, Y. Zhang, J. Luan, Z. Jiao, C.T. Liu, G. Zhao, Achieving superior low-temperature toughness in high-strength low-carbon steel via controlling lath boundary segregation, J. Mater. Res. Technol. 24 (2023) 1524–1536. https://doi.org/10.1016/J.JMRT.2023.03.110.

[225] N. Nadimi, M. Pouranvari, R. Ansari, M. Pouranvari, Understanding fusion zone hardness in resistance spot welds for advanced high strength steels: Strengthening mechanisms and data-driven modeling, J. Mater. Res. Technol. 26 (2023) 5549–5565. https://doi.org/10.1016/j.jmrt.2023.08.251.

[226] O.T. Betiku, D.C. Ramachandran, A. Ghatei-kalashami, C. DiGiovanni, O. Sherepenko, H. Ghassemi-Armaki, E. Biro, Improving the mechanical performance of press-hardened steel resistance spot welds via in-situ grain refinement, J. Mater. Process. Technol. 320 (2023) 118122. https://doi.org/10.1016/j.jmatprotec.2023.118122.

[227] C. Zhang, Q. Wang, J. Ren, R. Li, M. Wang, F. Zhang, K. Sun, Effect of martensitic morphology on mechanical properties of an as-quenched and tempered 25CrMo48V steel, Mater. Sci. Eng. A. 534 (2012) 339–346. https://doi.org/10.1016/j.msea.2011.11.078.

[228] S. Morito, J. Nishikawa, T. Maki, Dislocation Density within Lath Martensite in Fe-C and Fe-Ni Alloys, ISIJ Int. 43 (2003) 1475–1477. https://doi.org/10.2355/ISIJINTERNATIONAL.43.1475.

[229] R. Martin, D. Mari, R. Schaller, Influence of the carbon content on dislocation relaxation in martensitic steels, Mater. Sci. Eng. A. 521–522 (2009) 117–120. https://doi.org/10.1016/j.msea.2008.09.159.

[230] P. Wung, A force-based failure criterion for spot weld design, Exp. Mech. 2001 411. 41 (2001) 107–113. https://doi.org/10.1007/BF02323112.

[231] C. DiGiovanni, M. Shojaee, E. Biro, N.Y. Zhou, Effect of External Loading on Liquid Metal Embrittlement Severity during Resistance Spot Welding, Manuf. Lett. 33 (2022) 11–14. https://doi.org/10.1016/j.mfglet.2022.06.003.

[232] L. Bertin, Tensile Strength of Automotive Aluminum Joints Using Resistance Spot Welding, Self-Piercing Riveting and Adhesive Hybrid Joining, (2014). http://scholar.uwindsor.ca/etd.

[233] S. Kou, Welding Mettalurgy, 2nd ed., Wiley-Interscience, 2003.

[234] T. Huin, S. Dancette, D. Fabrègue, T. Dupuy, Investigation of the failure of advanced high strength steels heterogeneous spot welds, Metals (Basel). 6 (2016). https://doi.org/10.3390/met6050111.

Appendix A: In-situ Tracking of Projected Nugget Orientation Throughout CP Tests

The following analysis provides load components acting on the projected nugget edge as a function of coupon geometry and nugget orientation. Accounting for the evolution of load components at the FZ edge should lead to a more accurate estimation of critical load/moments since failure is always initiated from the notch region. A static equilibrium analysis was conducted on the coach peel coupons to estimate the evolution of bending moment, shear, and tensile forces acting on the RSW projected FZ edge throughout the tests. The coupon is assumed to be constructed of four rigid beams defined by eight point inspectors (P_1-P_8) that construct four position vectors $\overrightarrow{p_1p_2}$, $\overrightarrow{p_3p_4}$, $\overrightarrow{p_5p_6}$, and $\overrightarrow{p_7p_8}$. The intersection of vectors $\overrightarrow{p_1p_2}$ and $\overrightarrow{p_3p_4}$ is referred to as point P_9. A schematic representation of the undeformed and deformed coach peel coupon can be seen in Figure A.1 (a) and (b), respectively.

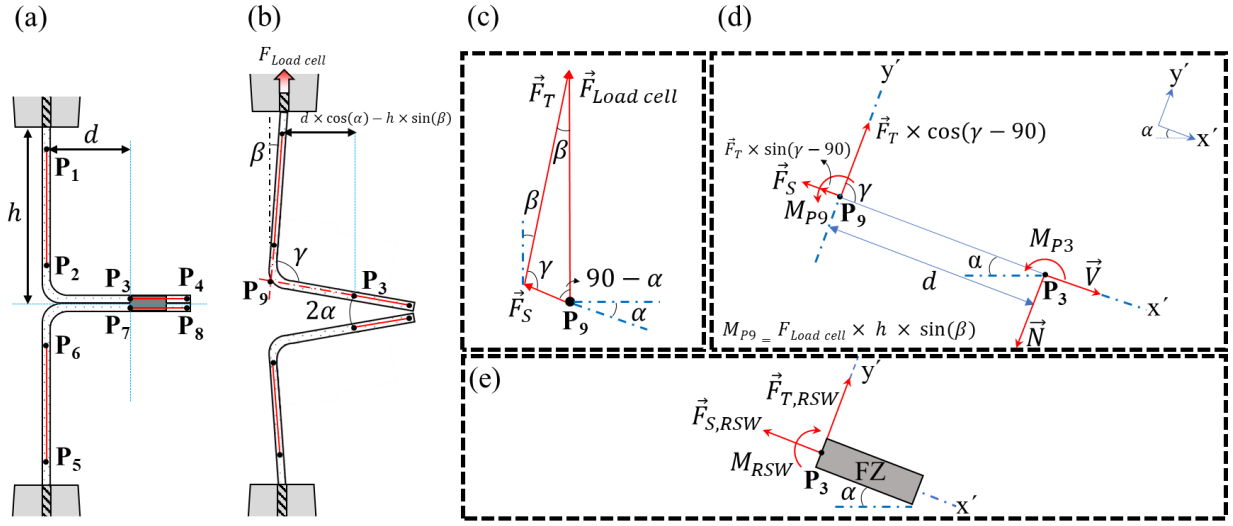


Figure A.1. Schematic drawing showing the configuration of the coach peel specimen (a) at the beginning of the test, and (b) n^{th} frame after starting the test. (c) Sine law can be implemented for the force triangle formed at P_9 to resolve the $\vec{F}_{Load\ cell}$ into components acting along the upper arm of $\overrightarrow{p_1p_2}$ ($\vec{F}_T$) and lower arm of $\overrightarrow{p_3p_4}$ ($\vec{F}_S$). (d) Free body diagram showing forces and moments acting on the P_9P_3 arm. (e) Resultant shear force, tensile force, and moments acting on projected RSW FZ edge. (angles and vector magnitudes are exaggerated for improved visualization).

The total opening angle, 2α, is determined by the dot product:

$$\cos(2\alpha) = \frac{\overrightarrow{p_3p_4} \cdot \overrightarrow{p_7p_8}}{|\overrightarrow{p_3p_4}||\overrightarrow{p_7p_8}|} \qquad \text{A (1)}$$

The upper and lower arms of the coach peel coupon do not necessarily remain perpendicular to one another. The angle γ, is readily calculated from the dot product:

$$\cos(\gamma) = \frac{\overrightarrow{p_1p_2} \cdot \overrightarrow{p_3p_4}}{|\overrightarrow{p_1p_2}||\overrightarrow{p_3p_4}|} \quad \text{A (2)}$$

The angle β, which develops due to rotation of the upper arm and its fixed position in the grip of the tensile frame can be calculated as:

$$\beta = 90 - tan^{-1}\left(\frac{\delta x_{p1p2}}{\delta y_{p1p2}}\right) \quad \text{A (3)}$$

The bending moment imposed upon the weld, M_{RSW}, can be defined using the measured force at the load cell, $F_{Load\ cell}$, and the effective moment arm, d_e:

$$M_{RSW} = \left|\vec{F}_{Load\ cell}\right| \times d_e = \left|\vec{F}_{Load\ cell}\right| \times [d \times cos(\alpha) - h \times sin(\beta)] \quad \text{A (4)}$$

Figure A.1 (c) shows the force triangle formed by resolving the $\vec{F}_{Load\ cell}$ into its respective components along the upper and lower arms of the top coach peel coupon ($\vec{F}_T$ and $\vec{F}_S$, respectively, are parallel with $\overrightarrow{p_1p_2}$ and $\overrightarrow{p_3p_4}$). The sine law is used to calculate the instantaneous magnitude of $\vec{F}_T$ and $\vec{F}_S$:

$$\left|\vec{F}_T\right| = \frac{\left|\vec{F}_{Load\ cell}\right| \cos(\alpha)}{\sin(\gamma)}; \left|\vec{F}_S\right| = \frac{\left|\vec{F}_{Load\ cell}\right| \sin(\beta)}{\sin(\gamma)} \quad \text{A (5)}$$

The free body diagram shown in Figure A.1 (d) illustrates the resultant forces and moments acting on the lower arm P_9P_3. It is noted that the orthogonal x′y′ coordinate system is defined based on the instantaneous orientation of the lower arm. The resultant shear and tensile forces $\vec{V}$ and $\vec{N}$ at the FZ boundary located at P_3 are readily determined from equilibrium:

$$\left|\vec{F}_{S,RSW}\right| = \left|\vec{V}\right| = \frac{\left|\vec{F}_{Load\ cell}\right|}{\sin(\gamma)}[\sin(\beta) - \cos(\alpha)\cos(\gamma)] \quad \text{A (6)}$$

$$\left|\vec{F}_{T,RSW}\right| = \left|\vec{N}\right| = \left|\vec{F}_{Load\ cell}\right| \cos(\alpha) \quad \text{A (7)}$$

where $\vec{F}_{S,\,RSW}$, and $\vec{F}_{T,\,RSW}$ are shear and tensile forces acting at the projected edge of the RSW FZ, respectively as shown in Figure A.1 (e). It is noted that any compressive contact between the lower arms due to the overhang distance, *s*, has been ignored. The overhang distance should be minimized with distances of 4.5-7.2 mm in the present study as outlined in Table 5.2. As shown

in Figure A.2, the most noticeable development of the shear force component was related to the long arm FDWS cases with average critical $F_{S,\,RSW}/F_{T,\,RSW}$ ratios of 0.498 and 0.191, for 3G-980 and 3G-1180, respectively. For all other cases, a negligible critical shear component was developed with $F_{S,\,RSW}/F_{T,\,RSW}$ ratios varying between 0.008 and 0.066. As for other force components, similar critical values, as reported in Figure 5.7, were calculated.

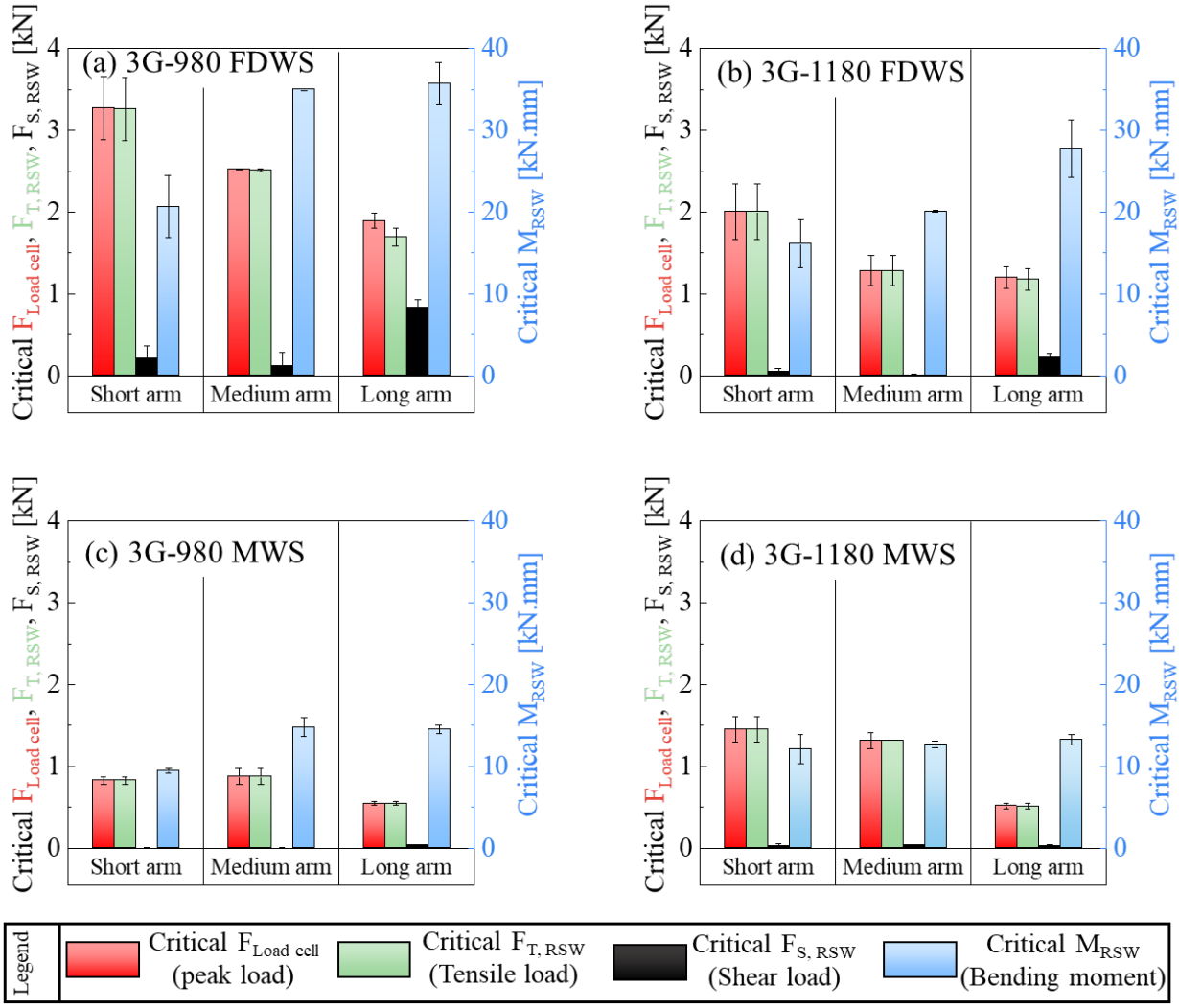


Figure A.2. Influence of coach peel coupon geometry on critical $F_{Load\ cell}$, $F_{T,\,RSW}$, $F_{S,\,RSW}$, and M_{RSW} applied to the projected edge of the RSW FZ for (a) 3G-980 FDWS, (b) 3G-1180 FDWS, (c) 3G-980 MWS, and (d) 3G-1180 MWS welding conditions.